Electrostatic MEMS Bifurcation Sensors

by

Majed Alghamdi

A thesis
presented to the University of Waterloo
in fulfillment of the
thesis requirement for the degree of
Doctor of Philosophy
in
Systems Design Engineering

Waterloo, Ontario, Canada, 2018

Examining Committee Membership

The following served on the Examining Committee for this thesis. The decision of the Examining Committee is by majority vote.

External Examiner	Jeffrey Rhoads Professor
Supervisor	Eihab Abdel-Rahman Professor
Internal Member	Glenn Heppler Professor
Internal Member	John Yeow Professor
Internal-external Member	Alexander Penlidis Professor

Author's Declaration

I hereby declare that I am the sole author of this thesis. This is a true copy of the thesis, including any required final revisions, as accepted by my examiners.

I understand that my thesis may be made electronically available to the public.

Abstract

We report experimental evidence of a new instability in electrostatic sensors, dubbed quasi-static pull-in, in two types of micro-sensors operating in ambient air. We find that the underlying mechanism and features of this instability are distinct from those characterizing hitherto known static and dynamic pull-in instabilities. Specifically, the mechanism instigating quasi-static pull-in is a global Shilnikov homoclinic bifurcation where a slow-varying waveform drives the sensor periodically through a saddle-node bifurcation. Based on these findings, we propose a new taxonomy of pull-in instabilities in electrostatic sensors.

Experimental evidence of nonlinear chaotic behaviors were observed in an electrostatic MEMS sensor. Period doubling bifurcation (P-2), period three (P-3), and period six (P-6) were observed. A new class of intermittency subsequent to homoclinic bifurcation in addition to the traditional intermittencies of type-I and type-II were demonstrated. Quasiperiodicity and homoclinic tangles leading to chaos were also reported. All of these nonlinear phenomena instigate either banded chaos or full chaos and both are observed in this work. Based on our knowledge, this is the first observation such chaotic behaviors in electrostatic MEMS sensors. All of the experimental observations have been measured optically via a laser Doppler-vibrometer (LDV) in ambient pressure.

Also, a new class of intermittencies was found in the oscillations of an electrostatic sensor. These intermittencies involve a dynamic system spending irregular time intervals in the vicinity of the ghost of an orbit before undergoing bursts that are arrested by landing on a larger attractor. Re-injection into the vicinity of the ghost orbit is noise induced. As a control parameter is increased, switching intermittency of type-I leads to a stable periodic orbit, whereas switching intermittency of type-II leads to a chaotic attractor.

These significant findings in nonlinear dynamic were used to develop novel MEMS sensors.

An electrostatic MEMS gas sensor is demonstrated. It employs a dynamic-bifurcation detection technique. In contrast to traditional gas or chemical sensors that measure (quantify) the concentration of an analyte in analog mode, this class of sensors does not seek to quantify the concentration. Rather, it detects the analyte's concentration in binary mode, reporting ON-state (1) for concentrations above a preset threshold and OFF-state (0) for concentrations below the threshold. The sensing mechanism exploits the qualitative difference between the sensor state before and after the dynamic pull-in bifurcation.

Experimental demonstration was carried out using a laser-Doppler vibrometer to measure the sensor response before and after detection. The sensor was able to detect ethanol vapor concentrations as 100 ppb in dry nitrogen. A closed-form expression for the sensitivity of dynamic bifurcation sensors was derived. It captured the dependence of sensitivity on the sensor dimensions, material properties, and electrostatic field.

An analog dynamic bifurcation mass sensor is developed to demonstrate a sensing mechanism that exploits a quantitative change in the sensor state before and after depositing added mass. A polymeric material was deposited on the top surface of the sensor plate to represent added mass. A variation in the frequency and current amplitude were utilized to demarcate the added mass optically and electrically.

A chemical sensor was also developed to detect mercury in deionized-water in a fashion of analog detection. A polymeric sensing material that has high selectivity to mercury was utilized to captured mercury molecules in water. The sensor was submerged completely in water with a pre-defined flow-rate. The sensor was excited electrostatically. A variation in the frequency response due to added mass was measured electrically using a lock-in amplifier. A frequency-shift was observed while releasing the mercury to the water.

Acknowledgements

First of all, I would like to thank my God for guiding and helping make everything possible while doing this work. I would like to express my deep appreciation to my supervisor, Prof. Eihab Abdel-Rahman for his guidance and help throughout this work. I am very grateful to him for spending a lot of time reviewing my thesis and the publications deriving from this work. Also, I would like to thank my co-advisors, Prof. Mahmoud Khater and Dr. Sangtak Park for their support, encouragement and for spending a lot of their valuable time helping me throughout this work.

I would like to thank my committee members: Prof. Jeffrey Rhoads, Prof. Alexander Penlidis, Prof. Glenn Heppler, and Prof. John Yeow for their comments and time in evaluating my work. I am very grateful to my colleagues Resul Sarta, Mohamed Arabi, Ayman Alneamy Hamid Nafissi, and Ridha Almikhlafi for their cooperations and suggestions through this work. Also, I would like to thank all of my friends at the University of Waterloo for their support and encouragement throughout my research study.

Special thanks to King Abdulaziz City for Science and Technology (KACST) for their scholarship and funding me during my Master degree.

I am extremely thankful to my parents for their sacrifices to help me reach this level of education. I am very grateful to my wife and sons for their support, encouragement and patience throughout my study. My thanks also go to my brothers and sisters for their encouragement and support. Without them I would not have been able to achieve it.

Thank you all so much.

Dedication

To my beloved father, Saleh

To my beloved mother, Azah

To my beloved wife, Shuruq

To my brothers, Mohammad, Hani and Emad

To my sisters, Maha, Manal, Tahani and Amani

and

To my beloved sons, Saleh and Firas

Table of Contents

List of Tables

List of Figures

Chapter 1

Introduction

1.1 Inertial MEMS Actuators and Sensors

Micro-Electro-Mechanical Systems (MEMS) fabrication technology combines electrical and mechanical capabilities in one device at the micro-scale $\propto 10^{-6}$m. Its ability to produce devices that replicate or improve on the performance of larger devices has shifted the way researchers, designers, and manufacturers think. It has introduced significant fabrication advantages, such as high precision, small size, low cost and low power consumption, into electronic and mechanical applications.

MEMS devices are mass produced which helps bring down costs. The size and cost of the large scale devices has restricted their applications. The availability of low cost and small size technology is especially advantageous; for instance, surgeons may require micro-forceps to perform intricate medical procedures. Size reduction of MEMS devices also allows for performance enhancements, such as the integration of several sensors on the same die. The wide range of MEMS applications also stems from their improved sensitivity when deployed as sensors. MEMS sensors have seen applications in a wide range of fields, such as automotive, chemical,

medical, biological, safety, aviation, and telecommunication sectors, where they are well known consumer products today.

MEMS devices are predominately made of silicon which is a semiconductor that can easily handle electrical signals. Most MEMS are fabricated using surface or bulk micromachining [1]. Surface micromachining is a standard process based on the patterning of thin film layers atop of a substrate. It depends on depositing and etching different film layers on the substrate to create MEMS structures. It is commonly utilized commercially in integrated circuit manufacturing [2]. Using surface micromachining, MEMS devices can be integrated with ICs on one chip, thereby enhancing their mechanical and electrical characteristics and further reducing their cost [1–3].

Bulk micromachining is also a standard fabrication process. It depends on patterning a substrate to create structures. It is less expensive than surface micromachining because it involves a lower number of fabrication steps than surface micromachining. It is particularly useful for devices that need thicker structural layers. Most commercially available MEMS pressure and inertial sensors are fabricated by bulk micromachining [1, 3].

By definition, MEMS devices are transducers that transform one form of energy to another. They are classified into sensors or actuators depending on their application. MEMS sensors are used to detect an environmental change and translate it into electrical signal, such as chemical and mechanical sensors. MEMS actuators convert an electrical signal into motion to perform various useful applications, such as the case in micro-motors [4]. In this research, we focus on inertial micro-sensors, which is the most common class of commercial MEMS sensors today. They include MEMS accelerometers, gyroscopes, magnetometers, and microfluidic sensors [2, 4–6]. The small size, low cost, and high performance of MEMS inertial sensors have allowed them to lead the market. Roben and Mounier [7] forecast that the price of inertial sensors will drop by 40% to 60% over the next five years due to increased production and a rise of competition.

MEMS accelerometers have been widely used in automotive applications, such as seat belt control and air bag deployment [8, 9]. Accelerometers are also used in a broad range of applications, such as pedometers, earthquake detection, Wii remote controllers, hard drive protection in laptops, and picture stabilization in camcorders [2, 5]. Accelerometers are designed to measure the acceleration of a body moving in space [1]. Many of them use a sprung proof-mass to measure the acceleration along a single axis [2]. For example, Jianbing et al. [10] introduced an in-plane accelerometer that determines acceleration along a single planar axis by measuring the differential capacitance between two sets of parallel plates when the proof-mass moves. It uses a thin SOI handle layer to enhance sensitivity and obtains a sensitivity of 2.25 V/g and a linearity of 0.5%.

Gyroscopes represent another popular MEMS inertial sensor. They measure angular velocity and are commonly used in navigation systems [2, 11]. The operating principle of vibratory MEMS gyroscopes is to excite oscillations in a drive mode that interacts with rotational motion via a Coriolis force to produce motions along a sense-mode [1]. Chen et al. [12] introduced a tuning fork gyroscope that uses a Lorentz force to excite a drive-mode along the x-axis. When a rotation is present around the z-axis, a Coriolis force causes a change in the capacitance of a parallel plate capacitor aligned along the sense-mode direction (y-axis).

Inertial Measurement Units (IMUs) are a prime example of the advantages of sensor integration facilitated by the small size of MEMS sensors. They combine accelerometers, gyroscopes and magnetometers in one chip [13] to measure translational acceleration and angular rotation around all three axes, as well as reduce drift errors. They offer a good example of the ability of sensor integration to drive enhanced overall performance and offer new capabilities. For example, Ding et al. [14] introduced an IMU specifically designed for medical applications, such as tracking forearm posture over time.

In this research effort, we investigate electrostatic MEMS actuators and sensors. Two cate-

gories of inertial sensors have been addressed: inertial gas sensors in gaseous media and inertial chemical sensors in aqueous media. The sensors considered here are based on novel operational principles that will be discuss in Chapter 3.

1.2 Nonlinear Instabilities in MEMS Actuators and Sensors

The ability of Micro-Electro-Mechanical Systems (MEMS) to replicate or improve on the performance of larger devices at the micro-scale has shifted the way researchers and engineers think. Actuation and sensing are the core applications of MEMS, such as switches [15], micromirrors, clocks, and filters [16, 17]. In all of these applications, electrostatic MEMS offer significant advantages including high force density, low power consumption, and a small foot-print. Recently, researcher have started to use the large oscillations of electrostatic MEMS to design sensors and actuators.

As interest shifts to larger motions, it is hard to ignore the nonlinearity in those systems [18–20]. Sources of nonlinearity in electrostatic MEMS include the dependence of the electrostatic force on displacement, geometric and inertial nonlinearities, and nonlinear damping mechanisms [6]. They result in static and dynamic bifurcations, multivaluedness, and chaos. These phenomena have been exploited to design high sensitivity sensors, large amplitude actuators, mechanical memory bits, and encryption keys [21–25].

One of the most important nonlinear phenomena in electrostatic MEMS is the pull-in instability [26] where the moving structure snaps to the actuation electrode. Recently, we presented a consistent taxonomy of pull-in instabilities and the mechanisms underlying them, Table 1.1, based on the ratio of the excitation frequency f to the actuator's fundamental natural frequency f_1.

Table 1.1: A taxonomy for pull-in instabilities

Type	Frequency Ratio	Mechanism
Static	$f/f_1 \simeq 0$	Saddle-node
Quasi-static	$f/f_1 << 1$	Shilnikov bifurcation
Dynamic	$f/f_n \propto (p/q)$	(i) homoclinic bifurcation (ii) homoclinic tangle (iii) cyclic-fold bifurcation

Static pull-in occurs in response to aperiodic waveforms $(f/f_1 \rightarrow 0)$, such as ramp and step functions, minimizing the impact of inertia and damping. As the voltage between the actuator and an electrode increases, the stable equilibrium (node) and unstable equilibrium (saddle) coincide at a saddle-node bifurcation which demarcates the stability limit. The DC voltage corresponding to that point is called the static pull-in voltage. The size of the margin of stability around the bifurcation is proportional to the rise time of the waveform and the quality factor of the actuator [22, 27–31].

Qausi-static pull-in develops when the excitation frequency is finite but much smaller than the fundamental natural frequency, $f/f_1 << 1$. It is characterized by the appearance of orbits homoclinic to a saddle-focus [32–34] as the instantaneous voltage of the waveform approaches the static pull-in voltage. The underlying mechanism of this instability is Shilnikov bifurcation [35] which demarcates the excitation frequency at which the Shilnikov orbits involving tapping oscillations past the saddle turn into Shilnikov-like orbits involving fast-slow dynamic interactions without tapping oscillations. Quasi-static pull-in is limited to excitation frequencies below the bifurcation point. The location of a Shilnikov bifurcation is a function of the shape and amplitude of the excitation waveform [36].

Dynamic pull-in occurs under resonant waveforms where the excitation frequency and one of the natural frequencies are approximately integer multiples or submultiples of each other $(f/f_n \approx p/q)$, such as the case for primary, superharmonic, and subharmonic resonances [37, 38]. Because of the dynamic amplification available at resonance, dynamic pull-in tends to occur at lower RMS voltage than static pull-in [39]. It occurs subsequent to a homoclinic bifurcation leading to a homoclinc entanglement and an erosion in the safe motion basin [38, 40–43]. Alsaleem et al. [44] found that pull-in occurs when erosion reaches about 50% of the basin of attraction. It may also occur subsequent to a cyclic-fold bifurcation [38, 44, 45], specially in the presence of significant damping.

A margin of stability for quasi-static pull-in and dynamic pull-in exists around the stable manifold of the saddle. Transients around a Shilnikov-like orbit or a stable orbit that cause the actuator to wander beyond this margin also lead to quasi-static or dynamic pull-in [28, 39], respectively. Further, the bifurcations underlying quasi-static pull-in and dynamic pull-in are sensitive to initial conditions. While it is possible to locate these bifurcations under steady-state conditions for a given waveform, it is not possible to define DC or AC voltage values corresponding to quasi-static or dynamic pull-in.

Another consequence of large motions in electrostatic MEMS is the appearance of chaotic motions. Chaos has been found to arise via various routes: homoclinic tangles, cascades of period-doubling bifurcations, intermittencies, and torus breakdown [46]. Rulle and Takens found that chaos occurred during the transition of viscous incompressible fluids from laminar to turbulent flow [47]. Cascades of period doubling bifurcations culminating in chaos were numerically observed in the population of seasonally breeding organisms [48] and Rayleigh-Benard flow [49, 50]. Simoyi et al. [51] first observed experimentally a period-doubling route to chaos and the periodic windows within the resulting chaotic attractor in a stirred flow reactor. The bifurcation set of an RLC circuit was found to include period-doubling routes to chaos and period-

doubling bubble structures [52]. It was also found that period-doubling routes to chaos arise subsequent to a symmetry breaking bifurcation [53].

Cascades of period-doubling bifurcation routes to Shilnikov chaos were observed in heterogeneous catalytic oxidation of methanol, peroxidase-oxidase reaction and a piecewise-linear model of a Rossler oscillator [54–56]. Further, Herzel et al. [54] observed type-II intermittency subsequent to a secondary subcritical Hopf bifurcation in their reaction. Parthimos et al. [57] showed experimentally and numerically the transition between Shilnikov chaos and a type-III intermittency due to a subcritical period-doubling in isolated rabbit ear arteries.

Chaotic behavior in MEMS actuators was predicted numerically in atomic force microscopes and other MEMS devices [58–65]. Liu et al. [62] developed a model for a micro-cantilever beam impacting the substrate and found period-doubling bifurcations, indeterminacy, chaos, and strange attractors. De et al. [65] numerically observed a cascade of period-doubling bifurcations leading to banded chaos in interdigitated biastable switches and micro-mirrors excited in superharmonic resonance. Najar et al. [43] studied electrostatically the dynamic behaviors of fixed-fixed beam excited at the primary resonance and superharmonic resonance of order one-half. Pull-in instabilities, period doubling bifurcation, and homoclinc bifurcation were intensively interpreted numerically. They found that a symmetry-breaking bifurcation is not essential to initiate the period doubling bifurcation as the orbit itself is asymmetric. Also, a homoclinc bifurcation was found when the excitation frequency approaches closely to the saddle.

Experimental evidence of chaos has been scarce in MEMS. Hu et al. [66] observed chaos in the transition of AFM probes from non-contact to tapping mode oscillations. Carmon et al. [67] observed cascades of period-doubling bifurcations leading to chaos in spheroid and toroid optical cavities excited optically.

In electrostatic MEMS, Wang et al. [68] demonstrated stable period-two and period-three

orbits as well as long-period and chaotic attractors in the motions of noninterdigitated electrostatic comb-finger actuators excited at primary resonance. Bienstman et al. [69] demonstrated a period-doubling route to chaos for a self-excited fixed-fixed beam actuator during impact motions with the substrate. Demartini et al. [70] demonstrated two-well chaos in the response of noninterdigitated comb finger actuators.

A new class of intermittencies, switching intermittency, was observed in the oscillations of an electrostatic MEMS actuator in ambient air [71]. Like other intermittencies, it is characterized by stretches of laminar flow in the vicinity of a ghost (or unstable) orbit interrupted at irregular interval by bursts. Unlike other intermittencies, the burst in this case is arrested by an attractor where the actuator spends irregular intervals of time before being re-injected into the area of the ghost orbit. In type-I switching intermittency bursts are arrested by a stable tapping-mode orbit . In type-II switching intermittency evolving bursts are arrested by a chaotic attractor.

1.3 Inertial Gas Sensors

Micro-mass sensors have been widely used as sensing platforms for inertial gas sensors in chemical, medical, and automotive application [72–74]. The sensors are coated with highly selective detector materials to capture target gases. They detect the presence of a gas in ambient air as a small variation in the sensor mass, on the order of atto- to zepto-grams [72, 75, 76]. The response of gas sensors can be measured optically [74, 77–80], capacitively [81–83], or piezoresistively [84–86]. Optical readout is more accurate but less practical than other measurement techniques. MEMS gas sensors have significant advantages in size, cost, and power consumption; however, they also have significant challenges in long-term reliability and selectivity [73, 87].

Lange et al. [88] detected n-octane and toluene vapors using an array of cantilever beams coated with PEUT. They found that the sensor sensitivity increased with the polymer coat thick-

ness. Sampath et al. [89] found analytically that the thickness of the sensor polymer coat can shift the natural frequency down by 30 %. These results illustrate the competing effects of the detector material. While increasing the surface coverage and thickness of the detector material increases the amount of gas sorbed, and thereby sensitivity to gas, the associated increase in the effective mass of the sensor reduces its mass sensitivity. Despite the variations in the polymer thickness affecting the sensitivity of a cantilever sensor, Dufour et al. [90] found that uncoated cantilever beams do not have intrinsic selectivity.

The two most commonly used detection modes in gas sensors are static and dynamic. The static mode measures mass sorbed onto the detector material as a change in structural displacement. Jensenius et al. [84] measured the static deflection of a cantilever alcohol vapor sensor. Zhu et al. [86] measured the static deflection of a V-shaped cantilever beam sensor to detect trinitrobenzene vapor. Datskos and Sauers [77] employed static optical sensing of a gold-coated cantilever to detect 2-mercaptoethanol vapor.

The dynamic mode measures the shift in one of the resonant frequencies induced by a mass sorbed onto the detector material [75]. The sensitivity of this sensing mode is higher than that of the static (or forced) sensing modes by 1-2 orders of magnitude [41, 91]. Therefore, it has the ability to increase absolute mass detection and realize highly sensitive gas sensors [92]. Exciting higher structural modes can further improve sensitivity by decreasing the effective mass and increasing the quality factor [78–80, 92–98]. Dohn et al.'s [78] experimental results revealed that the sensitivity of a cantilever beam mass sensor was increased 276 times when the fourth bending mode was utilized instead of the first bending mode. Xie et al. [80] experimentally compared mass detection of a ragweed pollen using the first and second bending modes as well as the higher frequency first torsional mode of a cantilever beam. They found that the sensitivity of the first torsional mode was one order-of-magnitude higher than the first and second bending modes. Debédá et al. [95] found that higher frequency longitudinal modes of a cantilever beam

sensor were more sensitive than lower frequency bending modes.

A class of inertial sensors seeks to use bifurcations to enhance sensitivity [6, 21, 22, 99, 100]. One group of researchers has employed bifurcations in the vicinity of principal parametric resonance. Zhang et al. [91] exploited the subcritical pitchfork bifurcation at the upper end of the instability window in an electrostatic comb-finger resonator to detect water vapor down to 0.7 pg. Li et al. [101] employed the supercritical pitchfork bifurcation at the lower end of the instability window of a piezoelectrically actuated fixed-fixed beam to detect 1.38 ppb of 2,4 DNT. Azizi et al. [102] investigated numerically a similar mass sensor employing the subcritical pitchfork bifurcation at the upper end of the instability window and predicted a minimum measurable mass of 20 fg.

Other groups have employed bifurcations of directly excited resonators. Harne et al. [103] demonstrated a mass sensor that detects added mass through a shift in the location of a cyclic-fold bifurcation in the vicinity of primary resonance of a bistable cantilever beam. Kumar et al. [104] demonstrated a methanol sensor that detects change in the response size past a cyclic-fold bifurcation of piezoelectrically excited cantilever beam.

Younis and Alsaleem [41] introduced two electrostatic MEMS sensors that measure added mass as a shift in the locations of a cycle-fold bifurcation in the vicinity of primary resonance and a subcritical pitchfork bifurcation in the vicinity of subharmonic resonance of order one-half. Nguyen et al. [105] proposed a method for detecting added mass onto electrostatically actuated clamped-clamped beams. It employs change in the response size past a cyclic-fold bifurcation in the vicinity of primary resonance. Bouchaala et al. [24] used electrostatically actuated fixed-fixed beams to detect water vapor by measuring the change in amplitude during frequency-up and down sweeps past a cyclic fold bifurcation in the vicinity of primary resonance. They measured a minimum detectable mass of 395 pg.

Nayfeh and co-workers [100, 106] proposed two types of binary electrostatic MEMS gas sensors: a static sensor based on the shift in the location of a saddle-node bifurcation and a dynamic sensor based on the shift in the location of a cyclic-fold bifurcation. They demonstrated experimentally that the static binary sensor can detect 5 ppm of ethanol in dry nitrogen (a mass of 165 pg) [22, 107].

In this work, we present the dynamic binary gas sensor and test its potential to detect ethanol vapor in dry nitrogen. The sensor exploits a cyclic-fold bifurcation in the vicinity of primary resonance of an electrostatic MEMS sensor to create the discrete (binary) output states. A jump in response from low to high indicates a gas concentration in excess of a threshold value. We present the experimental verification of this detection principle, in addition to a numerical model to interpret the sensor behavior. We present a closed-form expression for the sensor sensitivity using the multiple-scale method. Finally, we report the sensor outcomes and limitations.

1.4 Inertial Chemical Sensors

Microelectromechanical (MEMS) sensors are utilized substantially nowadays in many industrial applications especially in liquid media such as biological, chemical, environmental, navigational and medical applications [74, 90, 108–113]. Underwater pollutions is one of environmental issues that are incredibly increased nowadays. The demand of designing sensors to detect toxic materials, organisms and/or hazard substances as mercury, cadmium, and copper in water is significantly increased in order to save peoples lives [114]. Therefore, recently research has turned its attentions toward those toxic substances in various aqueous media utilizing MEMS sensors [74, 112, 115, 116]. However, dealing with aqueous medium is not easy especially for MEMS sensors. Many challenges exist when immersing MEMS sensors in liquid media such as fluid resistance, damping, surface tension, electrolysis and thermal conductivity [117–122].

The platform of detection is similar to the way of detecting a specific gas in air. A detector material is used to identify a certain substance in water compared to others in the vicinity. The response of the detection can be obtained optically [112, 118, 123–125], thermally [122], or electrically [121, 126–129].

The multi-user MEMS process (MUMPs) is a vulnerable technology that has many challenges when used in a fluid medium [118]. Electrolysis (bubbles), electrode polarization (formed an isolation layer), surface tension (stiction), thermal and electrical conductivity (bypass current) are the most common challenges in liquid media [118, 119]. However, most of those challenges can be treated experimentally utilizing various experimental techniques in order to avoid or reduce their effect on the sensor response.

Much experimental work has been carried out trying to overcome those hurdles. Based on the literature, some experimental solutions have been defenestrated while others have been verified, such as the validity of applying high frequency ($f \geq 1$ MHz) of a square signal with zero mean value (RMS) to deccelerate chemical reactions and minimize electrolysis and electrode polarization effects. Submerging the sensor completely in water helps to minimize the surface tension that causes stiction. Designing thermal structures with no alternating thermal expansions coefficients can help to reduce thermal conductivity. Lastly, utilizing de-ionized (DI) water can significantly reduce electrical conductivity [94, 118, 119, 122, 130, 131].

Fluid viscous damping and fluid added mass are two other challenges that affect the sensor's structural behavior. Those two structural challenges are proportional to the structure velocity and acceleration, respectively [108, 117, 124, 132–134]. Vibrating MEMS resonators/sensors in fluid exert a resistance leading to energy losses. Unlike the fluid air drag effect which can be neglected in air media, the fluid liquid drag effect has a severe affect on the sensor response in liquid media [94, 94, 116, 117, 123, 127, 135–137]. Some researches [94, 108, 135, 138] studied the effect of fluid viscosity and added mass, and they found that fluid viscosity is more prominent

than fluid added mass by at least three orders of magnitude. On the other hand, increasing the gap distance can be also used to reduce added mass effect [139, 140].

Sader et al. [117] developed an analytical model including the hydrodynamic force of a cantilever beam excited thermally in a viscous fluid. This model can be used quantitatively to approximate the fluid viscosity by obtaining the structural frequency-response curve. Dufour et al. [94] investigated analytically two cantilever beams operated in fluid to study the effect of fluid damping on the sensor sensitivity and its quality factor. Two beams, strong axis-bending (high stiffness) and weak axis bending (low stiffness), were studied at the first flexural vibration mode (out-of-plane mode). They found that using the strong axis-bending mode reduces fluid viscous damping and fluid inertial drag (added mass) which leads to enhanced sensor sensitivity. Also, scaling down the sensor's geometry to the nano-scale ($\approx 100\,\text{nm}$) reduces the viscous damping effect in liquid media [112].

Burg et al. [121] developed a U-microchannel fabricated inside of cantilever beam to avoid fluid drag and fluid damping effects. They used this technique to detect biomolecules, biotinylated bovine serum albumin (bBSA) and Avidin, by coating the structure via a detector material of poly-dimethylsiloxane (PDMS). The sensor was excited electrostatically, and the deflection was measured optically. The shift in the resonant frequency was measured using a lock-in amplifier. A clamped-free U-shaped beam was also investigated by Heinisch et al. [141]. The U-shape beam was made of Tungeston, which has low thermal expansion coefficient, in order to reduce the convection effect in fluid. The structure was immersed in acetone-isopropanopl as well as DI-water to study the effect of fluid viscosity and mass density on its resonant frequency and quality factor. The sensor was excited electromagnetically, via Lorentz force, at the first fundamental out-of plane mode. The change in the frequency response was measured utilizing a lock-in amplifier. Several experiments were conducted with various acetone viscosities at room temperature, T=25 °C. They proved experimentally that increasing the fluid viscosity decreases

the resonant frequency and quality factor.

Further, Vančura et al. [120,127] investigated analytically and experimentally the relationship between fluid mass (fluid drag) and fluid damping effect on a peizoresistive CMOS cantilever beam immersed in different liquids: pure water, glycerol and ethanol solutions with different concentrations using Sader's model [117]. The microcantilever was excited electromagnetically at the first out-of-plane mode, and the response was measured electrically using a Wheatstone bridge. They found that the fluid damping effect is dominant on the narrow cantilever beam compared to the wide one as it allows the fluid flow to move around causing dissipative energy loss. They investigated, in addition, the relationship between the shifts in resonant frequency due to added mass, fluid viscosity and fluid density. The results show that high frequency shift can be measured while increasing fluid density, which is inversely proportional to fluid viscosity. Further, they found that using an in-plane mode or torsional modes with high resonant frequencies leads to enhancing the sensor quality factor.

Youssry et al. [142] investigated analytically and experimentally the fluid viscosity and fluid density effects on a cantilever beam. The beam was immersed in Silicon oils and Dodecane in order to study the viscosity and density of the solutions. The cantilever was excited electromagnetically in a bending mode and the response was measured optically using a laser-Doppler vibrometer. Their results show that the resonant frequency and quality factor decreased significantly with fluid density increase.

Minimizing the effect of operating actuators in aqueous medium has grabbed attention of many researchers [108, 134, 141, 143–145]. Unlike the classical fluid sensors that operate at the fundamental out-of plane mode, high order flexural modes were investigated by [108, 134, 141, 143, 144]. Beardslee et al. [134] investigated the fluid effect by laterally exciting a microcantilever beam. They found that shearing the fluid laterally has the advantage of substantially reducing the fluid added mass effects. Also, they found that the added mass in the out-of plane

mode suppresses the resonant amplitude by 50%, whereas it suppresses it by only 5 –10% when exciting the sensor at the in-plane mode. Lucklum et al. [144] demonstrated a mass sensor based upon a clamped-clamped beam immersed in DI-water, alcohol, and oil fields. The sensor was excited electromagnetically via a Lorentz force, and the response was measured electrically via a network analyzer. Two flexural vibration modes were studied, namely, in-plane and out-of plane modes, in both air and liquids media. The sensor viscosity and added mass were measured based on measuring a shift in the frequency response. They also studied temperature effects on the fluid viscosity, density, sensor resonant frequency, and its quality factor. They found that as the temperature increases, the fluid viscosity decreases resulting in a elevation of the resonant frequency as well as quality factor.

Beardslee et al. [116] demonstrated a microfluidic tube (acrylic ring) fabricated on top of a microcantilever beam in order to study the in-plane flexural vibration mode. The cantilever was excited thermally and the response was measured peizoresistively. A drop of water was injected into the tube to measure the in-plane resonance frequency. They found that the quality factor dropped by about 98% from $Q = 2140$ in air to $Q = 44$ in water; however, the resonant frequency in water only dropped 6.5% compared to that in air medium. They concluded that designing a cantilever beam with a shorter, wider, thinner geometry leads to increasing the quality factor and sensitivity by 3–4 times compared to previous designs. They noted that increasing the beam stiffness leads to suppressing cantilever beam oscillations by generating heat conduction from the excitation resistors. Dufour et al. [90, 108] investigated the structural mode shapes effect on the quality factor in gaseous and liquid media of a cantilever beam excited thermally and measured piezoresistively. Three beams were studied in different directions: in-plane (lateral) bending, out-of-plane (transverse) bending, and axially. They found that the beam resonant frequency and its quality factor was reduced by one order of magnitude when exciting the beam at the out-of plane mode. Also, they explored the dominant factor of reducing the quality factor in liquids is

the hydrodynamic forces. On the other hand, they found that the lateral resonance frequency was reduced by 3-14 % in water compared to air. The quality factor in water was found as $Q = 86$ in lateral mode where it was measured in air as $Q = 10$ at the out-of-plane mode. Further, they found the resonant frequency dropped by only 1.8% at the axial mode when immersed in dodedane (1.5 cP). However, they found that the quality factor decreased significantly from $Q = 353$ in air to $Q = 101$ in dodedane (1.5 cP).

Fluid viscosity in air and water for a cantilever beam was studied analytically by Shabani et al. [145] . They observed a significant change in the structural natural frequencies at higher modes, where the dynamic vibrations of the higher modes play a role of reducing the added mass effect which leads to amplification of the dynamic motions. An analytical lumped-mass model of a laterally-excited tuning fork, of rectangular and circular cross-section, was developed by Heinisch et al. [146, 147]. The model was introduced to investigate the mass density and viscosity effects on the structural resonant frequencies and validate the results experimentally. The sensor was immersed in acetone-isopropanol solutions in a sealed glass tube. The tuning fork was excited electromagnetically and the resonant frequencies were measured using an electrodynamic pick-up, which had a coil with a permanent magnet inside it. A good agreement was found between experimental results and those predicted analytically. Using micro-polar fluid theory, Azma et al. [148] developed analytically an effective damping coefficient for a laterally oscillating comb-finger immersed in viscous fluid. They found that the damping ratio significantly increased as the micro-finger length (surface area) and temperature were increased. However, they observed a lower effect while increasing the gap size and thickness.

Water medium has a high dielectric constant 80 times compared to the air medium. Thus, immersing MEMS actuators/sensors has the advantage to achieve large responses with low power consumption compared to other mediums [118, 119, 125]. Zidan et al. [149] studied the pull-in voltage of a cantilever switch in water. They used COMSOL multiphysics to calculate pull-in

voltage in air and water media. As a result, they found the pull-in voltage in water was reduced significantly 8.2 times than in air, from $V_{pi} = 44\,\text{V}$ in air to $V_{pi} = 5.36\,\text{V}$ in water, and that due to the high permittivity of water, $\epsilon_r = 80.4$. The structure, though, was not immersed completely in water. It was immersed only 85% to avoid surface tension as well as a stiction effect of the drain side.

MEMS actuators in aqueous media have several excitation techniques including electrostatically, electromagnetically, or thermally. A micro-gripper was demonstrated by Su et al. [150] as a magnetic actuator operating in air and in water media. Two cantilevers were made of magnetic materials in order to develop attractive and/or repulsive forces between each other. Experimental results were measured using a vibrating magnetometer. Sameoto et al. [118] investigated optical, electrostatic, and electrothermal actuators in air and DI-water, using image analysis software (IMAQ). Parallel plate and comb drive actuators were excited electrostatically in air and in water. Standard thermal actuators (STA) and chevron actuators were excited thermally in both mediums. A drop of DI-water was placed on top of the actuators and covered with a glass lid. The electrostatic and thermal actuators were excited at $f = 1$ MHz and $f = (0.05 - 1)$ MHz, respectively. They found that the deflection of the electrostatic actuators, parallel plate and comb drive, increased significantly by 60-70 times in DI-water than in air. However, the deflection of the thermal actuators was found to be very low, due to the water thermal conductivity, since thermal conductivity of water is 20 times higher than air. The measured deflections of Chevron and STA actuators in water were found to be 5-9% and 0%, respectively.

In addition, Zhou et al. [122] developed three polymer-based actuators: Nafion ionic conduction actuator, Parylene thermal actuator, and Polyaniline (PANI) actuator, which have an advantage of achieving large deflection with low power consumption. They were actuated thermally, by either exciting them directly by passing current or by heating up the fluid environment. The actuators were based on the stress gradient due to moving ions across the structural layers,

the stress gradient due to the variation of the thermal expansion coefficients of the layers, and the volumetric change due to reversible electromechanical oxidation reduction (redox), respectively. They observed experimentally that electrolysis (bubbles) in DI-water can be treated significantly using parylene material deposited on top of the actuator metal layer when excited by a voltage $V > 1.8$ V. Ramos et al. [133] studied thermally the excited laser beam effect along a microcantilever coated with a gold layer at the first three flexural vibration modes. The microcantilever responses were detected using a photodetector and all of the experiments were conducted in DI-water and Poly-MethylMethAcrylate (PMMA). They found experimentally while exciting the laser beam at the middle of the microcantilever beam, that the amplitude at the resonance frequency increased significantly by 125 times compared to the free-end response. The heat transfer, therefore, was determined to be smaller at the cantilever free-end than along the micro cantilever root.

MEMS sensors in aqueous media have recently seen much attention. Two commonly used sensing mechanism to identify a target mass in a liquid media are static and dynamic sensing modes [94, 120, 124, 127]. The analyte can be detected statically or dynamically based on induced stress/strain changes (measuring deflection) or measuring variations in the frequency shift due to a target mass in the fluid media, respectively. Heinrich et al. [151] and Dufour et al. [90] introduced analytically a static model of a cantilever beam coated with a viscoelastic material. They used relaxation time, diffusion time of the analyte into the coating material as a detection mechanism. Sounart et al. [119] introduced a comb drive actuator excited electrostatically. Static deflection was measured optically via an optical microscope connected to a CCD camera and using image recognition software (NI IMAQ) in order to measure the actuator displacement while immersed in ethylene glycol (EG). They found that the actuation frequency can be increased at least one order of magnitude by accumulating a few nanometers of the native oxide layer in order to reduce electrolysis and polarization issues.

In dynamic detection, measuring variations of the resonant frequency are widely used to quantify absorbed mass in liquid media [90, 112, 123, 124, 129, 135]. Braun et al. [124] developed two bio-cantilever beams coated by avidin and biotin in order to detect proteins of biotinylated and streptavidin latex beads, respectively. The cantilever beam was actuated piezoelectrically and the response was measured optically using a position-sensitive detector (PSD) at its fundamental frequency. Frequency and phase shifts at its resonant frequency were used to detect latex beads. A comparison of its amplitude and phase before and after adding latex beads was used to indicate detection. Their results show that exciting high frequency modes leads to an increase in frequency shifts due to added mass and consequently enhances the sensor sensitivity to 2.5 pg/Hz. Vančura et al. [129] demonstrated biochemical sensors fabricated utilizing CMOS fabrication technology. The sensor consists of a microcantilever beam excited electromagnetically and measured piezoresistivelly, using a Wheatstone bridge. The sensor was coated by two polymers, poly(isobutene) and poly(epichlorohydrine) to detect ethylbenzene, xylene, and toluene with various concentrations (0–400) ppm mixed in DI-water. The variations in the resonant frequency was demonstrated as a detection mechanism. The minimum detectable mass was measured as 50 pg of xylenel at concentration of 6 mg/L.

In addition, Verbridge et al. [112] conducted experiments on biological sensors of nano clamped-clamped and cantilever beams vibrating at the first out-of plane mode. The sensors were excited and detected optically by modulating the amplitudes of a blue laser beam and red laser beam (photodiode), respectively. All of their experimental tests were conducted in air and in fluid using alcohol, water, acetone and buffer solutions. They found that the effect of viscous damping can be reduced significantly when the sensor dimensions were scaled down to the nano-scale. As a result, the sensor can achieve a quality factor of $Q \cong 400$ in air and $Q \cong$ 3 – 10 in liquid. IIic et al. [72] introduced a nano-cantilever detector that can detect a virus by measuring a shift in resonance frequency corresponding to its mass. They experimentally achieved a minimum

detectable mass of 3 fg. Tao et al. [135] demonstrated a bio-chemical sensor consisting of a cantilever beam operated in air and DI-water to detect Escherichia coli and Hg^{2+}. The sensor is excited electrothermally at the in-plane mode by passing a current through the excitation resistors in order to reduce fluid damping as well as fluid mass. The response was measured Piezoresistivelly using a Wheatstone bridge. They used a closed loop resonant system to enhance and develope a sensor quality factor in water in the range of $Q = 14$ to $Q = 249$.

Burg et al. [152] demonstrated a nano-cantilever beam excited electrostatically in soft vacuum. A U-microchannel was implemented in the structure to reduce fluid mass effect. Their detection was based on measuring the shift in the resonant frequency due to adsorbed mass. They measured nano-particles as bacteria and proteins optically, via photodetector (PSD), with a resolution of of 1 ag adsorbed mass with a quality factor of Q =15000. Park et al. [74] introduced a mass sensor supported by four folded springs in order to monitor the evaporation rates of microdroplets of water and dimethyl sulfoxide (DMSO) at various temperatures. The sensor was excited electomagntically in the out-of plane mode, and the motions were measured optically using a laser-Doppler vibrometer. Measuring the shift in the resonant frequency was conducted to demonstrate the microdroplet evaporation time at various temperatures.

Exciting MEMS sensors in water electrostatically has the advantage of achieving high electrical density with minimal current requirements. It produces large oscillations and well-regulated force with small power consumption [118, 119, 153]. Also, it does not put significant restrictions on the sensor design process which leads to a simplified the fabrication process, and thereby reduces its cost.

Recently, researches have moved on investigate nonlinearities in MEMS resonators/sensors immersed in fluids. Jabbari et al. [139] introduced an analytical model of an electrostatic cantilever beam excited at the first out-of plane mode immersed in water, acetone, and carbon tetrachloride. Frequency response curves were obtained as a function of fluid mass and fluid viscosity.

They found that the fluid viscosity has the effect of increasing the softening nonlinearity in the system. The highest response in amplitude was found while immersing the beam in water. Also, they found that the pull-in voltage in water is minimal compared to other fluids and this is due to the dielectric constant of water. Sharafkhani et al. [154] studied the stability and transient response of a fixed-fixed beam excited electrostatically in fluids of Butane, Benzene, Phenol, and Carbon tetrachioride. They found not only that the electrical properties can alter transient response, but also that fluid inertial effect (fluid added mass) leads to a shift in the structural stability point and its pull-in voltage. They also found that each fluid has a transient period and pull-in voltage different from others. They showed that the fluid density effect can be reduced as the structural gap is increased.

1.5 Scope

The objective of this research is to design and demonstrate MEMS actuators and sensors operating in gaseous and aqueous media. Bifurcation gas sensor was designed to detect qualitatively ethanol vapor in dry nitrogen in a fashion of a binary detection. An analog mass sensor was also designed to detect added mass electrically by measuring current. An analog chemical sensor submerged in water was designed to detect mercury in DI-Water.

We demonstrate a dynamic gas sensor based on a cyclic fold bifurcation where a stable orbit and an unstable orbit collide at the fold point. The sensor is actuated by a combined AC-DC voltage at a frequency close to that point. The region around that fold is sensitive to perturbations. At a threshold limit of perturbations, the response jump-up towards a 'larger' sized response. This phenomena will be used to realize binary detection. Releasing ethanol gas inside the test enclosure will cause a jump due to sorbed mass to a polymeric sensing material. A laser-Doppler vibrometer and an oscilloscope will be utilized to observe the jump-up optically and electrically.

We demonstrate an analog mass sensor and underwater sensor operating in air and water. The added mass sensor was utilized to measure the variation in the effective mass electrically. The underwater sensor was designed to detect mercury molecules in water. The detection mechanism is based on measuring a frequency-shift due to the effect of added mass. A polymeric sensing material, which has a high selectively to mercury, was deposited on the sensor. An electrical detection mechanism using a lock-in amplifier was utilized to measure the sensor response.

This research project is organized as follow: in Ch. 2, we present identification of the nonlinear dynamic behaviors of actuators. In Ch. 3, we present detailed numerical and experimental results for the dynamic gas sensor. In Ch. 4, we present experimental results of an analog mass sensor operated in air. In Ch. 5, we present experimental demonstration of the underwater sensor submerged in a mixture solution of DI-water with mercury. In Ch. 6, we conclude all the experimental findings and present the future plans for the existing projects.

1.6 Author's Current Contribution

My contribution in this work includes experimental and analytical studies of MEMS actuators and sensors. Experimental investigation of the nonlinear dynamic behaviors of actuators have been reported. Those numerous phenomenon have been employed for applications as gas and underwater sensors. Experimental and numerical study of bifurcation gas sensors were demonstrated. Also, a closed-form sensitivity for bifurcation sensors was derived. An analog mass sensor was also introduced. A chemical sensor submerged in water was demonstrated. I carried out this work under the supervision of Professor E. Abdel-Rahman and Professor. M. Khater. I hereby acknowledge that a part of the work presented in Chapter 2 and Chapter 3 have been submitted and are under review for publication:

- **M.S. Al-Ghamdi**, M. E. Khater, and E. M. Abdel-Rahman. "Large oscillations of electro-

static actuators", Physical Report, In press.

- **M. S. Al-Ghamdi**, M. E. Khater, and E. M. Abdel-Rahman. "Switching Intermittency, Submitted to Applied Physics Letter (APL) on June 18^{th}, 2018.

- **M.S. Al-Ghamdi**, M. E. Khater, K. M. E. Stewart, A. Alneamy, E. M. Abdel-Rahman, and A. Penlidis. "Dynamic Bifurcation MEMS Gas Sensors", Submitted to Journal of Micrelectromechanical Systems (JMEMS) on March 9^{th}, 2018.

- **M.S. Al-Ghamdi**, M. E. Khater, A. Alneamy, and E. M. Abdel-Rahman, Sensitivity Analysis of Cantilever-Based Bifurcation MEMS Sensors, accepted, International Conference on Structural Nonlinear Dynamics and Diagnosis, Tangier, Morocco, June 2018.

- M. E. Khater, **M. Al-Ghamdi**, S. Park, K. M. E. Stewart, E. M. Abdel-Rahman, A. Penlidis, A. H. Nayfeh, A. K. S. Abdel-Aziz, and M. Basha, "Binary MEMS gas sensors," Journal of Micromechanics and Microengineering, vol. 24, pp. 065007/1-9, 2014.

Chapter 2

Characterization of Nonlinear Electrostatic MEMS Sensors

In this chapter, characterization processes have been conducted to investigate the nonlinear dynamic behavior of sensors. Numerous nonlinear dynamics and routes to chaos have been found and illustrated. Global and local bifurcations under the mechanisms of Shilnikov bifurcation and cyclic-fold bifurcation were intensively investigated, respectively. Also, period doubling bifurcation P-2, period three P-3, and period six P-6 were observed.

In addition, experimental evidence of the new intermittency dubbed switching intermittency, as well as the traditional intermittencies of type-I and type-II were demonstrated. Quasiperiodicity and a homoclinic tangle leading to chaos were also reported.

2.1 Experimental Setup

Experiments were conducted on two types of electrostatic MEMS sensors vibrating in their first out-of-plane bending mode. Sensor # 1, Fig. 2.1 (a), is a microcantilever beam, whereas sen-

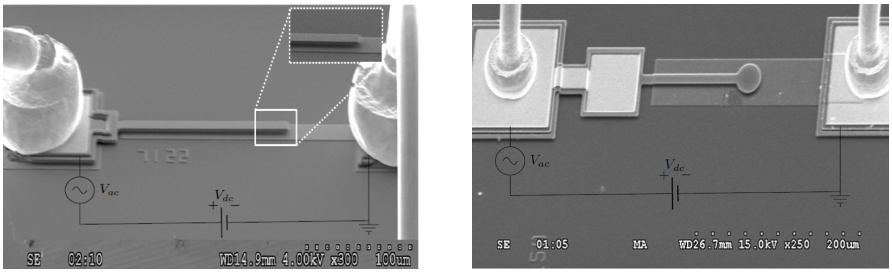

(a) sensor # 1 (b) sensor # 2

Figure 2.1: SEM pictures of the sensors

sor # 2, Fig. 2.1 (b), has a circular plate at the end of the beam. Substrate electrodes provide electrostatic actuation.

The sensors were fabricated using the PolyMUMPs fabrication process [155], Fig. 2.2 . The beams were fabricated in the Poly 1 structural layer with dimensions of ($175 \times 10 \times 2\,\mu m^3$) for sensor # 1 and ($115 \times 10 \times 2\,\mu m^3$), for sensor # 2. Substrate electrodes were patterned in the Poly0 layer under the full beam length. The gap underneath the beam is etched in the second oxide layer resulting in a gap distance of $d = 2$ µm for both sensors. The material properties of polysilicon are $\rho = 2300$ kg/m^3, $E = 160$ GPa and $\nu = 0.22$. A polysilicon electrode is patterned in the Poly0 layer, Fig. 2.2 (b) and (d), to act as a bottom electrode covering the full length of the beam.

Two gold pads are patterned at the root of the beam and end of the bottom electrode, Fig. 2.1. They are used to excite the sensor electrostatically with a harmonic waveform:

$$V(t) = V_a + V_a \cos(2\pi f t) \tag{2.1}$$

The modulation index was set to $m = 1$ throughout our experiments in order to maximize the sensor oscillations [19].

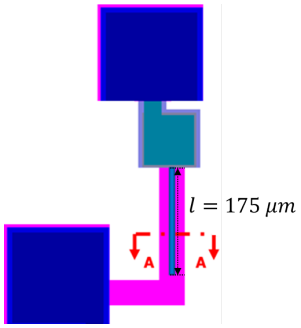

(a) Top-view

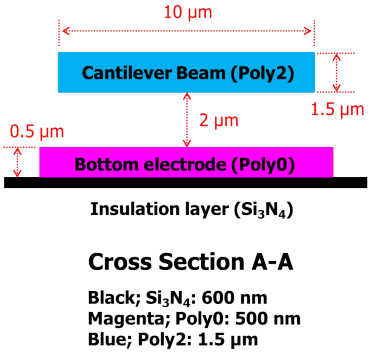

(b) Front-view section A-A

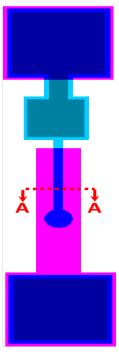

(c) Top-view

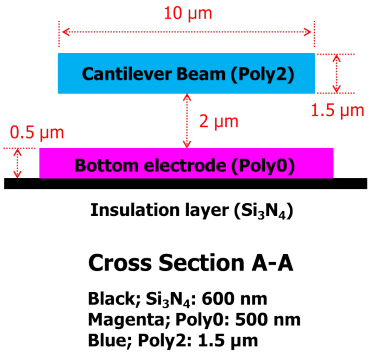

(d) Front-view section A-A

Figure 2.2: Layout of the PolyMUMPs fabricated sensor #1 and sensor #2

Electrostatic actuation typically results in multi-frequency excitation. This can be seen by observing the relationship among electrostatic force, voltage, and displacement $w(x,t)$:

$$F_e = \frac{\alpha V(t)^2}{(d-w)^2} \tag{2.2}$$

Substituting with the voltage waveform described in Eq.(2.1)

$$\begin{aligned} F_e &= \tfrac{\alpha}{(d-w)^2}\left(\tfrac{3}{2}V_a^2 + 2V_a^2\sin(2\pi ft) - \tfrac{1}{2}V_a^2\cos(4\pi ft)\right) \\ &= \tfrac{\alpha}{(d-w)^2}(F_{\mathrm{dc}} + F_1\sin(2\pi ft) - F_2\cos(4\pi ft)) \end{aligned} \tag{2.3}$$

We note that the electrostatic forcing is composed of voltage and displacement proportional components. The former comprise of static F_{dc}, first harmonic F_1, and second harmonic F_2 components, while the latter represents a hard nonlinearity that approaches a singularity as displacement increases. Therefore, the response of the sensor at any given frequency contains components corresponding to the excitation frequency f and its second harmonic $2f$. Setting the modulation index to unity guarantees that the dominant forcing term is the first harmonic F_1 except in frequency ranges where the second harmonic is resonant while the first is not.

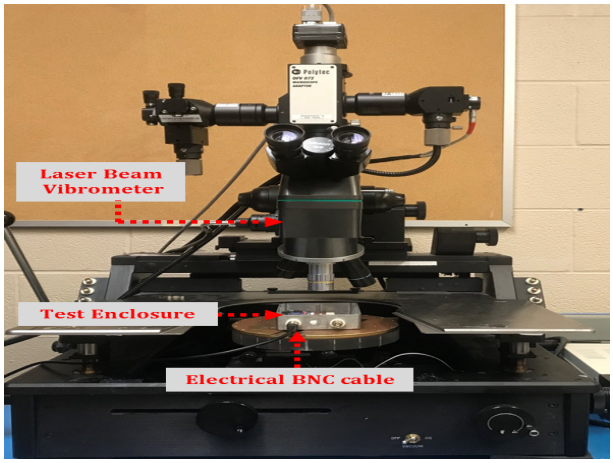

(a) vibrometer

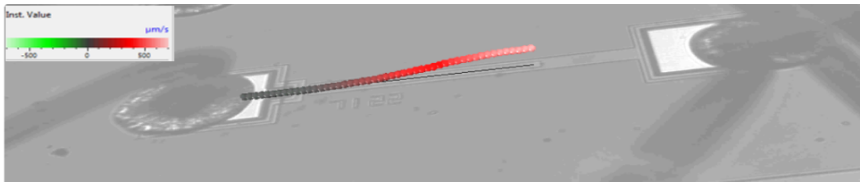

(b) Multi-points scan

Figure 2.3: The experimental setup

The sensor is placed in a metal test enclosure to protect against stray magnetic fields. A laser-Doppler vibrometer (LDV) [156] is used to measure sensor responses optically, Fig. 2.3 (a). A function generator applied the desired waveform and an oscilloscope collects optical measurements of the motions. A Multi-point scan was performed to investigate the out-of plane mode shape as shown in Fig. 2.3 (b).

2.1.1 Frequency Response

Sensor #1

We characterized the sensor by carrying out forward and backward frequency sweeps of the actuation waveform over a wide frequency range. The slew rate was set to 2.5 kHz/s to minimize transient effects. Time-domain data was collected using an oscilloscope in time windows of 0.4 s at a sampling rate of $f_s = 313$ kHz. The frequency response was obtained by evaluating the RMS of the measured signal over a time window of twenty excitation periods $(20T)$.

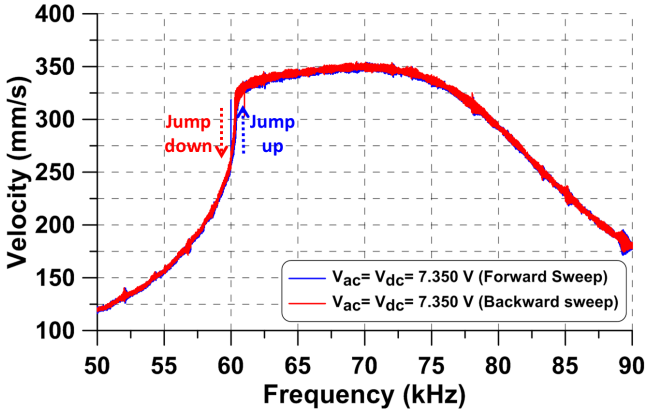

Figure 2.4: The measured frequency-response curve for $V_{\mathrm{a}} = 7.350$ V. Forward sweep is shown in blue line and backward sweep is shown in red

The frequency-response curve of the beam tip velocity over the range f = [50–90] kHz is shown in Fig. 2.4 for an excitation amplitude of $V_{\mathrm{a}} = 7.350$ V. The forward sweep is shown in blue and the backward sweep in red. The effective nonlinearity of the sensor is softening due to the dominance of electrostatic forcing over mechanical hardening. As a result, the dominant peak in the frequency-response curve (nonlinear resonance) is skewed to the left.

The curve is composed of an upper branch of larger orbits and a lower branch of smaller

orbits. The two branches terminate a cyclic-fold bifurcation. The response jumps up and down between the two branches at those bifurcation points without going through pull-in. The jump-up occurs during a forward sweeps while the jump-down occurs during a backward sweeps. This forcing level is slightly beyond the multivaluedness limit, as a result both bifurcations (and the resulting jumps) are located at almost the same frequency $f = 60.313\,\text{kHz}$. The flatness in the upper branch demarcates the increasing importance of the nonlinear squeeze-film damping mechanism for larger orbits that approach the substrate.

Discrete peaks appear in the frequency-response curve at $f = 60\,\text{kHz}$ in the forward sweep and $f = 61\,\text{kHz}$ in the backward sweep. At these locations, the sensor response diverges from smaller, lower branch, orbits to larger orbits and vice versa.

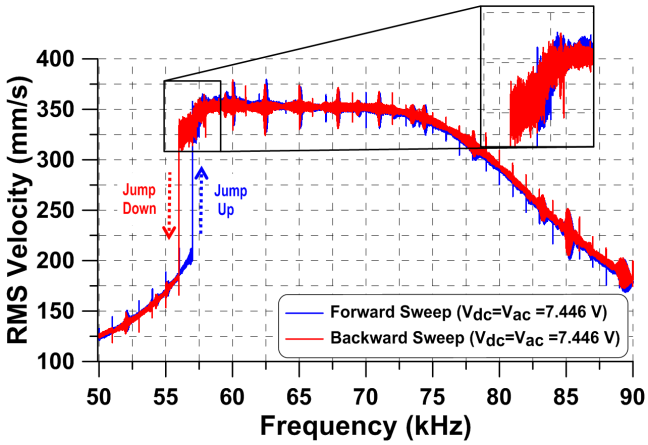

Figure 2.5: The measured frequency-response curve for $V_\text{a} = 7.446\,\text{V}$. Forward sweep is shown in blue and backward sweep is shown in red

The frequency-response curve of the beam tip velocity for a larger excitation amplitude of $V_\text{a} = 7.446\,\text{V}$ is shown in Fig. 2.5. The flat region in the upper branch extends over a larger frequency range as more orbits become larger and approach the substrate. We observed a middle branch between the upper and lower branches in this curve which does not appear at the lower

forcing level curve, Fig. 2.4. Tapping mode oscillations occur along this branch during which the sensor tip comes into line-contact with the substrate. The branch is characterized by a positive slope due to the substrate limiting the amplitude of sensor displacement to a distance similar to the capacitive gap. As a result, the measured velocity varies almost linearly with the excitation frequency along this branch.

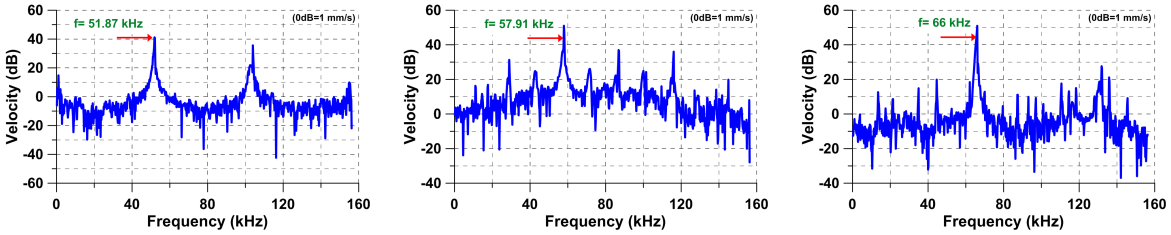

(a) $f = 51.87\,\text{kHz}$ (b) $f = 57.91\,\text{kHz}$ (c) $f = 66\,\text{kHz}$

Figure 2.6: The FFT of the tip velocity along the (a) lower, (b) middle and (c) upper branches

We compare the sensor response at typical points along these branches in Fig. 2.5. The figure shows the FFT of the tip velocity in dB-scale. Along the lower branch, forced response is observed at the excitation frequency $f = 51.87\,\text{kHz}$ and its higher harmonics, Fig. 2.6 (a). Along the middle branch, an excitation frequency of $f = 57.91\,\text{kHz}$ results in tapping mode oscillations, thereby elevating the noise floor by $\sim 18\,\text{dB}$ and introducing other harmonics in the response spectrum, Fig. 2.6 (b). Along the upper branch, the stronger nonlinearity present in the larger orbit at $f = 66\,\text{kHz}$ produces other harmonics beside f and its multiples but does not elevate the noise floor, Fig. 2.6 (c).

A homoclinic entanglement occurs at the meeting point of upper and middle branches ($f = 58\,\text{kHz}$). The entanglement between the stable and unstable manifolds of the saddle interrupts the safe basin of oscillations. It precludes larger orbits. Instead, it sends the sensor into contact

with the substrate and tapping mode oscillations. In backward sweeps, those oscillations persist along the mid-branch until the response passes the nonlinear resonance and falls down to the lower branch at $f = 55.986\,\text{kHz}$. During a forward sweeps, the response jumps up from the lower branch to the mid-branch at the lower cyclic fold bifurcation point $f = 56.810\,\text{kHz}$. A hysteric region appears between these jumps.

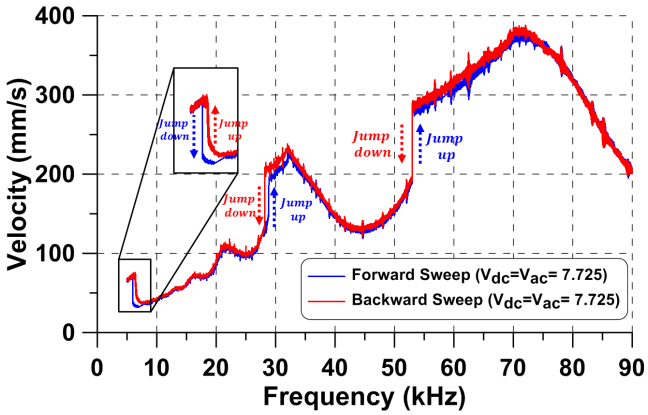

Figure 2.7: The measured frequency-response curve for $V_\text{a} = 7.725\,\text{V}$. Forward sweep is shown in blue line and backward sweep is shown in red

Increasing the excitation amplitude to $V_\text{a} = 7.725\,\text{V}$, we obtained the frequency response over a wider frequency range of $f = [5.0\text{–}90]\,\text{kHz}$, Fig. 2.7. For excitation frequencies below 5 kHz, no periodic motions were observed with the sensor going into and remaining in contact with the substrate throughout the excitation cycle. The frequency-response curve shows peaks in the vicinity of the superharmonic resonances of order two and three as well as primary resonance. Tapping mode (middle branch) orbits, characterized by a positive slope in the response curve, were observed in a low-frequency non-resonant region $f = [5.0 - 6.490]\,\text{kHz}$ and in the vicinity of the superharmonic resonance of order-two $f = [28.385 - 32.892]\,\text{kHz}$ as well as primary resonance $f = [53.0 - 70.0]\,\text{kHz}$.

Jumps were also observed at the superharmonic resonance of order-two where a hysteretic region developed with a jump-up occurring during forward sweeps at $f = 28.822\,\text{kHz}$ and a jump-down occurring during backward sweeps at $f = 28.385\,\text{kHz}$. At the primary resonance, there was no hysteresis with the jump-up during forward sweeps and and jump-down during backward sweeps occurring at the same frequency $f = 53\,\text{kHz}$. The mechanisms underlying the jumps at superharmonic resonance are the same as those discussed above. On the other hand, both jumps at primary resonance occur due to the homoclinic entanglement resulting in further erosion of the safe basin of motion as the excitation level increases. It precludes lower branch orbits at frequencies beyond $f = 53\,\text{kHz}$ and upper branch orbits at frequencies below $f = 71.097\,\text{kHz}$. Throughout this range, the only possible motions are tapping mode oscillations.

In the non-resonant region, a jump-down occurs during forward frequency sweeps from the tapping branch to the lower branch, whereas a jump-up from the lower branch to the tapping branch occurs during backward sweeps. A hysteretic region exists between these two jumps. We note that this behavior is the reverse of that observed in the hysteric regions located in the vicinity of primary resonance for $V_\text{a} = 7.446\,\text{V}$ and superhamronic resonance for $V_\text{a} = 7.725\,\text{V}$, where the jump-up occurs during forward sweeps and the jump-down during backward sweeps. Further, we note that the size of the tapping-mode orbits observed at low-frequency is large even though they occur in a non-resonant region $f/f_1 << 1$.

Sensor #2

Frequency-response curves of the tip velocity were obtained under a constant voltage waveform (electrostatic force) to characterize the sensors response over a wide frequency range. Each frequency-response curve is composed of a forward and a backward frequency sweep, Fig. 2.8. The voltage amplitude and frequency range were V_a=7.125 V and f = [5–60] kHz. The slew rate was set to 2.5 kHz/s to minimize transient effects. Data was collected in time windows of 0.4 s

at a sampling frequency of $f_s = 313\,\text{kHz}$. The time-domain data was post-processed to obtain the RMS velocity of the tip over a time window of 20 excitation periods (T) and assigned to the frequency value at the window mid-point.

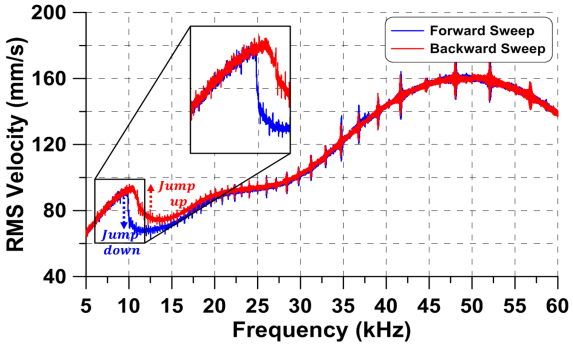

(a)

Figure 2.8: Frequency-response curves of sensors #2 excited at voltage amplitude V_{a}=7.125 V. Forward and backward frequency-sweeps are colored in blue and red, respectively

The positive slope lines appearing in the frequency range of $f = [5.0 - 10.627]\,\text{kHz}$, Fig. 2.8, are evidence of tapping mode oscillations where the sensor tip comes into regular contact with the substrate. In these ranges, the tip displacement is almost constant (similar to the gap distance $d = 2\,\mu\text{m}$) due to the limiting effect of the substrate. As a result, the velocity frequency-response varies almost linearly with frequency.

A jump-down occurs during the forward sweep for sensor #1 and sensor #2 from the branch of tapping orbits to a branch of freely oscillating orbits at $9.876\,\text{kHz}$, whereas a jump-up from that branch to the tapping branch occurs during backward sweeps at $10.627\,\text{kHz}$. A hysteretic region exists between the two jumps, Fig. 2.8.

We note that both sensors go under pull-in and tapping oscillations in a low-frequency region away from resonance, $f/f_1 << 1$. While dynamic pull-in and tapping oscillations also occur in

the vicinity of resonances for sensor # 1, sensor #2 does not experience pull-in or tapping in that region. This raises questions about the reason for the appearance of large oscillations away from resonance and the nature of the pull-in instability they trigger there.

2.2 Non-Resonant Dynamics

2.2.1 Sensor # 1

The sensor was excited by a voltage waveform $V_{\mathrm{a}} = 6.8625\,\mathrm{V}$ at discrete frequencies; $f = 10$ and $25\,\mathrm{kHz}$. The velocity and displacement time-histories of the sensor tip and the corresponding phase-portraits are shown in Fig. 2.9. The response at $f = 10\,\mathrm{kHz}$ displays the large oscillations mentioned above unlike the case at $f = 25\,\mathrm{kHz}$. The Planar projection of the phase-portrait at $f = 10\,\mathrm{kHz}$ reveals a Shilnikov orbit homoclinic to a saddle-focus, Fig. 2.9 (b). The orbit is composed of a flow along the unstable manifold of the saddle that is captured by a nearby stable focus to be re-injected in the vicinity of the saddle [46]. The red-dashed line in the phase portrait demarcates the gap limit of the sensor. The time-history, Fig. 2.9 (a), shows a fast-slow dynamics where the voltage varies slowly, the tip is pulled-in periodically coming into contact with the substrate where the displacement is held constant for a period of time before pulling off in a fast motions and settling down close to the equilibrium position. A 3-D phase-portrait of the orbit is shown in Fig. 2.9 (c).

The process of pulling-in corresponds to the flow along the unstable manifold of the saddle, settling down after pull-off corresponds to the stable focus, and re-injection occurs due to the cyclic rise in voltage. The sensor crosses the saddle point as the instantaneous voltage crosses the static pull-in voltage, V_{Ps}. However, we note that static pull-in is not relevant to this process. In fact, the RMS of the voltage waveform is less than V_{Ps}. This behavior is repeated periodically

over the excitation cycle. Beyond the bifurcation point at the peak of the tapping branch, the sensor presents a regular forced response as shown in Fig. 2.9 (d) and (e) at $f = 25\,\text{kHz}$. As a result, the orbit size shrinks from a displacement of 2 µm at $f = 10\,\text{kHz}$ to 1.120 µm at $f = 25\,\text{kHz}$.

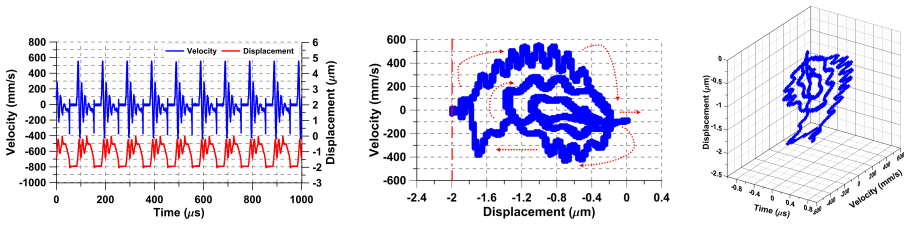

(a) $f = 10\,\text{kHz}$ (b) $f = 10\,\text{kHz}$ (c) $f = 10\,\text{kHz}$

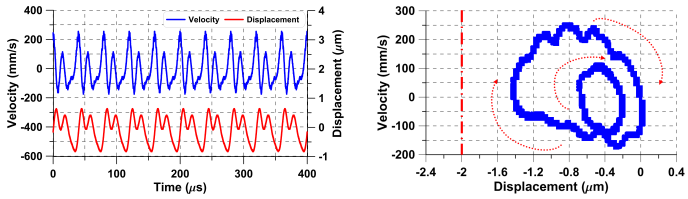

(d) $f = 25\,\text{kHz}$ (e) $f = 25\,\text{kHz}$

Figure 2.9: Tip velocity and displacement time-histories and phase portrait for the voltage waveform $V_\text{a} = 6.8625\,\text{V}$

Increasing the excitation voltage to $V_\text{a} = 7.725\,\text{V}$ shrinks the frequency domain where low frequency large oscillations occur. The experimentally measured velocity and displacement time-histories and the corresponding phase portraits at excitation frequencies of $f = 6.4$, and $7\,\text{kHz}$ are shown in Fig. 2.10 for time spans of 2.560, and 2800 excitation periods, respectively.

While similar behavior to that described above is observed here, Shilnikov bifurcation is located at $f = 6.49\,\text{kHz}$. Similarly, the orbit size shrinks from a displacement of 2.624 µm at $f = 6.4\,\text{kHz}$ to 1.12 µm at $f = 7.0\,\text{kHz}$. While oscillations typical of a stable foci can be

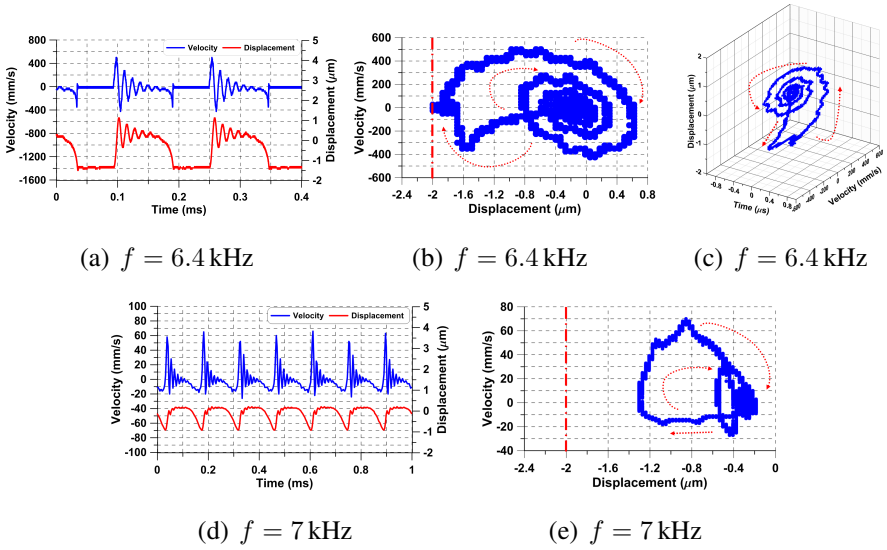

(a) $f = 6.4\,\text{kHz}$ (b) $f = 6.4\,\text{kHz}$ (c) $f = 6.4\,\text{kHz}$

(d) $f = 7\,\text{kHz}$ (e) $f = 7\,\text{kHz}$

Figure 2.10: Tip velocity and displacement time-histories and its phase portrait excited at voltage amplitude of $V_\text{a} = 7.725\,\text{V}$ at $f = 6.4$ and $7\,\text{kHz}$, respectively

observed in Fig. 2.10 (d), they result from the sensor rebounding from its maximum deflection point as can be seen in the corresponding time-history, Fig. 2.10 (d). The complexity of the orbit is merely a reflection of the interaction between the slow time-scale of the forcing and the fast time-scale of the sensor fundamental mode. No tapping or flow along the unstable manifold are observed in Fig. 2.10 (d) and (e). The fast-slow dynamics in this region result in two distinct trains of peaks in the frequency domain, corresponding to the forcing frequency and to the fundamental natural frequency of the sensor. For this waveform, we observed fast-slow dynamic interactions in the region extending from the bifurcation point ($f = 6.49\,\text{kHz}$) until it approaches the superharmonic resonance of order-three ($f \approx 25\,\text{kHz}$).

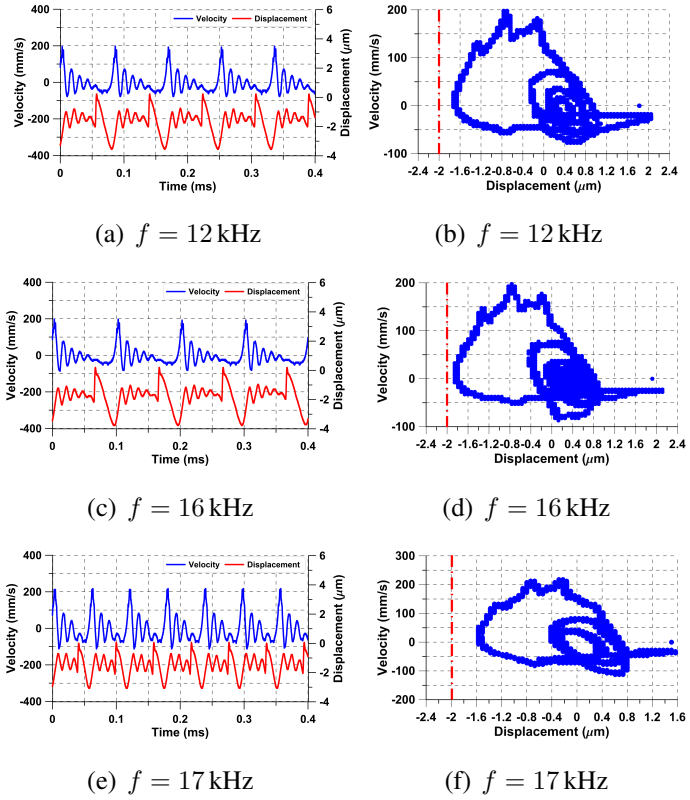

(a) $f = 12\,\text{kHz}$ (b) $f = 12\,\text{kHz}$

(c) $f = 16\,\text{kHz}$ (d) $f = 16\,\text{kHz}$

(e) $f = 17\,\text{kHz}$ (f) $f = 17\,\text{kHz}$

Figure 2.11: Tip velocity and displacement time-histories and corresponding to phase portraits at voltage waveform of $V_{\text{a}} = 7.725\,\text{V}$

As the excitation frequency increased, fast-slow dynamics were also observed beyond the Shilnikov bifurcation. In this case, the Shilnikov-like orbits do not involve tapping as seen in Fig. 2.11 at $f = 12, 16,$ and $17\,\text{kHz}$. The time-histories show that in all three cases the sensor oscillates freely in air, approaches but does not reach the substrate, before rebounding as the electrostatic force drops (slow dynamics). The corresponding phase portraits, show that the sensor spirals in towards the equilibrium position corresponding to the DC voltage (fast dynamics).

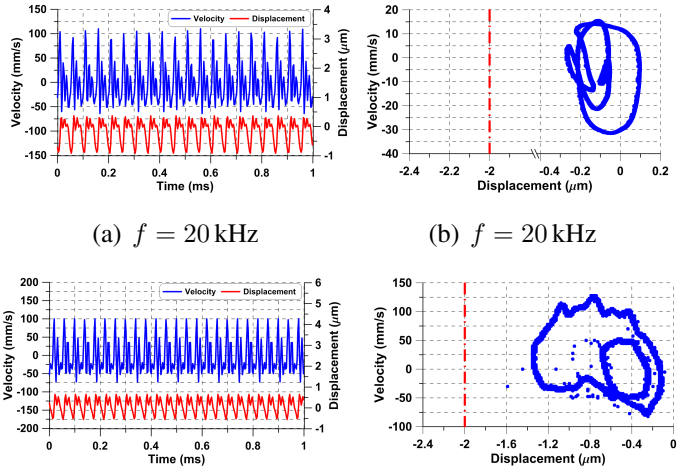

(a) $f = 20\,\text{kHz}$ (b) $f = 20\,\text{kHz}$

(c) $f = 25\,\text{kHz}$ (d) $f = 25\,\text{kHz}$

Figure 2.12: Tip velocity and displacement time-histories and corresponding to phase portraits under voltage waveform $V_\text{a} = 7.725\,\text{V}$

The size of the sensor orbit shrunk as the excitation frequency increased, which is seen at $f = 20$ and $25\,\text{kHz}$, Fig. 2.12. In this case, the response approaches that of a forced oscillator as the time-scale of forcing approach that of resonant dynamics. As a result, the orbit size shrinks from more than $3\,\mu\text{m}$ at $f = 17\,\text{kHz}$ to $1.2\,\mu\text{m}$ at $f = 25\,\text{kHz}$.

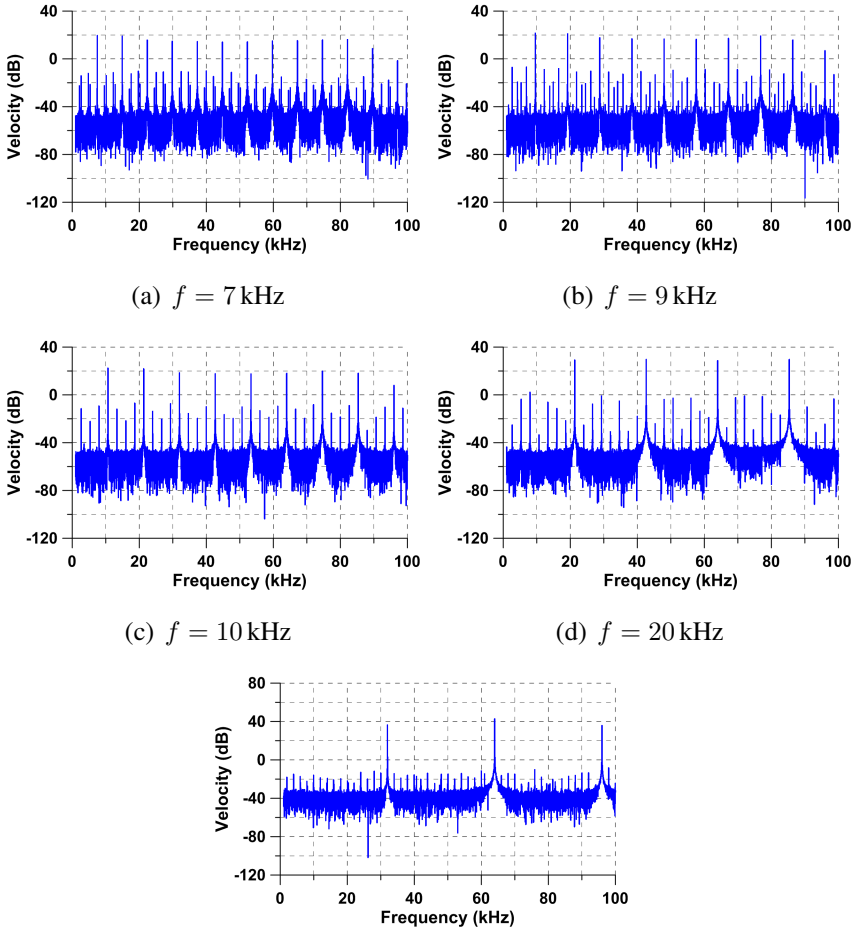

(a) $f = 7\,\text{kHz}$ (b) $f = 9\,\text{kHz}$

(c) $f = 10\,\text{kHz}$ (d) $f = 20\,\text{kHz}$

(e) $f = 32\,\text{kHz}$

Figure 2.13: Tip velocity FFTs response of the Sensor in dB-scale (0 dB = 1 mm/s) at a voltage amplitude of $V_\text{a} = 7.725\,\text{V}$

The fast dynamics, which results in ring-down oscillations as the sensor spirals in towards its equilibrium, leave telltale signs in the FFT of the sensor response. Equally-spaced peaks appear at submultiples of the forcing frequency corresponding the number of ring-down oscillations above the noise floor. As the frequency of excitation increase, the importance of fast-slow dynamics decrease as can be seen in the drop in the number of amplitude of the submultiple peaks in Fig. 2.13.

2.2.2 Sensor # 2

The same quasi-pull-in behavior was observed in sensor #1 while the sensor #2 was excited at a voltage amplitude of $V_{\mathrm{a}} = 7.125\,\mathrm{V}$. The sensor excited initially by a frequency of $f = 7\,\mathrm{kHz}$. The velocity and displacement time-histories, velocity FFTs, and corresponding to phase portrait were collected as shown in, Fig. 2.14. The sensor tip goes to pull-in while the voltage cycle increases and rebounds freely oscillating in air while the voltage cycle releases as shown in Fig. 2.14 (a).

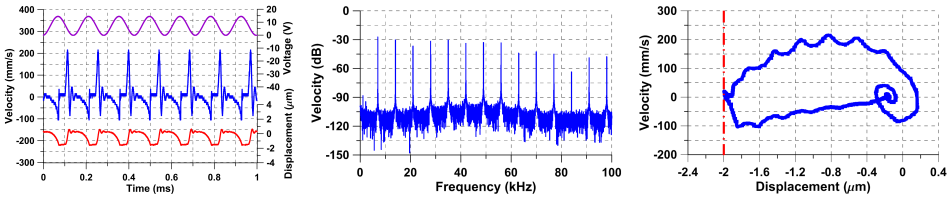

(a) $f = 7\,\mathrm{kHz}$ (b) $f = 7\,\mathrm{kHz}$ (c) $f = 7\,\mathrm{kHz}$

Figure 2.14: Voltage waveform, tip velocity, and tip displacement time-histories and corresponding to phase portraits for sensor # 2 under the voltage waveform $V_{\mathrm{a}} = 7.125\,\mathrm{V}$

Further, the excitation voltage was dropped to a voltage amplitude of $V_{\mathrm{a}} = 6.750\,\mathrm{V}$ at the excitation frequencies $f = 5, 6, 7, 8$ and $10\,\mathrm{kHz}$, we obtained the tip velocity and displacement time-histories and the corresponding phase-portraits shown in Fig. 2.15. Shilnikov orbits homoclinic to a saddle focus were observed in all of the cases, Figs. 2.15 (b), (d), (f), (h), and (j). The stable focus oscillations occur over a shorter settling time because of the sensor's lower quality factor $(Q = 2.1)$. Comparing the voltage waveform to the displacement time-history, Fig. 2.15 (a) and (c), shows that the sensor pulls-in as the instantaneous voltage crosses the value of static pull-in. Subsequently, it maintains in contact with the substrate until the instantaneous voltage drops below the pull-off voltage.

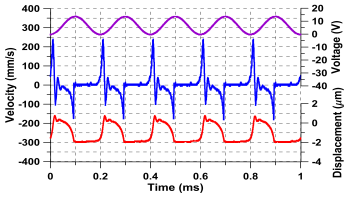

(a) $f = 5\,\text{kHz}$

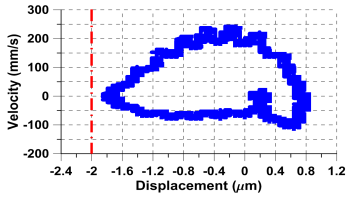

(b) $[f = 5\,\text{kHz}$

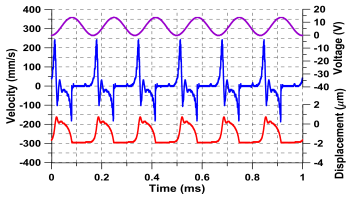

(c) $f = 6\,\text{kHz}$

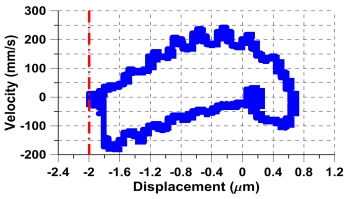

(d) $f = 6\,\text{kHz}$

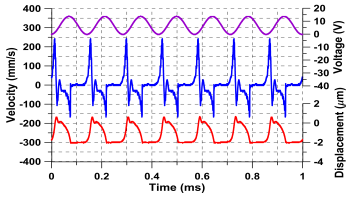

(e) $f = 7\,\text{kHz}$

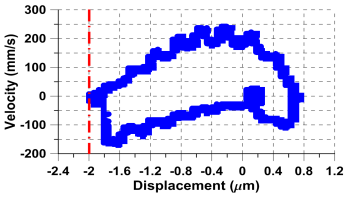

(f) $f = 7\,\text{kHz}$

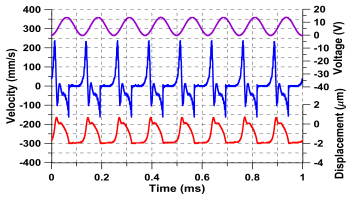

(g) $f = 8\,\text{kHz}$

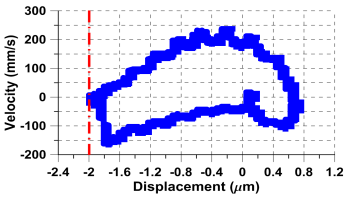

(h) $f = 8\,\text{kHz}$

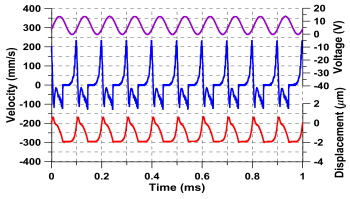

(i) $f = 10\,\text{kHz}$

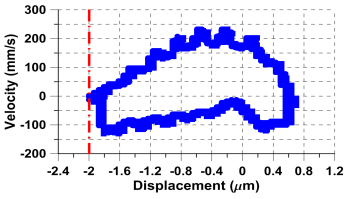

(j) $f = 10\,\text{kHz}$

Figure 2.15: Voltage waveform, tip velocity, and tip displacement time-histories and corresponding to phase portraits for sensor # 2 under the voltage waveform $V_{\text{a}} = 6.750\,\text{V}$

A forced response was found while the sensor was excited at frequencies of $f = 13, 15, 20$ and $25\,\text{kHz}$. The voltage waveform, velocity and displacement time-histories and corresponding to phase portraits are shown in Fig. 2.16. We note the sensor oscillates freely in air in this case with no interaction with the substrate.

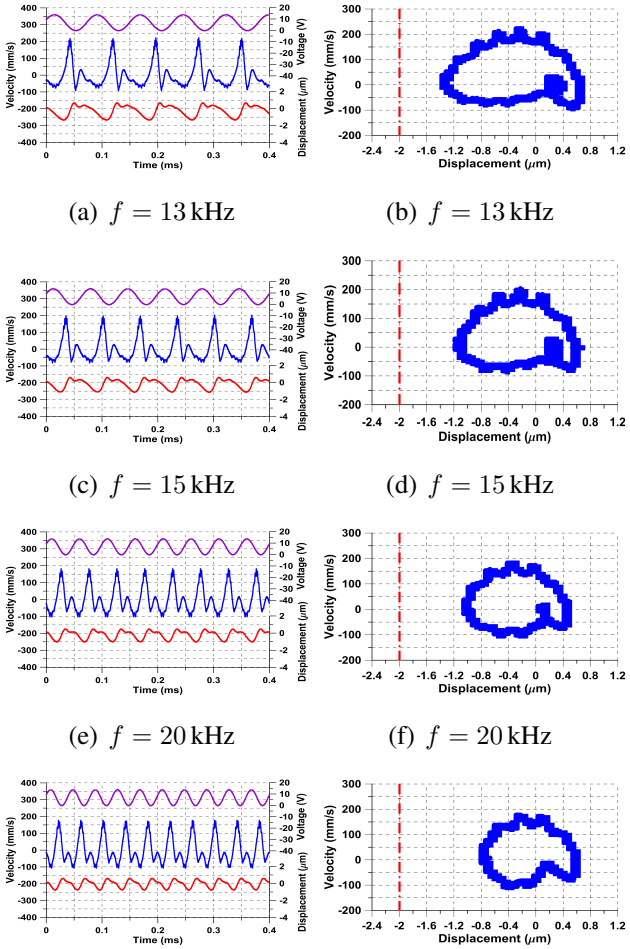

(a) $f = 13\,\text{kHz}$ (b) $f = 13\,\text{kHz}$

(c) $f = 15\,\text{kHz}$ (d) $f = 15\,\text{kHz}$

(e) $f = 20\,\text{kHz}$ (f) $f = 20\,\text{kHz}$

(g) $f = 25\,\text{kHz}$ (h) $f = 25\,\text{kHz}$

Figure 2.16: Voltage waveform, tip velocity, and tip displacement time-histories and the corresponding phase portraits for sensor # 2 under the voltage waveform $V_\text{a} = 6.750\,\text{V}$

Shilnikov Chaos

Shilnikov chaos was observed as an infinite countable set represented by an unstable saddle focus and stable real line, $(\rho \pm i\omega, -\lambda)$. It is occurs subsequent to a supercritical-Hopf bifurcation. This behavior is represented by the unstable saddle-focus forming unstable period-doubling spirals away from the saddle and contracted by the stable manifold to be re-injected it back to the saddle. The re-injection occurs due to tapping oscillations where the sensor tip interacts with the substrate.

Discrete excitation frequencies were conducted at $f = 10, 13.7, 13.734,$ and $30\,\text{kHz}$ at voltage amplitude of $V_\text{a} = 7.125\,\text{V}$. The velocity and displacement time-histories, velocity FFTs, and phase portrait were collected as shown, Fig. 2.17.

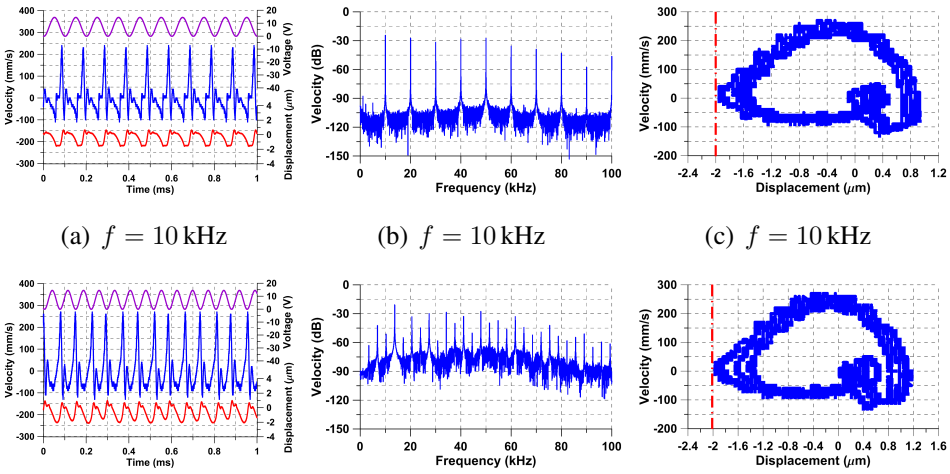

(a) $f = 10\,\text{kHz}$ (b) $f = 10\,\text{kHz}$ (c) $f = 10\,\text{kHz}$

(d) $f = 13.70\,\text{kHz}$ (e) $f = 13.70\,\text{kHz}$ (f) $f = 13.70\,\text{kHz}$

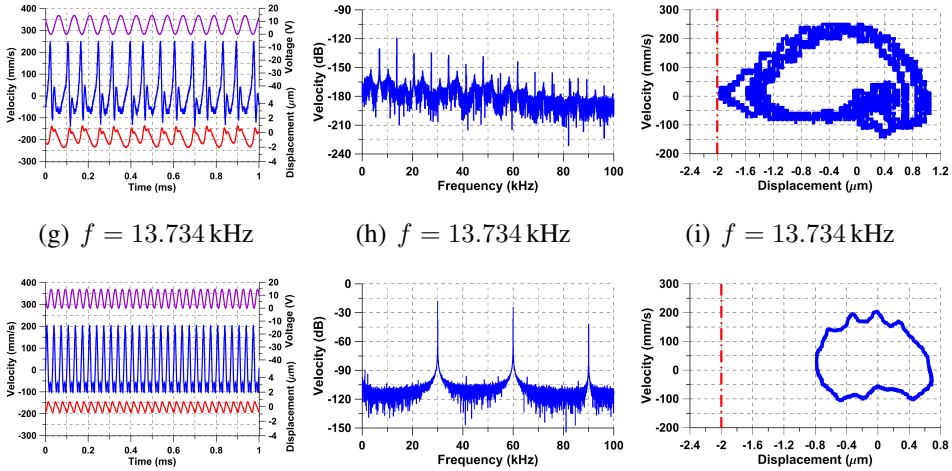

(g) $f = 13.734\,\text{kHz}$ (h) $f = 13.734\,\text{kHz}$ (i) $f = 13.734\,\text{kHz}$

(j) $f = 30\,\text{kHz}$ (k) $f = 30\,\text{kHz}$ (l) $f = 30\,\text{kHz}$

Figure 2.17: Voltage waveform, tip velocity, and tip displacement time-histories colored in magenta, blue, and red, respectively, velocity FFTs in dB-scale (0dB= 1m/s), and phase portrait under the voltage waveform of $V_\text{a} = 7.125\,\text{V}$

Shilnikov to a saddle-focus was also observed at the excitation frequency $f = 10\,13.70\,\text{kHz}$ and $f = 13.734\,\text{kHz}$ where the stable saddle-focus spirals toward the saddle and was re-injected through the unstable manifold to pull-in, Fig. 2.17 (a-i). The pull-in time period was found to shorten when the excitation frequency increased.

A period three P-3 under the mechanism of Shilnikov chaos was found while the excitation frequency increased to $f = 13.70$ and $13.734\,\text{kHz}$, Fig. 2.17 (g-i). We note the chaotic behavior of P-3 does not associate with pull-in where the sensor freely oscillates in air. A periodic behavior of period one P-1 was found at $f = 30\,\text{kHz}$, which is in the vicinity of superharmonic resonance, Fig. 2.17 (m-o) whereas the sensor response cleared from the chaotic region.

The voltage waveform was increased to $V_\text{a} = 7.650\,\text{V}$ under the same excitation frequency $f = 10$ and $13\,\text{kHz}$, Fig. 2.18, which resulted in Shilinikov chaos. The chaotic tapping oscilla-

tions are shown in the velocity and displacement time-histories, Fig. 2.18 (a), while the corresponding phase portrait, Fig. 2.18 (b), shows the resulting banded chaotic attractor. This chaotic attractor was found to extend over the frequency $[10 - 18]$ kHz during frequency up-sweep.

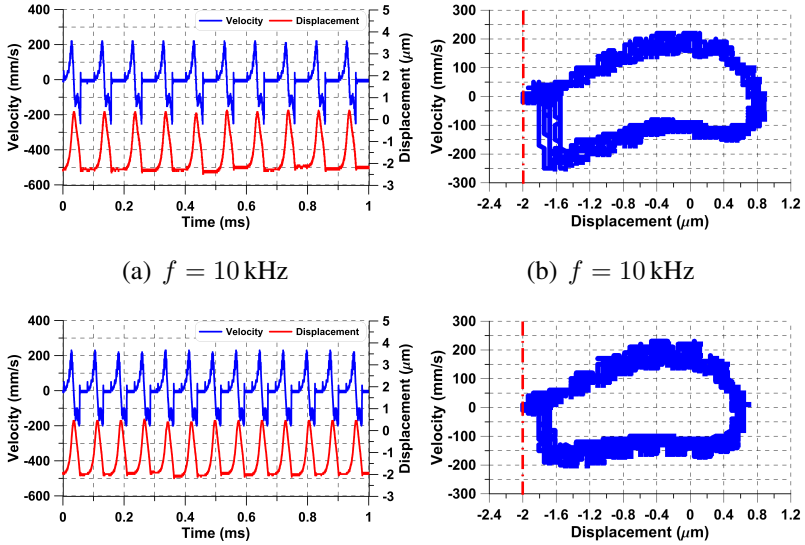

(a) $f = 10\,\text{kHz}$ (b) $f = 10\,\text{kHz}$

(c) $f = 13\,\text{kHz}$ (d) $f = 13\,\text{kHz}$

Figure 2.18: Tip velocity and displacement time-histories and corresponding to phase portraits under the voltage waveform $V_\text{a} = 7.650\,\text{V}$

Shilnikov chaos was observed at excitation frequencies of $f = 15.860, 16, 16.06, 16.139$ and $16.142\,\text{kHz}$, Fig. 2.19. The velocity in dB-scale and phase portraits show the chaotic behavior at this vicinity. The elevated noise floor in the velocity FFTs in dB-scale demarcate chaotic behavior interacting with the substrate.

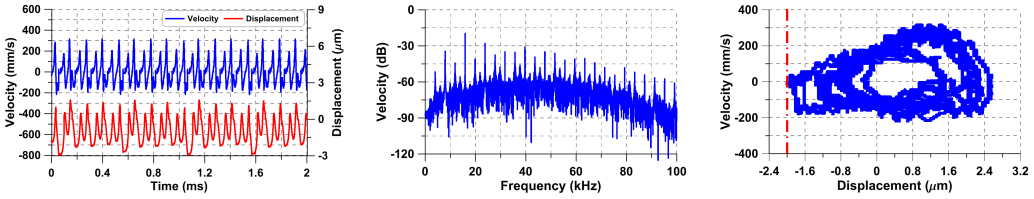

(a) $f = 15.860\,\text{kHz}$ (b) $f = 15.860\,\text{kHz}$ (c) $f = 15.860\,\text{kHz}$

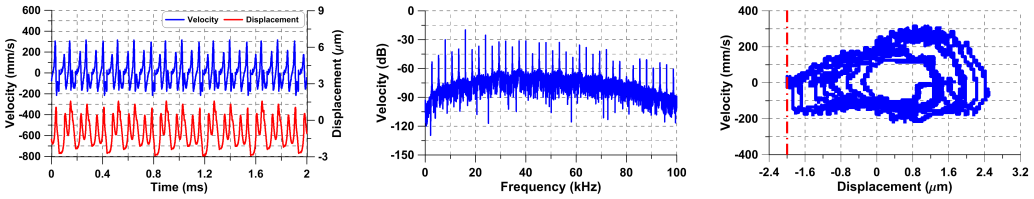

(d) $f = 16\,\text{kHz}$ (e) $f = 16\,\text{kHz}$ (f) $f = 16\,\text{kHz}$

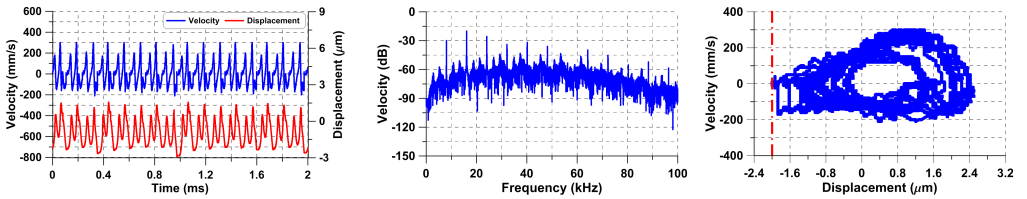

(g) $f = 16.060\,\text{kHz}$ (h) $f = 16.060\,\text{kHz}$ (i)

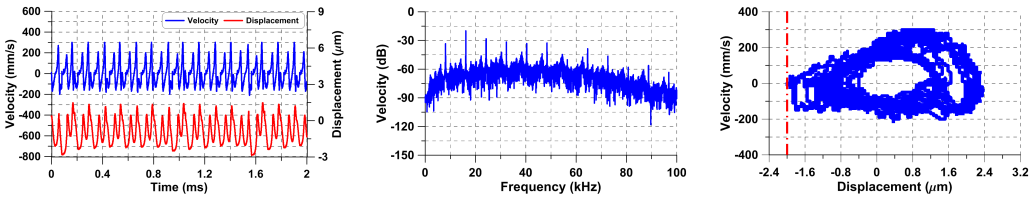

(j) $f = 16.139\,\text{kHz}$ (k) $f = 16.139\,\text{kHz}$ (l) $f = 16.139\,\text{kHz}$

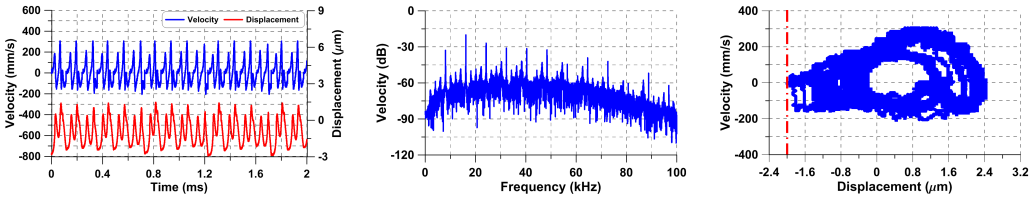

(m) $f = 16.142\,\text{kHz}$ (n) $f = 16.142\,\text{kHz}$ (o) $f = 16.142\,\text{kHz}$

Figure 2.19: Tip velocity and displacement time-histories, velocity FFTs in dB-scale scale (0 dB = 1 mm/s), and corresponding to phase portrait under the voltage waveform $V_{\text{a}} = 7.650\,\text{V}$

Intermittency Type-III

The excitation frequency was further increase to $f = 16.319, 16.320, 16.40, 16.430,$ and 16.480 kHz, Fig. 2.20. An intermittency type-III subsequent to a period-doubling bifurcation route to chaos was observed. Fast-slow dynamic behavior which represent two signals are atop of each other in the velocity and displacement time-histories: a carrier signal at high frequency where represents a departure line from the saddle, and a baseband signal with low frequency where it represents the saddle-focus approaching the saddle with a negative slope Fig. 2.20 (a,d,g,j). It is also showing clearly a chaotic behavior in the velocity in dB-scale and its phase portraits.

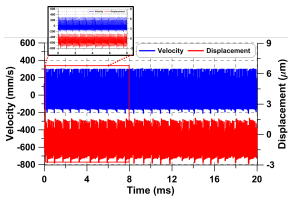

(a) $f = 16.319$ kHz

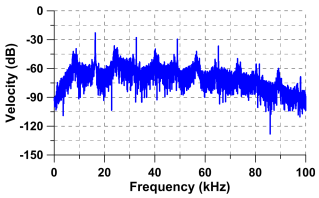

(b) $f = 16.319$ kHz

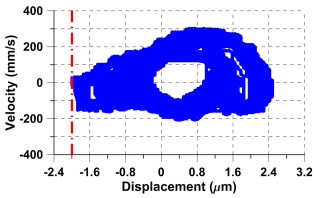

(c) $f = 16.319$ kHz

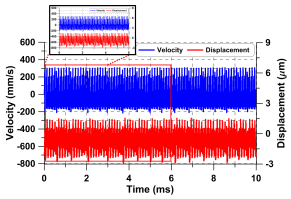

(d) $f = 16.320$ kHz

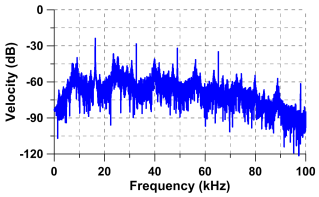

(e) $f = 16.320$ kHz

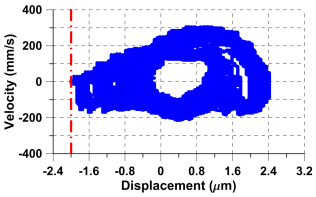

(f) $f = 16.320$ kHz

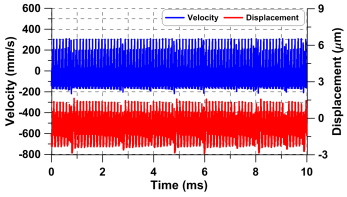

(g) $f = 16.40$ kHz

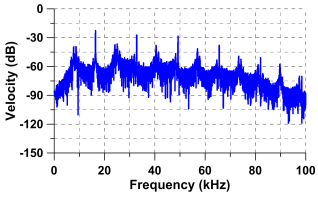

(h) $f = 16.40$ kHz

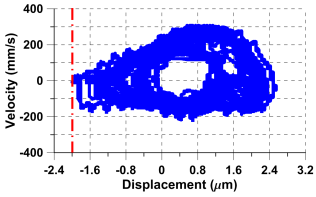

(i) $f = 16.40$ kHz

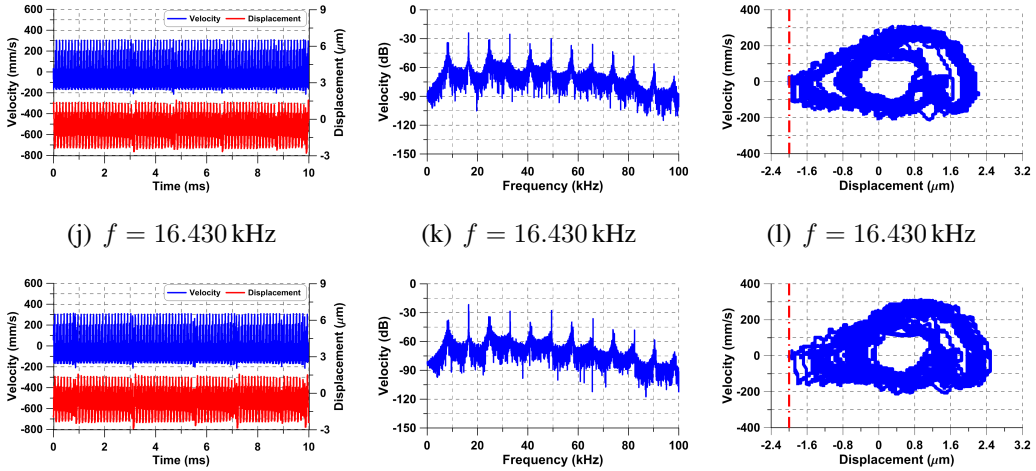

(j) $f = 16.430\,\text{kHz}$ (k) $f = 16.430\,\text{kHz}$ (l) $f = 16.430\,\text{kHz}$

(m) $f = 16.480\,\text{kHz}$ (n) $f = 16.480\,\text{kHz}$ (o) $f = 16.480\,\text{kHz}$

Figure 2.20: Voltage waveform, tip velocity, and tip displacement time-histories colored in magenta, blue, and red, respectively, velocity FFTs in dB-scale (0 dB = 1 mm/s), and phase portrait under the voltage waveform of $V_{\text{a}} = 7.650\,\text{V}$

The dynamic behavior went to period doubling bifurcations after the intermittency behavior. The velocity and displacement time-histories, velocity FFT and corresponding phase portrait were collected with time spans of 33.1, and 17.3 excitation periods, Fig. 2.21. Period-doubling of P-2 and period three P-3 were found at the excitation frequencies of $f = 16.55$, and $17.30\,\text{kHz}$, respectively. The tapping oscillations in the chaotic orbit of P-3 was observed in the displacement time-histories; however, the transversal flatness at the left-side of the phase portrait demarcates the tip interaction with the substrate, Fig. 2.21 (c). As the excitation frequency increased further to $f = 17.30$and $18\,\text{kHz}$, the sensor response cleared from the chaotic region to period-doubling of P-2, Fig. 2.21 (d-f) and (g-i). Lastly, the sensor went back to period one orbit while the excitation frequency increased to $f = 30\,\text{kHz}$, Fig. 2.21 (j-l).

A superharmonic resonance of order-three was also observed when the excitation frequency

increased to $f = 16.55\,\text{kHz}$, Fig. 2.21 (a-c). Tapping oscillations were observed in the displacement time-history. Fast-slow dynamics disappeared from the sensor response as it approached the superharmonic resonance of order-two at $f = 17.30$ and $18\,\text{kHz}$, Fig. 2.21 (f-i), with orbit peak-to-peak displacement reaching $3.01\,\mu\text{m}$ and $2.752\,\mu\text{m}$, respectively . As the excitation frequency increased away from the superharmonic resonance of order-two, the orbit size shrunk to a peak-to-peak displacement of $2.048\,\mu\text{m}$, Fig. 2.21 (l), at $f = 30\,\text{kHz}$.

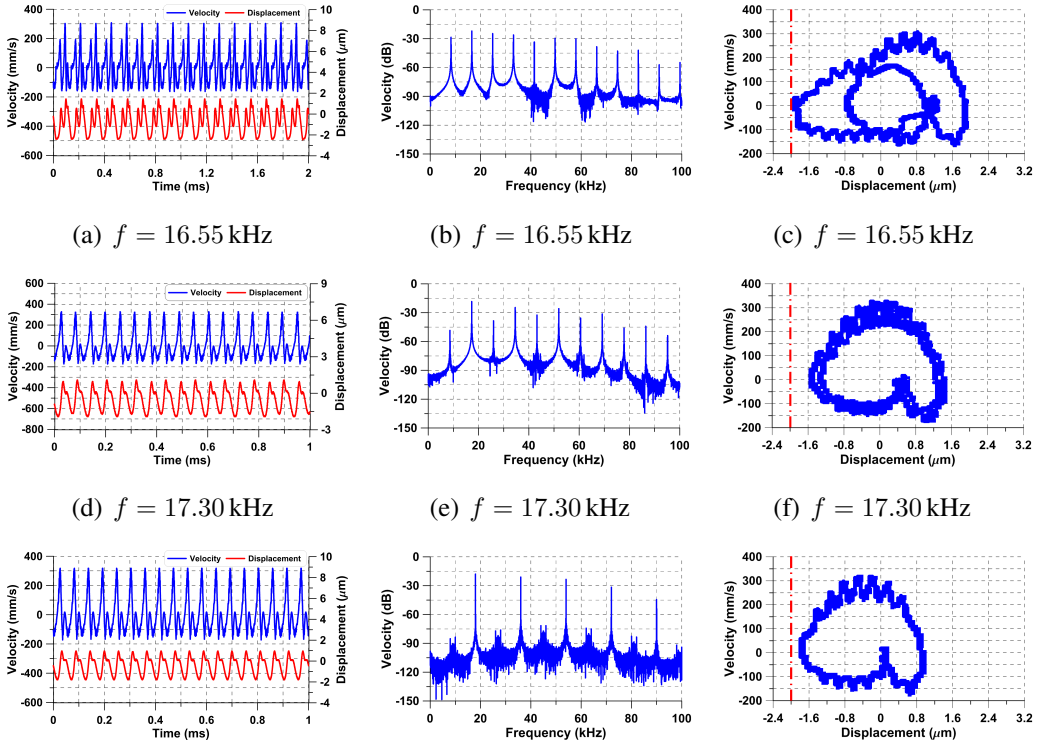

(a) $f = 16.55\,\text{kHz}$ (b) $f = 16.55\,\text{kHz}$ (c) $f = 16.55\,\text{kHz}$

(d) $f = 17.30\,\text{kHz}$ (e) $f = 17.30\,\text{kHz}$ (f) $f = 17.30\,\text{kHz}$

(g) $f = 18\,\text{kHz}$ (h) $f = 18\,\text{kHz}$ (i) $f = 18\,\text{kHz}$

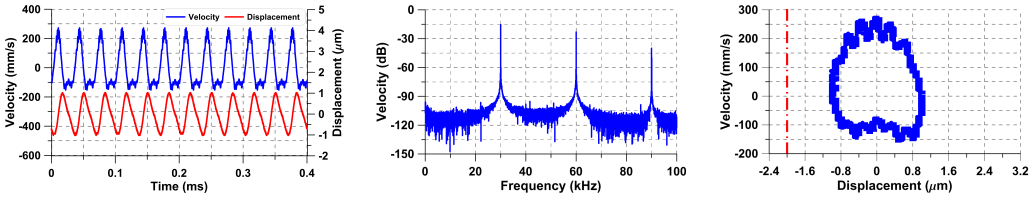

(j) $f = 30\,\text{kHz}$ (k) $f = 30\,\text{kHz}$ (l) $f = 30\,\text{kHz}$

Figure 2.21: Voltage waveform, tip velocity, and tip displacement time-histories colored in magenta, blue, and red, respectively, velocity FFTs in dB-scale (0 dB = 1 mm/s), and phase portrait under the voltage waveform of $V_{\text{a}} = 7.650\,\text{V}$

As a case study, a backward frequency sweep was conducted to investigate the sensor dynamic behavior in a reverse direction. The sensor was excited at frequencies of $f = 30, 13.70, 10,$ and $7\,\text{kHz}$ at voltage waveform of $V_{ac} = V_{dc} = 7.125\,\text{V}$, Fig. 2.22.

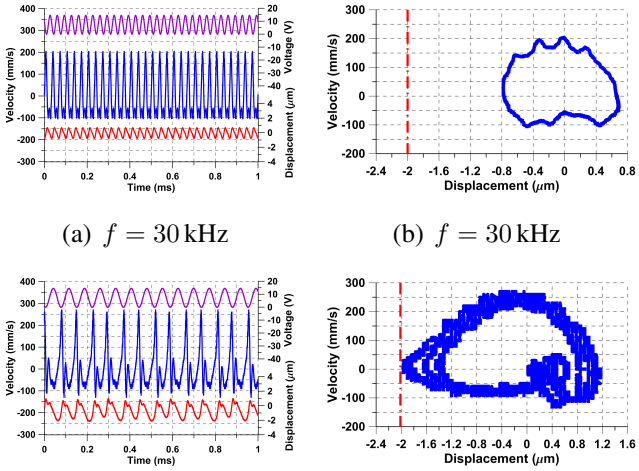

(a) $f = 30\,\text{kHz}$ (b) $f = 30\,\text{kHz}$

(c) $f = 13.70\,\text{kHz}$ (d) $f = 13.70\,\text{kHz}$

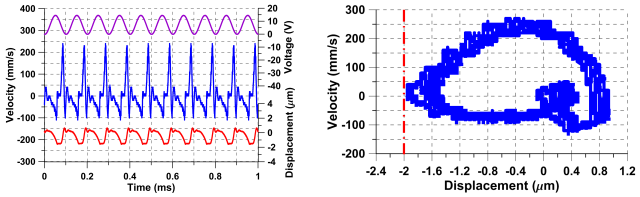

(e) $f = 10\,\text{kHz}$ (f) $f = 10\,\text{kHz}$

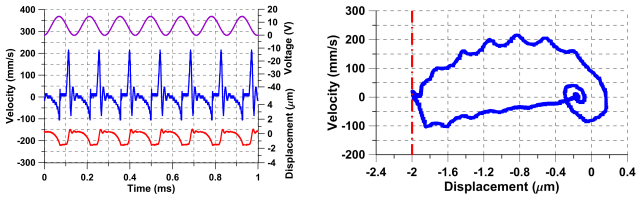

(g) $f = 7\,\text{kHz}$ (h) $f = 7\,\text{kHz}$

Figure 2.22: Voltage waveform, tip velocity, and tip displacement time-histories colored in magenta, blue, and red, respectively, and corresponding to phase portraits under the voltage waveform of $V_\text{a} = 7.125\,\text{V}$

The sensor response started by a periodic forced-orbit at an excitation frequency of $f = 30\,\text{kHz}$, Fig. 2.22 (a). Chaos appeared in the vicinity of the superharmonic resonance of order-three as the frequency dropped to $f = 13.70\,\text{kHz}$, Fig. 2.22 (c). The velocity and displacement time-histories and corresponding phase portraits confirm the existence of chaos. Shilnikov orbits homoclinic to a saddle focus were observed as the excitation frequency dropped further to $f = 10$ and $7\,\text{kHz}$. The velocity and displacement time-histories and the corresponding phase portraits show the characteristic spiraling oscillations of the focus and the tapping oscillations instigated by the unstable manifold of a saddle, Fig. 2.22 (e-h).

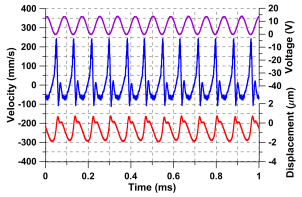

(a) $f = 12.032\,\text{kHz}$

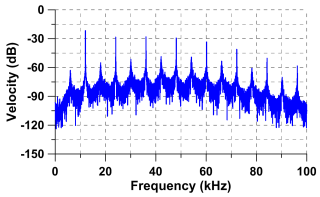

(b) $f = 12.032\,\text{kHz}$

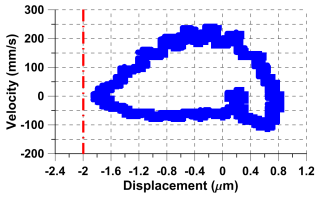

(c) $f = 12.032\,\text{kHz}$

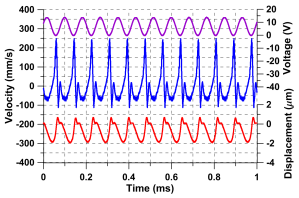

(d) $f = 12.018\,\text{kHz}$

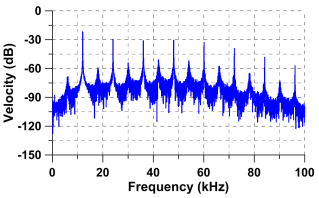

(e) $f = 12.018\,\text{kHz}$

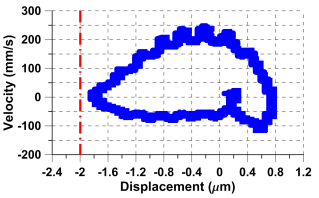

(f) $f = 12.018\,\text{kHz}$

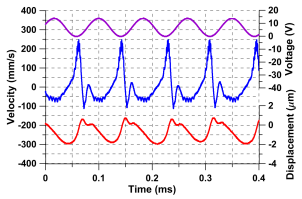

(g) $f = 11.998\,\text{kHz}$

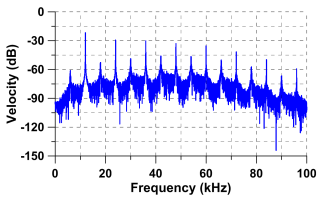

(h) $f = 11.998\,\text{kHz}$

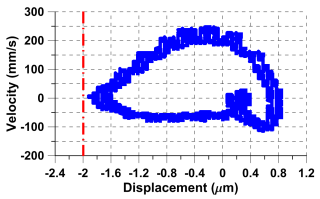

(i) $f = 11.998\,\text{kHz}$

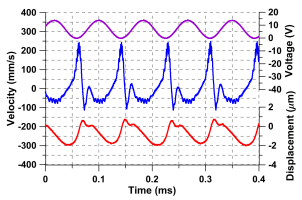

(j) $f = 11.992\,\text{kHz}$

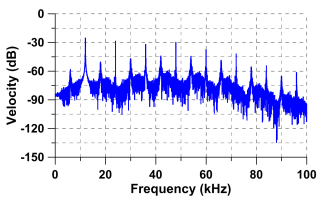

(k) $f = 11.992\,\text{kHz}$

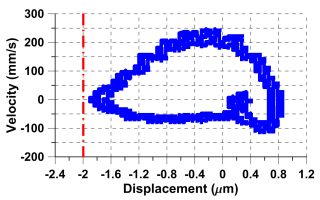

(l) $f = 11.992\,\text{kHz}$

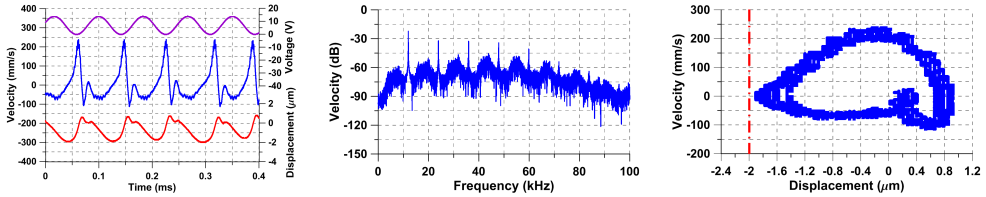

(m) $f = 11.972\,\text{kHz}$

(n) $f = 11.972\,\text{kHz}$

(o) $f = 11.972\,\text{kHz}$

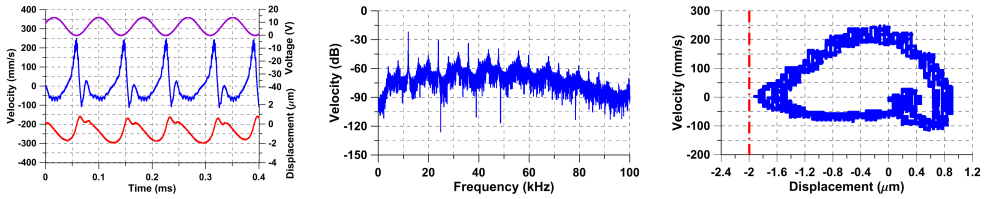

(p) $f = 11.955\,\text{kHz}$

(q) $f = 11.955\,\text{kHz}$

(r) $f = 11.955\,\text{kHz}$

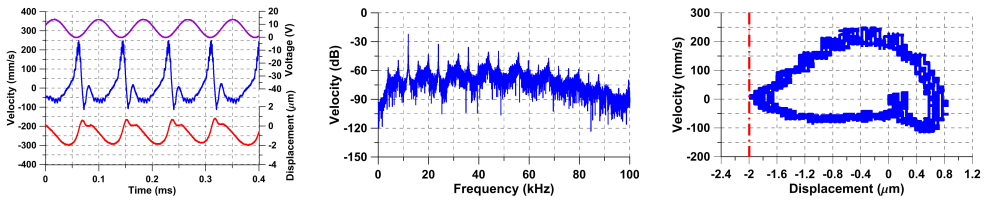

(s) $f = 11.950\,\text{kHz}$

(t) $f = 11.950\,\text{kHz}$

(u) $f = 11.950\,\text{kHz}$

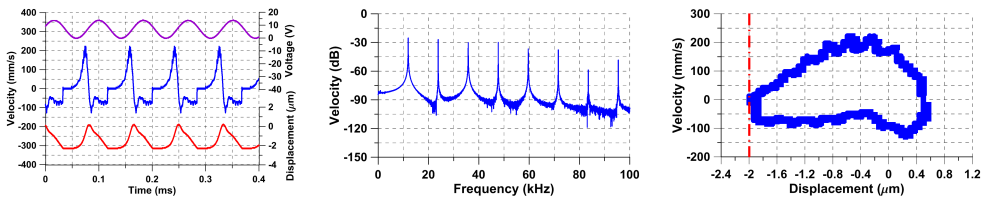

(v) $f = 11.930\,\text{kHz}$

(w) $f = 11.930\,\text{kHz}$

(x) $f = 11.930\,\text{kHz}$

Figure 2.23: Excitation signal, velocity, and displacement time-histories colored in magenta, blue, and red, respectively, velocity in logarithmic scale (0 dB = 1 mm/s), and phase portrait excited at voltage amplitude of $V_\text{a} = 6.750\,\text{V}$

Period doubling bifurcation of P-2 at $f = 12.032, 12.018, 11.998,$ and 11.992, Fig. 2.23 (a-i), route to chaotic behavior of P-3 at $f = 11.972, 11.955,$ and 11.950 were observed, Fig. 2.23 (m-

u). The elevated floor in the velocity response in dB-scale scale demarcates chaos where the tip interacts with the substrate. The sensor dynamic response went back to periodic orbit with tapping oscillations while the excitation frequency set to $f = 11.930\,\text{kHz}$, Fig. 2.23 (v-x).

2.3 Superharmonic Resonance of Sensor #1

Since the effective nonlinearity is softening, the frequency response curves of the sensor are skewed to the left. It is therefore more tractable to observe the evolution of the resonant dynamics in a descending frequency sequence as the response grows along the upper branch, is interrupted by tapping mode oscillations along the middle branch, then jumps down to the lower branch.

2.3.1 Period-Doubling

Initially, the orbit grows as the frequency of excitation drops toward the superharmonic resonance of order-two $f \to \frac{1}{2}f_1$. Large period-one (P-1) orbits were observed at the excitation frequency $f = 32\,\text{kHz}$ when exciting the sensor by an amplitude voltage of $V_\text{a} = 7.725\,\text{V}$ as shown in Fig. 2.24 (a-c). It results in a forced response, superharmonic resonance of order two, located at $f = \frac{1}{2}f_1$ and $f = f_n$, Period-doubling of P-2 following after P-1, Fig. 2.24 (d-f) was also observed while the sensor excited at a frequency of $f = 31\,\text{kHz}$.

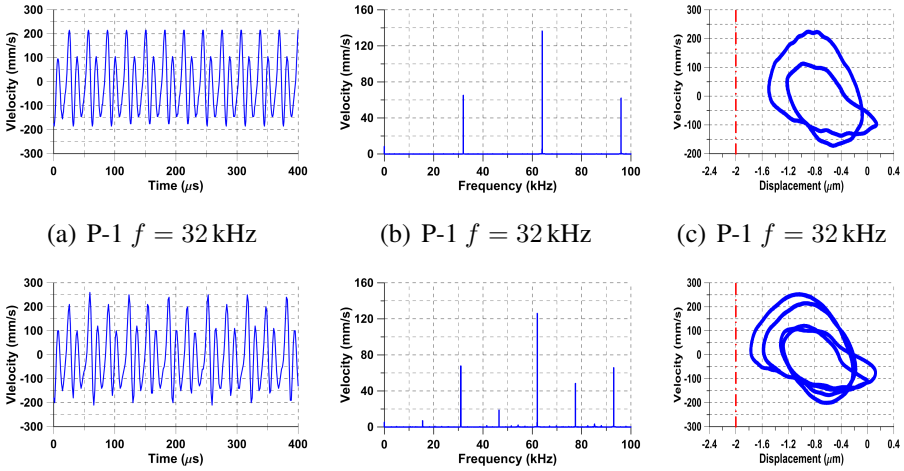

(a) P-1 $f = 32\,\text{kHz}$ (b) P-1 $f = 32\,\text{kHz}$ (c) P-1 $f = 32\,\text{kHz}$

(d) P-2 $f = 31\,\text{kHz}$ (e) P-2 $f = 31\,\text{kHz}$ (f) P-2 $f = 31\,\text{kHz}$

Figure 2.24: A period doubling from P-1 two P-2 occurs as the excitation frequency drops from $f = 32\,\text{kHz}$ to $f = 31\,\text{kHz}$ at a voltage amplitude of $V_\text{a} = 7.725\,\text{V}$

2.3.2 Shilnikov Chaos

Shilnikov chaos was observed as an infinite countable set represented by an unstable saddle focus and stable real line, $(\rho \pm i\omega, -\lambda)$. It is occurs subsequent to a supercritical-Hopf bifurcation. This behavior is represented by the unstable saddle-focus forming unstable period-doubling spirals away from the saddle and contracted by the stable manifold to be re-injected back to the saddle. The re-injection occurs due to tapping oscillations where the sensor tip interacts with the substrate. This behavior is also known by Rossler [157, 158]. This behavior was intensively observed in chemical [55, 159, 160] and optical [161–166] applications.

Chaotic behaviors of banded chaos, P-6, and P-3 were observed at excitation frequencies of $f = 31.20, 29.90,$ and$29.60\,\text{kHz}$ and voltage amplitude $V_\text{a} = 7.725\,\text{V}$. The tip velocity and displacement time-histories, velocity response in dB-scale, and corresponding to phase

portraits were collected over time span of $12.48, 11.96,$ and 11.84 excitation periods, respectively, Fig. 2.25. The velocity response in dB-scale demarcate the banded chaos at $f = 31.20\,\text{kHz}$, Fig. 2.25 (b) in addition to P-6 and P-5 inside the chaotic window at distinct frequencies of $f = 29.90,$ and $29.60\,\text{kHz}$, respectively, Fig. 2.25 (e) and (h).

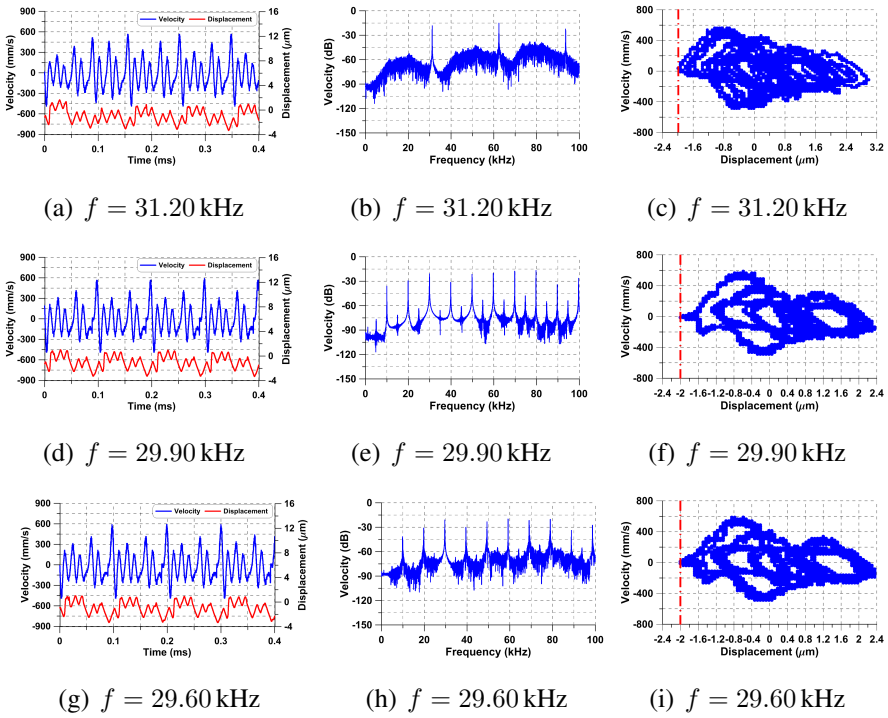

(a) $f = 31.20\,\text{kHz}$ (b) $f = 31.20\,\text{kHz}$ (c) $f = 31.20\,\text{kHz}$

(d) $f = 29.90\,\text{kHz}$ (e) $f = 29.90\,\text{kHz}$ (f) $f = 29.90\,\text{kHz}$

(g) $f = 29.60\,\text{kHz}$ (h) $f = 29.60\,\text{kHz}$ (i) $f = 29.60\,\text{kHz}$

Figure 2.25: Tip velocity and displacement time-histories, FFT velocity in dB-scale (0dB= 1m/s), and corresponding to phase portraits under voltage waveform $V_{\text{a}} = 7.725\,\text{V}$

A countable set of periodic unstable oscillations instigated by an unstable saddle-focus were found experimentally in the vicinity of superharmonic resonance Fig.2.26. The re-injected process occurred due to the tapping-mode oscillations. The velocity and displacement time-histories show the laminar flow was interpreted by bursts at regular intervals, Fig. 2.26 (a),(c) and (e). The

sensor was initially excited at $f = 30\,\text{kHz}$ at a voltage waveform of $V_\text{a} = 7.725\,\text{V}$. It shows Shilnikov chaos with evolving countable successive sets of periods over time span of 60 excitation periods. Same behavior was observed when the RMS voltage increased to $V_\text{a} = 7.950\,\text{V}$ at excitation frequency of $f = 30\,\text{kHz}$ over time span of 600, Fig 2.26 (c) and (d). Also, same behavior was found when the RMS voltage dropped to $V_\text{a} = 6.862\,\text{V}$ at the excitation frequency of $f = 26.50\,\text{kHz}$ over time span of 53 excitation periods, Fig 2.26 (e) and (f).

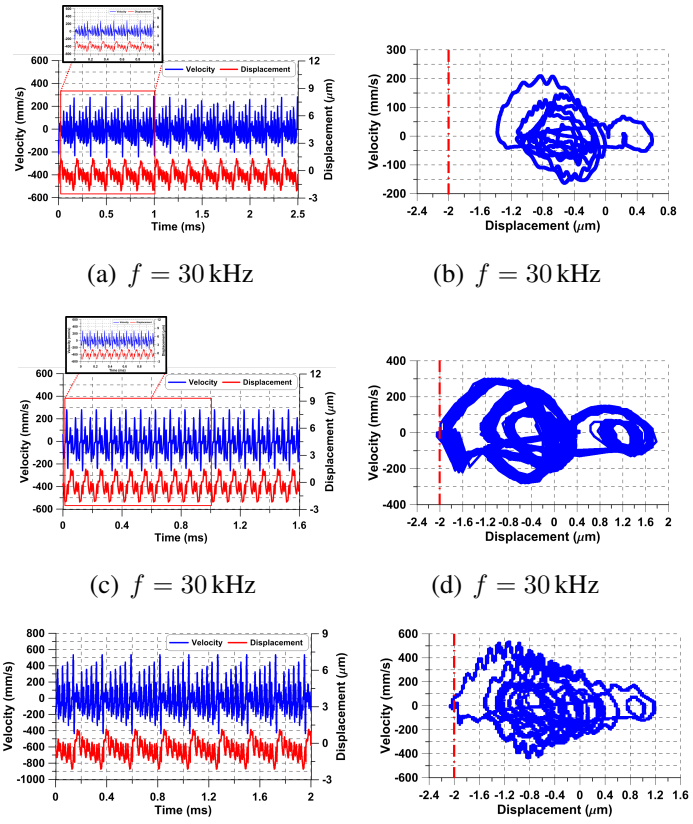

(a) $f = 30\,\text{kHz}$ (b) $f = 30\,\text{kHz}$

(c) $f = 30\,\text{kHz}$ (d) $f = 30\,\text{kHz}$

(e) $f = 26.50\,\text{kHz}$ (f) $f = 26.50\,\text{kHz}$

Figure 2.26: Tip velocity and displacement time-histories and corresponding phase portraits under a voltage waveform of $V_\text{a} = 7.725, 7.950,$ and $6.862\,\text{V}$

The sensor starts with a periodic forced response at the excitation frequency of $f = 27.30\,\text{kHz}$ and voltage amplitude of $V_\text{a} = 6.862\,\text{V}$. The tip velocity and displacement, velocity response in dB-scale, and corresponding phase portraits collected over a time span of 27.30 excitation periods are shown in Fig. 2.27 (a-c). The sensor response went to period-doubling of P-2 while the excitation frequency dropped to $f = 27.150\,\text{kHz}$. The tip velocity and displacement, velocity response in dB-scale, and corresponding phase portrait collected over a time span of 27.15 excitation periods are shown in Fig. 2.27 (d-f). Then, the sensor went to period-doubling of P-4 while the excitation frequency dropped further to $f = 27.030\,\text{kHz}$. The tip velocity and displacement, velocity response in dB-scale, and corresponding phase portrait collected over a time span of 27.030 excitation periods are shown in Fig. 2.27 (g-i). The elevated noise floor indicates this excitation frequency is located inside the chaotic window.

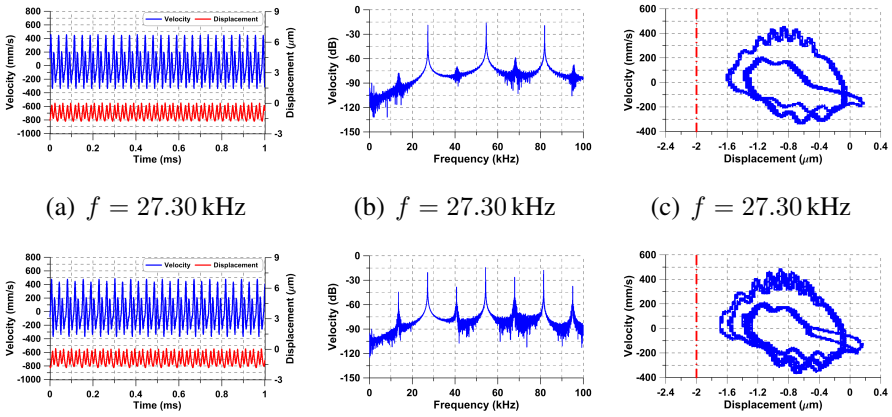

(a) $f = 27.30\,\text{kHz}$ (b) $f = 27.30\,\text{kHz}$ (c) $f = 27.30\,\text{kHz}$

(d) $f = 27.150\,\text{kHz}$ (e) $f = 27.150\,\text{kHz}$ (f) $f = 27.150\,\text{kHz}$

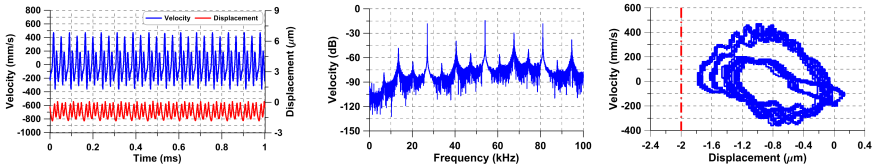

(g) $f = 27.030\,\text{kHz}$ (h) $f = 27.030\,\text{kHz}$ (i) $f = 27.030\,\text{kHz}$

Figure 2.27: Tip velocity and displacement time-histories, FFTs velocity in logarithmic dB-scale (0 dB = 1 mm/s) and corresponding phase portraits under voltage waveform $V_\text{a} = 6.862\,\text{V}$

In addition, chaotic behaviors were instigated right after the intermittency type-III at the excitation frequencies of $f = 26.980, 26.930, 26.890, 26.710,$ and $26.60\,\text{kHz}$ and a voltage waveform of $V_\text{a} = 6.862\,\text{V}$, Fig. 2.28. The displacement and voltage time-histories and corresponding phase portraits were collected over a time span of $26.98, 26.93, 26.89, 53.42,$ and 53.20 excitation periods, respectively. Also, the FFT velocity response was measured over a frequency bandwidth of $100\,\text{kHz}$.

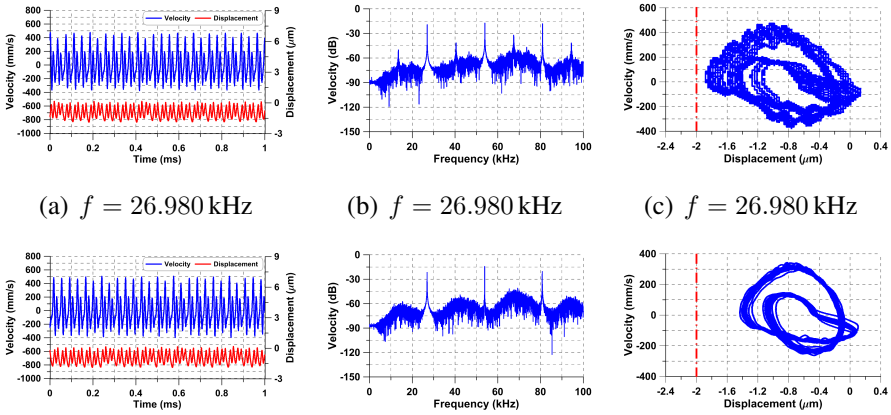

(a) $f = 26.980\,\text{kHz}$ (b) $f = 26.980\,\text{kHz}$ (c) $f = 26.980\,\text{kHz}$

(d) $f = 26.930\,\text{kHz}$ (e) $f = 26.930\,\text{kHz}$ (f) $f = 26.930\,\text{kHz}$

Figure 2.28: Tip velocity and displacement time-histories, velocity FFTs in dB-scale (0 dB = 1 mm/s), and phase portraits under voltage waveform $V_\text{a} = 6.862\,\text{V}$

The period-doubling bifurcation P-2 route to chaos was observed while the sensor was excited at $f = 26.980\,\text{kHz}$ Fig. 2.28 (a-c). A chaotic behavior of banded chaos was observed at $f = 26.930\,\text{kHz}$ Fig. 2.28 (d-f) as a evidence of the sensor is inside a chaotic region.

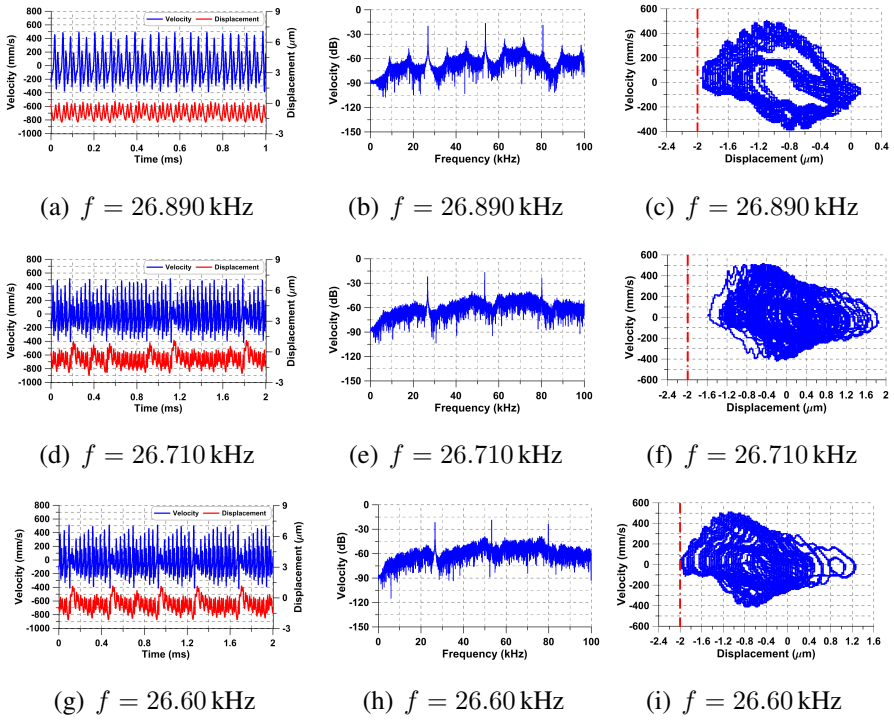

(a) $f = 26.890\,\text{kHz}$ (b) $f = 26.890\,\text{kHz}$ (c) $f = 26.890\,\text{kHz}$

(d) $f = 26.710\,\text{kHz}$ (e) $f = 26.710\,\text{kHz}$ (f) $f = 26.710\,\text{kHz}$

(g) $f = 26.60\,\text{kHz}$ (h) $f = 26.60\,\text{kHz}$ (i) $f = 26.60\,\text{kHz}$

Figure 2.29: Tip velocity and displacement time-histories, velocity FFTs in dB-scale (0 dB = 1 mm/s), and phase portraits under voltage waveform $V_\text{a} = 6.862\,\text{V}$

In addition, a chaotic orbit of period-3 was found at $f = 26.890\,\text{kHz}$, Fig. 2.29 (a-c). The laminar flow starts to develop with evolving intermittent bursts over a time span while dropping the excitation frequency further to $f = 26.710$ and $26.60\,\text{kHz}$. The tip velocity and displacement time-histories show the time span of bursts increases as the excitation frequency decreases, Fig. 2.29 (d) and (g). The raised noise floor of FFT velocity and phase portraits demarcate the

existence of tapping oscillations, Fig. 2.29 (b), (e) and (h). Loosing the sensor periodicity inside the chaotic region can be seen in, Fig. 2.29 (f) and (i).

2.3.3 Intermittency Type-II

Intermittency type-II was observed as aperiodic oscillations of the sensor at $f = 29\,\text{kHz}$. It occurs subsequent to subcritical-Hopf bifurcation [46]. The beam was excited electrostatically by $V_\text{a} = 7.725\,\text{V}$ as shown in Fig. 2.30.

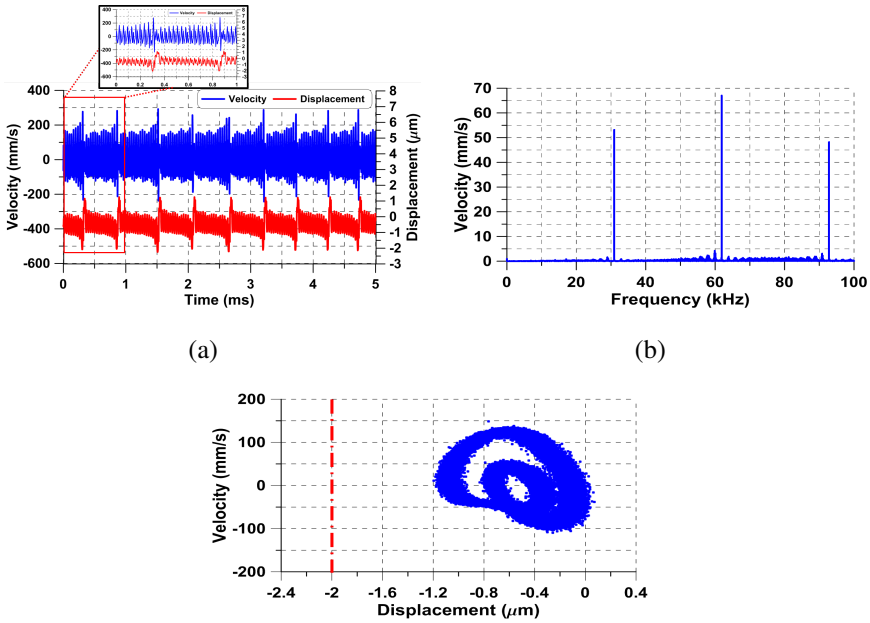

Figure 2.30: (a) Sensor tip velocity and displacement time-histories, (b) velocity response in linear-scale and (c) phase portrait at $f = 29\,\text{kHz}$ and voltage amplitude of $V_\text{a} = 7.725\,\text{V}$

The velocity and displacement time-histories were taken over 0.0116 million excitation periods. Aperiodic oscillations were interrupted by a set of bursts as shown in Fig. 2.30 (a). The

envelope of the time history looks like a beating modulation behavior which is considered a trademark of intermittency of type-II [54]. Also, the velocity FFTs depicts the presence mixture of low and high frequencies demarcate as a baseband and carrier of a modulated signal. A dense phase portrait, velocity and displacement responses, is shown in Fig. 2.30 (c).

2.3.4 Intermittency Type–III

Intermittency type-III was observed when the sensor was excited at excitation frequencies of $f = 26.260$ and $26\,\text{kHz}$ at voltage waveform of $V_\text{a} = 6.8625\,\text{V}$. laminar flow is observed in the vicinity of ghost orbit at the superharmonic resonance. The laminar flow grows over a time and interrupted by bursts at irregular intervals. Laminar flow is characterized by a time-envelope proportional to nT [46]. The re-injection to the ghost orbit was instigated by involving tapping-mode oscillations, where the tip comes into contact to the substrate. Twelve and eight bursts were measured over a time span of 52.52 and 104 excitation periods, respectively, Fig. 2.31. The velocity FFT response in dB-scale shows the elevated noise floor due the interaction with the substrate, Fig. 2.31 (b) and (e). The process of laminar flow derives to tapping oscillations were also shown in the phase portraits, Fig. 2.31 (c) and (f).

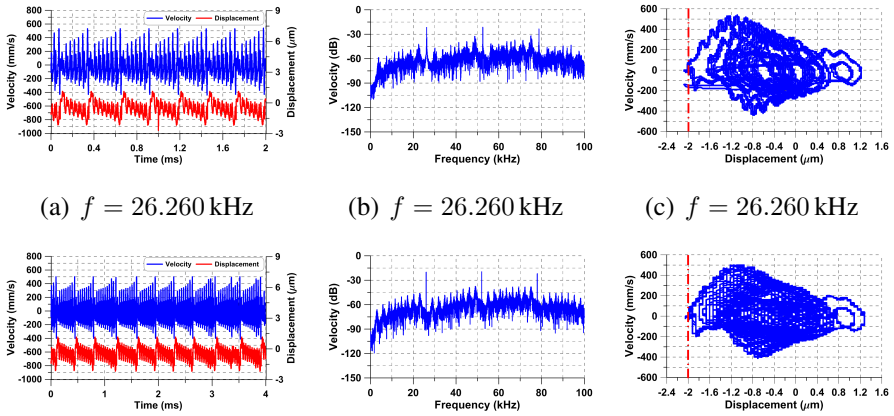

(a) $f = 26.260\,\text{kHz}$ (b) $f = 26.260\,\text{kHz}$ (c) $f = 26.260\,\text{kHz}$

(d) $f = 26\,\text{kHz}$ (e) $f = 26\,\text{kHz}$ (f) $f = 26\,\text{kHz}$

Figure 2.31: Tip velocity and displacement time-histories, FFTs velocity in dB-scale (0 dB = 1 mm/s), and corresponding phase portraits under voltage waveform $V_\text{a} = 6.8625\,\text{V}$

2.3.5 Full Chaos

Full chaos was experimentally observed in the electrostatic MEMS sensor. Non-periodic orbits were observed indicating classical chaos. The beam was excited electrostatically with an amplitude voltage of $V_\text{a} = 8.025\,\text{V}$ at excitation frequency of $f = 18.70\,\text{kHz}$ as shown in Fig. 2.32.

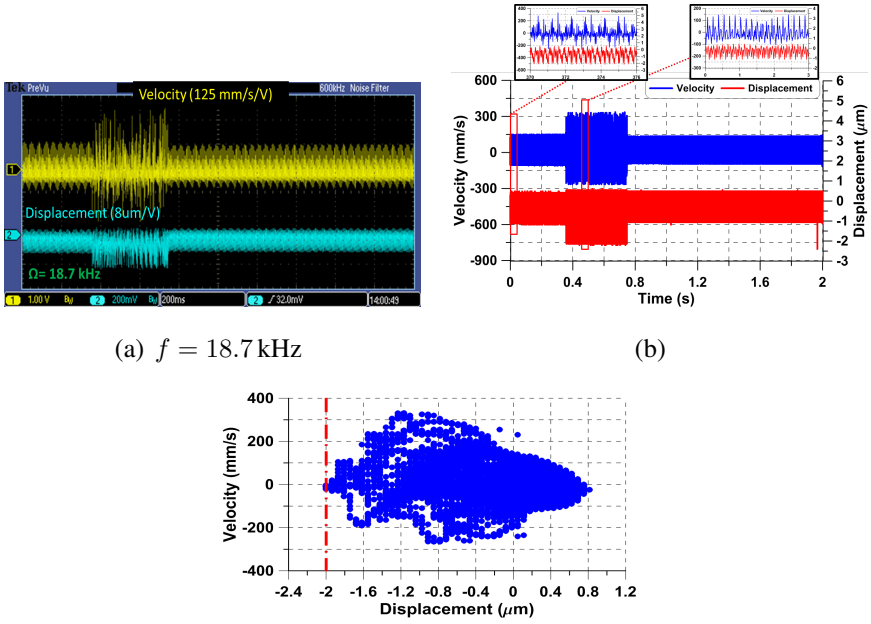

(a) $f = 18.7\,\text{kHz}$ (b)

(c)

Figure 2.32: Beam velocity and displacement time-histories and its phase portrait at $f = 18.70\,\text{kHz}$ excited electrostatically at amplitude voltage of $V_\text{a} = 8.025\,\text{V}$

The velocity and displacement time-histories were captured from the oscilloscope over a time span of $t = 2\,\text{s}$, Fig. 2.32(a). We can see clearly that the periodicity of the orbits were lost and are now filling the space in the phase portrait depicted in Fig. 2.32(b).

2.4 Primary Resonance of Sensor #1

We investigate the sensor response in the vicinity of the primary resonance. The impedance of the sensor at resonance is minimal which increases the chance of amplifying the response. However, the response is limited by the sensor capacitive gap.

Primary and Secondary Resonances

A low-frequency pulse train ($f = 1\,\text{kHz}$) with an amplitude of 3 V and a duty cycle of 0.8% was applied to the sensor #1 to determine its natural frequency. The velocity time-history and FFT of the tip velocity was measured and the dominant peak at $f_n = 78\,\text{kHz}$ was identified as the fundamental natural frequency, Fig. 2.33 (a) and (b). The quality factor was calculated from the measured FFs utilizing half-power bandwidth method and found to be $Q = 5.484$. A multi-points scan, comprising 60 measurement points along the beam axis, was carried out under the excitation signal of a pulse train to identify the fundamental out-of plane mode shape, Fig. 2.33 (c).

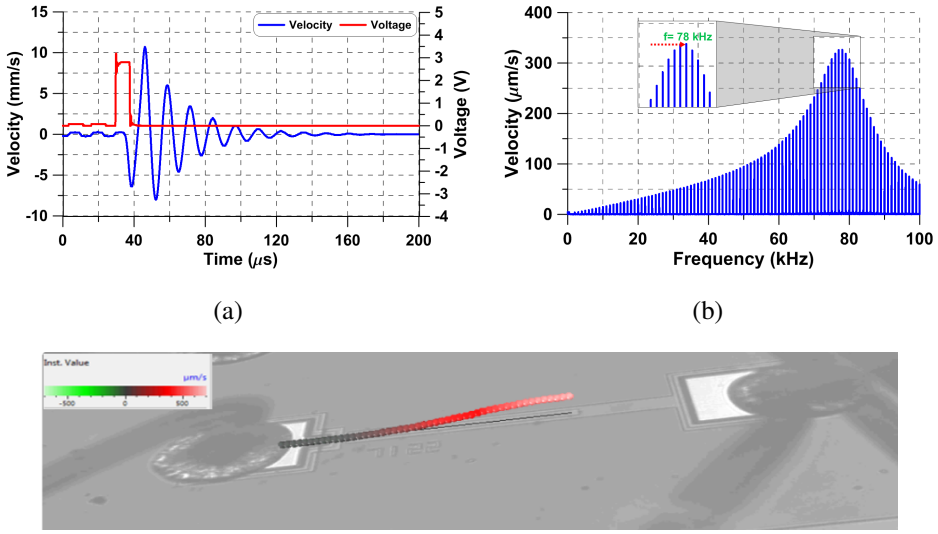

(a) (b)

(c) Multi-points scan

Figure 2.33: (a) The sensor velocity time-history and excitation voltage colored in blue and red, (b) the velocity FFTs response, and (c) multi-points scan

The sensor response under primary was investigated by applying an excitation amplitude of

$V_{\mathrm{a}} = 6\,\mathrm{V}$ at $f = f_n$. The response (tip velocity) is shown in Fig. 2.34 in the time and frequency domains. The FFT is db-scales with 0 dB set equivalent to 1 m/s. The dominant peak was found at the fundamental natural frequency, $f = f_n$. Higher harmonics also appeared at the even and odd multiples of the excitation frequency $2f_n$, $3f_n$, $4f_n$ and $5f_n$ due to the presence of strong quadratic and cubic nonlinearities.

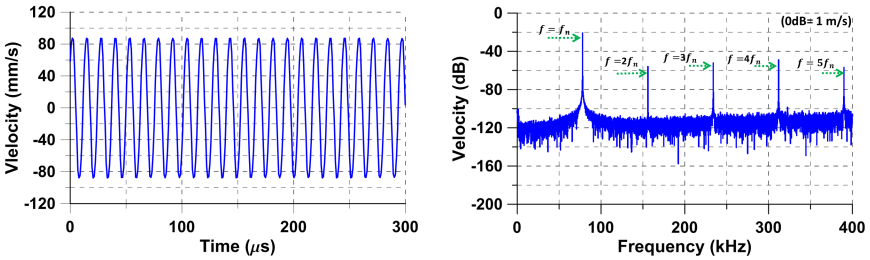

(a) sensor respnses in time doamin (b) sensor FFTs respnses in dB-scale

Figure 2.34: sensor tip velocity under primary resonance excitation $f = f_n = 78\,\mathrm{kHz}$

The same experimental procedure was employed to investigate superharmonic resonance with the excitation frequency set to $f = 39\,\mathrm{kHz}$. The response in time and frequency domains is shown in Fig. 2.35. In this case, peaks appear in the frequency domain at the forcing frequency $f = \frac{1}{2}f_n$ and its multiples f_n, $\frac{3}{2}f_n$, $2f_n$, $\frac{5}{2}f_n$, $3f_n$, $\frac{7}{2}f_n$, $4f_n$, and $\frac{9}{2}f_n$.

2.4.1 Banded Chaos

A banded chaotic attractor was Along this branch. Banded chaos, unlike classical full chaos, does not fill-in the attractor in phase-space. It was observed at excitation frequencies of $f = 61\,\mathrm{kHz}$, $f = 60.7\,\mathrm{kHz}$, $f = 60\,\mathrm{kHz}$, $f = 59.86\,\mathrm{kHz}$, and $f = 59.80\,\mathrm{kHz}$ as shown in Fig. 2.36.

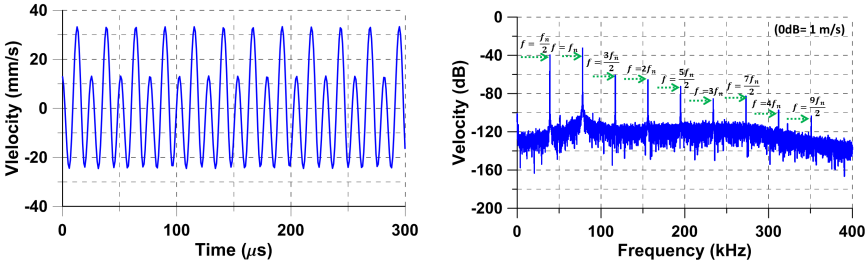

(a) (b)

Figure 2.35: sensor tip velocity under superharmonic resonance excitation $f = \frac{1}{2} f_n = 39\,\text{kHz}$

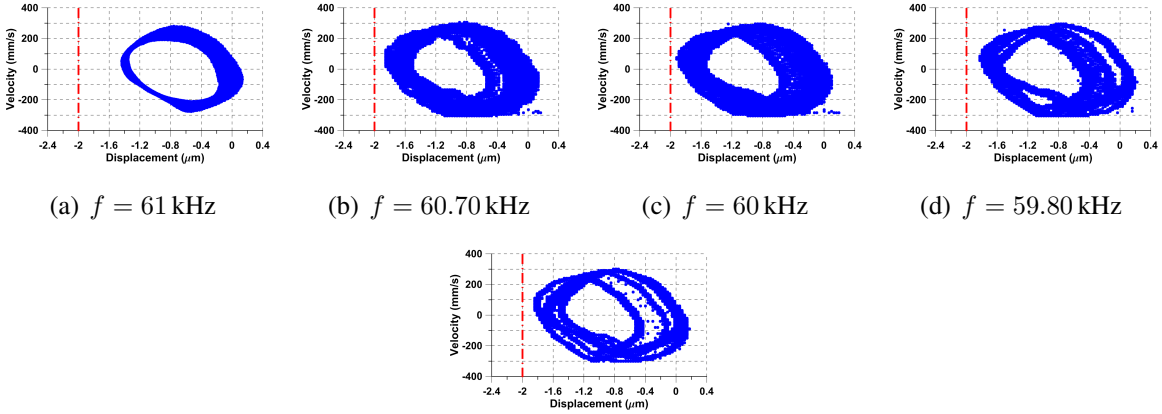

(a) $f = 61\,\text{kHz}$ (b) $f = 60.70\,\text{kHz}$ (c) $f = 60\,\text{kHz}$ (d) $f = 59.80\,\text{kHz}$

(e) $f = 59.86\,\text{kHz}$

Figure 2.36: Phase Portraits of banded chaos excited the sensor at voltage amplitude of $V_\text{a} = 7.725\,\text{V}$

The same phenomenon was also observed when the RMS voltage dropped to $V_\text{a} = 6.90\,\text{V}$ at frequencies of $f = 50.90\,\text{kHz}$, $f = 50.70\,\text{kHz}$, and $f = 50.50\,\text{kHz}$ as shown in Fig. 2.37.

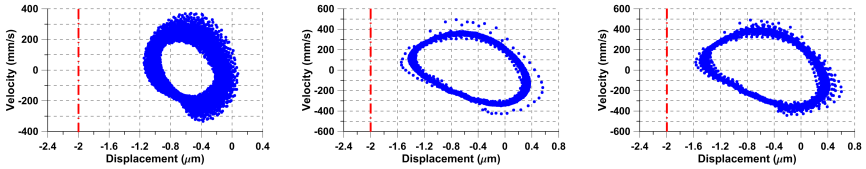

(a) $f = 50.90\,\text{kHz}$ (b) $f = 50.70\,\text{kHz}$ (c) $f = 50.50\,\text{kHz}$

Figure 2.37: Phase Portraits of banded chaos excited at voltage amplitude of $V_\text{a} = 6.90\,\text{V}$

It appears that the banded chaotic attractor develops through a Ruelle-Takens scenario [46, 167–170], where a secondary Hopf results in two-period periodic (quasiperiodic) orbits followed by another Hopf bifurcation, torus breakdown and chaos. This route to chaos was observed at a lower excitation level $V_\text{a} = 7.45\,\text{V}$. Fig. 2.38 shows linear and and dB-scale FFTs of the orbit obtained at $f_1 = 61\,\text{kHz}$. The side bands appearing around the excitation frequency at $nf_1 \pm f_2$ are a clear indicator of a quasiperiodic orbit [169, 171, 172]. We note that the frequency created by the secondary Hopf bifurcation $f_2 = 4\,\text{kHz}$ is incommensurate with f_1.

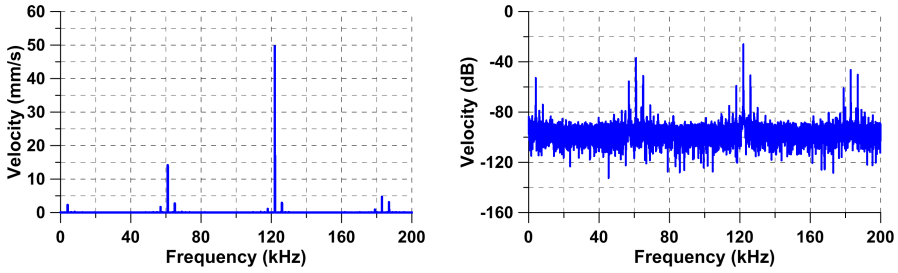

(a) (b)

Figure 2.38: Tip velocity and displacement time-histories, velocity FFTs in linear-scale and dB-scale (0 dB = 1 mm/s), and corresponding to phase portrait at voltage amplitude of $V_\text{a} = 7.45\,\text{V}$ at frequency of $f = 61\,\text{kHz}$

2.4.2 Isolated P-6 Windows

An isolated P-6 window was observed at $f_1 = 60\,\text{kHz}$ within the banded chaotic attractor. The tip velocity and displacement time-histories, the velocity FFT, and corresponding phase portrait of the orbit are shown in Fig. 2.39 (a)-(c). Harmonics of the P-6 orbit appears at $f_1 = 10\,\text{kHz}$ and its multiples in Fig. 2.39 (b). A quasiperiodic orbit was observed when the excitation frequency dropped to $f = 59.86\,\text{kHz}$, Fig. 2.39 (d)-(h) as indicated by the appearance of a secondary harmonic train at $nf_1 \pm f_2$, in addition to the nf_1 train, Fig. 2.39 (e). The new frequency, $f_2 \approx 4.56\,\text{kHz}$ appears due to a secondary Hopf bifurcation. The dense orbit in the phase space, Fig. 2.39 (f), is another indicator of quasiperiodicity.

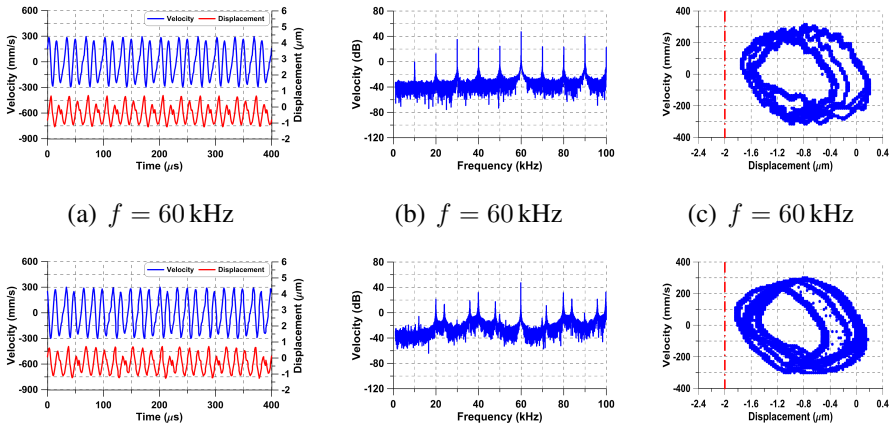

(a) $f = 60\,\text{kHz}$ (b) $f = 60\,\text{kHz}$ (c) $f = 60\,\text{kHz}$

(d) $f = 59.86\,\text{kHz}$ (e) $f = 59.86\,\text{kHz}$ (f) $f = 59.86\,\text{kHz}$

Figure 2.39: Tip velocity and displacement time-histories, velocity FFTs in dB-scale (0 dB = 1 mm/s), and corresponding to phase portrait at voltage amplitude of $V_\text{a} = 7.725\,\text{V}$

Another torus breakdown occurs resulting in banded chaos when the excitation frequency is decreased to $f = 59.80\,\text{kHz}$, Fig. 2.40 (a-c). As a result, the power level in the secondary peaks at $nf_a \pm f_2$ drops. Decreasing the excitation frequency further to $f = 58.40\,\text{kHz}$ brings back the

isolated P-6 periodic window, Fig. 2.40 (d-f).

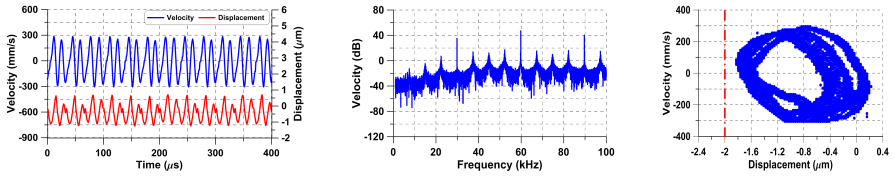

(a) $f = 59.80\,\text{kHz}$ (b) $f = 59.80\,\text{kHz}$ (c) $f = 59.80\,\text{kHz}$

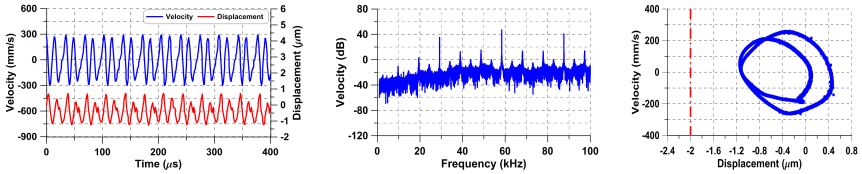

(d) $f = 58.40\,\text{kHz}$ (e) (f)

Figure 2.40: Tip velocity and displacement time-histories, FFTs velocity in dB-scale (0 dB = 1 mm/s), and corresponding to phase portrait at voltage amplitude of $V_\text{a} = 7.725\,\text{V}$

The same isolated P-6 window was also observed at a higher excitation voltage $V_\text{a} = 8.025\,\text{V}$ at $f_1 = 61.7\,\text{kHz}$, Fig. 2.41. In this case, the FFT of the orbit, Fig. 2.41 (b), is made of a train of $f_1/6\,\text{kHz}$ and its higher harmonics.

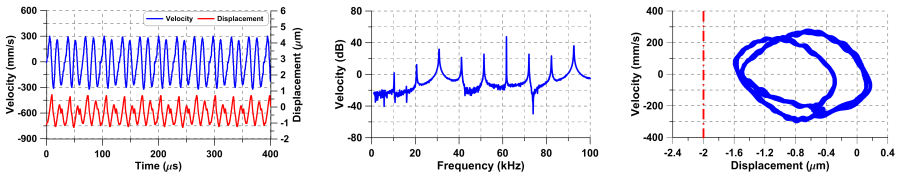

(a) (b) (c)

Figure 2.41: Tip velocity and displacement time-histories, velocity FFTs in dB-scale (0dB= 1 mm/s), and corresponding to phase portrait at voltage amplitude of $V_\text{a} = 8.025\,\text{V}$ at $f = 61.70\,\text{kHz}$

At $f = 56\,\text{kHz}$, Fig. 2.42 a P-2 orbit appears. It constitutes the lower bound on the banded chaotic attractor.

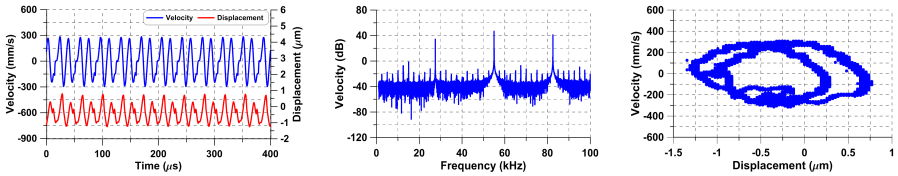

(a) P-1 $f = 56\,\text{kHz}$ (b) P-1 $f = 56\,\text{kHz}$ (c) P-1 $f = 56\,\text{kHz}$

Figure 2.42: Tip velocity and displacement time-histories, velocity FFTs in dB-scale (0 dB = 1 mm/s), and corresponding to phase portrait at voltage amplitude of $V_\text{a} = 7.725\,\text{V}$

2.4.3 Switching Intermittency of Type-II

During a forward frequency-sweep, the sensor was excited by the voltage waveform $V_\text{a} = 7.725\,\text{V}$ at an excitation frequency of $f = 57.0\,\text{kHz}$ further away from the lower cyclic-fold bifurcation. At this location, a homoclinic entanglement invades the safe basin of motion destroying the large freely oscillating orbit of the upper branch [43]. As a result, laminar flow is observed in the vicinity of that ghost orbit. The response grows over time before bursting away to be arrested by a chaotic attractor involving tapping-mode oscillations.

Experimental measurements of the velocity and displacement-time histories, collected over 0.57 million excitation periods, are shown in Fig. 2.43. The sensor spends irregular time intervals around the ghost orbit and on the chaotic attractor. Laminar flow is characterized by a time-envelope proportional to nT. The velocity and displacement time-histories show that laminar flow corresponds to free oscillations while the chaotic attractor involves tapping-mode oscillations.The re-injection from the chaotic attractor to the ghost orbit is noise induced. This

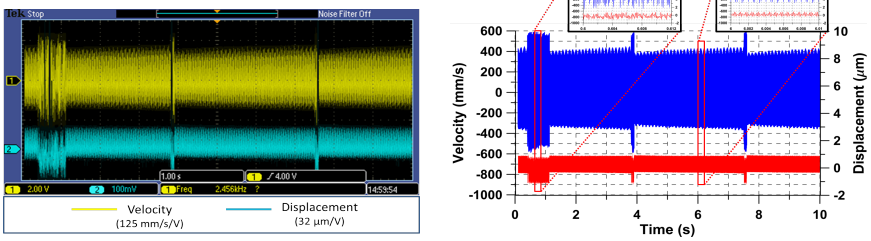

(a) $f = 57\,\text{kHz}$ (b) $f = 57\,\text{kHz}$

Figure 2.43: Velocity and displacement time-histories colored in blue and red, respectively, of the sensor tip excited by the voltage amplitude $V_{\text{a}} = 7.725\,\text{V}$

behavior was found to persist over long-time with the only variation being in the intervals of time spent in laminar flow and on the chaotic attractor.

Increasing the voltage waveform to $V_{ac} = V_{dc} = 7.87\,\text{V}$ while holding the frequency of excitation at $f = 57\,\text{kHz}$, increased the average time intervals the sensor spent on the chaotic attractor but did not introduce a significant change in the size of the attractor. Fig. 2.44 shows two shots of the velocity and displacement time-histories of sensor tip separated by 96 seconds. Each shot is composed of 0.57 million excitation cycles. The time stretches occupied by the chaotic attractor are marked by a sudden drop in the displacement range towards the substrate.

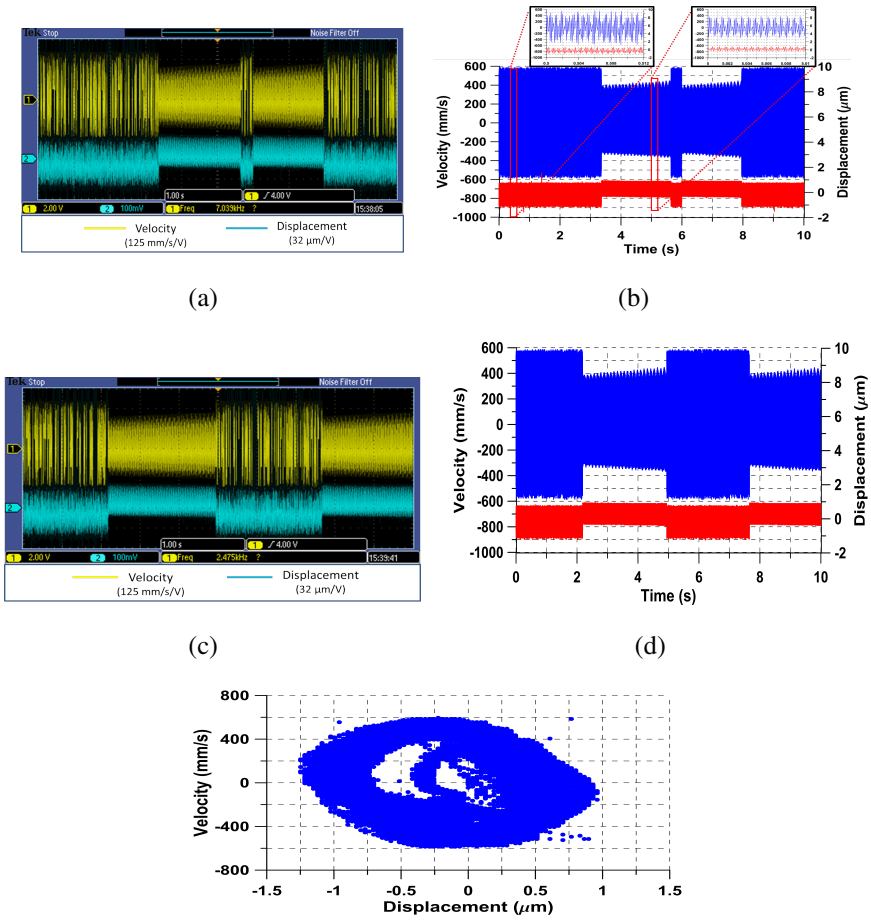

Figure 2.44: Velocity and displacement time-histories colored in blue and red, respectively, of the sensor tip excited by the voltage amplitude $V_{\mathrm{a}} = 7.870\,\mathrm{V}$ at $f = 57\,\mathrm{kHz}$

The same behavior was obtained while the excitation frequency increased to $f = 57.20\,\mathrm{kHz}$, Fig. 2.45. We found the laminar flow of the velocity and displacement time-histories increased over time span of 0.572 million excitation cycles as the excitation frequency increased resulting in less bursts occurred. The chaotic region was also spends more time compared the previous

case in Fig. 2.44.

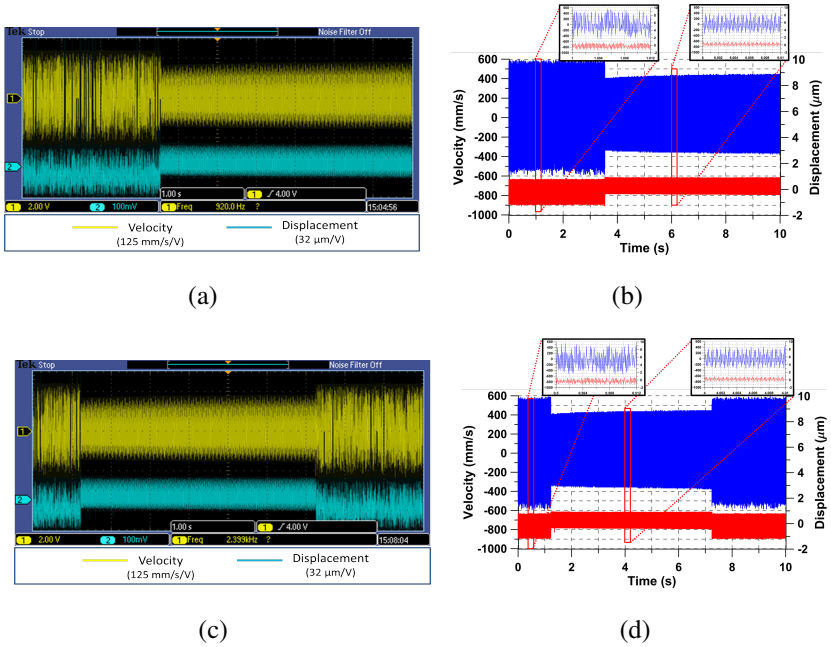

Figure 2.45: Velocity and displacement time-histories colored in blue and red, respectively, of the sensor tip excited by the voltage amplitude $V_{\mathrm{a}} = 7.870\,\mathrm{V}$ at $f = 57.20\,\mathrm{kHz}$

As frequency was further increased, the sensor spent more time on the chaotic attractor resulting in banded chaos at $f = 58\,\mathrm{kHz}$, as shown Fig. 2.46. A further increase in the frequency results in the sensor moving from the intermediate branch of the frequency response curve to the upper branch where oscillations become free and periodic.

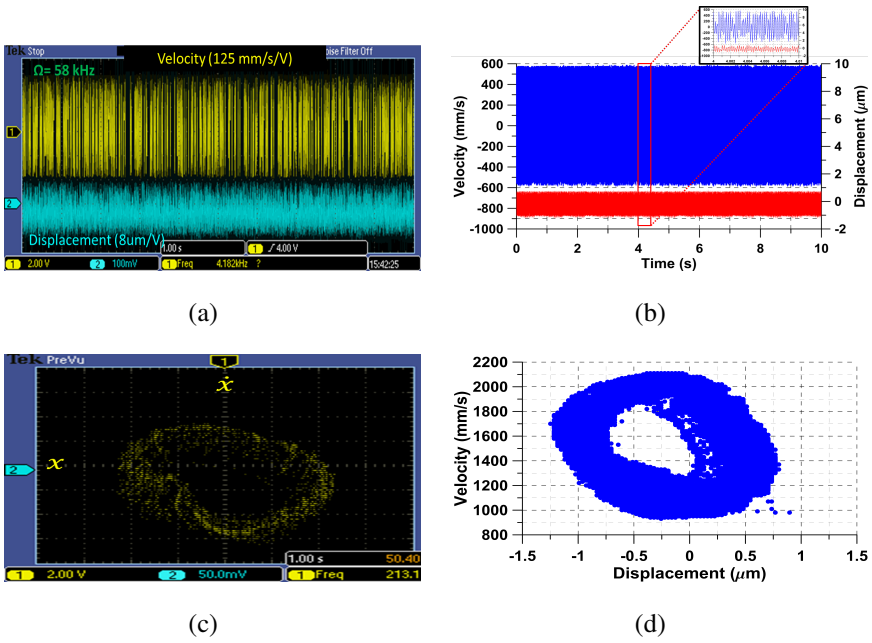

(a) (b)

(c) (d)

Figure 2.46: Velocity and displacement time-histories colored in blue and red, respectively, of the sensor tip excited by the voltage amplitude $V_{\mathrm{a}} = 7.870\,\mathrm{V}$ at $f = 58\,\mathrm{kHz}$

2.4.4 Switching Intermittency of Type-I

Also, switching intermittency of a ghost orbit to large orbits and a ghost orbits to chaotic orbits were also demonstrated.

The sensor was excited during a forward frequency sweep, the sensor was excited by the voltage waveform $V_{\mathrm{a}} = 7.870\,\mathrm{V}$ at an excitation frequency of $f = 54.40\,\mathrm{kHz}$. The elevated voltage increased the strength of the electrostatic field and moved the location of the cyclic-fold bifurcation below f. Instead of the intermittency of type-I expected beyond the cyclic-fold, we observed a switching intermittency of type-I.

The measured velocity time-history over 2.176 million excitation periods is shown in Fig. 2.47.

Laminar flow (smaller oscillations) in the vicinity of the ghost orbit gradually grows over time to be interrupted at irregular intervals by bursts. However, the bursts are not characterized by irregular dynamics as in the case of an intermittency of type-I. Instead, they are arrested by the substrate with the ensuing contraction resulting in a larger tapping-mode periodic orbit typical of the intermediate branch of the frequency-response curve. The sensor spent irregular time intervals on this attractor before being re-injected to the vicinity of the ghost orbit due to external disturbances.

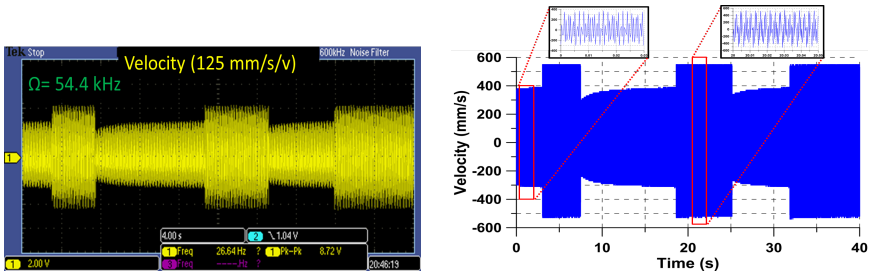

(a) (b)

Figure 2.47: Velocity time-history of the sensor tip excited at $f = 54.40\,\text{kHz}$ by the voltage amplitude of $V_\text{a} = 7.870\,\text{V}$

We found a finite frequency range where this behavior was persistent. Increasing the frequency of excitation to $f = 54.50\,\text{kHz}$, the same behavior was observed. However, we found that the average time spent on the tapping-mode orbit increased as shown in Fig. 2.48. Eventually, as the frequency of excitation increased the response settled-down on the intermediate branch where the time-history of the response is composed only of periodic tapping-mode oscillations.

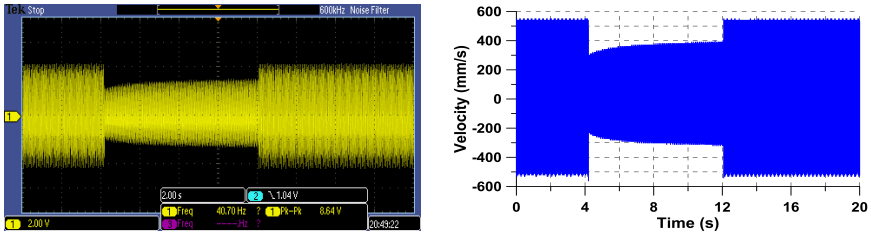

(a) (b)

Figure 2.48: Velocity time-history of the sensor tip excited at $f = 54.50\,\text{kHz}$ by the voltage amplitude of $V_\text{a} = 7.870\,\text{V}$

2.4.5 Intermittency Type-I

Intermittency type-I is one of the chaotic nonlinear dynamic behaviors. It has aperiodic oscillations leading to chaos [46]. Intermittency of type I was demonstrated experimentally in an electrostatic MEMS sensor. These nonlinear dynamic behaviors were observed as the control parameters, voltage and frequency, were varied.

During a forward frequency sweep, the sensor was excited by a voltage amplitude of $V_\text{a} = 7.780\,\text{V}$ at an excitation frequency of $f = 54\,\text{kHz}$. The elevated RMS voltage increased the strength of the electrostatic field and moved the location of the cyclic-fold bifurcation below f. Experimental measurements of the velocity time-history over 21.6 million excitation periods, Fig. 2.49, show laminar flow in the vicinity of the ghost orbit gradually growing over time to be interrupted at irregular intervals by bursts. The time-envelope of the laminar flow intervals is of the order of $\sqrt{nT}$ which is a characteristic of an intermittency of type-1 [46], where T is the period and n is an integer.

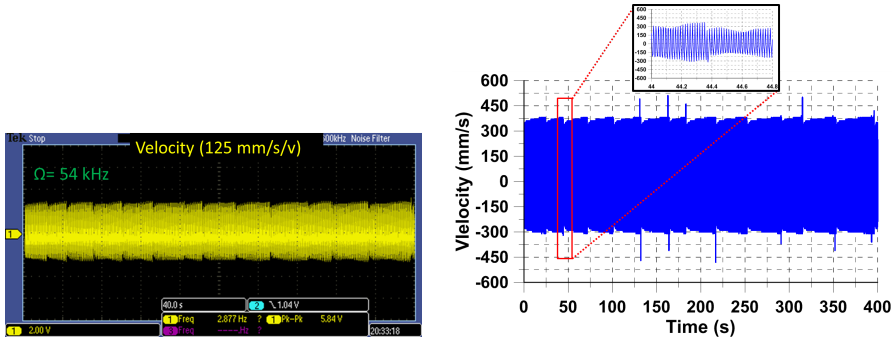

(a) (b)

Figure 2.49: Tip velocity time history at $f = 54\,\text{kHz}$ excited electrostatically at voltage amplitude of $V_\text{a} = 7.870\,\text{V}$

In Fig. 2.49, thirteen bursts were observed over 21.6 million excitation periods. The hard stroke at the end of each burst indicates tapping towards the substrate as shown in Fig. 2.49(b). This intermittent behavior leads to the chaotic behaviors. Further, we observed that the burst has taken more time to occur while the excitation frequency increased to $f = 54.20\,\text{kHz}$ as shown in Fig. 2.50. Two bursts were captured over 2.168 million excitation periods.

During a forward frequency-sweep, the sensor was excited by a voltage amplitude of $V_\text{a} = 7.780\,\text{V}$ at an excitation frequency of $f = 54.70\,\text{kHz}$ further away from the lower cyclic-fold bifurcation. At this location, a homoclinic bifurcation has destroyed the large freely oscillating orbit belonging to the upper branch of the frequency-response curve [43]. As a result, laminar flow is observed in the vicinity of that ghost orbit. The response grows over time before bursting and being re-injected back by involving tapping-mode to small oscillations, Fig. 2.51. Laminar flow is characterized by a time-envelope proportional to nT. The displacement time-history shows that laminar flow corresponds free oscillations while the chaotic attractor involves tapping-mode oscillations.

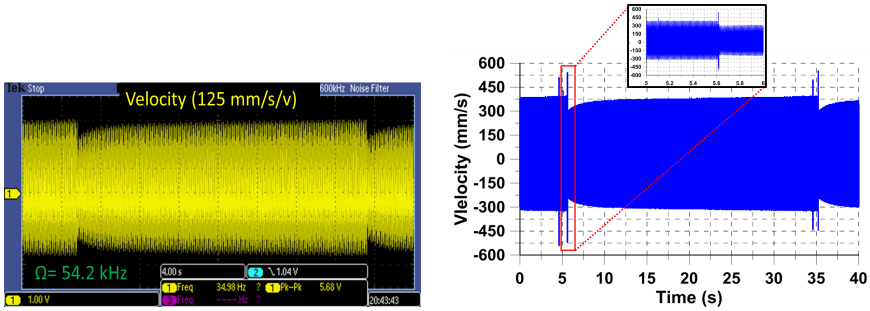

(a) (b)

Figure 2.50: Tip velocity time-history at $f = 54.20\,\text{kHz}$ excited electrostatically at amplitude voltage of $V_\text{a} = 7.870\,\text{V}$

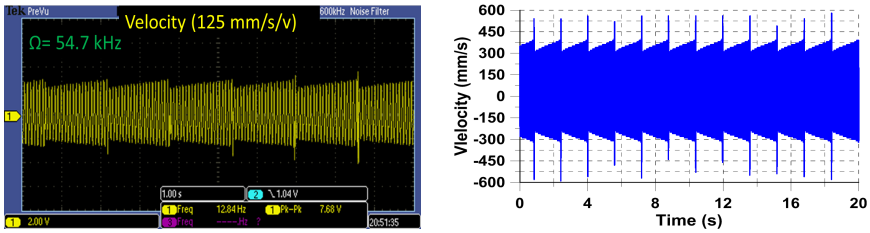

(a) (b)

Figure 2.51: Tip velocity time-history at $f = 54.70\,\text{kHz}$ excited electrostatically at voltage amplitude of $V_\text{a} = 7.870\,\text{V}$

Experimental measurements of the velocity and displacement time-histories, collected over 0.547 million excitation periods involving six bursts within the time span. The same behavior was observed while sweeping the frequency at $f = 56\,\text{kHz}$, $f = 56.50\,\text{kHz}$, and $f = 56.70\,\text{kHz}$ as shown in Fig. 2.52.

In addition, the excitation voltage was increased to $V_\text{a} = 8.025\,\text{V}$ in an effort to investigate

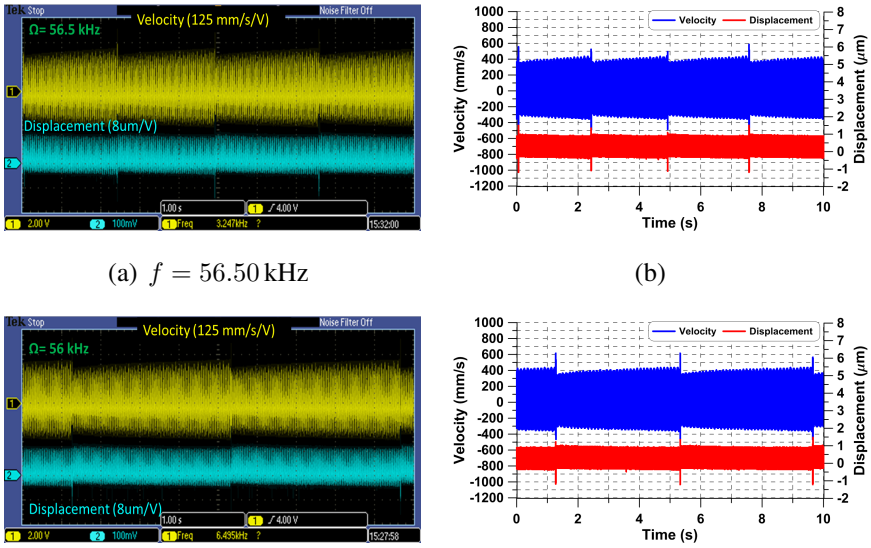

(a) $f = 56.50\,\text{kHz}$ (b)

(c) $f = 56\,\text{kHz}$ (d)

Figure 2.52: Tip velocity and displacement time-histories excited by voltage amplitude of $V_\text{a} = 7.870\,\text{V}$

all of the chaotic behaviors while varying the control parameters, namely, voltage and frequency. Five bursts were observed at $f = 54.80\,\text{kHz}$ observed over 1.096 million excitation periods, Fig. 2.53 (a) and (b). The phase portraits show the response confined in space while some irregular point present due to tapping oscillations, Fig. 2.53 (c) and (d).

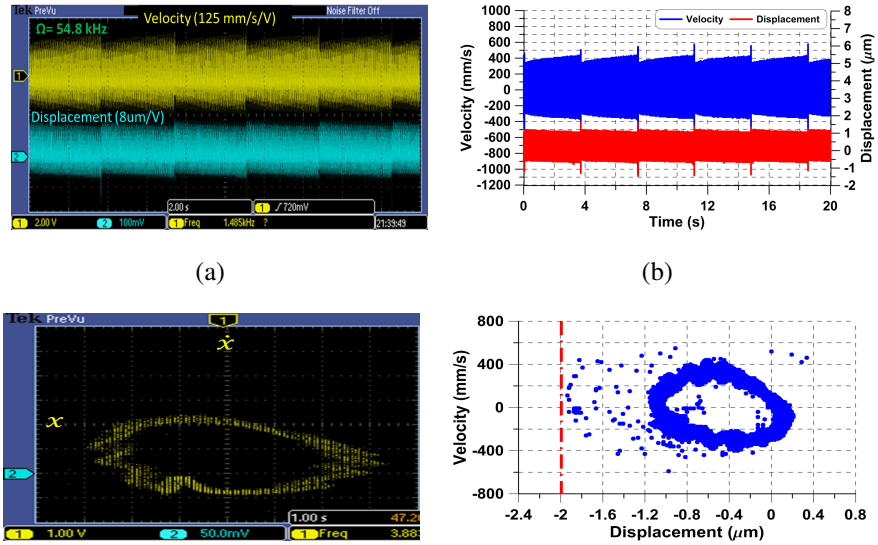

(a) (b)

(c) (d)

Figure 2.53: Tip velocity and displacement time-histories and corresponding phase portrait at $f = 54.80\,\text{kHz}$ and voltage amplitude of $V_\text{a} = 8.025\,\text{V}$ colored in yellow and blue, respectively

2.4.6 Chaotic Attractors

Period three (P-3) and six (P-6) were observed while the sensor excited at voltage amplitude of $V_\text{a} = 6.86\,\text{V}$. These class of periodic window is located inside the chaotic attractor. Period three (P-3) occurs as $f = \frac{k}{2} f_n$. It was found while the sensor excited at frequency of $f = 50.50\,\text{kHz}$ and $f = 52.40\,\text{kHz}$, Fig. 2.54. The tip velocity and displacement time-histories were measured and shown three periods in a one complete cycle, Fig. 2.54 (a) and (d). It is also clearly shown in the velocity FFTs response in dB-scale, Fig. 2.54 (b) and (e) as well as its phase portraits , Fig. 2.54 (c) and (f).

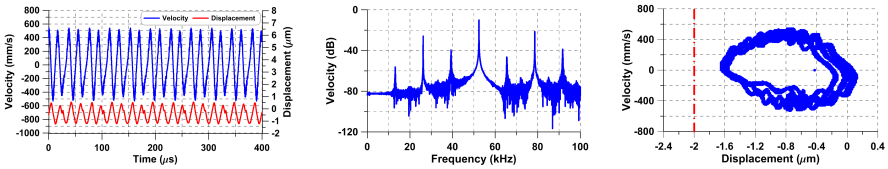

(a) P-3 $f = 52.40\,\text{kHz}$ (b) P-3 $f = 52.40\,\text{kHz}$ (c) P-3 $f = 52.40\,\text{kHz}$

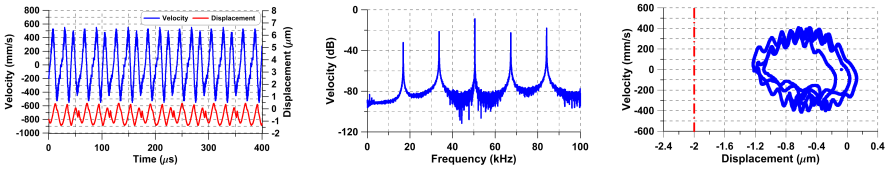

(d) P-3 $f = 50.50\,\text{kHz}$ (e) P-3 $f = 50.50\,\text{kHz}$ (f) P-3 $f = 50.50\,\text{kHz}$

Figure 2.54: Tip velocity and displacement time-histories, FFT velocity in dB-scale (0 dB = 1 mm/s), and corresponding phase portrait under excitation voltage amplitude of $V_\text{a} = 6.86\,\text{V}$

Period six, P-6, was also found inside the chaotic region at the excitation frequency of $f = 51.740\,\text{kHz}$ as shown in Fig. 2.55. The tip velocity and displacement time-histories show six periods in a complete one cycle, Fig. 2.55 (a). It is also clearly shown in the velocity response in dB-scale as well as its phase portrait, Fig. 2.55 (b) and (c).

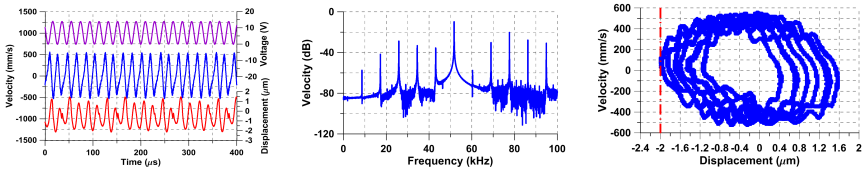

(a) P-6 $f = 51.740\,\text{kHz}$ (b) P-6 $f = 51.740\,\text{kHz}$ (c) P-6 $f = 51.740\,\text{kHz}$

Figure 2.55: Excitation signal, tip velocity, and displacement time-histories, velocity in dB-scale (0 dB = 1 mm/s), and corresponding phase portrait colred in magenta, blue and red, respectively, at excitation voltage of $V_\text{a} = 6.86\,\text{V}$

Further, a forced response was obtained when the excitation frequency was increased to $f =$

53 kHz and $f = 53.50$ kHz, respectively. Shrinking down the periodic orbits to P-1 interpret the end limit of the chaotic chaotic region of the sensor and presents the classical electrostatic forced responses, Eq.(2.2). The velocity and time-histories, velocity FFTs responses in dB-scale in addition to phase portrait were shown in Fig. 2.56.

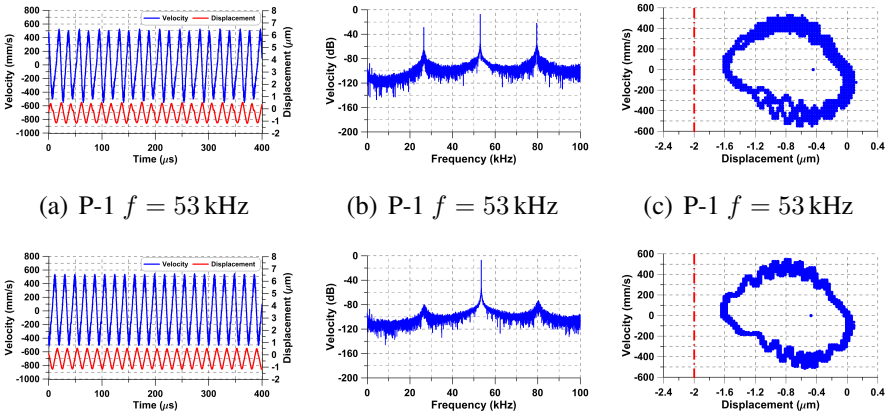

(a) P-1 $f = 53$ kHz (b) P-1 $f = 53$ kHz (c) P-1 $f = 53$ kHz

(d) P-1 $f = 53.50$ kHz (e) P-1 $f = 53.50$ kHz (f) P-1 $f = 53.50$ kHz

Figure 2.56: Tip velocity and displacement time-histories excited at a voltage amplitude of $V_{\mathrm{a}} = 6.86$ V

2.4.7 Period-Doubling Bifurcation

Period-doubling was demonstrated at half of the excitation frequency and its integer multiples, $f = \frac{k f_1}{2}$, where k is an integer. It results a forced response located at $f = f_1$ and $f = \frac{1}{2} f_1$. The velocity and displacement responses were collected in the steady state region, Fig. 2.57, at the excitation frequency of $f = 50.50$ kHz and voltage amplitude $V_{\mathrm{a}} = 6.90$ V. The velocity time history, Fig. 2.57 (a) shows four periods in each periodic cycle. The velocity FFTs shows the excitation frequency $f = 50.50$ kHz and its sub-integer multiples as $f = 12.625, 25.25,$ and 37.875 kHz, Fig. 2.57 (b). Also. the phase portrait show period-doubling

bifurcation P-2 as shown in, Fig. 2.57 (c).

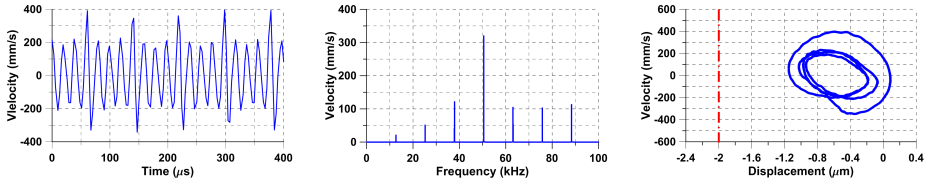

(a) (b) (c)

Figure 2.57: Tip velocity time history, FFTs velocity response, and corresponding phase portraits at frequencies at $f = 50.5\,\text{kHz}$ excited at voltage amplitude of $V_\text{a} = 6.90\,\text{V}$

2.4.8 Homoclinic Bifurcation

Homoclinic bifurcation were demonstrated as another route to chaos [40, 46]. A homoclinic bifurcation is a sequence of transverse intersections between the stable and unstable manifolds to a saddle point [40, 173]. A formation of a horseshoe is present as a results of homoclinic tangle [33]. One of the characteristics of the horseshoe phenomena is having a countable infinity set of periodic orbits [174]. In our case, a countable infinite set of periodic-orbits was observed experimentally. To our knowledge, this is the first time this phenomenon is being observed in electrostatic MEMS sensors.

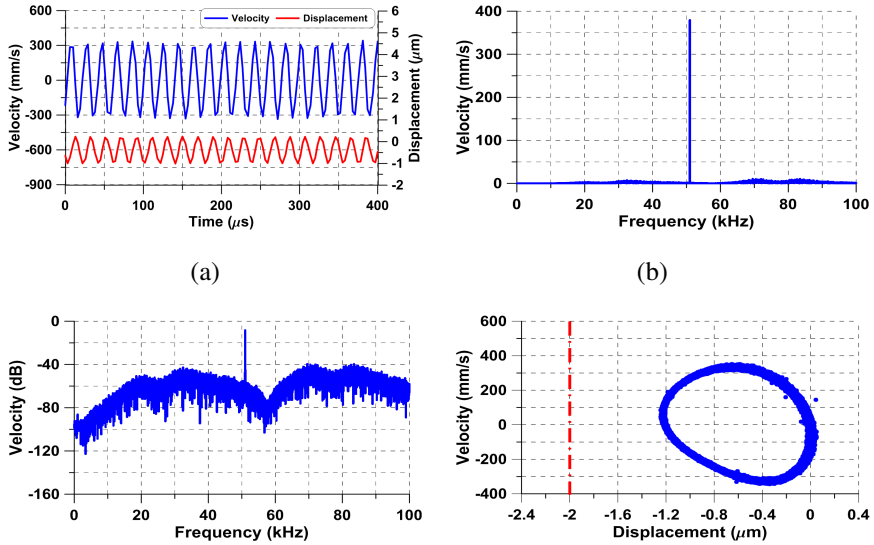

Figure 2.58: Beam velocity frequency response in logarithmic scale and its phase portrait at $f = 51$ kHz excited electrostatically at amplitude voltage of $V_{\mathrm{a}} = 6.90$ V, (0 dB = 1 mm/s)

A homoclinic orbit to a saddle was observed while the beam was excited at a frequency of $f = 51$ kHz and a voltage amplitude of $V_{\mathrm{a}} = 6.90$ V. The orbit falls on the homoclinic orbit of the sensor with a deformed un-symmetrical orbit with a nose directed toward the saddle as shown in Fig. 2.58 (b). The orbits start and end at the same saddle point indicating one of the homoclinic orbit characteristics. The elevated noise floor demarcates the sensor is inside chaotic region as shown in Fig. 2.58 (c) and (d).

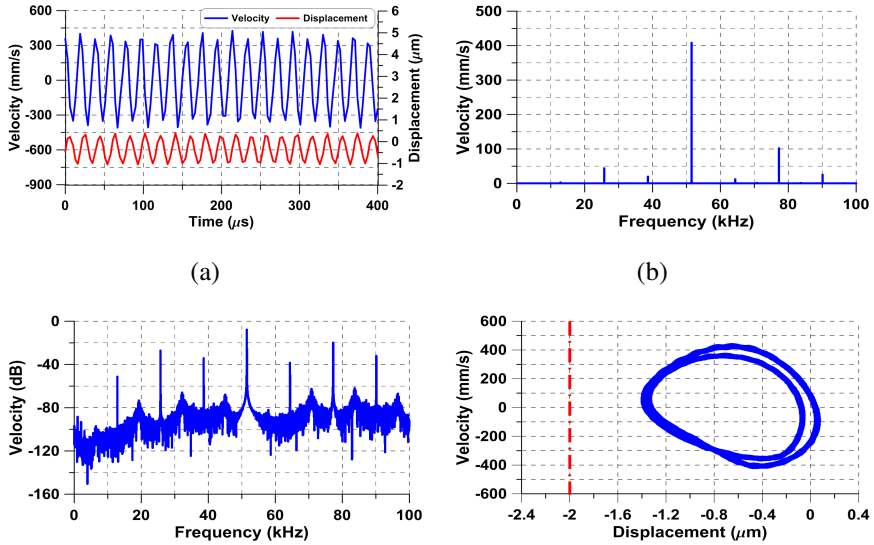

Figure 2.59: Beam velocity frequency response in logarithmic scale and its phase portrait at $f = 51.5$ kHz excited electrostatically at amplitude voltage of $V_{\mathrm{a}} = 6.90$ V, (0 dB = 1 mm/s)

Further, the symmetry of homoclinic orbits were broken into a period-doubling of P-2 when the excitation frequency increased to $f = 51.50$ kHz as shown in Fig. 2.59. The velocity and displacement time-histories, FFTs in linear scale, FFTs in dB-scale, and corresponds to phase portrait show the period-doubling of P-2, Fig. 2.59. This region show the upper-bound of homoclinic bifurcation region.

Chapter 3

Binary Dynamic MEMS Gas Sensors

Binary gas sensors detect the presence of a target gas in a binary fashion. Compared to analog sensors which quantify the concentration of a gas, binary sensors do not measure the concentration of the gas but indicate the status of gas concentration using a discrete signal as: '1', above a threshold, and '0', below it. The cyclic-fold bifurcation in electrostatic MEMS is exploited here to create those discrete (binary) output states. An electrostatic MEMS actuator is equipped with a polymer highly selective to ethanol to create an ethanol vapor gas sensor.

3.1 Gas Sensor

The sensor was fabricated using the PolyMUMPs fabrication process [155], Fig. 3.1, to satisfy the following design criteria:

- Minimize the thickness to increase sensitivity.
- Minimize the beam width to reduce squeeze-film damping.
- Maximize the distance between the actuation pads to reduce leakage current.

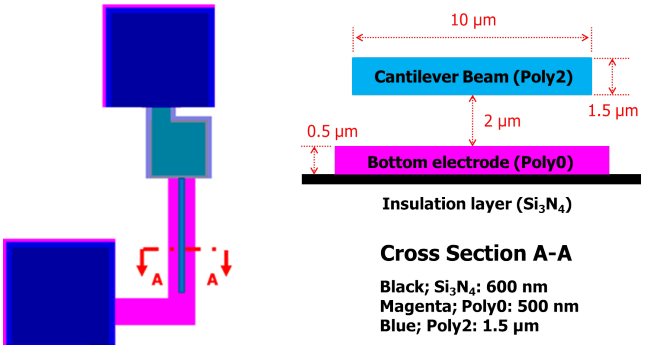

Figure 3.1: Layout of the PolyMUMPs fabricated gas sensor: (a) top-view and (b) front-view along section A–A

It features a cantilever beam fabricated in Poly2 structural layer with dimensions ($175 \times 10 \times 1.5\,\mu m^3$) and material properties $\rho = 2300\,kg/m^3$ and $E = 160\,GPa$. A gap ($d = 2\,\mu m$) is etched under the beam in the second oxide layer. The ground electrode is patterned in Poly0 layer under the length of the beam. Two gold pads are patterned at the root of the beam and the end of the bottom electrode to apply potential difference.

A polymer with affinity to ethanol vapor, poly (2,5-dimethyl aniline) (P25DMA) [175], was deposited onto the beam top surface using manual manipulator. The polymer was dispersed in a 1% solution of ethylene glycol. The reduced wettability of the solution prevents it from running off the beam edges. Six drops of polymer-glycol solution were deposited along the outer half of the beam length in stages to avoid solution overflow. The ethylene glycol was allowed to evaporate in air, leaving polymer residue atop the beam. Fig. 3.2 shows the sensor before, during, and after deposition.

The sensor is actuated by a biased voltage signal. It exploits the qualitative change before and after dynamic pull-in as a sensing mechanism. It acts as a binary logic gate with states of low (no detection) before pull-in and high (detection) after pull-in. Detection can be observed either optically, via a laser-Doppler vibrometer (LDV), or electrically by measuring impedance

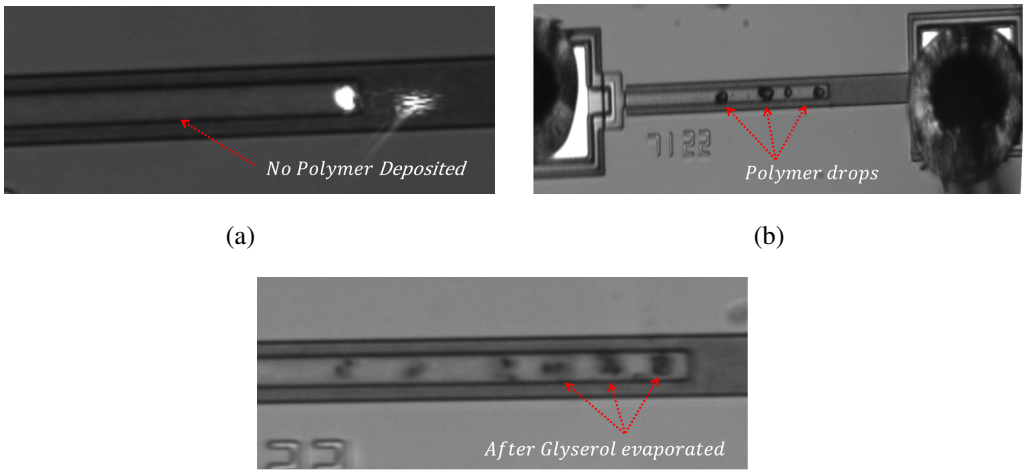

(a) (b)

(c)

Figure 3.2: The cantilever beam (a) before (b) during and (c) after deposition P25DMA and glycol evaporation

between the two pads.

3.2 Analytical Model

The gas sensor is actuated under a quasi- electrostatic MEMS actuator. It consists of a micro-cantilever beam vibrating in z-direction, as shown in Fig. 3.3 (a). The beam length, width, and thickness are denoted l, b, and h, respectively. The cantilever beam is coated with a detector polymer, coupled to an electrode located at a distance d underneath it, and actuated by AC and DC voltage. The detection mechanism is built based on detecting a jump, changing in amplitude, at a cyclic fold bifurcation point due to an added mass (sorbed ethanol molecules) to the cantilever beam.

The model of this sensor is developed based on Newton's second law, Eq.(3.1) which de-

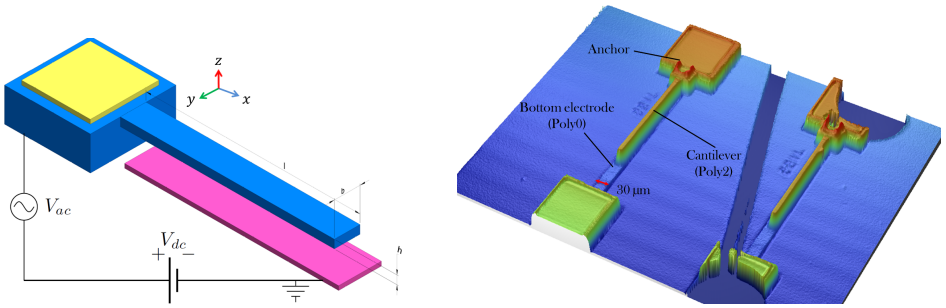

(a) Sensor schematic

(b) white light profilometer

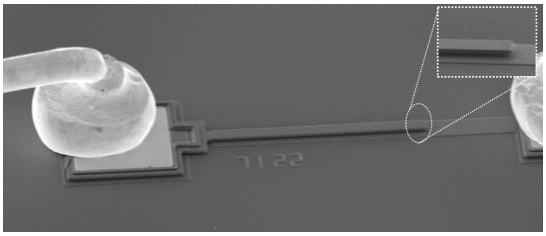

(c) SEM picture

Figure 3.3: Gas sensor

scribing the dynamic behavior of the system. It treats the microbeam as an elastic continuum and prismatic, an Euler-Bernoulli beam. From Newton's second law

$$\sum F_z = \rho A \frac{\partial^2 \hat{w}(\hat{x},\hat{t})}{\partial \hat{t}^2} d\hat{x} \tag{3.1}$$

where ρ is the beam mass density, A is the area cross-section, and $w(\hat{x},\hat{t})$ is the beam deflection.

The total forces subjected on the small element, $d\hat{x}$, shown in Fig. 3.4 (b) are

$$V - (V + dV) + f(\hat{x},\hat{t})d\hat{x} = \rho A \frac{\partial^2 \hat{w}(\hat{x},\hat{t})}{\partial \hat{t}^2} d\hat{x} \tag{3.2}$$

where V is the transverse internal shear force, dV is the change in transverse internal shear force, and $f(\hat{x},\hat{t})$ is applied distributed force per unit length. The change in the internal shear force can

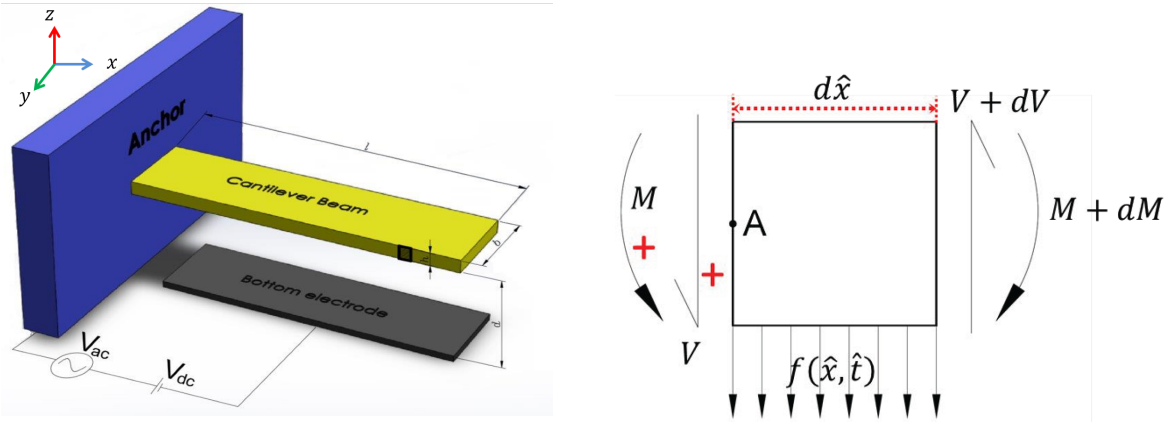

Figure 3.4: (a) A schematic of the gas sensor (b) A free body diagram of infinitesimal element along the beam

be written as

$$dV = \frac{\partial V}{\partial \hat{x}} d\hat{x} \tag{3.3}$$

Further, taking the total internal moments, $M(\hat{x}, \hat{t})$, at point A located at the left side of the small element, $d\hat{x}$, shown in Fig. 3.4 (b). We note that rotational inertia at point A is very small which can be neglected, we get

$$-M + f d\hat{x}\frac{d\hat{x}}{2} - (V + dV)d\hat{x} + (M + dM) = 0 \tag{3.4}$$

where M and dM refer to the internal moment and the change in the internal moment, respectively. Using Chain rule, the change in the internal moment can be written as

$$dM = \frac{\partial M}{\partial \hat{x}} d\hat{x} \tag{3.5}$$

Substituting Eqs.(3.3)–(3.5) into Eq.(3.4), we obtain

$$f\frac{d^2\hat{x}}{2} - V d\hat{x} - \frac{\partial V}{\partial \hat{x}} d^2\hat{x} + \frac{\partial M}{\partial \hat{x}} d\hat{x} = 0 \tag{3.6}$$

For small $d\hat{x}$, all the nonlinear terms in Eq.(3.6) are dropped to get

$$V = \frac{\partial M}{\partial \hat{x}} \tag{3.7}$$

Based on Euler-Bernoulli beam theory, the internal bending moment $M(\hat{x}, \hat{t})$ for a linear elastic beam can be described in terms of curvature $\frac{1}{\rho(\hat{x},\hat{t})}$ as

$$M(\hat{x}, \hat{t}) = \frac{EI}{\rho(\hat{x}, \hat{t})} \tag{3.8}$$

where E is Young's modulus of the structural material, and I is the cross-section moment of inertia. If the slop of the cantilever beam is small, then the curvature can be approximated [176] as

$$\frac{1}{\rho} \approx \frac{\partial^2 \hat{w}}{\partial \hat{x}^2} \tag{3.9}$$

where $\hat{w}(x, t)$ is the displacement of the beam. We excited the beam utilizing an electrostatic force as a applied force generating a voltage difference between moving beam and fixed electrode which follows as:

$$f(\hat{x}, \hat{t}) = \frac{1}{2}\varepsilon b \frac{V(\hat{t})^2}{(d - \hat{w})^2} \tag{3.10}$$

where $\varepsilon = 8.854 \times 10^{-12}$ F/m is the air permittivity, b is the beam width, d is the unactuated gap between cantilever beam and the substrate, and $V(\hat{t})$ is the applied voltage difference which can be defined as

$$V(\hat{t}) = V_{dc} + V_{ac}\, cos(\hat{\Omega}\hat{t}) \tag{3.11}$$

where V_{dc} is the bias voltage, V_{ac} is the amplitude of the alternating voltage, and $\hat{\Omega}$ is the excitation frequency. Substituting Eqs.(3.7)–(3.10) into Eq.(3.2) we get

$$EI\frac{\partial^4 w}{\partial \hat{x}^4} + \rho A \frac{\partial^2 \hat{w}}{\partial \hat{t}^2} = \frac{1}{2}\varepsilon b \frac{(V_{dc} + V_{ac})^2}{(d - \hat{w})^2} \tag{3.12}$$

which describes equation of motion for a transverse undamped-forced beam. Alternatively, it can be written as

$$\rho A\ \ddot{\hat{w}} + EI\ \hat{w}^{iv} = \frac{1}{2}\varepsilon b\frac{(V_{dc}+V_{ac})^2}{(d-\hat{w})^2} \tag{3.13}$$

where overdot stands for the derivative with respect to time $\hat{t}$ and the prime stands for the derivative with respect to position along the beam axis $\hat{x}$. The quadratic relationship between voltage and electrostatic force results in a multi-frequency excitation where a harmonic waveform produces a force component $(\propto 2V_{dc}V_{ac})$ with a frequency of Ω and another component $(\propto \frac{1}{2}V_{ac}^2)$ with a frequency of 2Ω .

Two main sources of damping were added in the system EOM which are: a linear viscous damping, $\hat{c}$, due to the structural damping in the system, and a nonlinear squeeze-film damping, $\hat{c}_s$, due to vibrating cantilever in a narrow gap resulting in air trapped, therefore Eq.(3.13) yields to

$$\rho A\ \ddot{\hat{w}} + (\hat{c}+\hat{c}_s)\ \dot{\hat{w}} + EI\ \hat{w}^{iv} = \frac{1}{2}\varepsilon b\frac{(V_{dc}+V_{ac})^2}{(d-\hat{w})^2} \tag{3.14}$$

where is the effect of squeeze-film damping can be formulated from [100, 177]as:

$$\hat{c}_s = \frac{\hat{\mu}\hat{b}^3}{(1+6\,K_n)(d-\hat{w})^3} \quad \text{where} \quad k_n = \frac{\lambda}{d} \tag{3.15}$$

$\hat{\mu}$, K_n, λ are the air viscosity, Knudsen number, the mean free path of air at ambient pressure, $\lambda = 60$ nm.

We included the in-extensibility effect [106], which account for the apparent beam length, L, shortening due to bending under electrostatic force. As a result, the beam stiffness increased and that will slightly alter the structural behavior. We note electrostatic force emerges a softening nonlinearity effect, which skewed the frequency response curve to the left, in-extensibility effect will cause hardening nonlinearity effect, which try to skewed the frequency response to the right.

The equation of motion, therefore, will be as

$$\rho A\,\ddot{\hat{w}} + (\hat{c} + \hat{c}_s)\,\dot{\hat{w}} + EI\,\hat{w}^{iv} - \frac{EA}{2L}\hat{w}'' \int_0^L \left(\hat{w}'\right)^2 d\hat{x} = \frac{1}{2}\varepsilon b \frac{(V_{dc} + V_{ac})^2}{(d - \hat{w})^2} \tag{3.16}$$

Also, accounting for electrostatic fringing field [178] by modifying the beam width by the effective beam width, we obtain

$$b_e = b\left(1 + 0.65\,\frac{d - \hat{w}}{b}\right) \tag{3.17}$$

thus equation of motion will become as follow:

$$\rho A\,\ddot{\hat{w}} + (\hat{c} + \hat{c}_s)\,\dot{\hat{w}} + EI\,\hat{w}^{iv} - \frac{EA}{2L}\hat{w}'' \int_0^L (\hat{w}')^2 d\hat{x} = \frac{1}{2}\varepsilon b_e \frac{(V_{dc} + V_{ac})^2}{(d - \hat{w})^2} \tag{3.18}$$

and the associate boundary conditions are

$$\begin{aligned} \hat{w}(0,\hat{t}) = 0 \quad &\text{and} \quad \hat{w}'(0,\hat{t}) = 0 \\ \hat{w}''(L,\hat{t}) = 0 \quad &\text{and} \quad \hat{w}'''(L,\hat{t}) = 0 \end{aligned} \tag{3.19}$$

For convenience, we introduce the nondimensional variables

$$w = \frac{\hat{w}}{d}, \qquad x = \frac{\hat{x}}{L}, \qquad t = \frac{\hat{t}}{\tau} \tag{3.20}$$

where τ is a time scale. Substituting Eq.(3.20) into Eq.(3.18), we obtain the nondimensional equation of motion in the form as follow:

$$\begin{aligned} \ddot{w} + (c + c_s)\,\dot{w} + w^{iv} - \alpha_1 w'' \int_0^1 \left(w'\right)^2 dx = \\ \alpha\left(1 + 0.65\,\frac{1 - w}{b/d}\right)\frac{(V_{dc} + V_{ac})^2}{(1 - w)^2} \end{aligned} \tag{3.21}$$

the associate boundary conditions are

$$\begin{aligned} w(0,t) = 0 \quad &\text{and} \quad w'(0,t) = 0 \\ w''(1,t) = 0 \quad &\text{and} \quad w'''(1,t) = 0 \end{aligned} \tag{3.22}$$

where parameters are defined as

$$\alpha = \frac{\varepsilon b L^4}{2EId^3}, \quad c = \frac{\mu_1 l^4}{EI\tau}, \quad \alpha_1 = 6\left(\frac{d}{h}\right)^2, \tag{3.23}$$
$$\tau = \sqrt{\frac{\rho A L^4}{EI}} \qquad \mu = \hat{\mu}\left(\frac{b}{d}\right)^3 \frac{\tau}{m}$$

The nondimensional squeeze-film damping coefficient c_s is formulated as [179]

$$c_s = \frac{\mu_2 \tau}{m(1+6K_n)}\left(\frac{b}{d(1-w)}\right)^3 \tag{3.24}$$

where μ_2 is air viscosity. Knudsen number $(K_n = \lambda/d)$ is the ratio of the mean free path of air particles at ambient temperature and pressure ($\lambda = 60$ nm) to the capacitive gap. The term $\frac{1}{(1-w)}$ is expanded in a first-order Taylor series around the static deflection $(w = w_s)$ and substituted back into Eq. (3.24) to obtain

$$c_s \approx \frac{\mu_2 b^3 \tau}{md^3(1-w_s)^2(1+6K_n)} \frac{1+w-2w_s}{(1-w)^2} \tag{3.25}$$

3.2.1 Eigenvalue Problem

To find out natural frequencies and mode shapes, we solved an eigenvalue problem for cantilever beam subjected to a free vibration mode. For simplicity, all nonlinear, damping, and forcing terms were dropped from Eq.(3.21). Therefore, we obtain

$$\ddot{w}(x,t) + w^{iv}(x,t) = 0 \tag{3.26}$$

To solve Eq.(3.26), we assumed a solution in the form

$$w(x,t) = \phi_n(x) e^{iw_n t} \tag{3.27}$$

Then, substituting Eq.(3.27) into Eq.(3.26), we get

$$\phi_n^{iv}(x) - w_n^2 \phi_n(x) = 0 \tag{3.28}$$

where the boundary conditions at $x = 0$ are

$$\phi_n = 0 \quad \text{and} \quad \phi_n^{'} = 0 \tag{3.29}$$

at $x = 1$

$$\phi_n^{''} = 0 \quad \text{and} \quad \phi_n^{'''} = 0 \tag{3.30}$$

To solve Eq. (3.28), we assume a solution in the from

$$\phi_n(x) = Ce^{sx} \tag{3.31}$$

Thus, substituting Eq.(3.31) in Eq.(3.28), it becomes

$$s^4 - w_n^2 = 0 \tag{3.32}$$

solving Eq.(3.32) which gives four roots as

$$s_{1,2} = \pm\sqrt{w_n} \quad \text{and} \quad s_{3,4} = \pm i\sqrt{w_n} \tag{3.33}$$

Then, substituting all the four roots of Eq.(3.33) into Eq.(3.31) to get the free vibration mode shape

$$\phi_n(x) = C_1\, e^{\sqrt{w_n}} + C_2\, e^{-\sqrt{w_n}} + C_3\, e^{i\sqrt{w_n}} + C_4\, e^{-i\sqrt{w_n}} \tag{3.34}$$

Or alternatively, it can be written as

$$\phi_n(x) = C_1\, cosh(\beta_1 x) + C_2\, sinh(\beta_2 x) + C_3\, cos(\beta_3 x) + C_4\, sin(\beta_4 x) \tag{3.35}$$

where C_i are constants which can be found from the structural boundary conditions, and β denoted by

$$\beta_{1,2} = \pm\sqrt{w_n} \quad \text{and} \quad \beta_{3,4} = \pm i\sqrt{w_n} \tag{3.36}$$

Applying the boundary conditions found in Eqs.(3.29,3.30) into Eq.(3.35)yields four algebraic equations in the C_i as follows:

$$\begin{bmatrix} 1 & 0 & 1 & 0 \\ 0 & \beta & 0 & \beta \\ \beta^2\, cosh\beta & \beta^2\, sinh\beta & -\beta^2\, cos\beta & -\beta^2\, sin\beta \\ \beta^3\, sinh\beta & \beta^3\, cosh\beta & \beta^3\, sin\beta & -\beta^3\, cos\beta \end{bmatrix} \begin{Bmatrix} C_1 \\ C_2 \\ C_3 \\ C_4 \end{Bmatrix} = \begin{Bmatrix} 0 \\ 0 \\ 0 \\ 0 \end{Bmatrix} \tag{3.37}$$

Solving Eq.(3.37) by equating the determinant of the coefficients by zero, and find nontrivial solutions. This leads to the characteristic equation which gives natural frequencies of the cantilever beam

$$cos\beta\ cosh\beta + 1 = 0 \tag{3.38}$$

We solved Eq.(3.38) numerically using Mathematica software to find n^{th} natural frequencies of the system. The system mode shapes are determined by manipulating Eq.(3.37), and found the three constants, C_1, C_2, and C_3 with respect to the forth one, C_4, which can be arbitrary. The general mode shape for undeflected cantilever beam is

$$\phi_n(x) = C_n[(cosh(\beta_n x) - \ cos(\beta_n x)) - k_n\ (sinh(\beta_n x) - \ sin(\beta_n x))] \tag{3.39}$$

where

$$k_n = \frac{cosh(\beta_n x) + \ cos(\beta_n x)}{sinh(\beta_n x) + \ sin(\beta_n x)}$$

The first three normalized nondimensional mode shapes, choosing $C_n = 1$, given in Eq.(3.39) are shown in Fig. 3.5. The first, second and third bending natural frequencies were found at $f_1 = 64.82$ kHz, $f_2 = 406.23$ kHz, and $f_3 = 1.14$ MHz, respectively.

The general solution of Eq.(3.21) can be obtained using Galerkin method, which is one of the weighted residual methods, to discretize the governing equation to transform partial differential

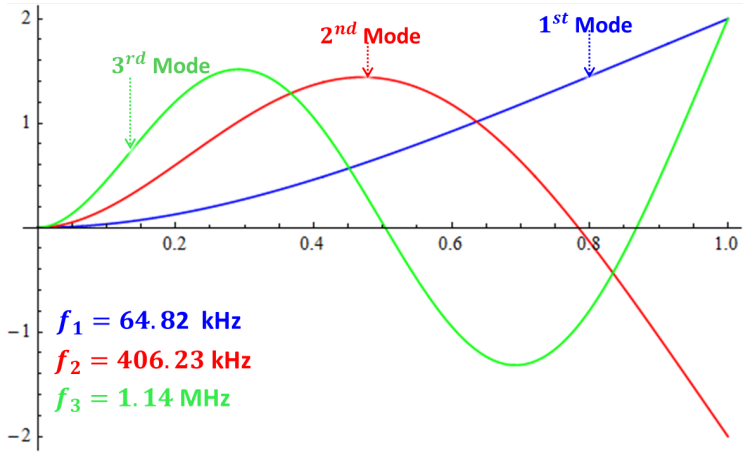

Figure 3.5: The first three nondimensional bending mode shapes of the cantilever beam length over its gap

equations (PDE) into a set of nonlinear ordinary differential equations (ODE) of the micro beam. The weighting functions are chosen to be the same as the trial functions according to the Galerkin method [180, 181]. We use the mode shapes as trial functions in the Galerkin method for the undamped free vibration problem of the cantilever beam. Thus, the solution is assumed in the form of

$$w(x,t) = \sum_{i=1}^{N} \phi_n(x) q_n(t) \tag{3.40}$$

where N is the required number of modes, $\phi_n(x)$ is the trial function, mode shape, and $q_n(t)$ is the generalize coordinates in the time domain. After multiplying Eq.(3.21) by $(1-w)^2$ in both sides, substituting Eq.(3.40) into Eq.(3.21), we get

$$\begin{aligned}\sum_{n=1}^{N} \left(\phi_n \ddot{q}_n + (c+c_s)\phi_n \dot{q}_n + \phi_n^{iv} q_n - \alpha_1 \phi_n'' q_n \int_0^1 \left(\sum_{n=1}^{N} \phi_n' q_n\right)^2 dx\right) \left(1 - \sum_{n=1}^{N} \phi_n q_n\right)^2 = \\ \alpha \left(V_{dc} + V_{ac}\right)^2 \left(1 + 0.65\frac{d}{b} - 0.65\frac{d}{b}\sum_{n=1}^{N} \phi_n q_n\right)\end{aligned} \tag{3.41}$$

We note this equation just represents the equation parameters for one mode only. However, we

accounted for three modes in our case. Applying Galerkin technique by multiplying Eq.(3.41) by ϕ_i in both sides and integrating along the cantilever beam length from $x = 0$ to $x = 1$. Then, solving the system by applying orthogonality conditions [180] to decouple the system into a set of n^{th} ordinary-differential equations in terms of the generalize coordinate, q_n describing modal participation.

A closed-form expression was developed for the static deflection, denoted $w_s(x)$, under DC voltage and estimate the maximum range of travel. The static problem can be formulated by setting the time derivatives and the AC forcing term in Eqs.(3.21) equal to zero, which yields

$$w_s^{iv}(x) - \alpha_1 w_s'' \int_0^l \left(w_s'\right)^2 dx = \alpha \left(1 + 0.65 \, \frac{1 - w_s(x)}{b/d}\right) \frac{V_{dc}^2}{(1-w)^2} \tag{3.42}$$

and the associate boundary conditions at $x = 0$ are

$$w_s(0) = 0 \quad \text{and} \quad w_s^{'}(0) = 0 \tag{3.43}$$

and at $x = 1$, the boundary conditions are

$$w_s^{''}(1) = 0 \quad \text{and} \quad w_s^{'''}(1) = 0 \tag{3.44}$$

The Galerkin method was used to transform Eq. (3.42) into a set of algebraic equations by substituting the modal expansion

$$w_s(x) = \sum_{i=1}^{N} q_i \phi_i(x) \tag{3.45}$$

into the equation, we obtained N algebraic equations describing the static equilibrium

$$\begin{aligned} \left(1 - \sum_{n=1}^{N} \phi_n q_n\right)^2 \left(\sum_{n=1}^{N} \phi_n^{iv} q_n - \alpha_1 \sum_{n=1}^{N} \phi_n'' q_n \int_0^1 \left(\sum_{n=1}^{N} \phi_n^{'} q_n\right)^2 dx\right) = \alpha \, V_{dc}^2 \\ \times \left(1 + 0.65 \, \frac{d}{b} \left(1 - \sum_{n=1}^{N} \phi_n q_n\right)\right) \end{aligned} \tag{3.46}$$

where $\phi_i(x)$ is the ith mode shape of a straight cantilever beam and q_i is the corresponding modal coefficient. Numerical solution of this set of algebraic equations showed that three modes were enough to converge to the stable and unstable branches of the static deflection-voltage curve while one-and two-mode expansions diverged at higher DC voltage values. Therefore, a three-mode approximation has been adopted to model the beam deflection throughout this work. The static pull-in voltage, where the stable and unstable equilibria branches collide at a saddle-node bifurcation [182], was found to be $V_{\text{pi}} = 14.421$ V corresponding to a maximum stable deflection of $w_{\text{pi}} = 39.7\,\%$ of the initial gap d.

Another Galerkin expansion was used to separate time and space in the dynamic response $w_d(x,t)$ and rewrite the total deflection as

$$w(x,t) = w_s(x) + \sum_{i=1}^{N} u_i(t)\phi_i(x) \tag{3.47}$$

where u_i is the ith dynamic modal coefficient. Substituting this form in Eqs. (3.21), imposing the orthogonality condition among the mode shapes, and using Eq. (3.42), we obtained a reduced-order model (ROM), a set of three ODEs, describing the dynamic response.

$$\begin{aligned}\Big(1 - w_s - \sum_{n=1}^{N}\phi_n q_n\Big)^2\Big(\sum_{n=1}^{N}\phi_n\ddot{q}_n + (c+c_s)\sum_{n=1}^{N}\phi_n\dot{q}_n + w_s^{iv} + \sum_{n=1}^{N}\phi_n^{iv}q_n \\ - \alpha_1\left(w_s'' + \sum_{n=1}^{N}\phi_n''q_n\right)\int_0^1\left(w_s' + \sum_{n=1}^{N}\phi_n'q_n\right)^2 dx\Big) = \alpha\left(V_{dc}+V_{ac}\right)^2 \\ \times\left(1 + 0.65\,\frac{d}{b}\left(1 - w_s - \sum_{n=1}^{N}\phi_n q_n\right)\right)\end{aligned} \tag{3.48}$$

Numerically integrating the ROM for 500 excitation periods ($T = 1/f$), we found the response as the RMS of the beam tip velocity evaluated over the last $100T$. The frequency response-curve was constructed numerically, tip velocity as a function of f , for the waveform $V_{dc} = 7.20$ V and $V_{\text{ac}} = 7.20$ V, Fig. 3.6. The forward frequency sweep is shown with a blue line and the backward sweep is shown with a red line.

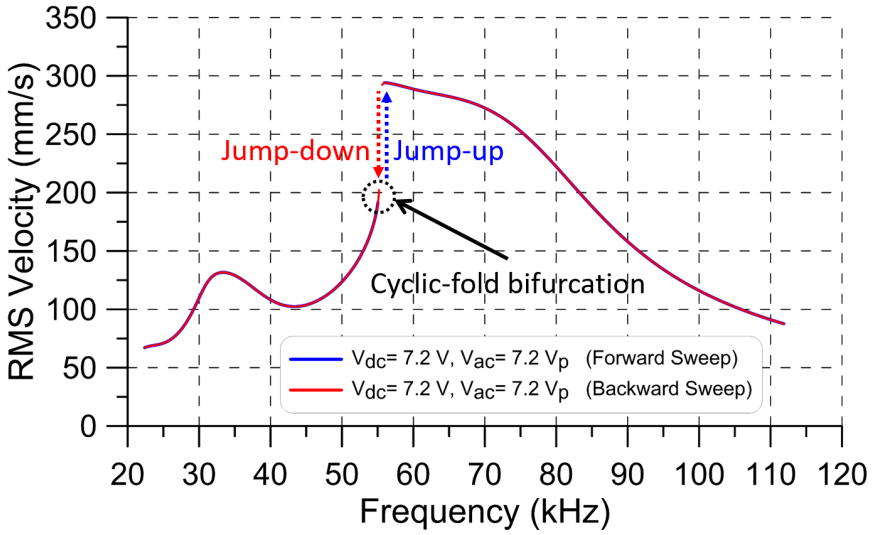

Figure 3.6: The simulated frequency-response curve for the waveform $V_{dc} = 7.20\,\mathrm{V}$ and $V_{\mathrm{ac}} = 7.20\,\mathrm{V}$

The peak in the vicinity of $f = 35\,\mathrm{kHz}$ results from the combined effects of a primary resonance of the forcing component proportional to $\frac{1}{2}V_{ac}^2$ and a superharmonic resonance of the forcing component proportional to $2V_{dc}V_{ac}$. The dominant peak in the frequency-response curve represents primary resonance of the force component proportional to $2V_{dc}V_{ac}$. It is skewed to the left due to the dominance of the softening electrostatic nonlinearity. An unstable branch (not shown) connects the left and right stable branches. A lower and an upper cyclic-fold bifurcation exist at the lower and upper ends of the unstable branch [182]. Our target in this study was to exploit the lower cyclic-fold bifurcation as a detection mechanism.

3.3 Sensitivity Analysis

The sensitivity of a bifurcation-based sensor is the ratio of the change in location of the bifurcation point to the added mass. We re-introduce the dimensional equation of motion of the beam as:

$$M\ddot{w} + \hat{c}\,l\,\dot{w} + k_e l w^{iv} - \frac{EA_s}{2} w'' \int_0^l (w')^2 dx = \frac{\epsilon A_e (V_{dc} + V_{ac})^2}{2(d-w)^2} \tag{3.49}$$

where M and $k_e = \Gamma_1 EI$ are the effective mass and stiffness of the sensor, Γ_1 is a modal coefficient defined in appendix (A), and A_s and A_e are the cross-sectional and electrode areas. To obtain the location of the cyclic-fold bifurcation, we derive the modulation equations of the beam. Assuming the absence of modal interactions, we adopt a one-mode approximation of the total displacement:

$$w(x,t) = q_s \phi_1(x) + u(t)\phi_1(x) \tag{3.50}$$

where q_s and $u(t)$ are the amplitudes of static and dynamic displacement, respectively, and $\phi_1(x)$ is the directly excited mode.

Substituting this approximation into Eq. (3.49), multiplying the result by $\phi_1(x)$, integrating over the cantilever beam length, and applying the orthogonality conditions [180], we reduce the system into an ordinary-differential equation in terms of the generalize coordinate q_s and $u(t)$:

$$\ddot{u} + \mu\, l\, \dot{u} + \omega_n^2 u + \omega_n^2 u^2 + \omega_n^2 u^3 = \lambda\, cos(\Omega t) \tag{3.51}$$

The effective mass of the sensor can be defined as

$$M = m + m_d = \rho bhl + m_d \approx \rho bhl \tag{3.52}$$

where m and m_d are the beam mass and the deposited polymer mass on the sensor, respectively.

We assume the deposited mass is negligible. The coefficients of Eq.(3.51) are defined as

$$\begin{aligned}
\mu &= \frac{\hat{c}}{M} \\
\omega_n^2 &= \frac{1}{12}h^3 E\,\Gamma_1\psi_2 - \frac{3}{2}q_s^2\,E\,\Gamma_2\,\psi_1 - C_2 V_{\rm dc}\psi_2 \\
\alpha_2 &= -\frac{3}{2}q_s\,E\,\Gamma_2\,\psi_1 - \frac{3}{2}C_3 V_{\rm dc}\psi_2 \\
\alpha_3 &= -\frac{1}{2}E\,\Gamma_2\,\psi_1 - 2C_4 V_{\rm dc}\psi_2 \\
\lambda &= C_1\psi_2
\end{aligned}$$

where modal coefficients Γ_1 and Γ_2 and the electrostatic field coefficients C_1, C_2, C_3, and C_4 are defined in appendix (A) and

$$\psi_1 = \frac{A_s}{M}, \quad \psi_2 = \frac{A_e}{M}$$

The frequency-response equation under primary resonance excitation $\Omega = \omega_n + \sigma$ can be written as [46]

$$a^2\,\sigma^2 + \kappa^2\,a^6 - 2A\,a^4\,\sigma + \frac{1}{4}\mu^2\,a^2 = \left(\frac{\lambda}{2\omega_n}\right)^2 \tag{3.53}$$

where $\omega_n = \sqrt{\alpha_1}$ and the coefficient of effective nonlinearity, κ, is

$$\kappa = \frac{9\,\omega_n^2\alpha_3 - 10\,\alpha_2^2}{24\,\omega_n^3} \tag{3.54}$$

and the forcing amplitude is

$$\lambda = \psi_2 C_1 f_{\rm ac}$$

and $f_{\rm ac}$ is the amplitude of the AC voltage.

The cyclic-fold bifurcation point occurs at a point in the frequency-response curve where the slope approaches infinity, or alternatively [182]

$$\frac{\partial\sigma}{\partial a} = 0 \tag{3.55}$$

Applying this condition to the frequency-response equation, Eq. (3.53), yields

$$\sigma_\circ = \kappa\, a_\circ^2 \tag{3.56}$$

where $(a_\circ, \sigma_\circ)$ are the amplitude and frequency, respectively, of the cyclic-fold bifurcation.

The beam sensitivity in the vicinity of the cyclic-fold bifurcation is defined as the change in the location of the bifurcation point, $\delta\sigma_\circ$, due to the change of the beam mass δM

$$S_m = \frac{\delta\sigma_\circ}{\delta M} \tag{3.57}$$

Using Eq. (3.56) in Eq. (3.57) yields,

$$S_m = a_\circ^2\, \frac{\delta\kappa}{\delta M} + 2a_\circ\kappa\, \frac{\delta a_\circ}{\delta M} \tag{3.58}$$

We solve for the response amplitude $a_\circ$ at the bifurcation point by substituting for $\sigma_\circ$ from Eq. (3.56) into Eq. (3.53) to get

$$a_\circ = \frac{\lambda}{\mu\, \omega_n} \tag{3.59}$$

Substituting for $a_\circ$ and κ, from Eqs. (3.54) and (3.59), in Eq. (3.58), we found the sensitivity as

$$S_m = \frac{l^2 b^4 Q^2}{128\, \hat{c}^2\, M^5\, \omega_n^5} \gamma V_{ac}^2 C_1^2 = \frac{l^2 b^4 Q^2}{128\, M^{3/2}\, k_e^{7/2}} \gamma V_{ac}^2 C_1^2 \tag{3.60}$$

where γ is a static constant which can be defined as

$$\begin{aligned}\gamma = {} & -4L^2 V_{dc}\big(15C_3^2 V_{dc} - 12C_2 C_4 V_{dc} + C_4 h^3 E\Gamma_1\big) \\ & + h\, L\, E\Gamma_2\Big(12V_{dc}\big(C_2 + 6C_4 q_s^2 - 10C_3 q_s\big) - h^3 E\Gamma_1\Big) \\ & - 42\, h^2\, E^2\, q_s^2 \Gamma_2^2\end{aligned}$$

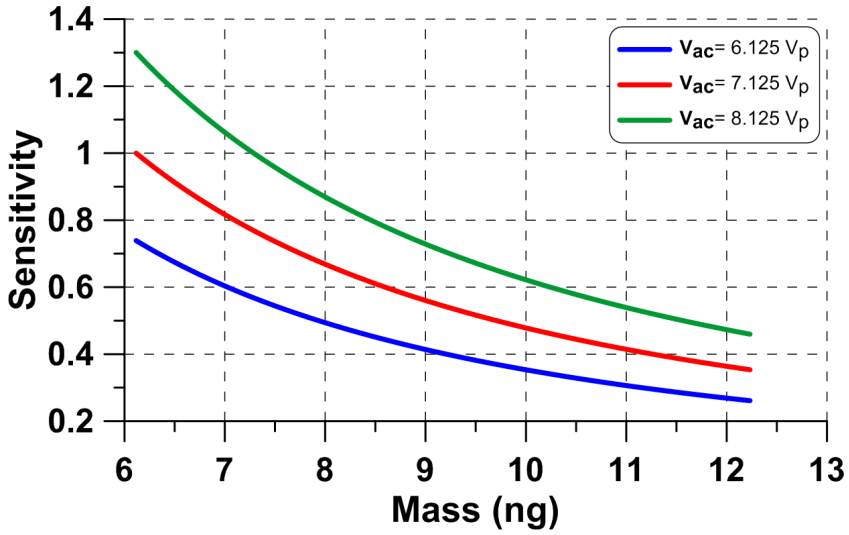

Figure 3.7: Sensitivity curves studied while increasing the AC-voltage amplitude at $V_{ac} = 6.125, 7.125,$ and 8.125 V colored in blue, red, and green, respectively, and effective mass

We used this formula to study the relationships among the strength of the electrostatic field, at a unity modulation index, the effective mass M, and sensitivity and obtained the sensitivity curves shown in Fig. 3.7. The curves were obtained for three levels of the electrostatic field corresponding to $V_{dc} = V_{ac} = 6.125, 7.125,$ and 8.125 V as the effective mass varies from that of the current sensor $M = 6.12$ pg to twice that value. We found that sensitivity increases nonlinearly with field strength and drops with the effective mass. The results indicate that the sensitivity formula, Eq. (3.60), can be utilized to optimize sensor sensitivity.

3.4 Sensor Characterization

A white light profilometer [183], Fig. 3.3 (b), was used to measure the beam length and width. They were found to be identical to the design values. On the other hand, we found significant

inter-chip and intra-chip variability in the beam thickness and capacitor gap. Variation was also found among PolyMUMPs fabrication runs.

3.4.1 Parameter Identification Of Sensor Dimensions

Uncertainties in the sensor dimensions play a role in determining the sensor response. Further, we found inter-chip and intra-chip dimensional and material property variability among PolyMUMPs runs used to fabricate the sensors. A white light profilometer [183] was used to measure the in-plane dimensions of the beam, Fig. 3.3 (b), listed in Table 3.1. The beam length, width and gap were found to be identical to the design values. We estimated the beam thickness as $h = 1.8\,\mu$m by matching the measured static pull-in voltage to that predicted numerically.

Table 3.1: Estimated sensor dimensions

L (μm)	b (μm)	h (μm)	d (μm)
175	10	1.8	2

3.4.2 Static Pull-in

The variation of the static deflection with the DC voltage is obtained by solving Eq.(3.46) for a given $V_{\rm dc}$. Four modes were employed in the Galerkin expansion resulting in four algebraic equations. Comparison with the results for 1-4 modal expansions showed that the three- and four-mode solutions were consistently convergent, while the one and two-mode solutions diverged for higher DC voltage values. Therefore, a three-mode approximation has been adopted to model the beam deflection throughout this work.

The model ignores the beam weight. To examine this assumption, we calculated the static deflection of the beam under its own weight and found that the maximum deflection at the beam tip as $w(1) = 6.2\,\text{nm}$. This is equivalent to 0.0031 % of the initial gap, small enough to validate our assumption.

The numerically calculated static deflection at the beam tip $w_s(1)$ is shown versus the DC voltage V_{dc} in Fig. 3.8. Two branches of solutions are observed: a lower branch (solid blue line) of stable equilibria and an upper branch (dashed red line) of unstable equilibria. Only the stable branch is realizable experimentally. The static deflection increases along the stable branch as the DC voltage increases until the 'pull-in' point. At this point the stable and unstable branches collide and the sensor loses stability. The voltage corresponding to this point is called the static pull-in voltage V_{ps}.

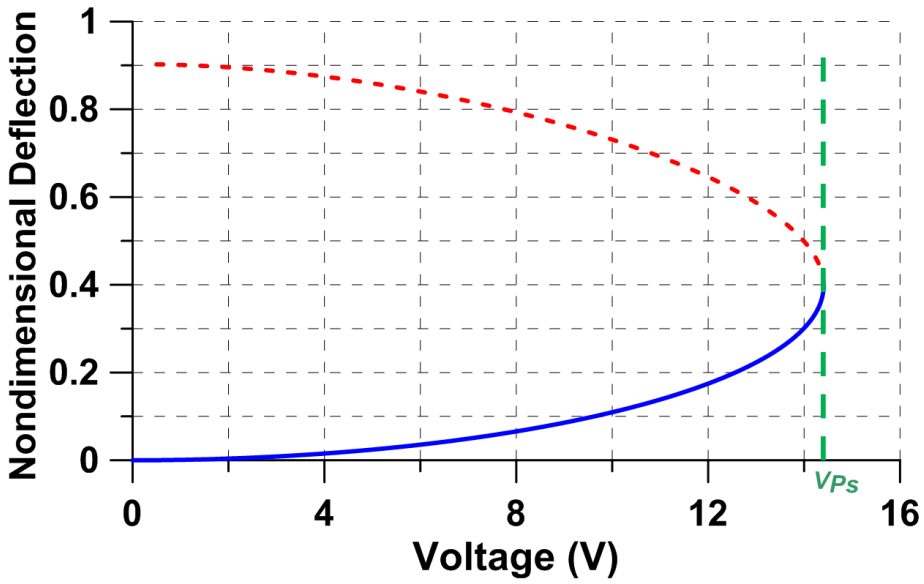

Figure 3.8: Nondimensional beam deflection $w_s(1)$ under DC voltage V_{dc}

Beyond V_{ps}, there are no equilibrium solutions and the cantilever beam jumps down to-

ward the bottom electrode. This qualitative change in the sensor state is called a saddle-node bifurcation [182]. The static pull-in voltage and deflection were calculated at the beam tip as $V_{\mathrm{ps}} = 14.421\,\mathrm{V}$ and $w_{\mathrm{ps}} = 39.7\,\%$ of the initial gap d as depicted in Fig. 3.8.

The model accounts for the electrostatic fringing-field. To study the impact of that field on the model, we calculated the beam tip deflection for $V_{\mathrm{dc}} = 13\,\mathrm{V}$ with and without the fringing-field. We found that accounting for the fringing-field increases the beam tip deflection by $w = 0.817\,\%$. We used a similar procedure to determine the impact of beam in-extensibility on the model and found that it decreases the beam tip deflection by $w = 5.88\,\%$ of the initial gap for $V_{\mathrm{dc}} = 13\,\mathrm{V}$.

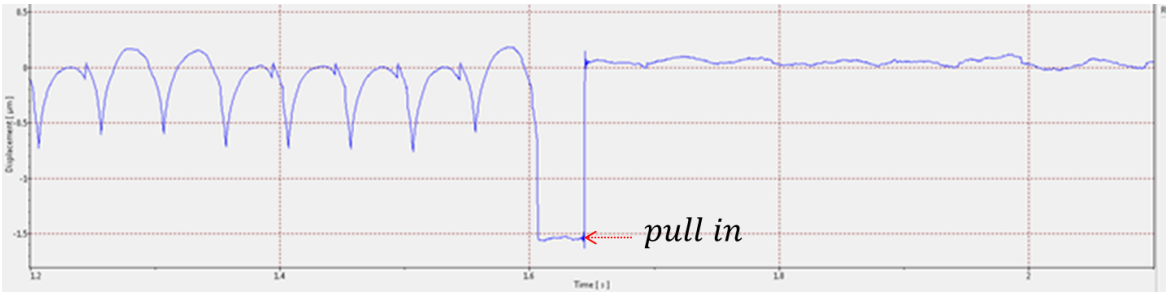

Figure 3.9: A screen capture of the laser vibrometer interface showing displacement of the cantilever beam tip $w(1)$ (solid line) during pull-in

A triangular voltage waveform was applied to the sensor using a function generator (AFG3000C). The signal frequency was set to $f = 150\,\mathrm{Hz}$ to ensure a quasi-static response. The beam tip velocity and displacement were measured using a laser Doppler vibrometer (MSV 400) [156], Fig. 3.9. An oscilloscope (MSO2024B) was used to record the excitation signal and the measured tip velocity and displacement, Fig. 3.10. As the voltage was increased linearly along the positive-slope ramp, the beam deflected continuously towards the substrate. The peak voltage of the waveform was increased manually in steps of 15 mV until pull-in occurred. It was detected as a sudden change in the beam deflection, Fig. 3.10. As the voltage dropped along the negative

ramp, the beam stayed in contact with the substrate until the voltage was close to 0 V.

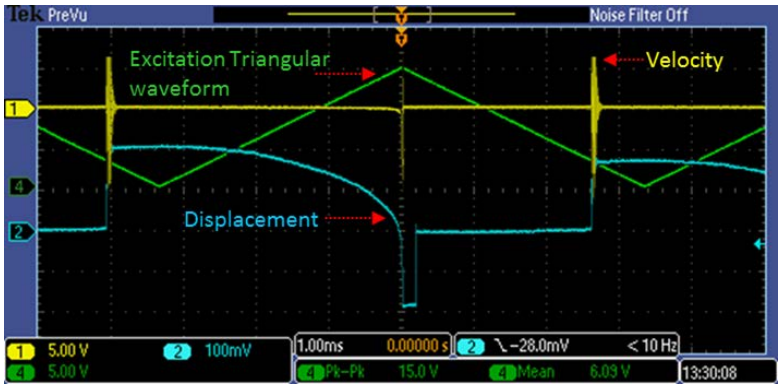

Figure 3.10: A screen capture showing the excitation voltage (green line), beam tip velocity (yellow line), and displacement (blue line)

This technique was used to estimate the static pull-in voltage as ($V_{pi} = 14.55\,\text{V}$). The capacitive gap ($w_s(1) = 1.63\,\mu\text{m}$) was measured as the displacement of the beam tip from its neutral position at 0 V to the pull-in position, in contact with the substrate. Using the gap distance and the measured dimensions in Eq. (3.42), we estimated the beam thickness as $h = 1.8\,\mu\text{m}$ by matching the measured static pull-in voltage to that predicted by the equation.

3.4.3 Fundamental Natural Frequency

The fundamental mode shape of the sensor was excited by applying the pulse train shown with a magenta line in Fig. 3.11, with amplitude of 3 V, frequency of 1 kHz, and a 0.8% duty cycle, to the beam in atmospheric pressure. The time-history of the beam tip velocity was measured optically using the vibrometer and recorded using the oscilloscope. It was averaged over 512 samples and is shown with the yellow line in Fig. 3.11. The damped natural frequency and quality factor were

obtained from the time-history as $f_d = 70\,\text{kHz}$ and $Q = 5.484$. The settling time was measured as $t_s = 73.8\,\mu\text{s}$.

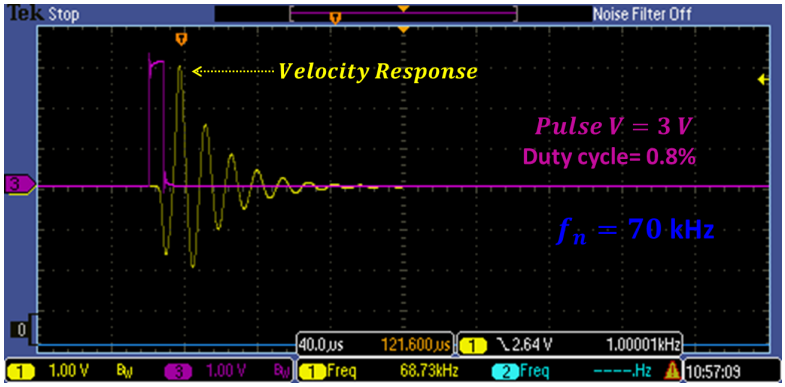

Figure 3.11: The averaged time-history of the beam tip velocity under a pulse train with $f = 1\,\text{kHz}$ and an amplitude of 3 V

3.4.4 Bifurcation Point

The frequency-response curve of the sensor was obtained in the vicinity of primary resonance to locate the cyclic-fold bifurcation. Forward and backward frequency sweeps were carried out over the frequency range $f = [40\text{–}90]\,\text{kHz}$. The bias voltage and excitation amplitude were set to $V_{\text{dc}} = V_{\text{ac}} = 6.86\,\text{V}$. A slow slew rate of $f = 2.5\,\text{kHz/s}$ was used to minimize transient effects. Data was collected using an oscilloscope in time windows of 0.4 s each and a sampling rate of $f_s = 313\,\text{kHz}$. The frequency-response curve, Fig. 3.12, was obtained by post-processing the data to evaluate the RMS of the beam tip velocity over a time window of $20T$ and assigning it to the frequency at the window mid-point.

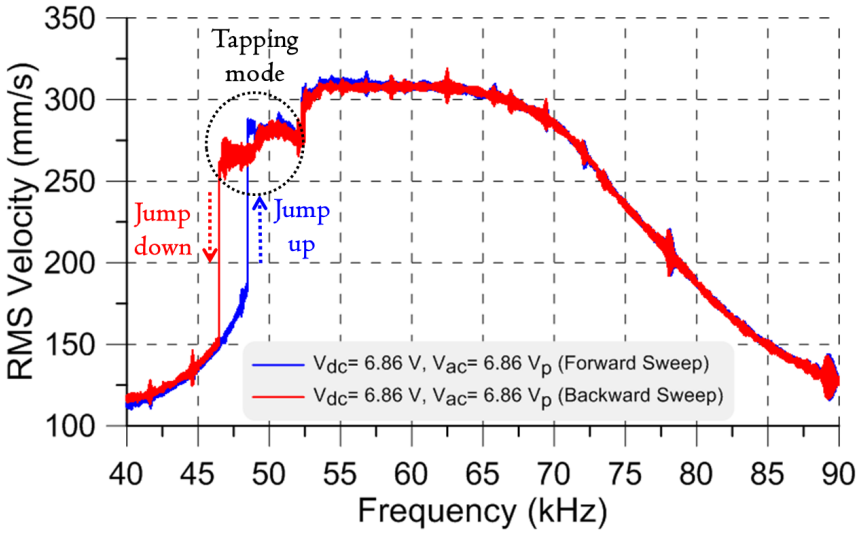

Figure 3.12: The measured frequency-response curve for $V_{\rm dc} = V_{\rm ac} = 6.86\,$V. The forward sweep is shown in blue and the backward sweep is shown in red

The forward sweep is shown in blue and the backward sweep in red, Fig. 3.12. The jump-up during the forward sweep at $f_{\rm pl} = 48.50\,$kHz corresponds to the lower cyclic-fold bifurcation. The jump-down during the backward sweep at $f_{\rm pu} = 46.50\,$kHz corresponds to the upper cyclic-fold bifurcation. The mid-sized orbits observed right after the jump-up and before the jump-down correspond to tapping-mode oscillations involving the beam tip interaction with the substrate. The region between the two jumps demarcates hysteresis in the sensor response. The flatness in the right branch of the curve is indicator of the dominance of squeeze-film damping for large orbits.

3.4.5 Experimental Limitations

Static Charge Shock

Static charges are generated from contact between two surfaces, such as fabrics. All materials are made of atoms and electrons; thus, electrons can move from one material to another upon contact. Low humidity helps to accumulate static charges [184]. The human body is a good insulator (highly resistive) as a result, it accumulates static charges. Thus, if an operator wears fabric material and/or rubber shoes, static charges tend to accumulate on his/her body. Upon touching a chip, the static charges are released into the specimen through electrical connections resulting in charge shock and stiction either in line-contact or area-contact as shown in Fig. 3.13. Operators were instructed to wear Electrical Discharge Strips (EDS) connected to the common ground of the vibrometer to protect the specimen from static charges.

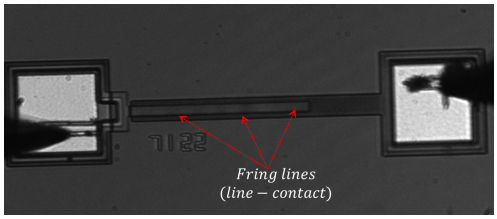

Figure 3.13: Fringe lines over the cantilever beam representing a stiction as a line-contact

Dielectric Charging

Electrostatic charging poses a serious impediment to experimental measurements. It occurs due to buildup of static charges on dielectric layers in a MEMS, which turns them into voltage sources within the MEMS. Specifically, charge buildup on a dielectric layer within the actuation capacitor with the same polarity as the excitation voltage will reduce the effective voltage drop across the

capacitor. This is particularly exacerbated by the cantilever beam coming into contact with the bottom electrode during static pull-in.

In our experiments, we observed that dynamic pull-in voltage increased/decreased after repeated pull-in cycles. We postulate that changes is due to the formation of a native oxide layer on the bottom polysilicon electrode due to extended exposure to air. Literature shows that extended exposure of bare polysilicon surfaces to air leads typically to the formation of $1 - 3$ nm thick native oxide layers [185, 186]. However, devices fabricated using PolyMUMPs have been shown to possess an extremely thick, up to 30 nm, native oxide layer [187]. This layer of silicon dioxide serves as a dielectric layer that contributes to contact resistance and leads buildup of trapped charges, thus modifying the pull-in voltage [188, 189]. The maximum observed increase in pull-voltage was ~ 220 mV.

3.4.6 Experimental Setup

The experimental setup, Fig. 3.14, is composed of the sensor placed inside a test chamber, a function generator, a high voltage amplifier, an oscilloscope, and two gas canisters containing nitrogen and a pre-calibrated ethanol vapor charge. A laser-Doppler vibrometer is used to measure the sensor response optically. The test chamber is equipped with two BNC ports and a quartz glass window to allow for optical detection. The gas pressure in both canisters is set to $P = 20$ psi to reduce variation between the sensor performance in air and inside the test chamber. This ensures any response is not due to the pressure effect.

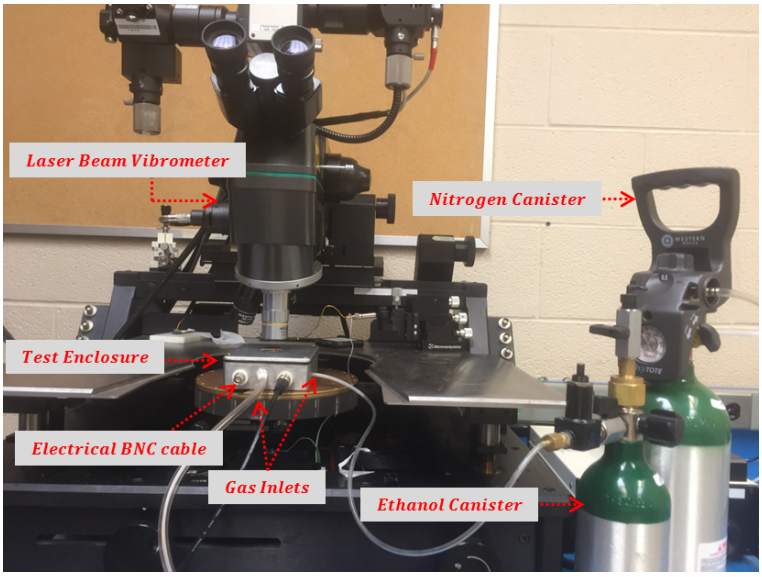

Figure 3.14: The experimental setup

During the experiment, the function generator applies the desired voltage waveform and frequency, $f_\circ$, to the sensor. Then, the nitrogen canister valve is opened, subjecting the polymeric sensing material to a flow of Grade IV nitrogen for 15 minutes in order to release ethanol and other sorbed molecules, thereby reseting it. Next, the valve of a pre-calibrated ethanol canister is opened to allow pre-calibrated ethanol flow into the test chamber. The sensor response is measured using the vibrometer and monitored using a CCD video camera to detect the jump corresponding to the cyclic-fold bifurcation. The oscilloscope records the beam tip velocity and displacement measured by the vibrometer.

The operating point of the sensor is set at a frequency $f_\circ$ just below the lower cyclic-fold bifurcation f_{pl}. A manual forward sweep starting from $f_{\mathrm{pl}} - 10$ Hz was carried out with a frequency step of $f = 1$ Hz to obtain a better estimate of the bifurcation point f_{pi}. We define the operational set-off frequency as: $\delta f = f_{\mathrm{pi}} - f_\circ$. A stability study was carried out to determine the closest operating point under ambient external disturbances by increasing the set-off frequency δf in

steps of 1 Hz. A set-off frequency was declared stable if it was sustainable for longer then 15 minutes. We found the minimum set-off frequency for the experimental setup to be $\delta f = 5$ Hz.

3.5 Results and Discussion

Test gases made of a mixture of ethanol vapor, with variable concentrations, and dry nitrogen were used to determine the sensor detection limit to ethanol vapor for the voltage waveform $V_{\mathrm{dc}} = V_{\mathrm{ac}} = 6.86$ V and set-off frequency of $\delta f = 50$ Hz.

3.5.1 Ethanol Concentration of 5 ppm

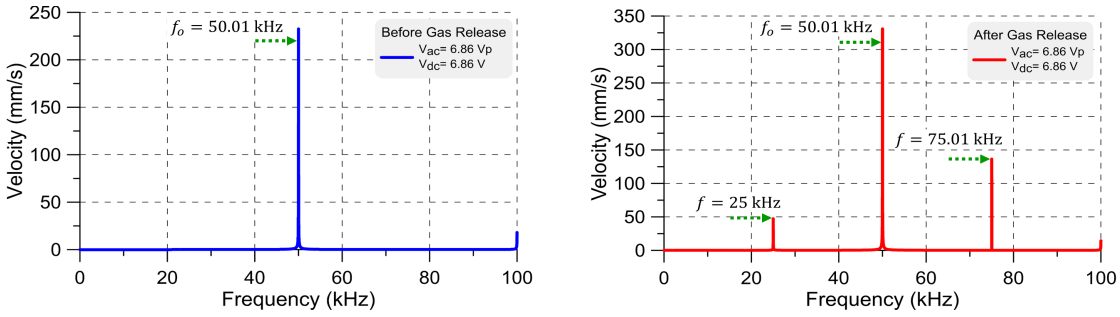

(a) Before (b) After

Figure 3.15: The FFT of the velocity before (a) and after (b) gas release at excitation voltage $V_{\mathrm{dc}} = V_{\mathrm{ac}} = 6.86$ V

A pre-calibrated gas mixture of 5 ppm ethanol vapor in dry nitrogen was slowly released into the chamber. Detection (dynamic pull-in) occurred within a second of gas release. The FFTs of the sensor velocity before and after detection are shown in Fig 3.15. Fast detection indicates that the sorbed mass is well beyond the sensor threshold for a set-off frequency of $\delta f = 50$ Hz.

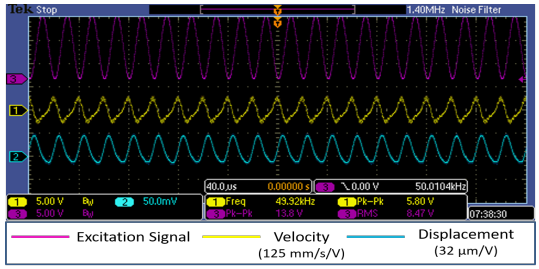

(a) Before

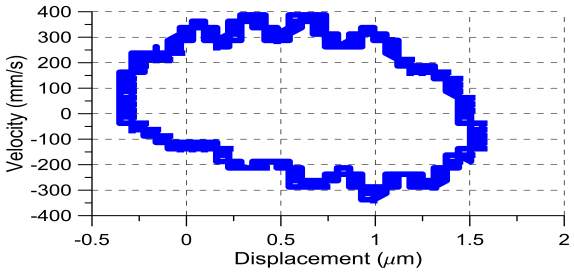

(b) Before

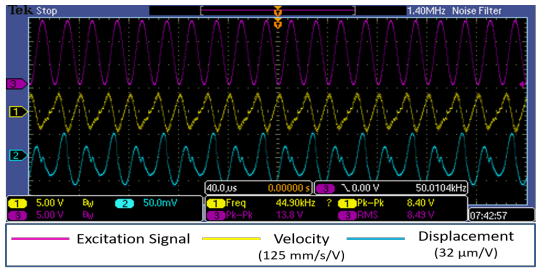

(c) After

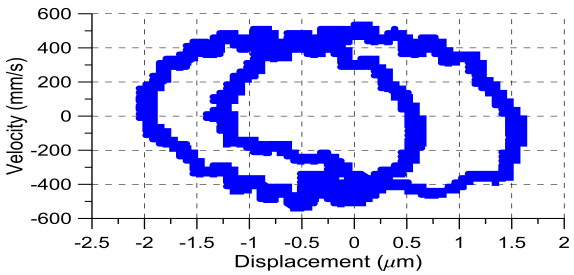

(d) After

Figure 3.16: The time-histories (a and c) of the sensor velocity (yellow), displacement (blue), and excitation signal (magenta), and phase portraits (b and d) before and after gas release at excitation voltage $V_{\mathrm{dc}} = V_{\mathrm{ac}} = 6.86\,\mathrm{V}$

The velocity and displacement time-histories before and after gas release, shown in Fig 3.16 (a) and (c), were recorded using the oscilloscope. Comparing figures Fig. 3.15 (a) and (b) and figures Fig. 3.16 (a) and (c) shows a significant increase in the response amplitude corresponding to a jump from the lower branch to the mid-branch of response. The orbit, Fig 3.16 (b), underwent a period-doubling bifurcation resulting in the observation of a P-2 orbit after detection, Fig 3.16 (d). To investigate repeatability, the experiment was repeated three times, appendix B.1, resulting in detection within 1 s in all three cases.

3.5.2 Ethanol Concentration of 1 ppm

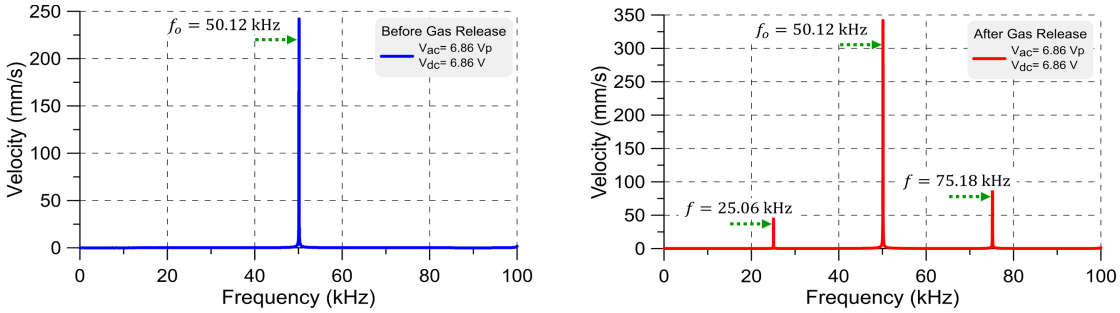

(a) Before (b) After

Figure 3.17: The FFT velocity response before (a) and after (b) at excitation voltage $V_{\mathrm{dc}} = V_{\mathrm{ac}} = 6.86\,\mathrm{V}$

A mixture of 1 ppm ethanol vapor in dry nitrogen was slowly released into the chamber. Detection occurred after 75 seconds of gas release, Fig 3.17. The length of time required for detection indicates that the sorbed mass was small enough to marginally exceed the cyclic-fold bifurcation point. Therefore, 1 ppm ethanol is closer to the sensor detection threshold for $\delta f = 50\,\mathrm{Hz}$.

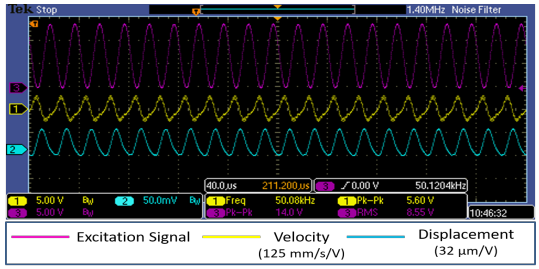

(a) Before

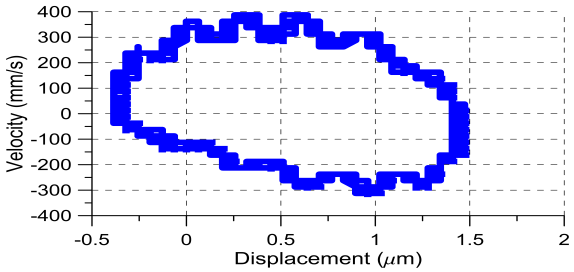

(b) Before

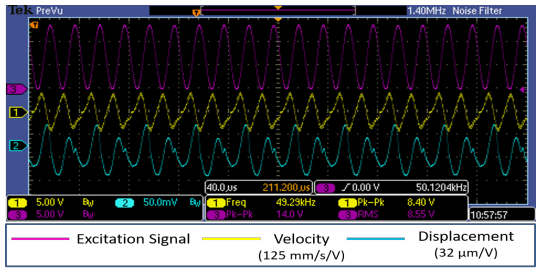

(c) After

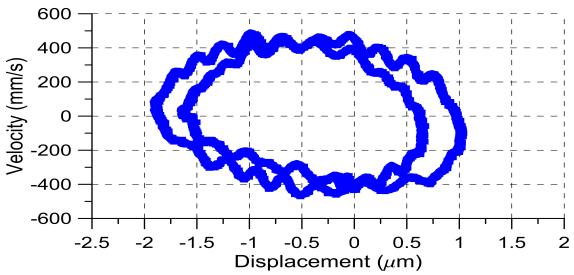

(d) After

Figure 3.18: The time-histories (a and c) of the sensor velocity (yellow), displacement (blue), and excitation signal (magenta), and phase portraits (b and d) before and after gas release at excitation voltage $V_{\mathrm{dc}} = V_{\mathrm{ac}} = 6.86\,\mathrm{V}$

The velocity and displacement time-histories of the sensor before and after detection are shown in Fig. 3.18. Comparing figures Fig. 3.17 (a) and (b) and figures Fig. 3.18 (a) and (c) shows a significant increase in the response amplitude corresponding to a jump from the lower branch to the mid-branch of response. Similarly, the phase portraits before and after detection, Fig 3.18 (b) and (d), show that the orbit underwent a period-doubling bifurcation resulting in a P-2 orbit after detection. The experiment was repeated three times, appendix B.2, resulting in detection in all three cases with a detection time of $79 \pm 22.23\,\mathrm{s}$.

3.5.3 Ethanol Concentration of 100 ppb

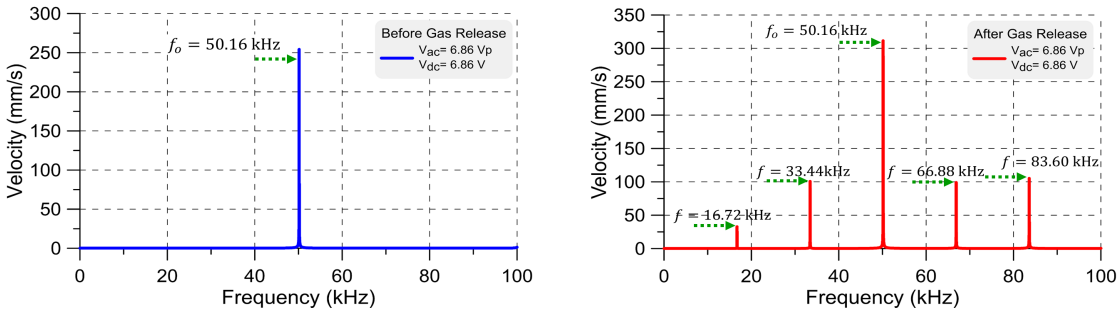

(a) Before (b) After

Figure 3.19: The FFT velocity response before (a) and after (b) gas release at excitation voltage $V_{\mathrm{dc}} = V_{\mathrm{ac}} = 6.86\,\mathrm{V}$

The same procedure was repeated for a mixture of 100 ppb ethanol vapor in dry nitrogen. Detection occurred after 121 seconds of gas release, Fig 3.19. Detection time increased again because the sorbed mass was much closer to the detection limit for our set-off frequency ($\delta f = 50\,\mathrm{Hz}$).

The time-histories and phase portraits of the sensor before and after detection are shown in Fig. 3.20. Comparing figures Fig. 3.19 (a) and (b) and figures Fig. 3.20 (a) and (c) show a significant increase in amplitude after detection corresponding to a jump from the lower branch to the mid-branch of response. In this case, the response orbit went from P-1, Fig 3.20 (b), to P-3, Fig 3.20 (d), after detection which indicates that it landed in a periodic window within a chaotic attractor just beyond the bifurcation point. The experiment was repeated three times, appendix B.3, resulting in detection with same characteristics in all three cases and a detection time of $137.67 \pm 13.89\,\mathrm{s}$.

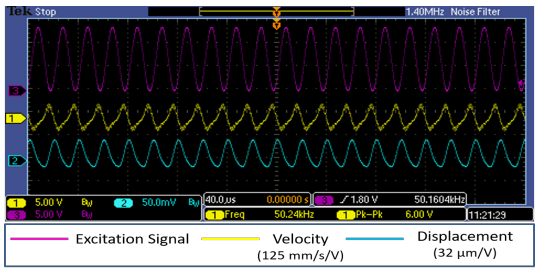

(a) Before

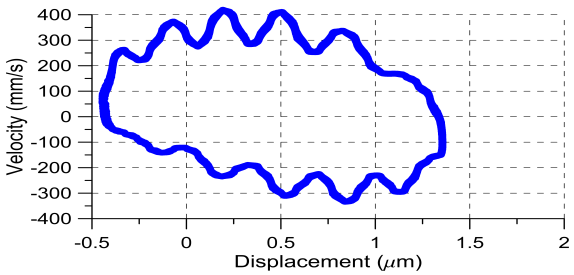

(b) Before

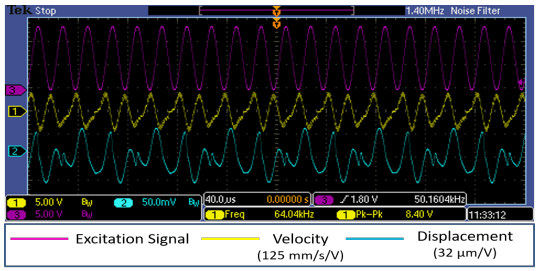

(c) After

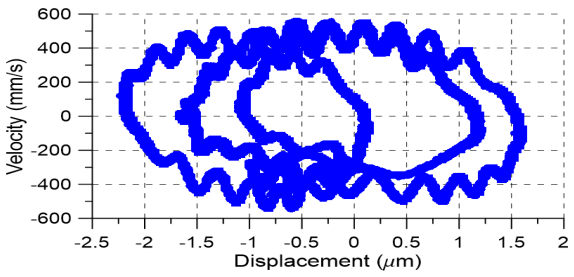

(d) After

Figure 3.20: The time-histories (a and c) of the sensor velocity (yellow), displacement (blue), and excitation signal (magenta), and phase portraits (b and d) before and after gas release at excitation voltage $V_{\mathrm{dc}} = V_{\mathrm{ac}} = 6.86\,\mathrm{V}$

3.5.4 Ethanol Concentration of 50 ppb

The same procedure was repeated again for a mixture of 50 ppb ethanol vapor in dry nitrogen. No detection was observed within 900 seconds of gas release indicating that the sorbed mass was not large enough to exceed the bifurcation point. The experiment was repeated three times, appendix B.4, resulting no detection in all three cases, thereby demonstrating that the detection limit at $\delta f = 50\,\mathrm{Hz}$ is more than 50 ppb.

Comparing the dynamic binary sensor to the static binary sensor [22, 107], we found that for an ethanol concentration of 5 ppm the dynamic sensor was faster at a detection time of 1 s compared to 7 s for the static sensor. In addition, the dynamic sensor was more sensitive at a

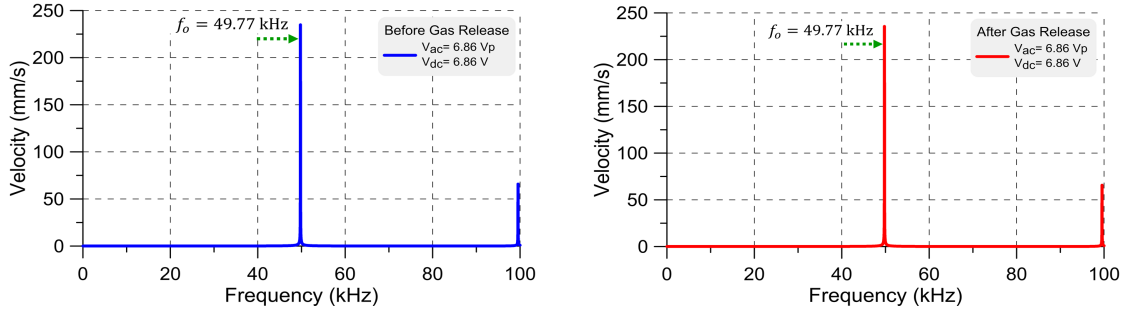

(a) Before (b) After

Figure 3.21: The FFT velocity response before (a) and after (b) gas release at excitation voltage $V_{\mathrm{dc}} = V_{\mathrm{ac}} = 6.86\,\mathrm{V}$

detection limit of 100 ppb compared to 5 ppm for the static sensor. Since our minimum stable set-off frequency was $\delta f = 5\,\mathrm{Hz}$, linear extrapolation suggests that the minimum detectable concentration of the dynamic binary sensor can be as low as 10 ppb.

While linear theory suggests that dynamic detection is more sensitive than static detection, it attributes that to dynamic amplification and limits sensitivity enhancement to the same order as the quality factor ($Q = 5.484$ in our case). This would have suggested a detection limit of 1 ppm. We attribute the discrepancy between this prediction and our experimentally demonstrated sensitivity of 100 ppb to sensitivity improvement achieved via bifurcation-based sensing.

Finally, we note that all experiments were conducted in air on a probe station that was not isolated from ground vibrations. Not only were there no precautions against external disturbances, but also deliberate attempts were made to disturb the sensors via tapping on the probe station. However, no false positives were detected in any of the experiments conducted on this sensor. This observation indicates that the stability of MEMS inertial sensors against external disturbances is better than that of macro-sized inertial sensors because of their minute masses.

Chapter 4

Analog Dynamic Bifurcation Mass Sensors

A mass sensor was designed to measure the variation of minute added mass as an analog fashion measurement. Unlike the binary sensor which quantifies the added mass qualitatively, analog sensors can be utilized to measure the added mass quantitatively as another way of detection. The Shilnikov bifurcation was employed to operate the sensor away from resonance and measure the shift in frequency as well as the change in current through tapping-mode oscillations. The change in frequency and current measurement will be utilized to quantify the added mass electrically. An electrostatic MEMS sensor is equipped with a polymer to represent the added mass on the actuator.

4.1 Sensor

The sensor was fabricated using the PolyMUMPs fabrication process [155], Fig. 4.1. It features a cantilever beam attached with a circular plate at the end. The structural layer was fabricated in Poly2 with material properties $\rho = 2300\,\text{kg/m}^3$, $E = 160\,\text{GPa}$, and $\nu = 0.22$. The beam dimensions are ($115 \times 10 \times 2\,\mu\text{m}^3$), and the radius of plate is $r = 15\,\mu\text{m}$. A gap ($d = 2\,\mu\text{m}$)

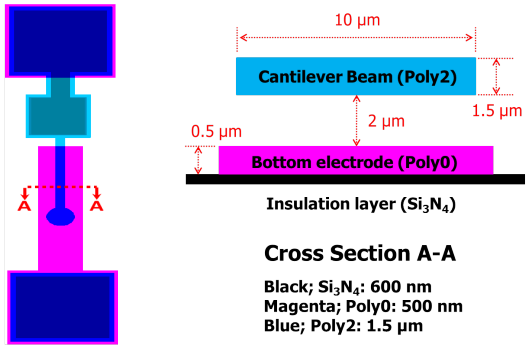

Figure 4.1: Layout of the PolyMUMPs fabricated gas sensor: (a) top-view and (b) front-view along section A–A

is etched under the beam in the second oxide layer. The ground electrode is patterned in Poly0 layer under the length of the beam. Two gold pads are patterned at the root of the beam and the end of the bottom electrode to apply potential difference.

4.2 Numerical Model

A finite element model (FEM) of the mass sensor was created in COMSOL to calculate its natural frequencies and mode shapes. The model was made of 23599 tetrahedral elements, 10420 triangular elements, 790 edge elements, and 20 vertex elements. It did not account for the electrostatic field or fluid-structure interactions. The model shows the first four mode shapes and natural frequencies of the mass sensor constructed from eigenvalue analysis in COMSOL, Fig. 4.2.

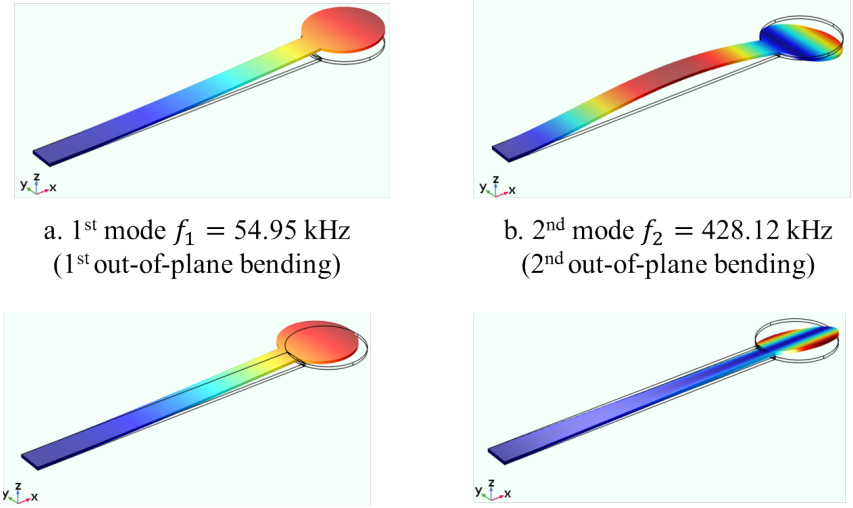

a. 1st mode $f_1 = 54.95$ kHz
(1st out-of-plane bending)

b. 2nd mode $f_2 = 428.12$ kHz
(2nd out-of-plane bending)

c. 3rd mode $f_3 = 474.51$ kHz
(In-plane bending)

d. 4th mode $f_4 = 763.74$ kHz
(Torsional)

Figure 4.2: The first four undamped mode shapes of the mass sensor obtained from eigenvalue analysis

The first mode shape is the first out-of-plane bending mode, Fig. 4.2 (a), with a natural frequency of $f_1 = 54.95$ kHz. The second mode shape is the second bending mode, Fig. 4.2 (b), with a natural frequency of $f_2 = 428.21$ kHz. The third mode shape is the first lateral bending mode, Fig. 4.2 (c), with a natural frequency of $f_3 = 474.51$ kHz. The fourth mode shape is the first torsional mode, Fig. 4.2 (d), with a natural frequency of $f_4 = 763.74$ kHz. The widely spaced modes reduce the possibility of modal interaction between the sensing mode, the first torsional mode, and other modes of sensor vibrations.

4.3 Experimental Setup

The experimental setup, Fig. 4.3, is composed of the sensor placed inside a test chamber, a function generator, a high voltage amplifier, an oscilloscope, lock-in amplifier and added mass, the detection polymer of P25DMA. A laser-Doppler vibrometer is used to measure the sensor response optically. Also, the lock-in amplifier is used to measure the sensor current electrically [190].

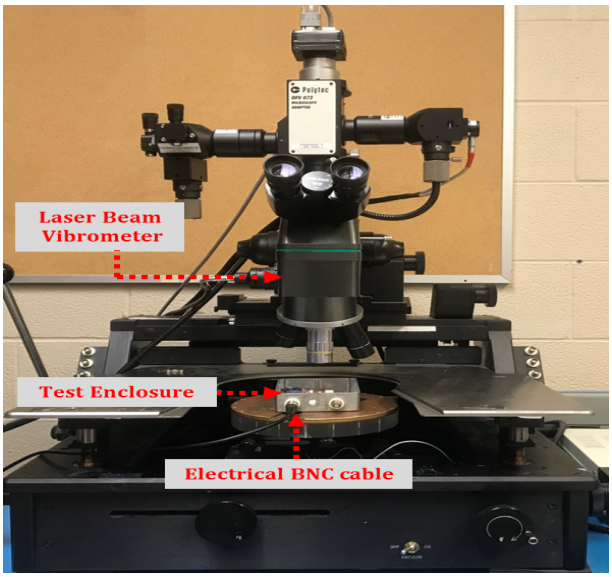

Figure 4.3: The experimental setup

A polymer, poly (2,5-dimethyl aniline) (P25DMA) [175], was utilized to represent added mass on the sensor. It is deposited onto the plate top surface. The polymer was dispersed in a 1% solution of ethylene glycol. The reduced wettability of the solution prevents it from running off the beam edges. Eight drops of polymer-glycol solution were deposited in the middle of the circular-plate to avoid solution overflow. The ethylene glycol was allowed to evaporate in air, leaving polymer residue atop the plate. Fig. 4.4 shows the sensor before, during, and after deposition process.

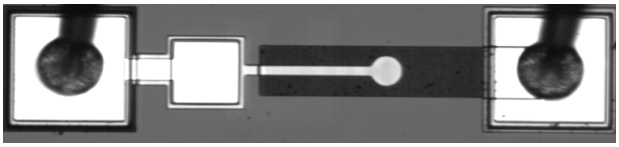

(a) No polymer

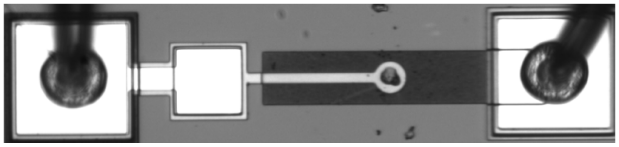

(b) During deposition

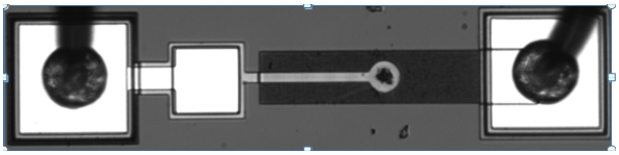

(c) After evaporation

Figure 4.4: Deposition of P25DMA and glycol evaporation

The sensor is actuated by a biased voltage waveform. It exploits the quantitative change before and after depositing the added mass. It acts as a analog mass sensor where the shift in frequency and change in current measurement will quantify the added mass. Detection can be measured either optically, via a Laser Doppler vibrometer, or electrically by measuring current between the two pads.

4.4 Sensor Characterization

The sensor is actuated by applying a voltage waveform of V_{dc}=V_{ac} across the beam and the substrate, Fig. 4.5. The sensor response was measured optically, via a Laser-Doppler vibrometer, and electrically by measuring impedance between the two pads.

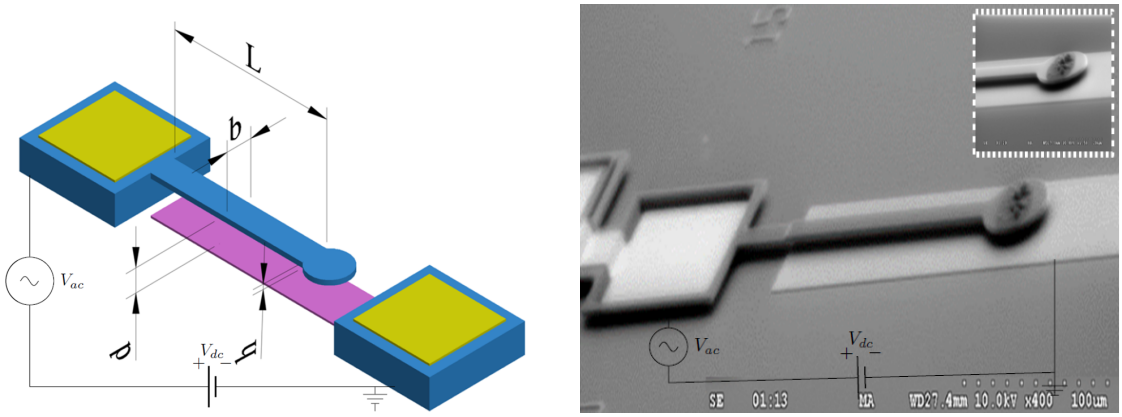

(a) (b)

Figure 4.5: Mass sensor (a) Sensor schematic and (b) SEM picture

4.4.1 Fundamental Natural Frequency

The fundamental mode shape of the sensor was excited by applying a pulse train shown with a magenta line in Fig. 4.6, with amplitude of 3 V, frequency of 1 kHz, and a 0.8% duty cycle, to the sensor in atmospheric pressure. The tip velocity time-history of the sensor was measured optically using the vibrometer and recorded using the oscilloscope. It was averaged over 512 samples and is shown with the yellow line in Fig. 4.6 (a). The damped natural frequency and quality factor were obtained from the time-history as $f_d = 54\,\text{kHz}$ and $Q = 2.1$. The settling time was measured as $t_s = 61.70\,\mu\text{s}$. The velocity FFTs response was also recorded from the vibrometer. It shows the highest peak velocity response at the sensor's natural frequency, $f_d = 54\,\text{kHz}$, Fig. 4.6 (b) .

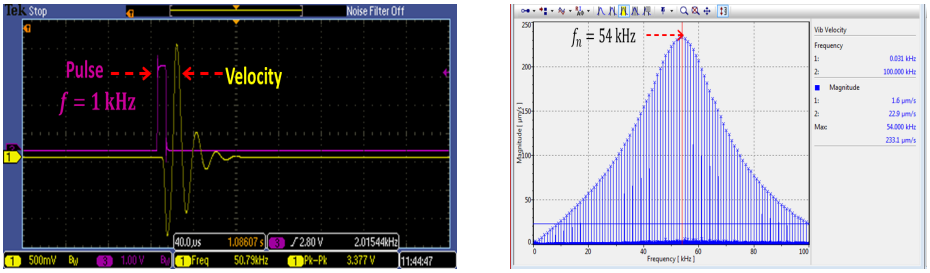

(a) Time-history (b) FFTs velocity

Figure 4.6: (a)the averaged tip velocity time-history under a pulse train with $f = 1\,\text{kHz}$ and an amplitude of 3 V colored in yellow and magenta, respectively, and (b) FFTs velocity response

4.4.2 Bifurcation Point Before Deposition

The frequency-response curve of the sensor was obtained in the vicinity of primary resonance to locate the Shilnikov bifurcation region. Forward and backward frequency sweeps were carried out over the frequency range $f = [5\text{–}60]\,\text{kHz}$. The excitation voltage waveform was set to $V_{\text{dc}} = V_{\text{ac}} = 7.125\,\text{V}$. A slow slew rate of $f = 2.5\,\text{kHz/s}$ was used to minimize transient effects. Data was collected using an oscilloscope in time windows of 0.4 s each and a sampling rate of $f_s = 313\,\text{kHz}$. The frequency-response curve, Fig. 4.7, was obtained by post-processing the data to evaluate the RMS of the beam tip velocity over a time window of $20T$ and assigning it to the frequency at the window mid-point.

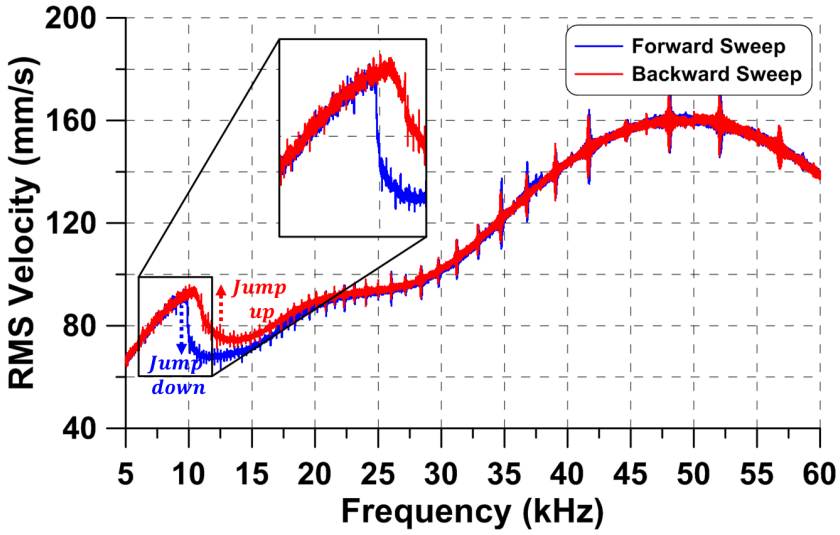

Figure 4.7: The measured frequency-response curve for $V_{\rm dc} = V_{\rm ac} = 7.125\,$V. Forward sweep is shown in blue and backward sweep is shown in red

The forward sweep is shown in blue and the backward sweep in red, Fig. 4.7. The jump-up during the backward sweep at $f_{\rm pu} = 10.627\,$kHz corresponds to the lower branch to the upper tapping branch. The jump-down during the forward sweep occurs at $f_{\rm pd} = 9.876\,$kHz and corresponds to the upper tapping branch to the lower branch. The positive slope in both forward and backward sweep demarcate the tapping-mode oscillations involving the sensor tip interaction with the substrate. The region between the two jumps demarcates hysteresis in the sensor response.

4.5 Results and Discussion

The mass sensor was characterized again after deposition to investigate the effect of added mass on the sensor natural frequency. The same experimental procedure as explained above in section 4.4.1 was conducted. The measured natural frequency was found as $f = 51\,$kHz, Fig. 4.8.

The FFTs velocity, Fig. 4.8 (a), and velocity time-history, Fig. 4.8 (b), demarcate a drop by 3 kHz in the sensor natural frequency, compared to the un-deposited one, and that is due to the effect of added mass.

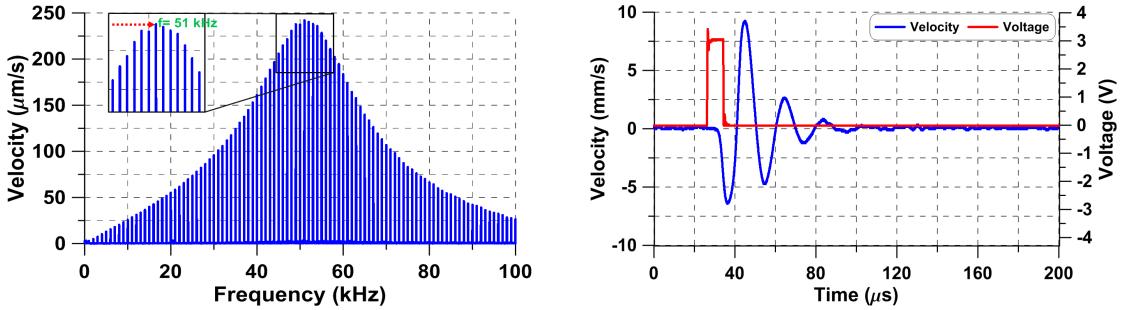

(a) Before (b) After

Figure 4.8: (a) The FFT of the velocity, and (b) velocity time-history under a pluse of $f = 1kHz$ with a voltage amplitude $V = 3$ V colored in blue and red, respectively

The frequency-response curve of the sensor was obtained again after deposition carrying out the same experimental procedure explained above in section 4.4.2. Forward and backward frequency sweeps were carried out over the frequency range $f =$ [5–60] kHz showing in Fig. 4.8 .

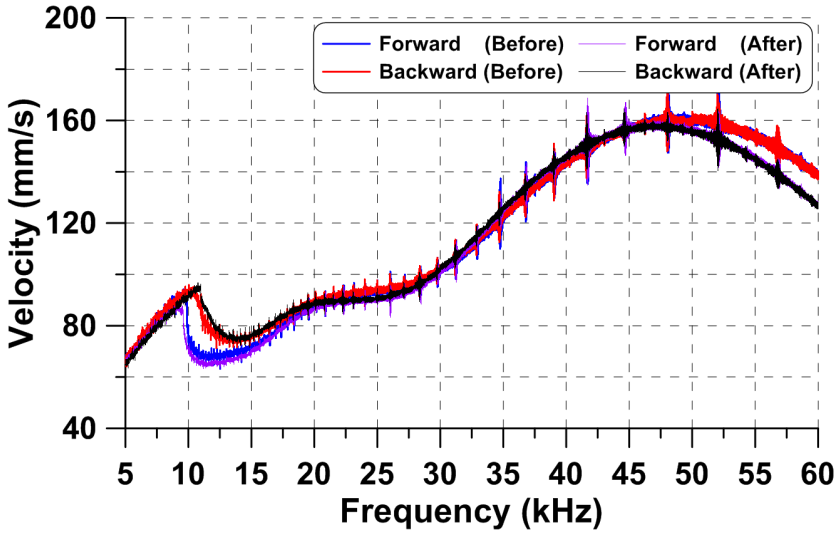

Figure 4.9: The measured frequency-response curve for $V_{\rm dc} = V_{\rm ac} = 7.125\,$V. Forward and backward sweeps before deposition is colored in blue and red, and after deposition colored in magenta and black

The forward sweep is represented by the magenta line and the backward sweep by the black line, Fig. 4.9. The jump-up during the backward sweep at $f_{\rm pu} = 11\,$kHz corresponds to the lower branch to the upper tapping branch. The jump-down during the forward sweep occurs at $f_{\rm pd} = 9.270\,$kHz and corresponds to the upper tapping branch to the lower branch, where the sensor oscillates freely in air. The positive slopes in both forward and backward sweeps demarcate the tapping-mode oscillations involving the sensor tip interaction with the substrate. The region between the two jumps demarcates hysteresis in the sensor response.

It is clearly seen that there is a frequency shift while doing froward and backward sweeps before and after depositing added mass. The shift in forward frequency-sweeps was found as $f_d - f_\circ = 606\,$Hz located in the vicinity of the Shilnikov bifurcation region. Also, the shift in backward frequency-sweeps was found as $f_d - f_\circ = 373\,$Hz existing in the vicinity of the Shilnikov bifurcation region. We note that all experiments were conducted in air on a probe

station that was not isolated from ground vibrations.

In addition, the lock-in amplifier was utilized to measure the motion induced current before and after depositing the added mass. A forward frequency sweep was obtained over a frequency range of $f = [10 - 80]$ kHz at the voltage waveform $V_{\rm dc} = V_{\rm ac} = 7.125$ V . The current measurement was looked at the second harmonic with respect to the excitation frequency and that due to the effect of electrostatic force, Fig. 4.10.

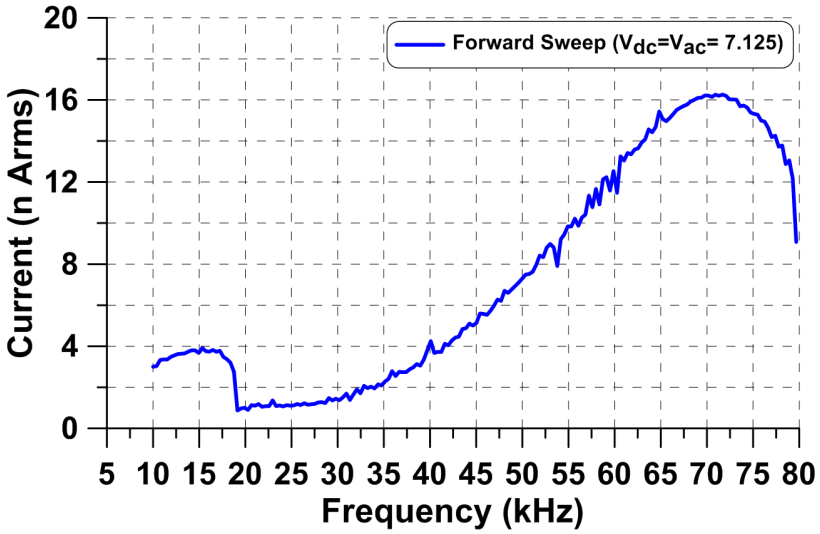

Figure 4.10: Forward frequency-response curve measured electrically for un-deposited sensor at the voltage waveform $V_{\rm dc} = V_{\rm ac} = 7.125$ V

The current amplitude was found in the Shilnikov bifurcation range $I_{sh} = 4$ nArms whereas at the primary resonance was found to be $I_p = 16.26$ nArms. Then, the current was measured after depositing the added mass and sweeping the frequency over a range of $f = [5 - 80]$ kHz at voltage waveform of $V_{\rm dc} = V_{\rm ac} = 6.90$ V, Fig. 4.11. We found the current amplitude after depositing the added mass increased six times in the vicinity of Shilnikov region and three times in the vicinity of the primary resonance, $I_{sh} = 24.48$ nArms and $I_p = 54.82$ nArms, respectively

.

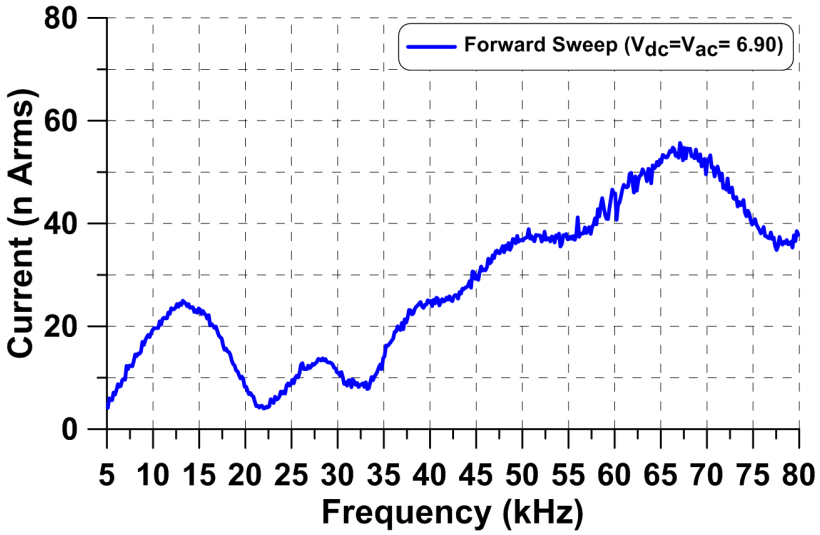

Figure 4.11: Forward frequency-response curve measured electrically for deposited sensor at the voltage waveform $V_{\mathrm{dc}} = V_{\mathrm{ac}} = 6.90\,\mathrm{V}$

To sum up, a new sensing mechanism under Shilnikov bifurcation was demonstrated. It exploits a quantitative change in the sensor state before and after depositing added mess via tapping mode oscillations. A polymeric sensing material was deposited atop surface of the sensor plate to represent added mass. A variation in the frequency as well as current amplitude were observed before and after depositing the added mass. The sensor was excited electrostatically. Two detection methods were conducted: optically via LDV and electrically using the lock-in amplifier. We found the current increased six-fold in vicinity of Shilnikov bifurcation due to adding a mass of 301 pg. Also, the current was found increased three-fold in vicinity of primary resonance.

Further, this detection method will be extend in the future to implement an analog bifurcation-based gas sensor instigating in the vicinity of Shilnikov bifurcation region where the tapping

oscillations will be employed to measure the added mass electrically. The polymeric sensing material which has high selectivity to a target gas will be employ to sorbed added mass to enhanced the sensor sensitivity and selectivity.

Chapter 5

Underwater Sensors

In this chapter, a chemical sensor was designed to detect mercury acetate in water. A frequency-shift mechanism due to the variation of added-mass was utilized as the detection mechanism to simply differentiate between safe and unsafe concentrations. The sensor is equipped with a polymer highly selective to mercury. A mercury acetate solution of 100 ppm in deionized-water (DI-water) was utilized to demonstrate the functionality of the sensor. The sensor is excited electrostatically, and the response was measured electrically.

5.1 Sensor Design

Two sensors were fabricated using an SOI fabrication process [191]. The structural layer of sensor #1, Fig. 5.1 (a), and of sensor #2, Fig. 5.1 (b), are made of a silicon layer (Si) with Young's modulus of $E = 129$ GPa. The sensors consist of a cantilever beam with dimensions of ($175 \times 10.5 \times 30\,\mu m^3$) and ($250 \times 25 \times 30\,\mu m^3$), respectively. The lateral gap in between the sensor and side-electrode is $g = 3\,\mu m$. Two side electrodes are patterned on either side of the platform. A gold contact pads is patterned and attached to the cantilever beam as well as at the back-side

of the lateral electrodes. The pads are used to to apply actuation voltage and to drive current through the silicon structural layer to reset the sensor via Joule heating.

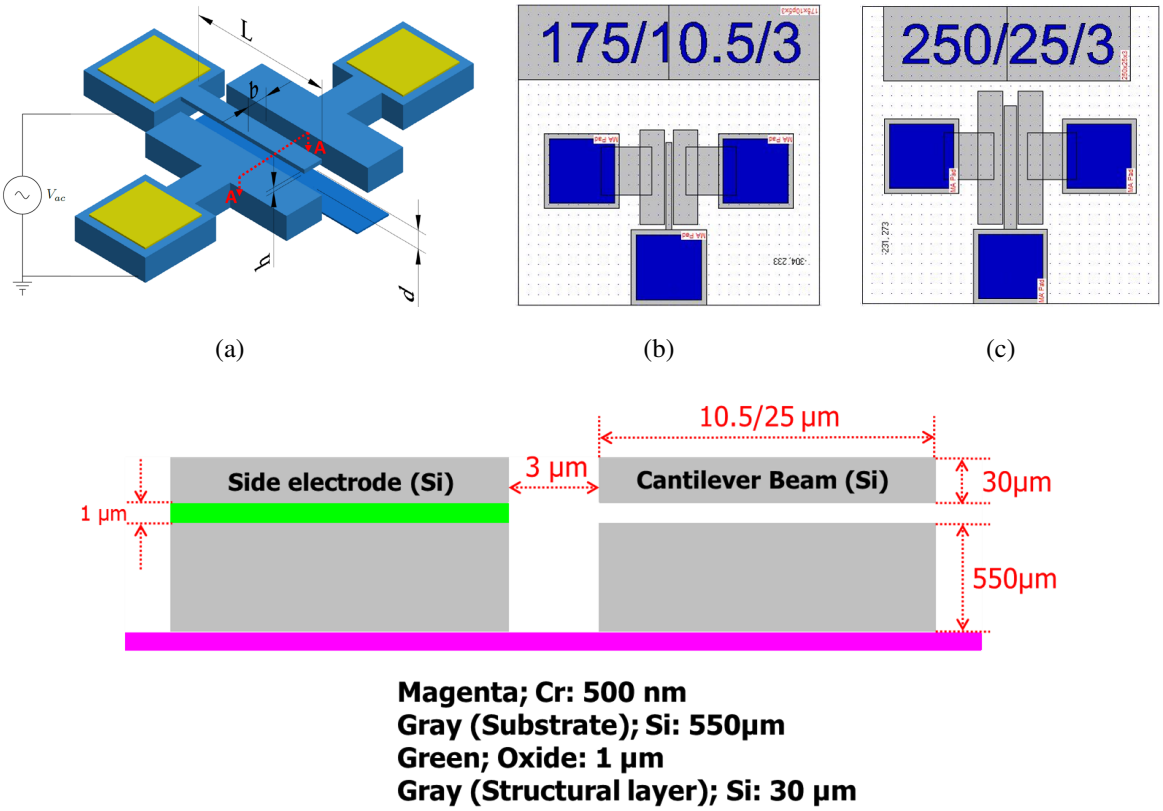

Figure 5.1: Layout of the SOI fabricated underwater sensor (a) sensor #1 top-view, (b) sensor #2 top-view and (c) front-view of the cross-section A-A

The sensor was designed by following these criteria:

- Maximize the beam cross-sectional dimensions to increase the sensor natural frequencies and, therefore, sensitivity and quality factor.

- Maximize the beam thickness to minimize fluid damping.
- Maximize the distance between the actuation electrodes and the sensor-platform to minimize squeeze film damping, electrolysis, and leakage current.

5.2 Modal Analysis

A finite element model (FEM) was utilized to construct the sensors' undamped natural frequencies and those corresponding mode shape in air. Higher modes were investigated. We choose to target the mode shapes in the vicinity of $f = [60 - 78]$ MHz. The eighth mode shapes of sensor #1 were determined as shown in Fig. 5.2. The model is made of 12096 tetrahedral elements of 2220 triangular elements, of 216 edge elements, and of 8 vertex elements. It does not account for the electrostatic field or fluid-structure interactions.

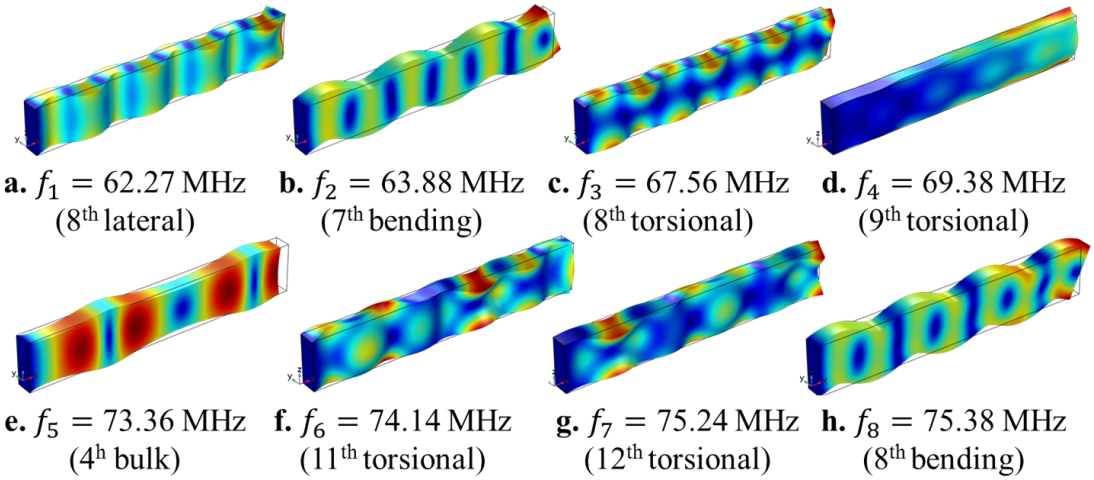

Figure 5.2: Undamped mode shapes of sensor #1 obtained from eigenvalue analysis

The first mode shape is the eighth lateral bending mode, Fig. 5.2 (a), with a natural frequency of $f_1 = 62.27$ MHz. The second mode shape is the seventh out-of plane bending mode,

Fig. 5.2 (b), with a natural frequency of $f_2 = 63.88\,\text{MHz}$. The third mode shape is the eighth torsional mode, Fig. 5.2 (c), with a natural frequency of $f_3 = 67.56\,\text{MHz}$. The fourth mode shape is the ninth torsional mode, Fig. 5.2 (d), with a natural frequency of $f_4 = 69.38\,\text{MHz}$. The fifth mode shape is the forth bulk mode, Fig. 5.2 (e), with a natural frequency of $f_5 = 73.36\,\text{MHz}$.The sixth mode shape is the eleventh torsional mode, Fig. 5.2 (f), with a natural frequency of $f_6 = 74.14\,\text{MHz}$. The seventh mode shape is the twelfth torsional mode, Fig. 5.2 (g), with a natural frequency of $f_7 = 75.24\,\text{MHz}$. The eighth mode shape is the eighth out-of plane bending mode, Fig. 5.2 (h), with a natural frequency of $f_8 = 75.38\,\text{MHz}$.

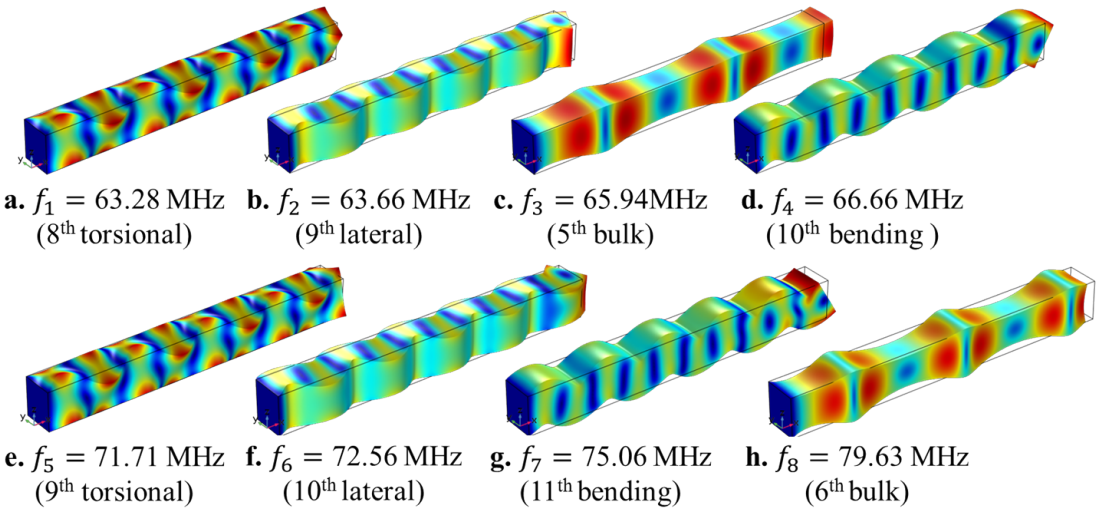

Figure 5.3: The sixth undamped mode shapes of sensor #2 obtained from eigenvalue analysis

Similarly, the eighth mode shapes of sensor #2 were determined in the vicinity of $f = [60 - 80]\,\text{MHz}$ as shown in Fig. 5.3. The model is made of 43946 tetrahedral elements of 4216 triangular elements, 300 edge elements, and 8 vertex elements. It does not account for the electrostatic field or fluid-structure interactions.

The first mode shape is the eighth torsional mode, Fig. 5.3 (a), with a natural frequency of

$f_1 = 63.28$ MHz. The second mode shape is the ninth lateral mode, Fig. 5.3 (b), with a natural frequency of $f_2 = 63.66$ MHz. The third mode shape is the fifth bulk mode, Fig. 5.3 (c), with a natural frequency of $f_3 = 65.94$ MHz. The fourth mode shape is the tenth out-of plane bending mode, Fig. 5.3 (d), with a natural frequency of $f_4 = 66.66$ MHz. The fifth mode shape is the ninth torsional mode, Fig. 5.3 (e), with a natural frequency of $f_5 = 71.71$ MHz. The sixth mode shape is the tenth lateral mode, Fig. 5.3 (f), with a natural frequency of $f_6 = 72.56$ MHz. The seventh mode shape is the eleventh out-of plane bending mode, Fig. 5.3 (g), with a natural frequency of $f_7 = 75.06$ MHz. The eighth mode shape is the sixth bulk mode, Fig. 5.3 (h), with a natural frequency of $f_8 = 79.63$ MHz.

We are interested in operating the sensor laterally to reduce the added mass and fluid damping and thus limits the change in the sensor resonant frequency to the range of [5-10]% [134], since shearing the water laterally reduces fluid resistance [108, 144].

5.3 Electrostatic Actuation

The underwater sensor employs electrostatic actuation by applying a voltage difference between the platform and one of the two side electrodes, an electrostatic force develops and vibrates the beam laterally [1, 153]. The operation of electrostatic parallel-plate actuators underwater increases their efficiency 60 to 70 times compared to air [118], since the dielectric constant of water is 80 times larger than that of air. It has the advantage of achieving large response with low power consumption compared to operation in other media [118, 119, 125]. Electrolysis can be avoided by exciting the sensor with a modulated signal where the carrier frequency is high enough ($f \geq 1$ MHz) to minimize the effects of the slow chemical reactions responsible for separating water molecules and generating gas bubbles [94, 118, 119]

5.4 Detection Method

The sensor employs an analog detection based on measuring a frequency-shift in water. Unlike the dynamic pull-in phenomenon discussed in Section 3.4.2 which measures the added mass qualitatively, a quantitative method of detection was applied to detect mercury ions in water. A polymeric sensing material which has high selectivity to mercury was utilized to capture the mercury ions and increase the sensor effective mass. Mercury (II) acetate in solution was utilized as a target to demonstrate the sensor functionality with a concentration of 100 ppm. As the target concentration in water increases, the number of ions captured by the polymer increases until their 'added mass' reaches a critical value. The variation in the frequency-response curve will be utilized as a metric for electric detection. The sensor was excited electrostatically by an AC voltage, V_{ac}, to eliminate electrolysis and bubble effects. A lock-in amplifier was utilized to measure the current between the beam and the side-electrode.

5.5 Experimental Setup

The experimental setup is similar to that of the mass sensor described in Section 4.3. It is composed of the sensor inside a test enclosure, a function generator, an actuation printed circuit board (PCB), and a transimpedance amplifier. A test enclosure with dimensions of ($19 \times 19 \times 3$ mm^3) was fabricated utilizing Polydimethylsiloxane (PDMS) to allow for dual optical, through the CCD camera, and electrical, using the transimpedance-amplifier, detection. It was housed on top of an actuation PCB as shown in Fig. 5.4. A pico-pump was utilized to control the water flow-rate and reduce the possibility of stiction.

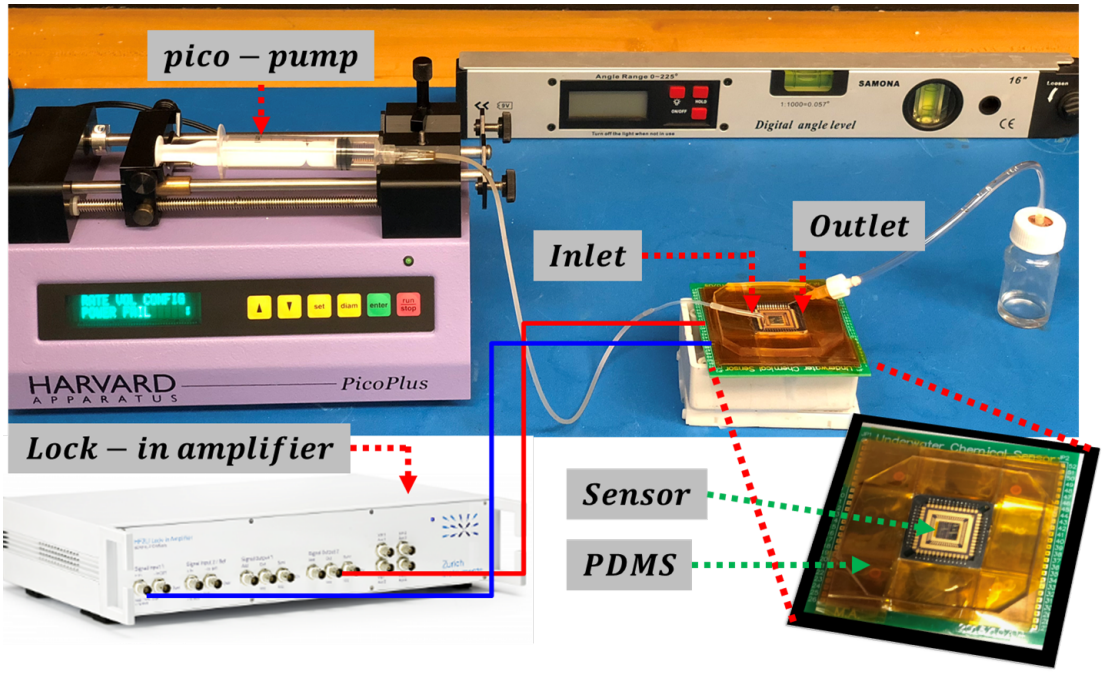

Figure 5.4: Experimental setup

The board dimensions are ($70 \times 70\,\mathrm{mm}^2$), Fig. 5.5 (a). It was coated by a solder resist made of a liquid photoimageable ink (Probimer 77) to avoid electrically leakage once the enclosure is filled with water. It used to provide electrical access to the sensor inside the enclosure. Electrical traces was designed and printed on the back side of the board to protect against water leakage from test enclosure as shown in Fig. 5.5 (b).

A polymer with affinity to mercury, Polyacrylamide (PAM), was deposited onto the beam top surface. The polymer was dispersed in a solution of ethylene glycol. The reduced wettability of the solution prevents it from running off the beam edges. Five and seven drops of polymer-glycol solution were deposited onto sensor #1 and sensor #2, respectively, along the beam length in stages to avoid solution overflow. The ethylene glycol was allowed to evaporate in air, leaving

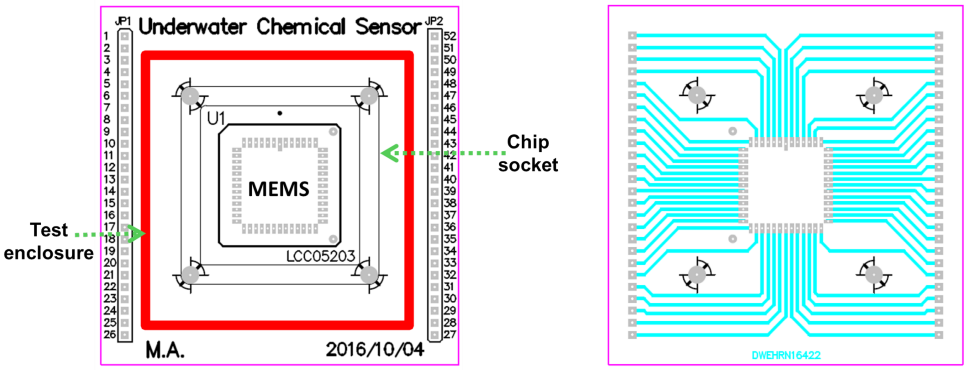

(a) (b)

Figure 5.5: (a) The front-side of the actuation PCB showing the chip socket and (b) the back side of the board showing the electrical traces

polymer residue atop the beam. Fig. 5.6 shows the sensor before, during, and after deposition.

5.6 Results and Discussion

Experiments was conducted by placing the sensor inside the chip socket and covering them with the test enclosure. The test enclosure was filled with deionized (DI) water at a flow rate of 1.5 µL/s to avoid stiction. The operating voltage $V_\circ$ was applied, while the sensor was completely immersed in water with the analyte at the desired concentration. The sensor response was monitored continuously using a video CCD camera and a transimpedance amplifier to measure output current. A frequency sweep was conducted on the two sensors and the results compared while submerging the sensor in water solution only and in water and mercury acetate acetate solution. The pH of the water solution and that of the of mercury acetate with water solution were measured using pH indicator paper and found as 5 and 6, respectively.

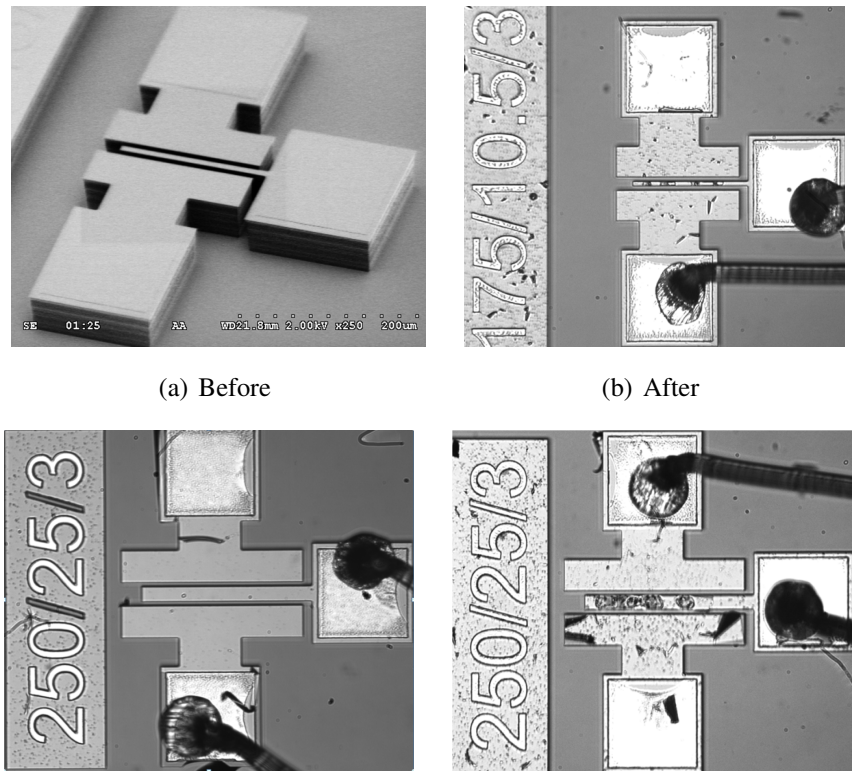

(a) Before (b) After

(c) Before (d) After

Figure 5.6: Sensor #1 (top) and sensor #2 (bottom) before and after deposition of PAM and ethylene glycol evaporation

The effect of pH variations between water and mercury acetate solution were further studied by submerging two electrodes into two separate vials of water and the mixture solution. The two electrodes were excited electrostatically by a voltage amplitude of $V_{\text{ac}} = 9\,\text{V}$ and the current was measured using lock-in amplifier over a frequency range of $f = [32 - 37]\,\text{MHz}$, Fig. 5.7 (a). We found a noticeable drop in the current amplitude measurement in the vicinity of $f = 33.3\,\text{MHz}$ as $\Delta i \propto 997\,\text{pArms}$ as well as a drop in frequency by $\Delta f \propto 100.502\,\text{kHz}$. Similarly, the sweeping range was increased to $f = [32 - 39]\,\text{MHz}$ at the same excitation voltage, Fig. 5.7 (b).

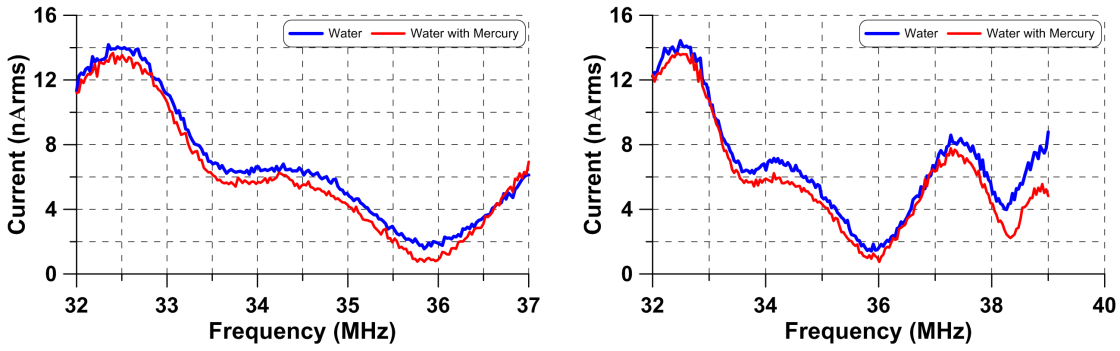

(a) (b)

Figure 5.7: The current measurement of excited electrodes in Water vial and mixture of water with mercury in another vial over a frequency range of (a) $f = [32 - 37]$ MHz and (b) $f = [32 - 39]$ MHz

We found also a noticeable drop in the current measurement in the vicinity of $f = 38$ MHz as $\Delta i_1 \propto 1.691$ nArms, as well as a drop in frequency $\Delta f \propto 70.351$ kHz.

5.6.1 Sensor #1

The same experimental procedure was utilized after submerging the sensor completely with a pre-defined rate. The sensor was excited electrostatically at voltage amplitude of $V_(\mathrm{ac}) = 9$ V, sweeping the frequency over a range of $f = [32 - 37]$ MHz and collecting the current measurement, Fig. 5.8 (a). A significant drop in frequency was observed by $\Delta f = 1.18$ MHz while injecting the mercury acetate solution. Also, we observed a significant increased in the current amplitude $\Delta i = 1.27$ nArms. We postulate the increase in amplitude due to the pH, which might cause the effective mass of the sensor to vary.

Similarly, the sweeping range was increased to $f = [32 - 39]$ MHz at the same excitation voltage, Fig. 5.8 (b). A significant drop in frequency was observed by $\Delta f = 1.10$ MHz while in-

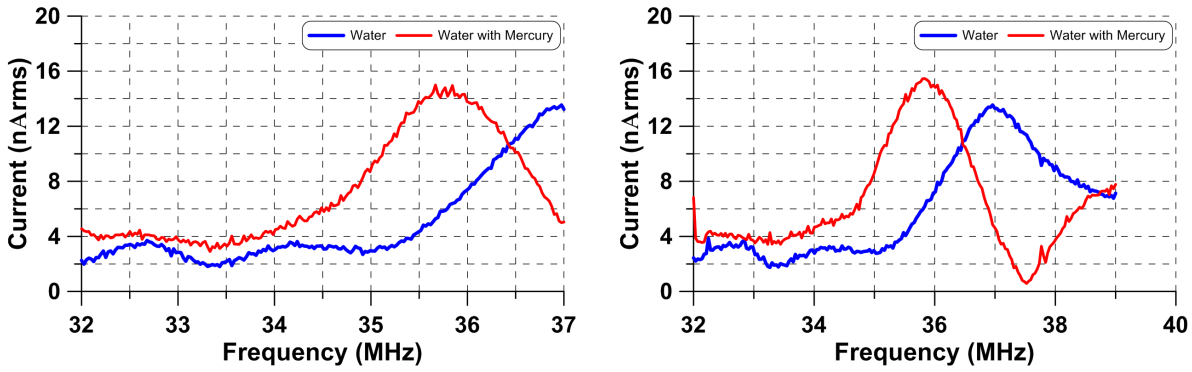

(a) (b)

Figure 5.8: The current measurement of sensor #1 submerged in water and mercury acetate solution excited at voltage amplitude $V_{ac} = 9\,\text{V}$ and over a frequency range of (a) $f = [32 - 37]\,\text{MHz}$ and (b) $f = [32 - 39]\,\text{MHz}$

jecting the mercury acetate solution to the sensor. Also, we again observed a significant increase in the current amplitude $\Delta i = 2.08\,\text{nArms}$.

5.6.2 Sensor #2

Same experimental procedure was employed as explained above. The sensor was excited electrostatically at voltage amplitude of $V_(\text{ac}) = 9\,\text{V}$, sweeping the frequency over a range of $f = [32 - 37]\,\text{MHz}$ and collecting the current measurement, Fig. 5.9 (a). A significant drop in frequency was observed by $\Delta f = 4.371\,\text{MHz}$ while injecting the mercury acetate solution. Also, we observed a significant increased in the current amplitude $\Delta i = 14.68\,\text{nArms}$. We postulate the increased in amplitude due to the pH, which might cause the effective mass of the sensor to vary.

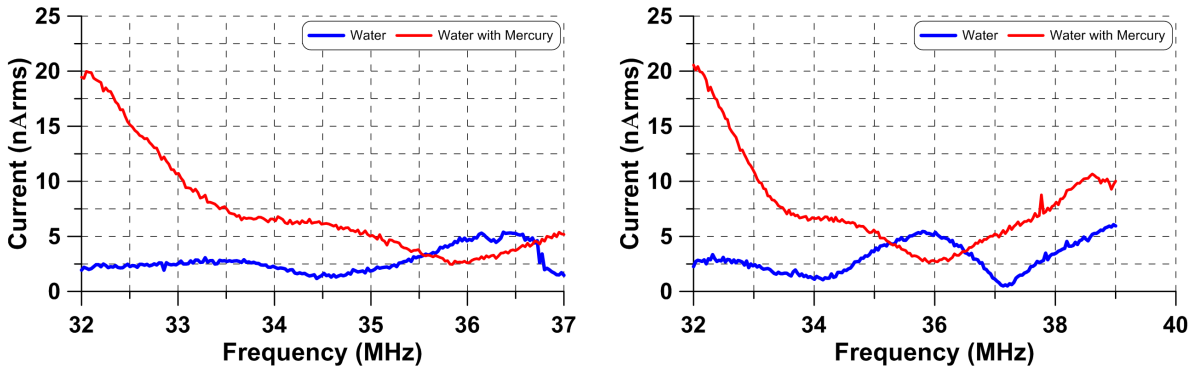

(a) (b)

Figure 5.9: The current measurement of sensor #2 submerged in water and mercury acetate solution excited at voltage amplitude $V_{ac} = 9\,\text{V}$ and over a frequency range of (a) $f = [32 - 37]\,\text{MHz}$ and (b) $f = [32 - 39]\,\text{MHz}$

Subsequently, the sweeping range was increased to $f = [32 - 39]\,\text{MHz}$ at the same excitation voltage, Fig. 5.8 (b). A significant drop in frequency was observed by $\Delta f = 3.7638\,\text{MHz}$ while injecting the mercury acetate. Also, we observed a significant increase in the current amplitude $\Delta i = 14.646\,\text{nArms}$. We postulate the mode interaction has a role of varying the current measurement.

To sum up, we demonstrated an electrostatic sensor operated in aqueous media to detect mercury ions. The sensor was submerged completely in deionized-water with a pre-defined flow-rate of 1.5 µL/s. The sensor was excited in higher modes to reduce the side-effects of the chemical reactions, bubbles, as well as enhancing sensor sensitivity. A polymeric sensing material (PAM) was utilized to sorb mercury in water. A solution of water and mercury acetate with a concentration of 100 ppm was released to the sensor utilizing the same pre-defined flow-rate. The response was measured electrically using the lock-in amplifier. Our sensor was able to measure frequency shift $\Delta f = 1.18\,\text{MHz}$ in sensor #1 and $\Delta f = 4.37\,\text{MHz}$ in sensor #2.

Chapter 6

Conclusions and Future Work

6.1 Nonlinear Electrostatic MEMS Sensors

We identified a new type of pull-in instabilities in electrostatic sensors dubbed quasi-static pull-in. It occurs under periodic excitations, unlike the case for the traditional static pull-in instability, in a non-resonant frequency range much lower than the fundamental natural frequency $f/f_1 << 1$, unlike the case for the dynamic pull-in instability. The phenomenon were replicated and verified in two independent MEMS electrostatic sensors oscillating in ambient air.

We found that quasi-static pull-in is driven by a fast-slow dynamic interaction between the slowly varying electrostatic excitation and the fast response of the sensor's fundamental mode. It manifests itself by the appearance of Shilnikov orbits homoclinic to a saddle-focus under waveforms where the instantaneous voltage approaches static pull-in voltage V_{Ps}. It is characterized by large tapping-mode oscillations where the sensor periodically goes to pull-in through a saddle-node bifurcation before pulling-off and settling close to the unactuated equilibrium. The settling time is function of the sensor's quality factor. While stable focus oscillations were clearly observable in sensor # 1 due to a higher quality factor $(Q = 5.4)$ and a longer settling time, they

were not as clear for sensor # 2 with where the quality factor was lower at $Q = 2.1$.

A Shilnikov bifurcation demarcates the boundary between the frequency range of Shilnikov orbits involving quasi-static pull-in and Shilnikov-like orbits involving fast-slow dynamics but no tapping interactions with the substrate. A hysteretic region exists in the vicinity of the Shilnikov bifurcation bounded at the lower end by a jump-down during forward frequency sweeps and a jump-up during backward frequency sweeps. This is in contrast to the hysteric region observed in the vicinity of dynamic pull-in under a softening effective nonlinearity.

In addition, nonlinear chaotic behaviors were observed experimentally for the two sensors, sensor #1 and sensor #2. Shilinikov chaos instigated by Shilnikov to a saddle-focus was observed in the vicinity of a slow-varying region where the excitation frequency is way less than the sensor resonances, $f/f_1 << 1$. Secondary resonances and period doubling of P-2, P-3, and P-6 were experimentally investigated. Different routes to chaos were found and demonstrated in the vicinity of resonances. Intermittency type-I, and type-II were observed as a results of cyclic-fold bifurcation and secondary Hopf-bifurcation, respectively. A new class of intermittencies, dubbed switching intermittency, was found in the oscillations of an electrostatic MEMS sensor in ambient air. Switching intermittency is characterized by stretches of laminar flow in the vicinity of a ghost orbit interrupted at irregular interval by bursts. Unlike other intermittencies, the bursts do not involve irregular motions. Instead they were arrested by a contracting orbit where they can spend irregular intervals of time before being re-injected into the area of the ghost orbit. In our case, contraction is provided by impacts of the sensor tip on the substrate and re-injection is noise induced.

We identified two types of switching intermittencies. In type-I, the intermittency evolves as a control parameter is increased into stable periodic tapping mode oscillations. In type-II, the intermittency evolves as a control parameter increases into a chaotic attractor. Both types were found to occupy a finite region in the forcing parameter space, amplitude and frequency

of the voltage waveform in our case. Further, banded chaos was demonstrated as a result of intermittency, quasiperiodicity orbits, and homoclinic tangles. Full chaos was further observed as a result of losing orbit periodicity. We note that all the experimental results were demonstrated in air.

6.2 Binary Dynamic Gas Sensor

We utilized a novel sensing mechanism that exploits the qualitative change in the sensor state before and after a dynamic bifurcation in electrostatic MEMS (dynamic pull-in) to realize an ethanol vapor sensor. Our sensing mechanism has the dual advantages of allowing for binary sensing and improving sensitivity. A mathematical model of the sensor was introduced and solved numerically to estimate the location of the cyclic-fold bifurcation underlying dynamic pull-in. To determine the exact location of the bifurcation point, the frequency-response of the sensor was obtained experimentally. In the process, we identified a middle-branch of response between the lower and upper branches of response traditionally observed in electrostatic MEMS. The sensor oscillates in air on the lower and upper branches but taps intermittently on the substrate along the middle branch. This is the first time this branch has been observed experimentally in electrostatic MEMS.

A closed-form sensitivity formula was derived for bifurcation-based sensors exploiting a cyclic-fold bifurcation. We found that sensitivity was proportional to the electrostatic field and counter-proportional to the effective mass. We note that our sensitivity function represents a set-off frequency infinitesimally close to the bifurcation point ($\delta f \rightarrow \infty$), whereas the set-off frequency in our experiment was finite $\delta f = 50\,\text{Hz}$. As the set-off frequency decreases, the realized sensitivity will approach that predicted by Eq. (3.60). Further, this formula should be used to optimize the sensor dimensions and operating conditions in order to maximize sensitivity.

The sensor was excited by biased waveform with an amplitude and frequency that place it close to the bifurcation point, such that the added mass sorbed by the detector material in the presence of ethanol would send it past it. The minimum detectable gas concentration is dependent on the minimum realizable set-off frequency δf as well as the type and distribution of the detector polymer coat on the sensor surface. However, no attempt was made to optimize the set-off frequency δf or the polymer distribution, since the purpose of this study is limited to demonstration of feasibility.

Experimental investigation demonstrated that at a set-off frequency of $\delta f = 50$ Hz our sensor can detect a binary logic high for ethanol concentrations down to a minimum of 100 ppb within a maximum detection time of 137.67 ± 13.89 s. A stable period P-2 orbit was observed for ethanol concentrations of 5 ppm and 1 ppm, which resulted in sorbed masses large enough to take the sensor beyond a stable period-doubling bifurcation lying within the mid-branch of response, Fig. 3.12. The smaller sorbed mass at the lower concentration of 100 ppb, landed the sensor within a chaotic attractor, also on the mid-branch but closer to the bifurcation point. In this case, the sorbed mass was marginally larger than the detection limit as indicated by the long time required for the sensor to clear the bottleneck in the vicinity of the cyclic-fold bifurcation [182].

6.3 Analog Dynamic Bifurcation Mass Sensor

We demonstrated a new sensing mechanism under Shilnikov bifurcation that exploits a quantitative change in the sensor state before and after depositing added mess via tapping mode oscillations. A polymeric material was deposited on the top surface of the sensor plate to represent added mass. A variation in the frequency as well as current amplitude were observed before and after depositing the added mass. The sensor was excited electrostatically and the response was measured optically as well as electrically using laser-Doppler vibrometer and lock-in amplifier,

respectively. We found the current increased six-fold due to adding a mass of 301 pg in vicinity of Shilnikov bifurcation. Also, the current increased three-fold due to adding a mass of 301 pg in vicinity of primary resonance. This method will be extend in the future to implement an analog gas sensor instigating in the vicinity of Shilnikov bifurcation region where the tapping oscillations will be employed to measure the added mass electrically. The polymeric sensing material which has high selectivity to a target gas will be employ to sorbed added mass. This method could be utilized to quantify the added precisely at specific frequency via current measurement.

6.4 Underwater Sensor

We demonstrate a sensing mechanism to detect mercury ions in deionized-water. The sensor was submerged completely in water with a pre-defined flow-rate of 1.5 µl/s. A polymeric sensing material (PAM) was utilized to sorb mercury in water. A solution of water and mercury acetate with a concentration of 100 ppm was released to the sensor utilizing the same pre-defined flow-rate. The senor was excited electrostatically, and the response measured electrically using lock-in amplifier. Higher excitation modes were employed to reduce the side-effects from chemical reactions as well as enhancing sensor sensitivity. A frequency-shift was observed while the sensor was subjected to mercury solution. Our sensors were able to measure a frequency shift of $\Delta f = 1.18$ MHz in sensor #1 and $\Delta f = 4.37$ MHz in sensor #2. More investigations required in the future to reach the ultimate target of this sensor to implement a binary bifurcation sensor operating in a regular tap water. The bifurcation sensing mechanism will allow us to detect a minute mercury ion concentration in water.

6.5 Contributions

6.5.1 Journal Papers

1. **M. S., Al-Ghamdi**, M. E., Khater, K. M. E. Stewart, A. Alneamy, E. M. Abdel-Rahman, and A. Penlidis. "Dynamic bifurcation MEMS gas sensors", Submitted to Journal of Micromechanics and Microengineering on Aug. 14^{th}, 2018.

2. **M. S., Al-Ghamdi**, M. E., Khater, and E. M. Abdel-Rahman. "Switching intermittency", Submitted to Applied Physics Letter (APL) on June 18^{th}, 2018.

3. A. Alneamy, M. Khater, **M. Alghamdi**, S. Park, G. Heppler, and E. M. Abdel-Rahman, "Dual actuation micromirrors" Journal of Micromechanics and Microengineering, 28(7), 075014, 2018.

4. **M.S. Al-Ghamdi**, A.M. Alneamy, S. Park, B. Li, M.E. Khater, E.M. Abdel-Rahman, G.R. Heppler, M. Yavuz," Nonlinear parameter identification of a resonant electrostatic MEMS actuator," Nonlinear Parameter Identification of a Resonant Electrostatic MEMS Actuator. Sensors, 17(5), 1121, 2017.

5. S. Park, **M. Al-Ghamdi**, M. Khater, and E. M. Abdel-Rahman, "A tunable MEMS magnetic sensor," Journal of Microelectromechanical Systems, 26: 255-263, 2017.

6. M. E. Khater, **M. Al-Ghamdi**, S. Park, K. M. E. Stewart, E. M. Abdel-Rahman, A. Penlidis, A. H. Nayfeh, A. K. S. Abdel-Aziz, and M. Basha, "Binary MEMS gas sensors," Journal of Micromechanics and Microengineering, vol. 24, pp. 065007/1-9, 2014.

6.5.2 Conference Papers

1. **M. S. Al-Ghamdi**, M. E. Khater, A. Alneamy, and E. M. Abdel-Rahman,"Sensitivity Analysis of Cantilever-Based Bifurcation MEMS Sensors," accepted, International Conference on Structural Nonlinear Dynamics and Diagnosis, Tangier, Morocco, June 2018.

2. R. Saritas, **M. Al-Ghamdi**, M. Taylan Das, and E. M. Abdel-Rahman, "A novel Method for Rapid Microfabrication," accepted, the 12^{th} International Conference of American Society of Mechanical Engineering (ASME) on Micro-and Nano Systems, Quebec city, Canada, Aug. 2018.

3. M. Gopanchuk, M. Arabi, N. Nelson-Fitzpatrick, **M.S. Al-Ghamdi**, E. M. Abdel-Rahman, and M. Yavuz, "Characterization of a non-interdigitated comb drive," accepted, the 12^{th} International Conference of American Society of Mechanical Engineering (ASME) on Micro-and Nano Systems, Quebec City, Canada, Aug. 2018.

4. **M. S. Al-Ghamdi**, M. Khater, K. M. E. Stewart, A. Alneamy, R. Almikhlafi, S. Park, E. M. Abdel-Rahman, and A. Penlidis, "Demonstration of Electrostatic MEMS Bifurcation Sensors," European Nonlinear Dynamics Conference, Budapest, Hungary, June, 2017, paper # 378.

5. A. M. Alneamy, **M. S. Al-Ghamdi**, M. Khater, B. Li, R. S. Almikhlafi, S. Park, E. M. Abdel-Rahman, and G. R. Heppler, "On the Dynamics of Dimpled Electrostatic MEMS Actuators," European Nonlinear Dynamics Conference, Budapest, Hungary, June, 2017, paper # 399.

6. S. Park, M. Khater, B. Li, **M. Al-Ghamdi**, A. Abdel Aziz, E. M. Abdel-Rahman, A. H. Nayfeh, and M. Yavuz, "Evidence of an Intermittency Route to Chaos in Electro-

static MEMS," International Congress of Theoretical and Applied Mechanics, Montreal, Canada, August 2016, paper # 130098.

7. S. Park,**M. Al-Ghamdi**, M. Khater, E. M. Abdel-Rahman, M. Yavuz, "Adjustable Sensitivity MEMS Magnetic Sensor," ASME International Design Engineering Technical Conferences, Buffalo, NY, August 2014, DETC2014-35004.

References

[1] V. Kaajakari, *Practical MEMS*. Small Gear Publishing, 2009.

[2] N. Yazdi, F. Ayazi, and K. Najafi, "Micromachined inertial sensors," *Proceedings of the IEEE*, vol. 86, no. 8, pp. 1640–1659, 1998.

[3] H. van Heeren and P. Salomon, "MEMS: recent developments, future directions," *Wolfson school of mechanical and manufacturing engineering, Loughborough University, Loughborough*, 2007.

[4] P. F. Partnership, "An introduction to MEMS (Micro-electromechanical systems)," 2002.

[5] K. Maenaka, "MEMS inertial sensors and their applications," in *5th international conference o networked sensing systems*, pp. 71–73, IEEE, June 2008.

[6] J. F. Rhoads, S. W. Shaw, and K. L. Turner, "Nonlinear dynamics and its dpplications in Micro-and Nanoresonators," *Journal of Dynamic Systems, Measurement, and Control*, vol. 132, no. 3, p. 034001, 2010.

[7] L. Robin and E. Mounier, "Inertial sensor market moves to combo sensors and sensor hubs," *MEMSTrends, ISSUE*, no. 16, 2013.

[8] G. A. Doty, D. Point, and G. Industries, "United states patent," 1987.

[9] B. W. Smith, J. D. Erickson, P. D. Jamison, P. A. Tyroller, D. Bergfried, B. Mattes, and W. Nitschke, "Air bag system for a motor vehicle," May 2 1995. US Patent 5,411,289.

[10] X. Jianbing, S. Meng, and Y. Weizheng, "A high sensitivity micromachined accelerometer with an enhanced inertial mass SOI MEMS process," in *Nano/Micro engineered and molecular systems (NEMS), 8th IEEE international conference*, pp. 336–339, IEEE, 2013.

[11] P. Salvini, "Direct tuning of inertia sensors of a navigation system using the neural network approach," *Inverse Problems in Science and Engineering*, vol. 18, no. 1, pp. 131–144, 2010.

[12] Y. Chen, J. Jiao, B. Xiong, L. Che, X. Li, and Y. Wang, "A novel tuning fork gyroscope with high Q-factors working at atmospheric pressure," *Microsystem Technologies*, vol. 11, no. 2-3, pp. 111–116, 2005.

[13] G. A. Aydemir and A. Saranlı, "Characterization and calibration of MEMS inertial sensors for sate and parameter estimation applications," *Measurement*, vol. 45, no. 5, pp. 1210–1225, 2012.

[14] Z. Ding, Z. Luo, A. Causo, I. Chen, K. Yue, S. Yeo, and K. Ling, "Inertia sensor-based guidance system for upperlimb posture correction," *Medical Engineering & Physics*, vol. 35, no. 2, pp. 269–276, 2013.

[15] G. M. Rebeiz, *RF MEMS: theory, design, and technology*. John Wiley & Sons, 2004.

[16] R. Bauer, A. Paterson, C. Clark, D. Uttamchandani, and W. Lubeigt, "Output characteristics of Q-switched solid-state lasers using intracavity MEMS micromirrors," *IEEE Journal of Selected Topics in Quantum Electronics*, vol. 21, no. 1, 2015.

[17] J. Van Beek and R. Puers, "A review of MEMS oscillators for frequency reference and timing applications," *Journal of Micromechanics and Microengineering*, vol. 22, no. 1, p. 013001, 2011.

[18] S. Ilyas, N. Jaber, and M. I. Younis, "A MEMS coupled resonator for frequency filtering in air," *Mechatronics*, 2018.

[19] S. B. Sassi, M. Khater, F. Najar, and E. Abdel-Rahman, "A square wave is the most efficient and reliable waveform for resonant actuation of micro switches," *Journal of Micromechanics and Microengineering*, vol. 28, no. 5, p. 055002, 2018.

[20] N. Jaber, S. Ilyas, O. Shekhah, M. Eddaoudi, and M. I. Younis, "Resonant gas sensor and switch operating in air with metal-organic frameworks coating," *Journal of Microelectromechanical Systems*, vol. 27, no. 2, pp. 156–163, 2018.

[21] Z. Yie, M. A. Zielke, C. B. Burgner, and K. L. Turner, "Comparison of parametric and linear mass detection in the presence of detection noise," *Journal of Micromechanics and Microengineering*, vol. 21, no. 2, p. 025027, 2011.

[22] M. E. Khater, M. Al-Ghamdi, S. Park, K. M. E. Stewart, E. M. Abdel-Rahman, A. Penlidis, A. H. Nayfeh, A. K. S. Abdel-Aziz, and M. Basha, "Binary MEMS gas sensors," *Journal of Micromechanics and Microengineering*, vol. 24, no. 6, p. 065007, 2014.

[23] S. Towfighian, G. Heppler, and E. Abdel-Rahman, "Analysis of a chaotic electrostatic Micro-oscillator," *Journal of Computational and Nonlinear Dynamics*, vol. 6, no. 1, p. 011001, 2011.

[24] A. Bouchaala, N. Jaber, O. Yassine, O. Shekhah, V. Chernikova, M. Eddaoudi, and M. I. Younis, "Nonlinear-based MEMS sensors and active switches for gas detection," *Sensors*, vol. 16, no. 6, p. 758, 2016.

[25] M. A. A. Hafiz, L. Kosuru, A. Ramini, K. N. Chappanda, and M. I. Younis, "In-plane MEMS shallow arch beam for mechanical memory," *Micromachines*, vol. 7, no. 10, p. 191, 2016.

[26] W.-M. Zhang, H. Yan, Z.-K. Peng, and G. Meng, "Electrostatic pull-in instability in MEMS/NEMS: A review," *Sensors and Actuators A: Physical*, vol. 214, pp. 187–218, 2014.

[27] R. K. Gupta and S. D. Senturia, "Pull-in time dynamics as a measure of absolute pressure," in *Micro Electro Mechanical Systems, 1997. MEMS'97, Proceedings, IEEE., Tenth Annual International Workshop on*, pp. 290–294, IEEE, 1997.

[28] S. Krylov and R. Maimon, "Pull-in dynamics of an elastic beam actuated by continuously distributed electrostatic force," *Journal of Vibration and Acoustics*, vol. 126, no. 3, pp. 332–342, 2004.

[29] G. N. Nielson and G. Barbastathis, "Dynamic pull-in of parallel-plate and torsional electrostatic MEMS actuators," *Journal of Microelectromechanical Systems*, vol. 15, no. 4, pp. 811–821, 2006.

[30] P. C. Chao, C. Chiu, and T.-H. Liu, "DC dynamic pull-in predictions for a generalized clamped–clamped micro-beam based on a continuous model and bifurcation analysis," *Journal of Micromechanics and Microengineering*, vol. 18, no. 11, p. 115008, 2008.

[31] Y. Fang and P. Li, "A new approach and model for accurate determination of the dynamic pull-in parameters of microbeams actuated by a step voltage," *Journal of Micromechanics and Microengineering*, vol. 23, no. 4, p. 045010, 2013.

[32] L. Shil'Nikov, "A case of the existence of a countable number of periodic motions," in *Sov. Math. Dokl.*, vol. 6, pp. 163–166, 1965.

[33] S. Wiggins, *Introduction to applied nonlinear dynamical systems and chaos*, vol. 2. Springer Science & Business Media, 2003.

[34] V. S. Afraimovich, S. V. Gonchenko, L. M. Lerman, A. L. Shilnikov, and D. V. Turaev, "Scientific heritage of lp shilnikov," *Regular and Chaotic Dynamics*, vol. 19, no. 4, pp. 435–460, 2014.

[35] A. H. Nayfeh and C.-M. Chin, "Nonlinear interactions in a parametrically excited system with widely spaced frequencies," *Nonlinear Dynamics*, vol. 7, no. 2, pp. 195–216, 1995.

[36] K. M. E. Alghamdi, Majed and E. Abdel-Rahman, "Quasi-static pull-in: an instability in electrostatic actuators," vol. Under review, 2018.

[37] A. H. Nayfeh and M. I. Younis, "Dynamics of MEMS resonators under superharmonic and subharmonic excitations," *Journal of Micromechanics and Microengineering*, vol. 15, no. 10, p. 1840, 2005.

[38] A. H. Nayfeh, M. I. Younis, and E. M. Abdel-Rahman, "Dynamic pull-in phenomenon in MEMS resonators," *Nonlinear Dynamics*, vol. 48, no. 1-2, pp. 153–163, 2007.

[39] M. Khater, K. Vummidi, E. Abdel-Rahman, A. Nayfeh, and S. Raman, "Dynamic actuation methods for capacitive MEMS shunt switches," *Journal of Micromechanics and Microengineering*, vol. 21, no. 3, p. 035009, 2011.

[40] S. Lenci and G. Rega, "Control of pull-in dynamics in a nonlinear thermoelastic electrically actuated microbeam," *Journal of Micromechanics and Microengineering*, vol. 16, no. 2, p. 390, 2006.

[41] M. I. Younis and F. Alsaleem, "Exploration of new concepts for mass detection in electrostatically-actuated structures based on nonlinear phenomena," *Journal of Computational and Nonlinear Dynamics*, vol. 4, no. 2, p. 021010, 2009.

[42] F. M. Alsaleem, M. I. Younis, and H. M. Ouakad, "On the nonlinear resonances and dynamic pull-in of electrostatically actuated resonators," *Journal of Micromechanics and Microengineering*, vol. 19, no. 4, p. 045013, 2009.

[43] F. Najar, A. H. Nayfeh, E. M. Abdel-Rahman, S. Choura, and S. El-Borgi, "Dynamics and global stability of beam-based electrostatic microactuators," *Journal of Vibration and Control*, vol. 16, no. 5, pp. 721–748, 2010.

[44] F. M. Alsaleem, M. I. Younis, and L. Ruzziconi, "An experimental and theoretical investigation of dynamic pull-in in MEMS resonators actuated electrostatically," *Journal of Microelectromechanical Systems*, vol. 19, no. 4, pp. 794–806, 2010.

[45] F. Najar, A. Nayfeh, E. Abdel-Rahman, S. Choura, and S. El-Borgi, "Nonlinear analysis of MEMS electrostatic microactuators: primary and secondary resonances of the first mode," *Journal of Vibration and Control*, vol. 16, no. 9, pp. 1321–1349, 2010.

[46] A. H. Nayfeh and D. T. Mook, *Nonlinear oscillations*. John Wiley & Sons, 2008.

[47] D. Ruelle and F. Takens, "On the nature of turbulence," *Communications in mathematical physics*, vol. 20, no. 3, pp. 167–192, 1971.

[48] R. M. May and G. F. Oster, "Bifurcations and dynamic complexity in simple ecological models," *The American Naturalist*, vol. 110, no. 974, pp. 573–599, 1976.

[49] M. J. Feigenbaum, "The onset spectrum of turbulence," *Physics Letters A*, vol. 74, no. 6, pp. 375–378, 1979.

[50] M. J. Feigenbaum, "The transition to aperiodic behavior in turbulent systems," *Communications in Mathematical Physics*, vol. 77, no. 1, pp. 65–86, 1980.

[51] R. H. Simoyi, A. Wolf, and H. L. Swinney, "One-dimensional dynamics in a multicomponent chemical reaction," *Physical Review Letters*, vol. 49, no. 4, p. 245, 1982.

[52] T. Klinker, W. Meyer-Ilse, and W. Lauterborn, "Period doubling and chaotic behavior in a driven toda oscillator," *Physics Letters A*, vol. 101, no. 8, pp. 371–375, 1984.

[53] E. Freire, A. Rodriguez-Luis, E. Gamero, and E. Ponce, "A case study for homoclinic chaos in an autonomous electronic circuit: A trip from takens-bogdanov to hopf-šil'nikov," *Physica D: Nonlinear Phenomena*, vol. 62, no. 1-4, pp. 230–253, 1993.

[54] H. Herzel, P. Plath, and P. Svensson, "Experimental evidence of homoclinic chaos and type-ii intermittency during the oxidation of methanol," *Physica D: Nonlinear Phenomena*, vol. 48, no. 2-3, pp. 340–352, 1991.

[55] M. J. Hauser and L. F. Olsen, "Mixed-mode oscillations and homoclinic chaos in an enzyme reaction," *Journal of the Chemical Society, Faraday Transactions*, vol. 92, no. 16, pp. 2857–2863, 1996.

[56] A. Pisarchik and R. Jaimes-Reátegui, "Homoclinic orbits in a piecewise linear rössler-like circuit," in *Journal of Physics: conference series*, vol. 23, p. 122, IOP Publishing, 2005.

[57] D. Parthimos, D. H. Edwards, and T. M. Griffith, "Shilnikov homoclinic chaos is intimately related to type-iii intermittency in isolated rabbit arteries: role of nitric oxide," *Physical Review E*, vol. 67, no. 5, p. 051922, 2003.

[58] P. Gaspard, "Local birth of homoclinic chaos," *Physica D: Nonlinear Phenomena*, vol. 62, no. 1-4, pp. 94–122, 1993.

[59] M. Basso, L. Giarre, M. Dahleh, and I. Mezic, "Numerical analysis of complex dynamics in atomic force microscopes," in *Control applications, 1998. proceedings of the 1998 IEEE international conference on*, vol. 2, pp. 1026–1030, IEEE, 1998.

[60] M. Ashhab, M. V. Salapaka, M. Dahleh, and I. Mezić, "Dynamical analysis and control of microcantilevers," *Automatica*, vol. 35, no. 10, pp. 1663–1670, 1999.

[61] M. Ashhab, M. Salapaka, M. Dahleh, and I. Mezić, "Melnikov-based dynamical analysis of microcantilevers in scanning probe microscopy," *Nonlinear Dynamics*, vol. 20, no. 3, pp. 197–220, 1999.

[62] S. Liu, A. Davidson, and Q. Lin, "Simulating nonlinear dynamics and chaos in a mems cantilever using poincare mapping," in *Transducers, Solid-state sensors, actuators and microsystems, 12th international conference on, 2003*, vol. 2, pp. 1092–1095, IEEE, 2003.

[63] A. C. J. Luo and F.-Y. Wang, "Nonlinear dynamics of a micro-electro-mechanical system with time-varying capacitors," *Journal of Vibration and Acoustics*, vol. 126, pp. 77–83, 2004.

[64] F. Jamitzky, M. Stark, W. Bunk, W. Heckl, and R. Stark, "Chaos in dynamic atomic force microscopy," *Nanotechnology*, vol. 17, no. 7, p. S213, 2006.

[65] S. K. De and N. Aluru, "Complex nonlinear oscillations in electrostatically actuated microstructures," *Journal of Microelectromechanical Systems*, vol. 15, no. 2, pp. 355–369, 2006.

[66] S. Hu and A. Raman, "Chaos in atomic force microscopy," *Physical Review Letters*, vol. 96, no. 3, p. 036107, 2006.

[67] T. Carmon, M. Cross, and K. J. Vahala, "Chaotic quivering of micron-scaled on-chip resonators excited by centrifugal optical pressure," *Physical Review Letters*, vol. 98, no. 16, p. 167203, 2007.

[68] Y. C. Wang, S. G. Adams, J. S. Thorp, N. C. MacDonald, P. Hartwell, and F. Bertsch, "Chaos in MEMS, parameter estimation and its potential application," *IEEE Transactions on Circuits and Systems I: fundamental theory and applications*, vol. 45, no. 10, pp. 1013–1020, 1998.

[69] J. Bienstman, R. Puers, and J. Vandewalle, "Periodic and chaotic behaviour of the autonomous impact resonator," in *Micro Electro Mechanical Systems, 1998. MEMS 98. proceedings., the eleventh annual international workshop on*, pp. 562–567, IEEE, 1998.

[70] B. E. DeMartini, H. E. Butterfield, J. Moehlis, and K. L. Turner, "Chaos for a microelectromechanical oscillator governed by the nonlinear mathieu equation," *Journal of Microelectromechanical Systems*, vol. 16, no. 6, pp. 1314–1323, 2007.

[71] K. M. E. Alghamdi, Majed and E. Abdel-Rahman, "Switching intermittency," *Applied physics letters*, vol. Under review, 2018.

[72] B. Ilic, Y. Yang, and H. Craighead, "Virus detection using nanoelectromechanical devices," *Applied Physics Letters*, vol. 85, no. 13, pp. 2604–2606, 2004.

[73] A. Zribi, A. Knobloch, W.-C. Tian, and S. Goodwin, "Micromachined resonant multiple gas sensor," *Sensors and Actuators A: Physical*, vol. 122, no. 1, pp. 31–38, 2005.

[74] K. Park, N. Kim, D. T. Morisette, N. Aluru, and R. Bashir, "Resonant MEMS mass sensors for measurement of microdroplet evaporation," *Microelectromechanical Systems*, vol. 21, no. 3, pp. 702–711, 2012.

[75] J. H. Pikul, P. Graf, S. Mishra, K. Barton, Y.-K. Kim, J. A. Rogers, A. Alleyne, P. M. Ferreira, and W. P. King, "High precision electrohydrodynamic printing of polymer onto microcantilever sensors," *IEEE Sensors Journal*, vol. 11, no. 10, pp. 2246–2253, 2011.

[76] J. Tamayo, P. M. Kosaka, J. J. Ruz, Á. San Paulo, and M. Calleja, "Biosensors based on nanomechanical systems," *Chemical Society Reviews*, vol. 42, no. 3, pp. 1287–1311, 2013.

[77] P. G. Datskos and I. Sauers, "Detection of 2-mercaptoethanol using gold-coated micromachined cantilevers," *Sensors and Actuators B: Chemical*, vol. 61, no. 1, pp. 75–82, 1999.

[78] S. Dohn, R. Sandberg, W. Svendsen, and A. Boisen, "Enhanced functionality of cantilever based mass sensors using higher modes and functionalized particles," in *Transducers, The 13th IEEE international conference*, vol. 1, pp. 636–639, IEEE, 2005.

[79] N. Lobontiu, I. Lupea, R. Ilic, and H. G. Craighead, "Modeling, design, and characterization of multisegment cantilevers for resonant mass detection," *Journal of Applied Physics*, vol. 103, no. 6, p. 064306, 2008.

[80] H. Xie, J. Vitard, S. Haliyo, and S. Régnier, "Enhanced sensitivity of mass detection using the first torsional mode of microcantilevers," in *Mechatronics and Automation, international conference*, pp. 39–44, IEEE, 2008.

[81] S. Dohn, O. Hansen, and A. Boisen, "Cantilever based mass sensor with hard contact readout," *Applied Physics Letters*, vol. 88, no. 26, p. 264104, 2006.

[82] W.-T. S. Chen, K. M. Stewart, C. K. Yang, R. R. Mansour, J. Carroll, and A. Penlidis, "Wearable RF sensor array implementing coupling-matrix readout extraction technique," *IEEE Transactions on Microwave Theory and Techniques*, vol. 63, no. 12, pp. 4157–4168, 2015.

[83] W. Chen, K. Stewart, R. Mansour, and A. Penlidis, "Novel undercoupled radio-frequency (RF) resonant sensor for gaseous ethanol and interferents detection," *Sensors and Actuators A: Physical*, vol. 230, pp. 63–73, 2015.

[84] H. Jensenius, J. Thaysen, A. A. Rasmussen, L. H. Veje, O. Hansen, and A. Boisen, "A microcantilever-based alcohol vapor sensor-application and response model," *Applied Physics Letters*, vol. 76, no. 18, pp. 2615–2617, 2000.

[85] J. H. Seo and O. Brand, "Self-magnetic excitation for in-plane mode resonant microsensor," in *19th IEEE international conference on micro electro mechanical systems*, pp. 74–77, IEEE, 2006.

[86] W. Zhu, J. S. Park, J. L. Sessler, and A. Gaitas, "A colorimetric receptor combined with a microcantilever sensor for explosive vapor detection," *Applied Physics Letters*, vol. 98, no. 12, p. 123501, 2011.

[87] T. Thundat, P. Oden, and R. Warmack, "Microcantilever sensors," *Microscale Thermophysical Engineering*, vol. 1, no. 3, pp. 185–199, 1997.

[88] D. Lange, C. Hagleitner, A. Hierlemann, O. Brand, and H. Baltes, "Complementary metal oxide semiconductor cantilever arrays on a single chip: Mass-sensitive detection of volatile organic compounds," *Analytical Chemistry*, vol. 74, no. 13, pp. 3084–3095, 2002.

[89] U. Sampath, S. M. Heinrich, F. Josse, F. Lochon, I. Dufour, and D. Rebiere, "Study of viscoelastic effect on the frequency shift of microcantilever chemical sensors," *IEEE transactions on ultrasonics, ferroelectrics, and frequency control*, vol. 53, no. 11, pp. 2166–2173, 2006.

[90] I. Dufour, F. Josse, S. M. Heinrich, C. Lucat, C. Ayela, F. Ménil, and O. Brand, "Unconventional uses of microcantilevers as chemical sensors in gas and liquid media," *Sensors and Actuators B: Chemical*, vol. 170, pp. 115–121, 2012.

[91] W. Zhang and K. L. Turner, "Application of parametric resonance amplification in a single-crystal silicon micro-oscillator based mass sensor," *Sensors and Actuators A: Physical*, vol. 122, no. 1, pp. 23–30, 2005.

[92] P. S. Waggoner and H. G. Craighead, "Micro-And Nanomechanical Sensors For Environmental, Chemical, And Biological Detection," *Lab On a Chip*, vol. 7, no. 10, pp. 1238–1255, 2007.

[93] L. Sharos, A. Raman, S. Crittenden, and R. Reifenberger, "Enhanced mass sensing using torsional and lateral resonances in microcantilevers," *Applied Physics Letters*, vol. 84, no. 23, pp. 4638–4640, 2004.

[94] I. Dufour, S. M. Heinrich, and F. Josse, "Strong-axis bending mode vibrations for resonant microcantilever (bio) chemical sensors in gas or liquid phase," in *Frequency control symposium and exposition, 2004. proceedings of the 2004 IEEE international*, pp. 193–199, IEEE, 2004.

[95] H. Debéda, R. Lakhmi, C. Lucat, and I. Dufour, "Use of the longitudinal mode of screen-printed piezoelectric cantilevers coated with peut for toluene detection: Comparison with silicon cantilevers," *Sensors and Actuators B: Chemical*, vol. 187, pp. 198–203, 2013.

[96] A. M. Bouchaala and M. I. Younis, "A model of electrostatically actuated mems and carbon nanotubes resonators for biological mass detection," in *Design and Modeling of Mechanical Systems-II*, pp. 501–512, Springer, 2015.

[97] A. Bouchaala, A. H. Nayfeh, and M. I. Younis, "Frequency shifts of micro and nano cantilever beam resonators due to added masses," *Journal of Dynamic Systems, Measurement, and Control*, vol. 138, no. 9, p. 091002, 2016.

[98] A. Bouchaala, A. H. Nayfeh, and M. I. Younis, "Analytical study of the frequency shifts of micro and nano clamped–clamped beam resonators due to an added mass," *Meccanica*, pp. 1–16, 2016.

[99] J. F. Rhoads, N. J. Miller, S. W. Shaw, and B. F. Feeny, "Mechanical domain parametric amplification," *Journal of Vibration and Acoustics*, vol. 130, no. 6, p. 061006, 2008.

[100] E. M. Abdel-Rahman, M. E. Khater, and A. H. Nayfeh, "Methods and systems for detection using threshold-type electrostatic sensors," June 1 2010. US Patent App. 12/791,293.

[101] L. L. Li, E. L. Holthoff, L. A. Shaw, C. B. Burgner, and K. L. Turner, "Noise squeezing controlled parametric bifurcation tracking of mip-coated microbeam mems sensor for tnt explosive gas sensing," *Journal of Microelectromechanical Systems*, vol. 23, no. 5, pp. 1228–1236, 2014.

[102] S. Azizi, A. R. Kivi, and J. Marzbanrad, "Mass detection based on pure parametric excitation of a micro beam actuated by piezoelectric layers," *Microsystem Technologies*, pp. 1–8, 2016.

[103] R. Harne and K. Wang, "A bifurcation-based coupled linear-bistable system for microscale mass sensing," *Journal of Sound and Vibration*, vol. 333, no. 8, pp. 2241–2252, 2014.

[104] V. Kumar, Y. Yang, J. W. Boley, G. T.-C. Chiu, and J. F. Rhoads, "Modeling, analysis, and experimental validation of a bifurcation-based microsensor," *Journal of Microelectromechanical Systems*, vol. 21, no. 3, pp. 549–558, 2012.

[105] V.-N. Nguyen, S. Baguet, C.-H. Lamarque, and R. Dufour, "Bifurcation-based micro-/nanoelectromechanical mass detection," *Nonlinear Dynamics*, vol. 79, no. 1, pp. 647–662, 2015.

[106] M. E. Khater, E. M. Abdel-Rahman, and A. H. Nayfeh, "A mass sensing technique for electrostatically-actuated MEMS," in *ASME 2009 international design engineering technical conferences and computers and information in engineering conference*, pp. 655–661, American Society of Mechanical Engineers, 2009.

[107] M. Alghamdi, "Inertial MEMS sensors," Master's thesis, University of Waterloo, 2015.

[108] I. Dufour, E. Lemaire, B. Caillard, H. Debéda, C. Lucat, S. M. Heinrich, F. Josse, and O. Brand, "Effect of hydrodynamic force on microcantilever vibrations: Applications to liquid-phase chemical sensing," *Sensors and Actuators B: Chemical*, vol. 192, pp. 664–672, 2014.

[109] M. A. Rahman, M. Nawi, A. Manaf, and M. Arshad, "Microfluidic-based capacitive sensor for underwater acoustic application," in *Sensing technology (ICST), 2013 seventh international conference on*, pp. 472–476, IEEE, 2013.

[110] L. Zhang, V. Masek, and N. Sanatdoost, "Design of cost-effective reliable MEMS gyroscopes for underwater/under-ice applications," in *2014 Oceans-St. John's*, pp. 1–5, IEEE, 2014.

[111] R. Zhang, W. Zhang, C. He, J. Song, L. Mu, J. Cui, Y. Zhang, and C. Xue, "Design of capacitive micromachined ultrasonic transducer (cmut) linear array for underwater imaging," *Sensor Review*, vol. 36, no. 1, pp. 77–85, 2016.

[112] S. S. Verbridge, L. M. Bellan, J. M. Parpia, and H. Craighead, "Optically driven resonance of nanoscale flexural oscillators in liquid," *Nano Letters*, vol. 6, no. 9, pp. 2109–2114, 2006.

[113] A. Kim, C. R. Powell, and B. Ziaie, "An universal packaging technique for low-drift implantable pressure sensors," *Biomedical Microdevices*, vol. 18, no. 2, pp. 1–8, 2016.

[114] O. Zielinski, J. A. Busch, A. D. Cembella, K. L. Daly, J. Engelbrektsson, A. K. Hannides, and H. Schmidt, "Detecting marine hazardous substances and organisms: Sensors for pollutants, toxins, and pathogens," *Marine science faculty publications*, 2009.

[115] M. R. Arshad, "Recent advancement in sensor technology for underwater applications," *Indian J. Mar. Sci*, vol. 38, no. 3, pp. 267–273, 2009.

[116] L. Beardslee, F. Josse, S. M. Heinrich, I. Dufour, and O. Brand, "Geometrical considerations for the design of liquid-phase biochemical sensors using a cantilever's fundamental in-plane mode," *Sensors and Actuators B: Chemical*, vol. 164, no. 1, pp. 7–14, 2012.

[117] J. E. Sader, "Frequency response of cantilever beams immersed in viscous fluids with applications to the atomic force microscope," *Journal of Applied Physics*, vol. 84, no. 1, pp. 64–76, 1998.

[118] D. Sameoto, T. Hubbard, and M. Kujath, "Operation of electrothermal and electrostatic MUMPs microactuators underwater," *Journal of Micromechanics and Microengineering*, vol. 14, no. 10, p. 1359, 2004.

[119] T. L. Sounart, T. A. Michalske, and K. R. Zavadil, "Frequency-Dependent Electrostatic Actuation In Microfluidic MEMS," *Journal of Microelectromechanical Systems*, vol. 14, no. 1, pp. 125–133, 2005.

[120] C. Vančura, I. Dufour, S. M. Heinrich, F. Josse, and A. Hierlemann, "Analysis of resonating microcantilevers operating in a viscous liquid environment," *Sensors and Actuators A: Physical*, vol. 141, no. 1, pp. 43–51, 2008.

[121] T. P. Burg and S. R. Manalis, "Suspended microchannel resonators for biomolecular detection," *Applied Physics Letters*, vol. 83, no. 13, pp. 2698–2700, 2003.

[122] J. W. Zhou, H.-Y. Chan, T. K. To, K. W. Lai, and W. J. Li, "Polymer MEMS actuators for underwater micromanipulation," *IEEE/ASME Transactions on Mechatronics*, vol. 9, no. 2, pp. 334–342, 2004.

[123] L. A. Bottomley, M. A. Poggi, and S. Shen, "Impact of nano-and mesoscale particles on the performance of microcantilever-based sensors," *Analytical Chemistry*, vol. 76, no. 19, pp. 5685–5689, 2004.

[124] T. Braun, V. Barwich, M. K. Ghatkesar, A. H. Bredekamp, C. Gerber, M. Hegner, and H. P. Lang, "Micromechanical mass sensors for biomolecular detection in a physiological environment," *Physical Review E*, vol. 72, no. 3, p. 031907, 2005.

[125] N. Scuor, P. Gallina, O. Sbaizero, H. Panchawagh, and R. Mahajan, "Dynamic characterization of MEMS cantilevers in liquid environment using a low-Cost optical system," *Measurement Science and Technology*, vol. 17, no. 1, p. 173, 2005.

[126] P. Rasmussen, J. Thaysen, O. Hansen, S. Eriksen, and A. Boisen, "Optimised cantilever biosensor with piezoresistive read-out," *Ultramicroscopy*, vol. 97, no. 1, pp. 371–376, 2003.

[127] C. Vančura, J. Lichtenberg, A. Hierlemann, and F. Josse, "Characterization of magnetically actuated resonant cantilevers in viscous fluids," *Applied Physics Letters*, vol. 87, no. 16, p. 162510, 2005.

[128] A. Barlian, R. Narain, J. Li, C. Quance, A. Ho, V. Mukundan, and B. Pruitt, "Piezoresistive MEMS underwater shear stress sensors," in *19th IEEE international conference on micro electro mechanical systems*, pp. 626–629, IEEE, 2006.

[129] C. Vancura, Y. Li, J. Lichtenberg, K.-U. Kirstein, A. Hierlemann, and F. Josse, "Liquid-phase chemical and biochemical detection using fully integrated magnetically actuated complementary metal oxide semiconductor resonant cantilever sensor systems," *Analytical Chemistry*, vol. 79, no. 4, pp. 1646–1654, 2007.

[130] P. Selvaganapathy, Y.-s. L. Ki, P. Renaud, and C. H. Mastrangelo, "Bubble-free electrokinetic pumping," *Journal of Microelectromechanical Systems*, vol. 11, no. 5, pp. 448–453, 2002.

[131] S. S. Zumdahl, *Chemical Principles*. Houghton Mifflin, 1998.

[132] S. Basak, A. Raman, and S. V. Garimella, "Hydrodynamic loading of microcantilevers vibrating in viscous fluids," *Journal of Applied Physics*, vol. 99, no. 11, p. 114906, 2006.

[133] D. Ramos, J. Tamayo, J. Mertens, and M. Calleja, "Photothermal excitation of microcantilevers in liquids," *Journal of Applied Physics*, vol. 99, no. 12, p. 124904, 2006.

[134] L. A. Beardslee, A. M. Addous, S. Heinrich, F. Josse, I. Dufour, and O. Brand, "Thermal excitation and piezoresistive detection of cantilever in-plane resonance modes for sensing applications," *Journal of Microelectromechanical Systems*, vol. 19, no. 4, pp. 1015–1017, 2010.

[135] Y. Tao, X. Li, T. Xu, H. Yu, P. Xu, B. Xiong, and C. Wei, "Resonant cantilever sensors operated in a high-q in-plane mode for real-time bio/chemical detection in liquids," *Sensors and Actuators B: Chemical*, vol. 157, no. 2, pp. 606–614, 2011.

[136] G. Pfusterschmied, M. Kucera, V. Ruiz-Díez, A. Bittner, J. L. Sánchez-Rojas, and U. Schmid, "Multi roof tile-shaped vibration modes in mems cantilever sensors for liquid monitoring purposes," in *2015 28th IEEE international conference on micro electro mechanical systems (MEMS)*, pp. 718–721, IEEE, 2015.

[137] G. Pfusterschmied, M. Kucera, W. Steindl, T. Manzaneque, V. R. Díez, A. Bittner, M. Schneider, J. Sánchez-Rojas, and U. Schmid, "Roof tile-shaped modes in quasi free–free supported piezoelectric microplate resonators in high viscous fluids," *Sensors and Actuators B: Chemical*, 2016.

[138] I. Dufour, S. M. Heinrich, and F. Josse, "Theoretical analysis of strong-axis bending mode vibrations for resonant microcantilever (bio) chemical sensors in gas or liquid phase," *Journal of Microelectromechanical Systems*, vol. 16, no. 1, pp. 44–49, 2007.

[139] G. Jabbari, R. Shabani, and G. Rezazadeh, "Frequency response of an electrostatically actuated micro resonator in contact with incompressible fluid," *Microsystem Technologies*, pp. 1–11, 2016.

[140] T. Naik, E. K. Longmire, and S. C. Mantell, "Dynamic response of a cantilever in liquid near a solid wall," *Sensors and Actuators A: Physical*, vol. 102, no. 3, pp. 240–254, 2003.

[141] M. Heinisch, T. Voglhuber-Brunnmaier, E. K. Reichel, I. Dufour, and B. Jakoby, "Reduced order models for resonant viscosity and mass density sensors," *Sensors and Actuators A: Physical*, vol. 220, pp. 76–84, 2014.

[142] M. Youssry, N. Belmiloud, B. Caillard, C. Ayela, C. Pellet, and I. Dufour, "A straightforward determination of fluid viscosity and density using microcantilevers: From experimental data to analytical expressions," *Sensors and Actuators A: Physical*, vol. 172, no. 1, pp. 40–46, 2011.

[143] D. Jin, X. Li, Z. Zhang, H. Bao, Y. Wang, J. Liu, and H. Yu, "Intergrated resonant cantilever sensors with 2nd torsion-mode for fg-level resoluble biomedical detection," in *Micro Electro Mechanical Systems, IEEE 20th international conference*, pp. 107–110, IEEE, 2007.

[144] F. Lucklum, E. K. Reichel, and B. Jakoby, "Miniature density–viscosity measurement cell utilizing electrodynamic-acoustic resonator sensors," *Sensors and Actuators A: Physical*, vol. 172, no. 1, pp. 75–81, 2011.

[145] R. Shabani, H. Hatami, F. Golzar, S. Tariverdilo, and G. Rezazadeh, "Coupled vibration of a cantilever micro-beam submerged in a bounded incompressible fluid domain," *Acta Mechanica*, vol. 224, no. 4, pp. 841–850, 2013.

[146] M. Heinisch, T. Voglhuber-Brunnmaier, E. K. Reichel, I. Dufour, and B. Jakoby, "Reduced order models for resonant viscosity and mass density sensors," *Sensors and Actuators A: Physical*, vol. 220, pp. 76–84, 2014.

[147] M. Heinisch, T. Voglhuber-Brunnmaier, I. Dufour, and B. Jakoby, "Validity of describing resonant viscosity and mass density sensors by linear 2nd order resonators," *Procedia Engineering*, vol. 87, pp. 644–647, 2014.

[148] S. Azma, G. Rezazadeh, R. Shabani, and E. Alizadeh-Haghighi, "Viscous fluid damping in a laterally oscillating finger of a comb-drive micro-resonator based on micro-polar fluid theory," *Acta Mechanica Sinica*, pp. 1–9, 2016.

[149] M. A. Zidan, J. Kosel, and K. N. Salama, "Low pull-in voltage electrostatic MEMS switch using liquid dielectric," in *2014 IEEE 57th international midwest symposium on circuits and systems (MWSCAS)*, pp. 169–172, IEEE, 2014.

[150] H.-T. Su, T.-L. Tang, and W. Fang, "A novel underwater actuator driven by magnetization repulsion/attraction," in *Micro Electro Mechanical Systems, IEEE 22nd international conference on*, pp. 1051–1054, IEEE, 2009.

[151] S. M. Heinrich, M. J. Wenzel, F. Josse, and I. Dufour, "An analytical model for transient deformation of viscoelastically coated beams: Applications to static-mode microcantilever chemical sensors," *Journal of Applied Physics*, vol. 105, no. 12, p. 124903, 2009.

[152] T. P. Burg, M. Godin, S. M. Knudsen, W. Shen, G. Carlson, J. S. Foster, K. Babcock, and S. R. Manalis, "Weighing of biomolecules, single cells and single nanoparticles in fluid," *Nature*, vol. 446, no. 7139, pp. 1066–1069, 2007.

[153] S. Senturia, *Microsystem Design*. Springer US, 2013.

[154] N. Sharafkhani, R. Shabani, S. Tariverdilo, and G. Rezazadeh, "Stability analysis and transient response of electrostatically actuated microbeam interacting with bounded compressible fluids," *Journal of Applied Mechanics*, vol. 80, no. 1, p. 011024, 2013.

[155] D. Koester, A. Cowen, R. Mahadevan, M. Stonefield, and B. Hardy, "PolyMUMPs design handbook," *MEMSCAP Inc*, 2003.

[156] Polytec Inc., "OFV-5000 Vibrometer Controller User Manual," www.polytec.com.

[157] O. E. Rössler, "Chaotic behavior in simple reaction systems," *Zeitschrift für Naturforschung A*, vol. 31, no. 3-4, pp. 259–264, 1976.

[158] R. Schmitz, K. Graziani, and J. L. Hudson, "Experimental evidence of chaotic states in the belousov–zhabotinskii reaction," *The Journal of Chemical Physics*, vol. 67, no. 7, pp. 3040–3044, 1977.

[159] F. Argoul, A. Arneodo, and P. Richetti, "Experimental evidence for homoclinic chaos in the belousov-zhabotinskii reaction," *Physics Letters A*, vol. 120, no. 6, pp. 269–275, 1987.

[160] D. Barkley, "Slow manifolds and mixed-mode oscillations in the belousov–zhabotinskii reaction," *The Journal of Chemical Physics*, vol. 89, no. 9, pp. 5547–5559, 1988.

[161] D. Hennequin, F. de Tomasi, B. Zambon, and E. Arimondo, "Homoclinic orbits and cycles in the instabilities of a laser with a saturable absorber," *Physical Review A*, vol. 37, no. 6, p. 2243, 1988.

[162] T. Braun, J. A. Lisboa, and J. A. Gallas, "Evidence of homoclinic chaos in the plasma of a glow discharge," *Physical Review Letters*, vol. 68, no. 18, p. 2770, 1992.

[163] R. Herrero, F. Boixader, J. Farjas, F. Pi, G. Orriols, and J. Rosell, "Rössler chaos in opto-thermal bistable devices," *Optics Communications*, vol. 113, no. 1-3, pp. 324–334, 1994.

[164] E. A. Viktorov, D. R. Klemer, and M. A. Karim, "Shilnikov case of antiphase dynamics in a multimode laser," *Optics Communications*, vol. 113, no. 4–6, pp. 441–448, 1995.

[165] A. Pisarchik, R. Meucci, and F. Arecchi, "Discrete homoclinic orbits in a laser with feedback," *Physical Review E*, vol. 62, no. 6, p. 8823, 2000.

[166] F. Arecchi, R. Meucci, A. Di Garbo, and E. Allaria, "Homoclinic chaos in a laser: synchronization and its implications in biological systems," *Optics and Lasers in Engineering*, vol. 39, no. 3, pp. 293–304, 2003.

[167] S. Newhouse, D. Ruelle, and F. Takens, "Occurrence of strange axiom a attractors near quasi periodic flows on T^m, $m \geqq 3$," *Communications in Mathematical Physics*, vol. 64, no. 1, pp. 35–40, 1978.

[168] J.-P. Eckmann, "Roads to turbulence in dissipative dynamical systems," *Reviews of Modern Physics*, vol. 53, no. 4, p. 643, 1981.

[169] S. Martin, H. Leber, and W. Martienssen, "Oscillatory and chaotic states of the electrical conduction in barium sodium niobate crystals," *Physical review letters*, vol. 53, no. 4, p. 303, 1984.

[170] A. Cumming and P. S. Linsay, "Quasiperiodicity and chaos in a system with three competing frequencies," *Physical Review Letters*, vol. 60, no. 26, p. 2719, 1988.

[171] M. Gorman, L. A. Reith, and H. L. Swinney, "Modulation patterns, multiple frequencies, and other phenomena in circular couette flow," *Annals of the New York Academy of Sciences*, vol. 357, no. 1, pp. 10–21, 1980.

[172] R. Walden, P. Kolodner, A. Passner, and C. Surko, "Nonchaotic Rayleigh-Bénard convection with four and five incommensurate frequencies," *Physical review letters*, vol. 53, no. 3, p. 242, 1984.

[173] P. Drazin, *Nonlinear Systems*. Cambridge Texts in Applied Mathematics, Cambridge University Press, 1992.

[174] J. Thompson and H. Stewart, *Nonlinear Dynamics and Chaos*. Wiley, 2002.

[175] K. Stewart, N. M. McManus, E. Abdel-Rahman, and A. Penlidis, "Doped polyaniline for the detection of formaldehyde," *Journal of Macromolecular Science, Part A*, vol. 49, no. 1, pp. 1–6, 2012.

[176] J. Gere, *Mechanics of materials*. Cengage Learning, 2003.

[177] S. Krylov, "Lyapunov exponents as a criterion for the dynamic pull-in instability of electrostatically actuated microstructures," *International Journal of Non-Linear Mechanics*, vol. 42, no. 4, pp. 626–642, 2007.

[178] P. M. Osterberg and S. D. Senturia, "M-test: a test chip for mems material property measurement using electrostatically actuated test structures," *Journal of Microelectromechanical systems*, vol. 6, no. 2, pp. 107–118, 1997.

[179] S. Krylov, "Lyapunov exponents as a criterion for the dynamic pull-in instability of electrostatically actuated microstructures," *International Journal of Non-Linear Mechanics*, vol. 42, no. 4, pp. 626–642, 2007.

[180] L. Meirovitch, *Fundamentals of Vibration*. McGraw-Hill Education, 2003.

[181] A. Shabana, *Vibration Of Discrete And Continuous Systems*. Springer Science & Business Media, 2012.

[182] A. H. Nayfeh and B. Balachandran, *Applied Nonlinear Dynamics*. John Wiley & Sons, 2008.

[183] Veeco Inc., "Wyko-NT1100 Optical Profiling System Datasheet," www.veeco.com.

[184] N. Wilson, "The risk of fire or explosion due to static charges on textile clothing," *Journal of Electrostatics*, vol. 4, no. 1, pp. 67 – 84, 1977.

[185] H. Kahn, A. Avishai, R. Ballarini, and A. Heuer, "Surface oxide effects on failure of polysilicon mems after cyclic and monotonic loading," *Scripta Materialia*, vol. 59, no. 9, pp. 912–915, 2008.

[186] H. Kahn, C. Deeb, I. Chasiotis, and A. H. Heuer, "Anodic oxidation during mems processing of silicon and polysilicon: Native oxides can be thicker than you think," *Journal of Microelectromechanical Systems*, vol. 14, no. 5, pp. 914–923, 2005.

[187] C. Muhlstein, E. Stach, and R. Ritchie, "A reaction-layer mechanism for the delayed failure of micron-scale polycrystalline silicon structural films subjected to high-cycle fatigue loading," *Acta Materialia*, vol. 50, no. 14, pp. 3579–3595, 2002.

[188] J. Wibbeler, G. Pfeifer, and M. Hietschold, "Parasitic charging of dielectric surfaces in capacitive microelectromechanical systems (MEMS)," *Sensors and Actuators A: Physical*, vol. 71, no. 1, pp. 74–80, 1998.

[189] W. Merlijn van Spengen, "MEMS reliability from a failure mechanisms perspective," *Microelectronics Reliability*, vol. 43, no. 7, pp. 1049–1060, 2003.

[190] S. Park, M. Khater, D. Effa, E. Abdel-Rahman, and M. Yavuz, "Detection of cyclic-fold bifurcation in electrostatic mems transducers by motion-induced current," *Journal of Micromechanics and Microengineering*, vol. 27, no. 8, p. 085007, 2017.

[191] A. Cowen, G. Hames, D. Monk, S. Wilcenski, and B. Hardy, "SOIMUMPs design handbook," *MEMSCAP Inc*, 2011.

Appendices

Appendix A

Sensitivity Analysis of Bifurcation Sensor

The electrostatic force was expanded using Taylor series expansion accounting for quadratic and cubic nonlinearities. Using a Galerkin expansion for both the static and dynamic components and applying orthogonality conditions [180] to decouple the system to an ordinary-differential equation in terms of the generalize coordinate q_s and $u(t)$. The dynamic equation of motion can be written in terms of the generalized coordinate $u(t)$

$$\begin{aligned}\ddot{u} \quad &+\mu\, l\, \dot{u} + \Big(\tfrac{1}{12}h^2\, l\, E\, \Gamma_1 \psi_1 - \tfrac{3}{2}\, E\, \psi_1 q_s^2\, \Gamma_2 - C_2 V_{\rm dc}\psi_2\Big) u \\ &-\tfrac{3}{2}\big(E q_s\, \Gamma_2\, \psi_1 + C_3 V_{\rm dc}\psi_2\big) u^2 \\ &-\big(\tfrac{1}{2}E\, \Gamma_2\ \psi_1 + 2C_4 V_{\rm dc}\psi_2\big)\, u^3 = C_1\, \psi_2\, V_{ac} \\ &+2C_2\, \psi_2\, V_{ac}\, u + 3C_3\, \psi_2\, V_{ac}\, u^2 + 4C_4\, \psi_2\, V_{ac}\, u^3\end{aligned}$$

A small bookkeeping parameter, ε is utilized to scale the dynamic components of the response [46]. Expanding the electrostatic force term around the equilibrium position $w_s(x)$, ordering displacement at $O(\varepsilon)$, damping at $O(\varepsilon^2)$, forcing term at $O(\varepsilon^3)$, and dropping terms of

order $O(\varepsilon^4)$ and higher, the equation of motion reduces to

$$\begin{aligned}
&\ddot{u} + \mu\, l\, \dot{u} + \big(\tfrac{1}{12} h^2\, L\, E\psi_1\Gamma_1 - \tfrac{3}{2}\, E\, \psi_1 q_s^2 \Gamma_2 - \psi_2 V_{dc} C_2\big) u \\
&-\tfrac{3}{2}\big(E\psi_1 q_s \Gamma_2 + \psi_2 V_{dc} C_3\big) u^2 - \big(\tfrac{1}{2} E\, \psi_1\, \Gamma_2 + 2\psi_2 V_{dc} C_4\big) u^3 \\
&= \psi_2 V_{ac} C_1
\end{aligned}$$

where the parameters are defined as

$$\begin{aligned}
\Gamma_1 = &\quad \int_0^l \phi^{iv}(x)\, \phi(x) dx \\
\Gamma_2 = &\quad \int_0^l \phi(x)'^2 dx \int_0^l \phi(x)''\, \phi(x) dx \\
C_1 = &\quad \epsilon V_{dc} \int_0^l \tfrac{1}{(d-w_s)^2}\, \phi(x) dx \\
C_2 = &\quad 2\epsilon V_{dc}\, \int_0^l \tfrac{1}{(d-w_s)^3}\, \phi(x)^2 dx \\
C_3 = &\quad 3\epsilon V_{dc}\, \int_0^l \tfrac{1}{(d-w_s)^4}\, \phi(x)^3 dx \\
C_4 = &\quad 4\epsilon V_{dc}\, \int_0^l \tfrac{1}{(d-w_s)^5}\, \phi(x)^4 dx \\
C_i = &\quad \varepsilon V_{dc}\, \int_0^i \tfrac{\phi^i(x)}{(d-q_s\phi(x))^{i+1}} dx
\end{aligned}$$

where C_i $(i = 1, 2, 3, 4)$ is a general form of the electrostatic force coefficients.

Appendix B

Experimental Results of Bifurcation Dynamic Gas Sensor

All the repeated results of the bifurcation gas sensors subjected to 5 ppm, 1 ppm, 100 ppb, and 50 ppb ethanol concentrations were reported. All these repeated results used the same experimental procedure that interprets in section 3.4.6. The operating frequency was set at $f_\circ = -50$ Hz below cyclic fold-bifurcation point.

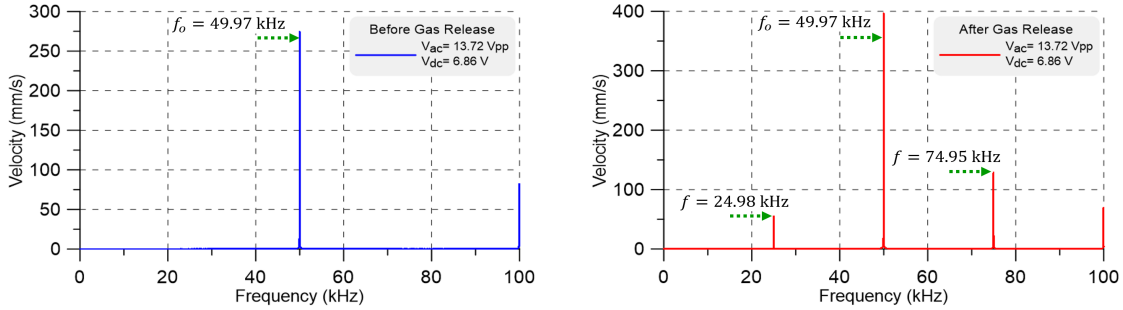

(a) Before (b) After

Figure B.1: The velocity FFT response before (a) and after (b) at excitation voltage $V_{\mathrm{dc}} = V_{\mathrm{ac}} = 6.86\,\mathrm{V}$

B.1 5 ppm Ethanol Vapor In Dry Nitrogen

2^{nd} **trial** After purging the test chamber with dry nitrogen for 15 minutes, a mixture of 5 ppm ethanol vapor in dry nitrogen was slowly released into the chamber. Detection (dynamic pull-in) occurred in a second from gas release, Fig. B.1. Fast detection indicates that the sorbed mass is well beyond the sensor threshold at this operating point ($f_\circ - 50\,\mathrm{Hz}$).

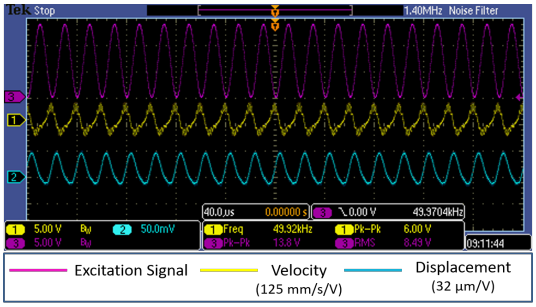

(a) Before

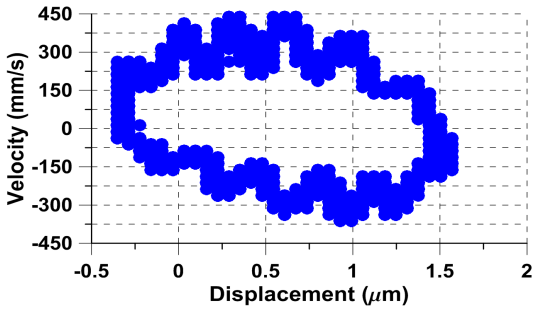

(b) Before

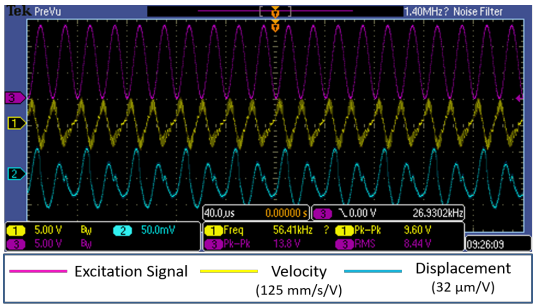

(c) After

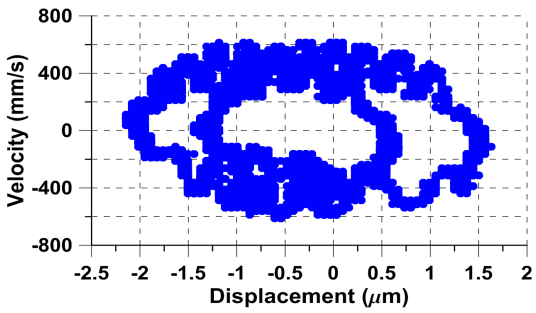

(d) After

Figure B.2: The time-histories (a and c) of the sensor velocity (yellow), displacement (blue), and excitation signal (magenta), and phase portraits (b and d) before and after gas release at excitation voltage $V_{\mathrm{dc}} = V_{\mathrm{ac}} = 6.86\,\mathrm{V}$

The velocity and displacement time histories were recorded using the oscilloscope before and after gas release as shown in Fig. B.2 (a) and (c). Period doubling bifurcation of order two was observed after detection occurred due to the sorbed mass as shown in Fig. B.2 (b) and (d).

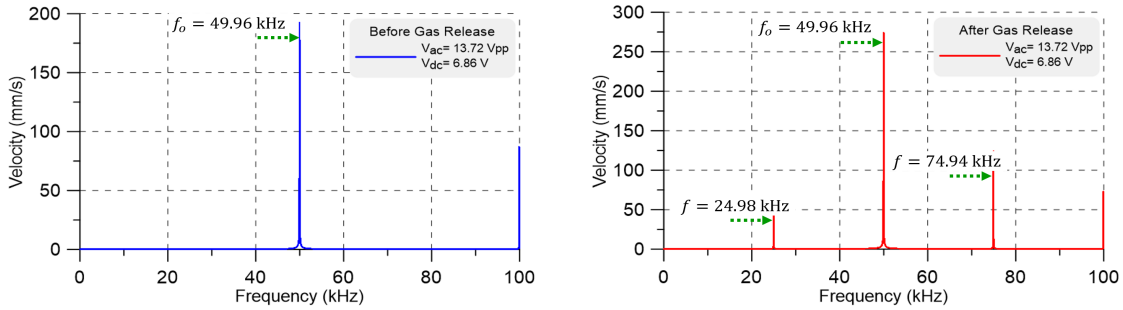

(a) Before (b) After

Figure B.3: The velocity FFT response before (a) and after (b) at excitation voltage $V_{\mathrm{dc}} = V_{\mathrm{ac}} = 6.86\,\mathrm{V}$

3^{nd} **trial** After purging the test chamber with dry nitrogen for 15 minutes, a mixture of 5 ppm ethanol vapor in dry nitrogen was slowly released into the chamber. Detection (dynamic pull-in) occurred in one second from gas release, Fig. B.3. Fast detection indicates that the sorbed mass is well beyond the sensor threshold at this operating point ($f_\circ - 50\,\mathrm{Hz}$).

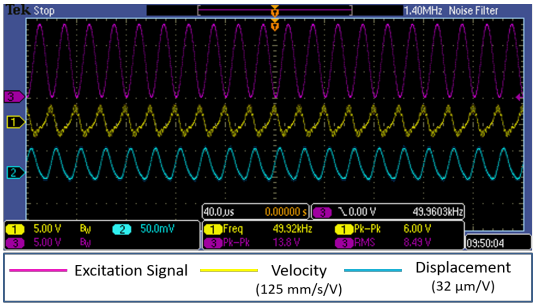

(a) Before

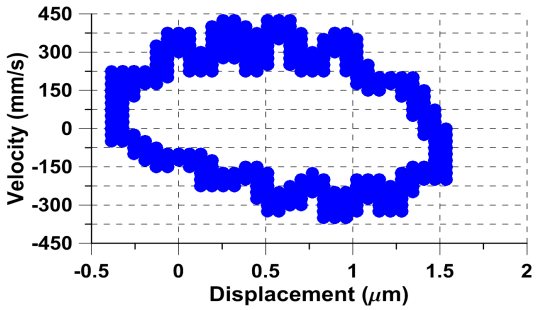

(b) Before

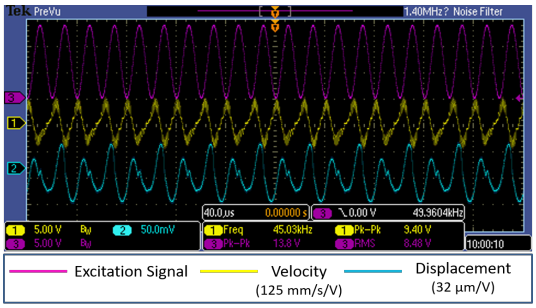

(c) After

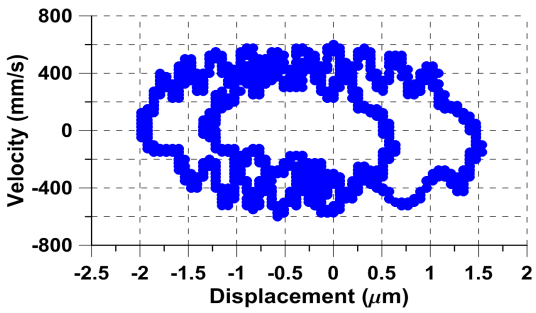

(d) After

Figure B.4: The time-histories (a and c) of the sensor velocity (yellow), displacement (blue), and excitation signal (magenta), and phase portraits (b and d) before and after gas release at excitation voltage $V_{\mathrm{dc}} = V_{\mathrm{ac}} = 6.86\,\mathrm{V}$

The velocity and displacement time histories were recorded using the oscilloscope before and after gas release as shown in Fig. B.4 (a) and (c). Period doubling bifurcation of order two was observed after detection occurred due to the sorbed mass as shown in Fig. B.4 (b) and (d).

B.2 1 ppm Ethanol Vapor In Dry Nitrogen

2^{nd} **trial** After purging the test chamber with dry nitrogen for 15 minutes, a mixture of 1 ppm ethanol vapor in dry nitrogen was slowly released into the chamber. Detection (dynamic pull-in) occurred in 45 seconds from gas release, Fig. B.5. The length of time required for detection indicates that the sorbed mass was small enough to marginally exceed the cyclic-fold bifurcation point. Therefore, 1 ppm ethanol is very close to the sensor detection threshold at this operating point.

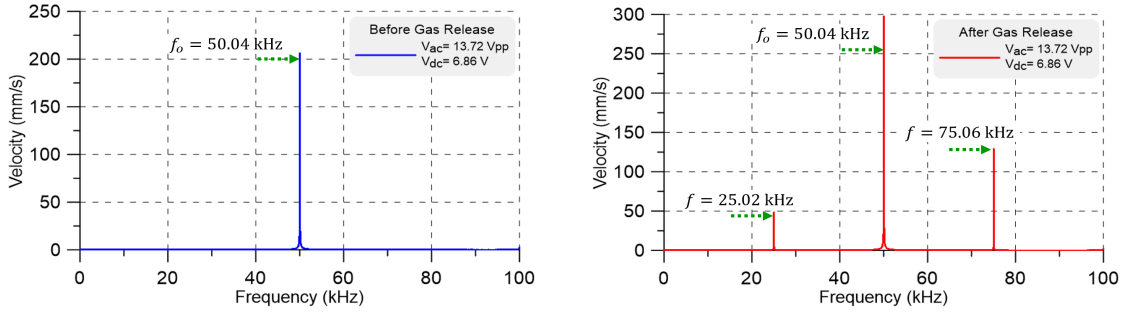

(a) Before (b) After

Figure B.5: The velocity FFT response before (a) and after (b) at excitation voltage $V_{\rm dc} = V_{\rm ac} = 6.86$ V

The velocity and displacement time histories were recorded using the oscilloscope before and after gas release as shown in Fig. B.6 (a) and (c). Period doubling bifurcation of order two was observed after detection occurred due to the sorbed mass as shown in Fig. B.6 (b) and (d).

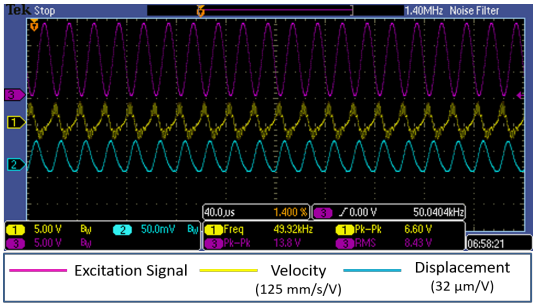

(a) Before

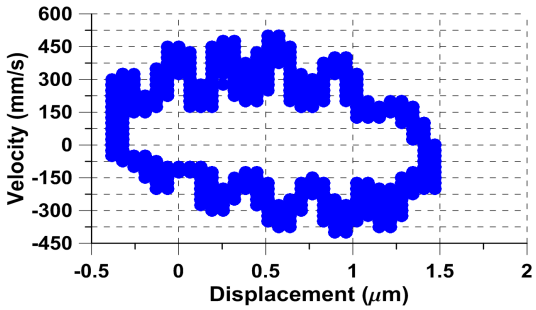

(b) Before

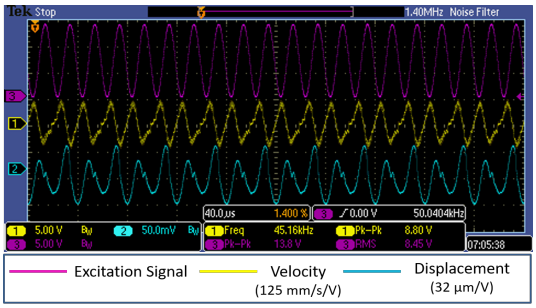

(c) After

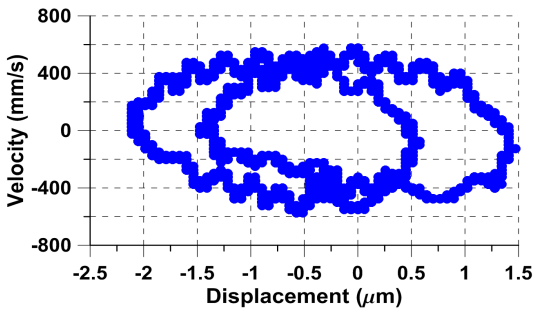

(d) After

Figure B.6: The time-histories (a and c) of the sensor velocity (yellow), displacement (blue), and excitation signal (magenta), and phase portraits (b and d) before and after gas release at excitation voltage $V_{\mathrm{dc}} = V_{\mathrm{ac}} = 6.86\,\mathrm{V}$

3^{nd} **trial** After purging the test chamber with dry nitrogen for 15 minutes, a mixture of 1 ppm ethanol vapor in dry nitrogen was slowly released into the chamber. Detection (dynamic pull-in) occurred in one minute and 48 seconds from gas release, Fig. B.7. The length of time required for detection indicates that the sorbed mass was small enough to marginally exceed the cyclic-fold bifurcation point. Therefore, 1 ppm ethanol is very close to the sensor detection threshold at this operating point.

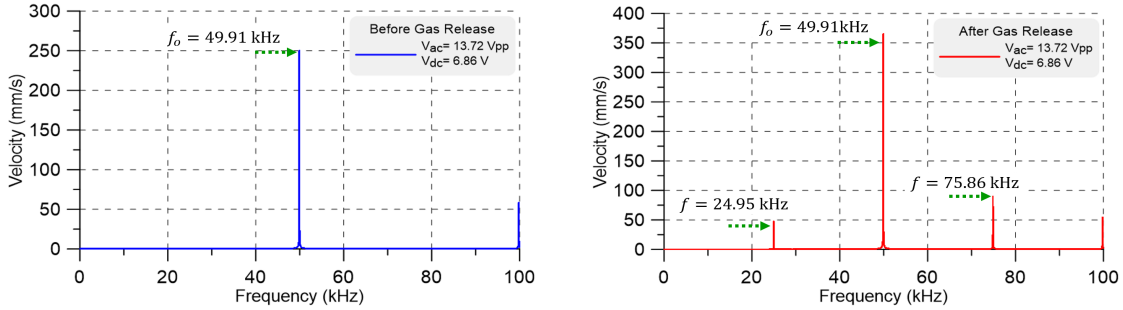

(a) Before (b) After

Figure B.7: The velocity FFT response before (a) and after (b) at excitation voltage $V_{\mathrm{dc}} = V_{\mathrm{ac}} = 6.86$ V

The velocity and displacement time histories were recorded using the oscilloscope before and after gas release as shown in Fig. B.8 (a) and (c). Period doubling bifurcation of order two was observed after detection occurred due to the sorbed mass as shown in Fig. B.8 (b) and (d).

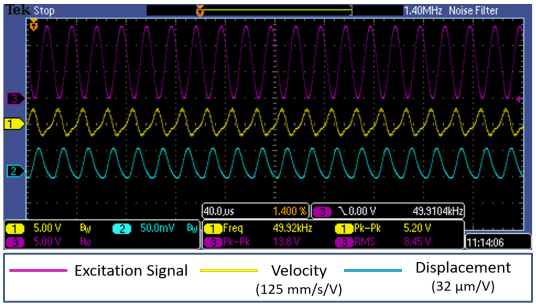

(a) Before

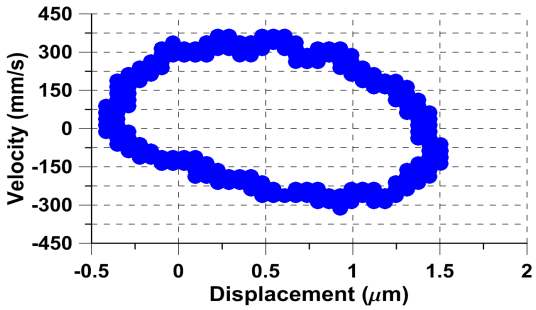

(b) Before

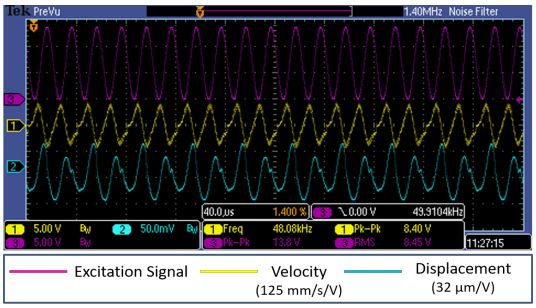

(c) After

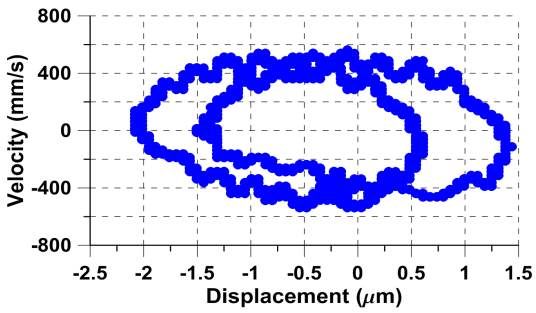

(d) After

Figure B.8: The time-histories (a and c) of the sensor velocity (yellow), displacement (blue), and excitation signal (magenta), and phase portraits (b and d) before and after gas release at excitation voltage $V_{\mathrm{dc}} = V_{\mathrm{ac}} = 6.86\,\mathrm{V}$

B.3 100 ppb Ethanol Vapor In Dry Nitrogen

2^{nd} **trial** After purging the test chamber with dry nitrogen for 15 minutes, a mixture of 1 ppm ethanol vapor in dry nitrogen was slowly released into the chamber. Detection (dynamic pull-in) occurred in two minutes and 35 seconds from gas release, Fig. B.9. The length of time required for detection indicates that the sorbed mass was small enough to marginally exceed the cyclic-fold bifurcation point. Therefore, 1 ppm ethanol is very close to the sensor detection threshold at

[H]

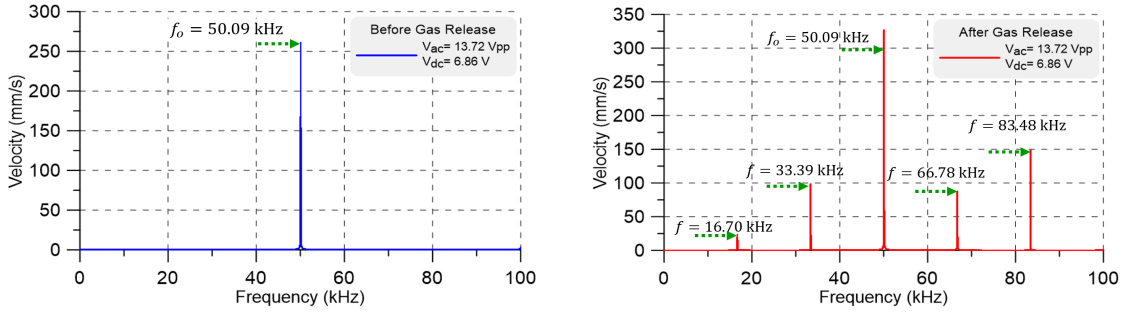

(a) Before (b) After

Figure B.9: The velocity FFT response before (a) and after (b) at excitation voltage $V_{\mathrm{dc}} = V_{\mathrm{ac}} = 6.86$ V

this operating point.

The velocity and displacement time histories were recorded using the oscilloscope before and after gas release as shown in Fig. B.10 (a) and (c). Period doubling bifurcation of order two was observed after detection occurred due to the sorbed mass as shown in Fig. B.10 (b) and (d).

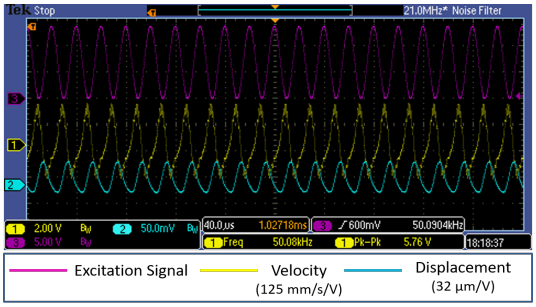

(a) Before

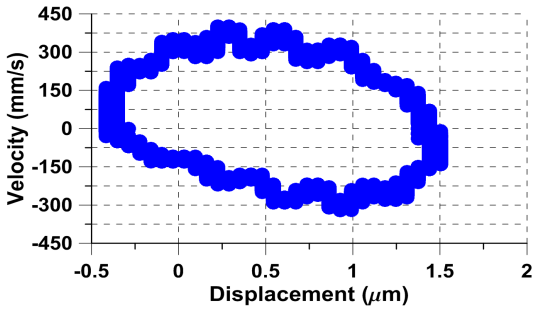

(b) Before

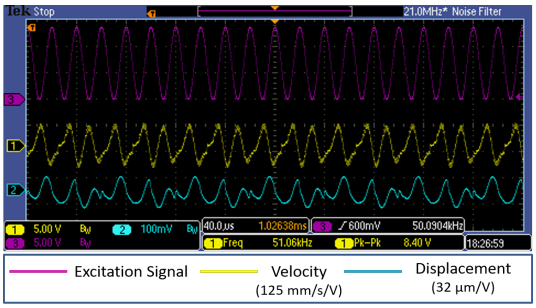

(c) After

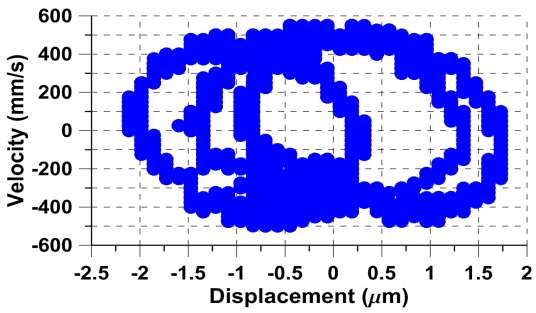

(d) After

Figure B.10: The time-histories (a and c) of the sensor velocity (yellow), displacement (blue), and excitation signal (magenta), and phase portraits (b and d) before and after gas release at excitation voltage $V_{\mathrm{dc}} = V_{\mathrm{ac}} = 6.86\,\mathrm{V}$

3^{nd} **trial** After purging the test chamber with dry nitrogen for 15 minutes, a mixture of 1 ppm ethanol vapor in dry nitrogen was slowly released into the chamber. Detection (dynamic pull-in) occurred in two minutes and 17 seconds from gas release, Fig. B.11. The length of time required for detection indicates that the sorbed mass was small enough to marginally exceed the cyclic-fold bifurcation point. Therefore, 1 ppm ethanol is very close to the sensor detection threshold at this operating point.

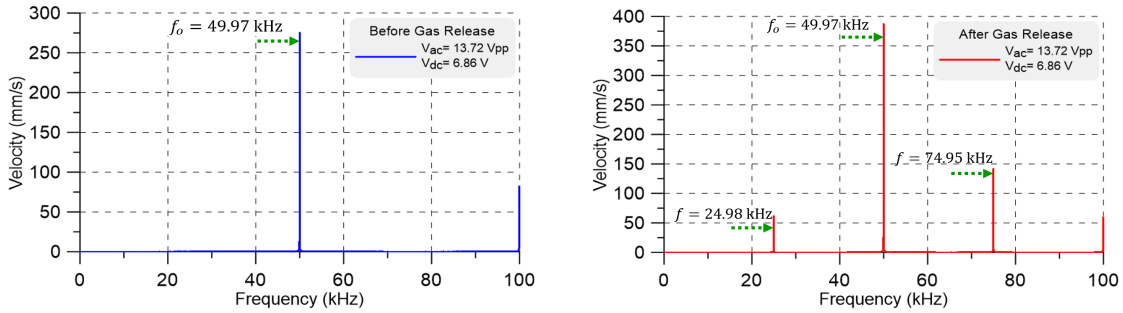

(a) Before (b) After

Figure B.11: The velocity FFT response before (a) and after (b) at excitation voltage $V_{\mathrm{dc}} = V_{\mathrm{ac}} = 6.86$ V

The velocity and displacement time histories were recorded using the oscilloscope before and after gas release as shown in Fig. B.12 (a) and (c). Period doubling bifurcation of order two was observed after detection occurred due to the sorbed mass as shown in Fig. B.12 (b) and (d).

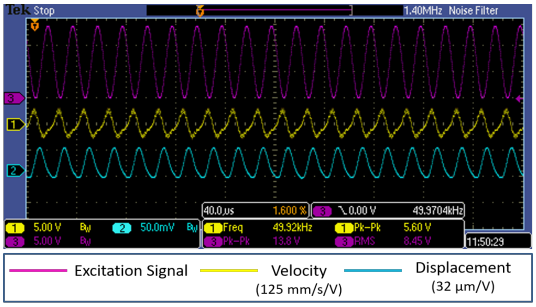

(a) Before

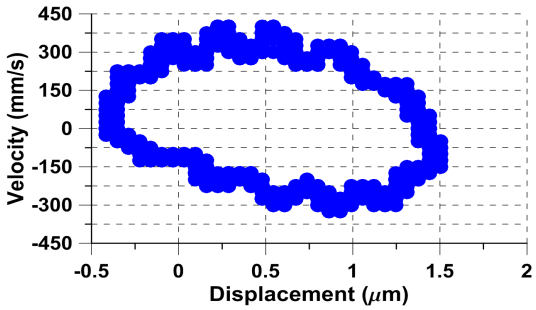

(b) Before

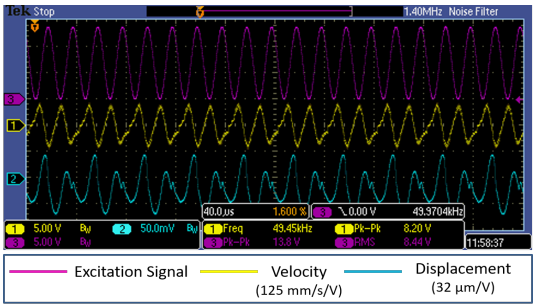

(c) After

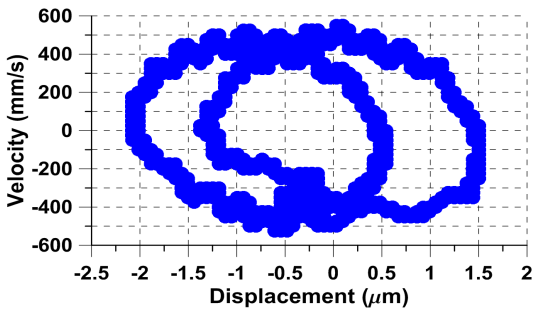

(d) After

Figure B.12: The time-histories (a and c) of the sensor velocity (yellow), displacement (blue), and excitation signal (magenta), and phase portraits (b and d) before and after gas release at excitation voltage $V_{\mathrm{dc}} = V_{\mathrm{ac}} = 6.86\,\mathrm{V}$

B.4 50 ppb Ethanol Vapor In Dry Nitrogen

2^{nd} **trial** Same procedure was applied by releasing slowly a mixture of 100 ppb ethanol vapor in dry nitrogen into the chamber. No detection (dynamic pull-in) was observed during 15 minutes from gas release, Fig. B.13. As a results, this demonstrates the upper bound of the sensor limit to detect ethanol at the operating frequency, $f_{\circ} = -50\,\mathrm{Hz}$. The sorbed mass was small enough to remain but did not exceed the cyclic fold bifurcation point.

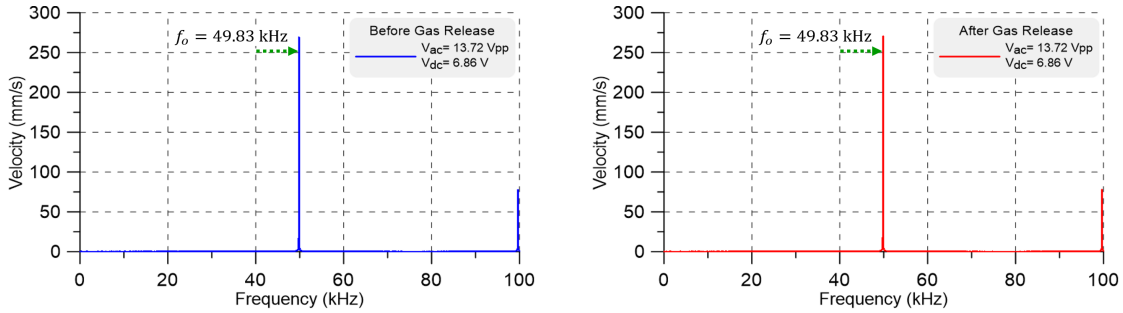

(a) Before (b) After

Figure B.13: The velocity FFT response before (a) and after (b) at excitation voltage $V_{\mathrm{dc}} = V_{\mathrm{ac}} = 6.86$ V

The velocity and displacement time-histories of the sensor before and after detection were recorded using the oscilloscope, Fig. B.14 (a) and (c). No changes in the velocity amplitude was observed in the two figures. Also, the phase portrait shows only one orbit before and after gas release, Fig B.14 (b) and (d).

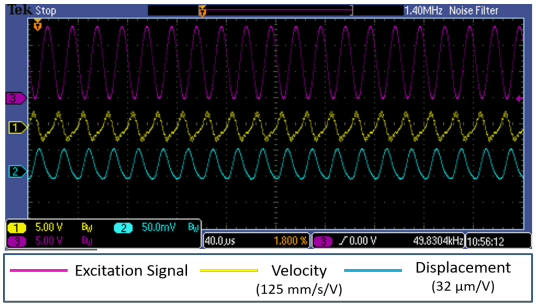

(a) Before

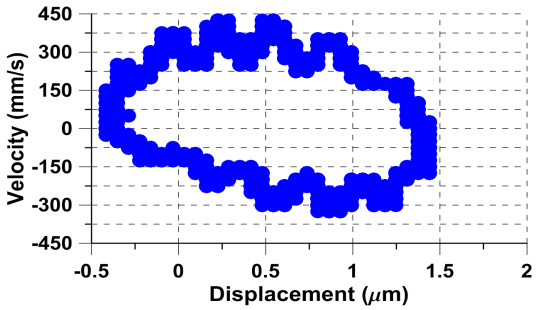

(b) Before

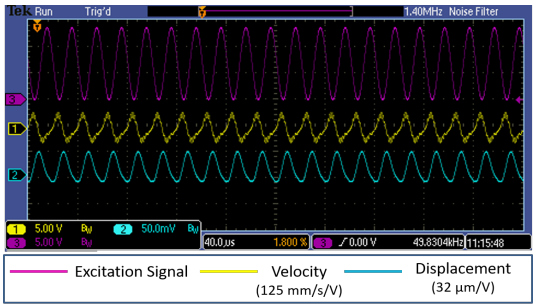

(c) After

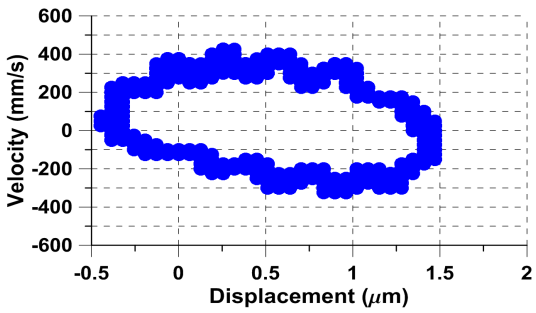

(d) After

Figure B.14: The time-histories (a and c) of the sensor velocity (yellow), displacement (blue), and excitation signal (magenta), and phase portraits (b and d) before and after gas release at excitation voltage $V_{\mathrm{dc}} = V_{\mathrm{ac}} = 6.86\,\mathrm{V}$

3^{nd} **trial** Same procedure was applied by releasing slowly a mixture of 100 ppb ethanol vapor in dry nitrogen into the chamber. No detection (dynamic pull-in) was observed during 15 minutes from gas release, Fig. B.15. As a results, this demonstrates the upper bound of the sensor limit to detect ethanol at the operating frequency, $f_\circ = -50\,\mathrm{Hz}$. The sorbed mass was small enough to remain but did not exceed the cyclic fold bifurcation point.

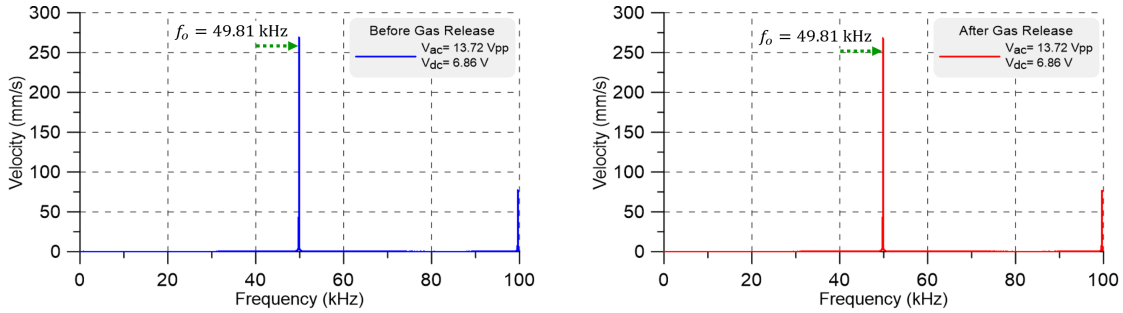

(a) Before (b) After

Figure B.15: The velocity FFT response before (a) and after (b) at excitation voltage $V_{\mathrm{dc}} = V_{\mathrm{ac}} = 6.86$ V

The velocity and displacement time-histories of the sensor before and after detection were recorded using the oscilloscope, Fig. B.16 (a) and (c). No changes in the velocity amplitude were observed in the two figures. Also, the phase portrait shows only one orbit before and after gas release, Fig. B.16 (b) and (d).

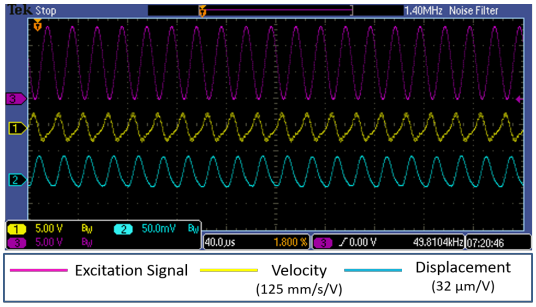

(a) Before

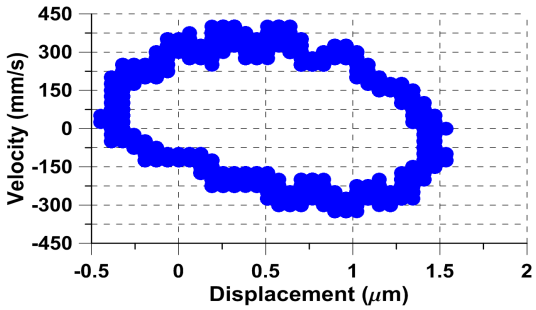

(b) Before

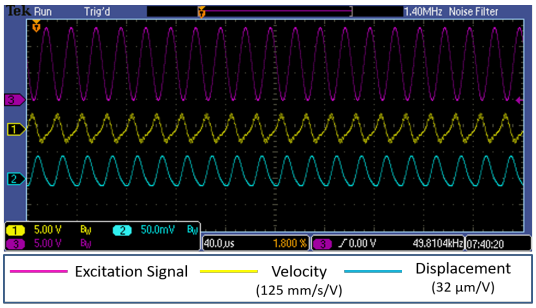

(c) After

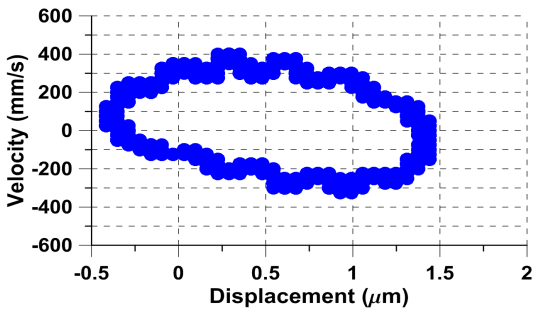

(d) After

Figure B.16: The time-histories (a and c) of the sensor velocity (yellow), displacement (blue), and excitation signal (magenta), and phase portraits (b and d) before and after gas release at excitation voltage $V_{\mathrm{dc}} = V_{\mathrm{ac}} = 6.86\,\mathrm{V}$